Assessing indoor overheating in cities using building- and urban-scale models with enhanced methods for longwave radiation, wind and natural ventilation

A thesis submitted for the degree of Doctor of Philosophy

School of the Built Environment

Xiaoxiong Xie

December 2022

Declaration

I confirm that this is my own work and the use of all material from other sources has been properly and fully acknowledged.

Xiaoxiong Xie

Acknowledgements

Firstly, I am deeply grateful to my supervisors Prof. Zhiwen (Vincent) Luo and Prof. Sue Grimmond, who gave me the opportunity to conduct this research. I would like to thank them for the continuous support throughout the PhD with valuable discussions, advice and encouragement. Special thanks go to Dr. Ting Sun for his help in coding and SUEWS modelling. I have been so fortunate to work with him and have learnt a great deal from him.

I would like to thank all the co-authors I have worked with, in particular: Dr. Lewis Blunn for helping me a lot in SUEWS modelling and modifying wind pressure coefficients; Dr. William Morrison for providing observation data for evaluating the longwave radiation calculation method; and all other co-authors who have contributed to the generation of urbanised weather data with SUEWS.

Thanks to colleagues and friends in the School of the Built Environment, UrbanMet group in the Department of Meteorology, and those who have visited Reading. They have greatly enriched my PhD life and given me the sense of belonging to the community.

Thanks to my past instructors and advisors who inspired and supported my interest in research, particularly Dr. Abigail Hathway and Dr. Danielle Densley Tingley during my master study, and Prof. Lin (Vivien) Lu, Prof. Kwok Wai (Horace) Mui and Prof. Mingli Chen during my undergraduate study.

Finally, I must thank my family for their unconditional support in any decision I make. Also, thanks to my friends for bringing me pleasure despite being in different places around the world.

Abstract

Buildings in densely populated urban areas may be at higher risk of overheating due to the canopy layer urban heat island, especially in hot-humid climates like Sri Lanka when there is limited use of air-conditioners. Previous efforts to combine a building energy simulation (BES) tool with neighbourhood-scale urban-canopy models do not adequately account for all neighbourhood factors, notably the modelling of longwave radiation and natural ventilation with urbanised wind speeds are not well addressed. As a result, influences of urban neighbourhood characteristics are not well understood when using BES tools to assess the risk of indoor overheating.

This thesis uses the urban land surface model, Surface Urban Energy and Water Balance Scheme (SUEWS), and BES tool EnergyPlus to assess the indoor overheating risk of neighbourhood buildings in urban areas. An iterative approach is proposed for EnergyPlus longwave radiation simulations. Up to 60 % difference in nocturnal overheating degree-hours is found compared to the default method, clearly demonstrating improvement. Modifications are made to wind pressure coefficients to improve the EnergyPlus natural ventilation calculation for urban buildings.

The new method is applied in different multi-scale case studies. The natural ventilation potential is assessed in idealised neighbourhoods across Chinese climate zones, suggesting it is influenced by the combined effects of regional climate, neighbourhood-scale climate and time of the year.

The spatial and temporal distribution of the population to heat exposure during a heatwave in Colombo, Sri Lanka are accounted for. Analyses undertaken for a typical Colombo dwelling in different neighbourhoods highlights the urban and neighbourhood influences on indoor overheating risks and mitigation measures.

Findings of this thesis extend current understanding of influences of urban factors on indoor thermal environment. The methods, datasets, and models created in this thesis can be used in future research and to assist policy making.

Table of Contents

Chapter 1 Introduction

1.1. Motivation

Since the 1950s, with climate change extreme heat events have been observed to occur more often and last longer, and this trend is projected to continue and/or increase in the future decades (IPCC, 2014). Heat exposure may cause thermal discomfort to heat-related fatal diseases (Kovats and Hajat, 2008), with heatwaves causing a large number of deaths worldwide in recent years. For example, the August 2003 European heatwave resulted in 15000 excess deaths in France and over 2000 excess deaths in England, with the vast majority being elderly (Public Health England, 2015). Heatwaves periods lead to severe heat exposure impacts in both outdoor and indoor environments.

With 55% of the world's population living in urban areas (in 2018), and a probable increase to 68% by 2050 (United Nations, 2018), urban areas have higher heat exposure risks than rural areas exacerbated by periods with large canopy layer urban heat island (CL-UHI) intensities (Kovats and Hajat, 2007; Oudin Åström et al., 2011). Heatwaves can enhance CL-UHI magnitude under certain conditions related to increased solar radiation, more anthropogenic heat emissions from air conditioning systems, enhanced evaporation in rural areas and increased heat storage (Kong et al., 2021; Li and Bou-Zeid, 2013; Ramamurthy and Bou-Zeid, 2017). Thus, during extreme heat events, more densely populated urban areas have higher overheating risks.

Urban characteristics influence indoor overheating in many ways (Mills, 2006; Oke et al., 2017). Densely built urban morphology can block solar radiation, reducing indoor solar heat gain, but increase longwave radiation receipt given the large view factors of warm surrounding buildings (cf. cooler sky). Reduced wind speed weakens natural ventilation cooling effect and reduce heat convection from building surfaces. With heavyweight building materials, the release of daytime stored heat at night increases the nocturnal overheating risks. The impervious surfaces reduce the source of moisture for evaporative cooling. Intense human activities in cities release anthropogenic heat and expels warm air. All these factors should be considered when assessing the indoor overheating risk of urban buildings.

Building energy simulation (BES) tools are used to dynamically simulate the building thermal characteristics, heating/cooling loads and operation energy consumption (Clarke, 2001). They are also useful for predicting and assessing the indoor overheating risk. In recent years, various BES tools have been developed, including the free, open-source software EnergyPlus (U.S. Department of Energy, 2020a) which is well evaluated and widely used to assess both building energy performance (Chan, 2011; Liu et al., 2015; Ciancio et al., 2018; Yang et al., 2019) and overheating risks (Demanuele et al., 2012; Mavrogianni et al., 2012; Oikonomou et al., 2012; Virk et al., 2015; Hwang et al., 2017). However, BES tools like EnergyPlus originally (and typically) treat buildings as being isolated, using weather data input acquired from meteorological stations located in open country. When modelling urban buildings, using rural weather data as input will cause biases. In existing studies using EnergyPlus to simulate indoor overheating risks, the influence of urban climate is often ignored. Previous studies have made efforts to address this issue by combining EnergyPlus with urban climate models (Bueno et al., 2011; Miller et al., 2018; Yang et al., 2012), but none of these studies fully considered urban impacts on buildings mentioned above, especially neglected the urban wind field and the longwave radiation.

South Asia countries are strongly affected by climate change. For example, the 2015 heatwave caused around 3500 deaths (ESCAP, 2015), and April 2022 the hottest in South Asia since 1900 affected more than a billion people (Mogul et al., 2022). Amongst the largest temperature changes in the region in recent decades have occurred in Sri Lanka (Sharma et al., 2022) but there is little residential air conditioning available (5% of single-storey houses, 10% of multi-storey houses in 2018) (Sri Lanka Ministry of Environment, 2019). Measurements and surveys find Sri Lankan buildings can have high indoor overheating risks without air-conditioners. For example, in Colombo office buildings air temperatures of up to 42 °C measured on a typical hot sunny day in 2017 (Rajapaksha, 2020). This suggests many households in Sri Lanka need to rely on passive cooling measures to protect them from the overheating risk. The limited Sri Lankan indoor overheating research has not considered urban impacts when assessing indoor overheating.

This thesis aims to assess the indoor overheating risk of urban buildings while taking urban climate into account with the capital city of Sri Lanka, Colombo, taken as a case study. Methods are proposed to improve EnergyPlus' ability to simulate inter-building longwave radiative exchange and natural ventilation rate for urban buildings. The set of methods is applied in idealised and real urban scenarios, respectively. In idealised scenarios, the natural ventilation potential of a simplified building is assessed in different neighbourhood and climate settings. In real scenarios, the spatial and temporal distributions of population heat exposure during a heatwave period in 2020 is mapped for Colombo, Sri Lanka. Indoor overheating risks and effects of passive cooling interventions are assessed for a typical dwelling in selected neighbourhoods.

1.2. Objectives and thesis structure

The specific objectives of this PhD thesis are:

- To improve existing indoor overheating risk assessment by accounting for the urban impacts via combining an urban land surface model [Surface Urban Energy and Water Balance Scheme (SUEWS)] and building energy simulation tool [EnergyPlus]
- To propose a new approach to enhance the inter-building long-wave radiation calculation in EnergyPlus
- To improve the existing approach in EnergyPlus determining wind-driven natural ventilation especially for urban buildings
- To apply the new building-urban climate modelling framework to investigate the impacts of local-scale climate on indoor overheating risks of naturally ventilated dwellings using Colombo, Sri Lanka as a case study

To achieve these objectives, the PhD is structured in the following way:

Chapter 2 gives the detailed background of the research topic and reviews of current understanding in the literature.

In Chapter 3 [1] an approach to improve EnergyPlus's ability to account for longwave radiation from surrounding buildings on the external facets of a building of interest is

[1] Published as:
Xie, X., Luo, Z., Grimmond, S., Sun, T., Morrison, W., 2022. Impact of inter-building longwave radiative exchanges on building energy performance and indoor overheating. Build. Environ. 209, 108628.

proposed, and assessed considering impacts of these changes on building indoor thermal environment and overheating risks in different building densities and climates.

In Chapter 4 [1] current problems of natural ventilation calculation in EnergyPlus are identified that are due to incorrect use of wind pressure coefficients. Modifications are proposed to improve the accuracy of EnergyPlus's natural ventilation simulation, especially for buildings in urban settings.

In Chapter 5 [2] the approaches from Chapter 3 and 4 are used together with the neighbourhood-scale model SUEWS to investigate the natural ventilation potential of buildings in idealised neighbourhoods, considering different building densities and climates.

In Chapter 6 [2] SUEWS is used to map the spatial (in 500 m resolution) and temporal (hourly) distribution of population *outdoor* heat exposure in Colombo, Sri Lanka during a heatwave in 2020, and assesses effects of urban-scale cooling strategies for a 2035 projection scenario.

In Chapter 7 [2], SUEWS-EnergyPlus are used to investigate *indoor* overheating risks and effects of different passive cooling interventions of a typical Colombo dwelling in different neighbourhoods during the heatwave period.

---

[1] Published as:
Xie, X., Luo, Z., Grimmond, S., Blunn, L., 2022. Use of wind pressure coefficients to simulate natural ventilation and building energy for isolated and surrounded buildings. Build. Environ. 230, 109951.

[2] In form of papers.

Chapter 2 Background and literature review

This thesis addresses both indoor and outdoor processes relative to buildings and overheating.

Section 2.1 provides an overview of the definition and current approaches used to assess indoor overheating risks. Section 2.2 summarizes the factors that contribute to indoor overheating at both urban and building scales. In Section 2.3, existing methods of building energy simulation in the urban context are reviewed, with a particular focus on the neighbourhood and building-scale models used in this thesis. Finally, Section 2.4 summarizes the research gaps and outlines the overall research design of this thesis.

2.1. Indoor overheating assessment

The human body generates heat through metabolism, and gains or loses heat from the environment due to convection, radiation and sweat evaporation. However, the physiological function of the human body requires that the body temperature must be kept approximately constant to ensure the functions of the body stay normal, i.e. the vital organs require the ‘core temperature’ to be relatively constant (Nicol et al., 2012). Despite this there is no uniform definition of the term ‘overheating’, with it interpreted as either thermal discomfort or heat stress in different contexts (Beckmann et al., 2021; Holmes et al., 2016; Rahif et al., 2021), so both are summarised here.

2.1.1. Thermal discomfort assessment

When the ambient temperature changes, thermal sensation changes much faster than body temperature (Gagge et al., 1967). Hence, increased ambient temperature can quickly cause thermal discomfort. ASHRAE Standard 55 (ANSI/ASHRAE, 2013a) defines thermal comfort as the condition of mind that expresses satisfaction with the thermal environment and is assessed by subjective evaluation. Thermal discomfort can negatively impact productivity (Lan et al., 2011; Mohamed and Srinavin, 2005; Schellen et al., 2010).

The assessment of thermal comfort can be categorised into steady-state heat balance and adaptive approaches.

The most representative steady-state heat balance approach is Fanger's Predicted Mean Vote (PMV) (1970), which is to describe the relationship between the thermal load and the thermal sensation on the ASHRAE scale (Table 2.1). The PMV model is developed based on thermal comfort experiments in climate chambers with stable indoor environmental variables. It considers variables including the air and radiant temperature, air velocity, humidity, clothing insulation and metabolic rates (ANSI/ASHRAE, 2013a). The PMV represents the average thermal feeling in the certain environment, hence can be used to evaluate whether it is comfortable. As individual differences PMV may not represent the feelings of all people, the Predicted Percent Dissatisfied (PPD) describes the percentage of people who are dissatisfied with the thermal environment (Fanger, 1970). The Fanger's (1970) relation between PMV and PPD is adopted by ISO 7730 (1984).

If people are in naturally ventilated buildings, both the indoor and outdoor meteorological variables will by dynamic. As in naturally ventilated conditions actual thermal sensation survey results can differ from PMV (de Dear and Brager, 2002; Fanger and Toftum, 2002; Humphreys and Nicol, 2002), 'adaptive thermal comfort' is proposed (de Dear and Brager, 2002; Nicol and Humphreys, 2002). This assumes occupants do not passively accept a given thermal environment but recognizes there is a complex interaction between occupants and the indoor environment. Occupants can use psychological, behavioural and physiological adaptation measures to minimise the influence of factors causing discomfort and to improve their thermal comfort (de Dear and Brager, 1998; Nicol et al., 2012). Hence, the actual sensation to the thermal environment is different from the heat balance described by the steady-state model.

The first adaptive thermal comfort model used around 21000 field survey - measurement data sets collected from four continents and a broad spectrum of climatic zones to link indoor comfort (or thermal neutral) operative temperature (T_{comf}) with the monthly mean outdoor air temperature (de Dear and Brager, 1998). The provided linear regression equation, is adopted by ASHRAE 55 (ANSI/ASHRAE, 2013a). Similarly, the adaptive model for the European climate (Nicol and Humphreys, 2002)) is adopted by the European standard EN 15251 (CEN, 2007). Other adaptive models have been developed for different both countries and climates, with some adopted in international building codes (Table 1 of de Dear et al. (2020), Table 4 of Rahif et al. (2021)).

Despite limitations the adaptive model has become the mainstream approach to reflect the realistic thermal requirements for the occupants of built environments (de Dear et al., 2020). A key criticism of adaptive models is there 'black box' nature of giving a comfort temperature without the behavioural and physical causes (Nicol et al., 2012). Second, it uses outdoor air temperature as the input variable without considering other factors influencing indoor thermal comfort (e.g. indoor air velocity and humidity) (Nicol, 2004; Vellei et al., 2017). Third, it provides comfort zones rather than thermal sensation. Fourth, it has a relatively short history (cf. the steady-state model) so further work is needed to improve it (de Dear et al., 2020).

Both too cool and too warm temperatures can cause thermal discomfort. Here overheating refers to discomfort from high temperatures. The sense of discomfort essentially gives us information about skin temperature, providing warning of conditions that might pose a danger to the core temperature (Nicol et al., 2012). Therefore, thermal (dis)comfort approaches are usually used to assess the indoor overheating risk for residential buildings by various international standards and national building codes (de Dear et al., 2020; Rahif et al., 2021).

Here we summarise frequently referenced standards in indoor overheating studies and their indoor overheating assessment criteria (Table 2.2). Critical thresholds are either fixed or calculated from adaptive thermal comfort models. Fixed thresholds provide a 'light-touch' risk assessment option, which may be preferable for the housing industry, but only applicable to particular combinations of indoor thermal and occupant conditions (Pathan et al., 2017). Fixed thresholds are more applicable in steady conditions (e.g. air-conditioned buildings) while for naturally ventilated buildings the adaptive model is recommended (Rahif et al., 2021). With temperature thresholds, the overheating risks are often quantified as the number of hours and degree-hours exceeding the thresholds. Older standards (e.g. CIBSE Guide A (2006)) only consider overheating hours, which measure the occurrence of overheating but not the severity. Nicol et al. (2009) suggest that a building exceeding the discomfort threshold temperature by 5 °C for 3 hours would be considered more serious than exceeding by 1 °C for 20 hours to a larger proportion of building occupants. The newer CIBSE TM52 (2013) standard now has both overheating hours and degree-hours criteria.

The adaptive model used in CIBSE TM52 is (Nicol and Humphreys, 2010):

$$T_{comf} = 0.33 \times T_{rm} + 18.8 \qquad (2.1)$$

where the running mean outdoor temperature T_{rm} is (Nicol and Humphreys, 2010):

$$T_{rm} = (1-k)(T_{od-1} + kT_{od-2} + k^2T_{od-3} \cdots + k^6T_{od-7}) \qquad (2.2)$$

where k is a constant between 0 and 1, with 0.8 used as recommended (Nicol and Humphreys, 2010), T_{od-n} is the daily mean outdoor temperature n days ago (°C).

The maximum acceptable temperature T_{max} is defined as 3 °C above T_{comf}, which corresponds to the PPD ≤ 10% (90 % satisfaction) according to EN 15251 (CEN, 2007):

$$T_{max} = 0.33 \times T_{rm} + 21.8 \qquad (2.3)$$

Of three criteria, if a building fails two or more, CIBSE TM52 deems it to be at unacceptable risk of overheating:

- *Hours of Exceedance:* a limit of 3% of occupied hours when the operative temperature exceeds T_{max} during a typical non-heating season (i.e. 1 May to 30 September).
- *Daily Weighted Exceedance:* weighted sum of daily degree-hours exceeding T_{max} should ≤ 6
- *Upper Limit Temperature (T_{upp}):* absolute maximum acceptable temperature for a room should not exceed: $T_{upp} = T_{max} + 4$

These criteria cover the duration and severity of overheating and extreme conditions and provide examples of overheating risk quantification. In applications, these criteria may not be all used, but both overheating hours and degree-hours are often used to compare overheating risks with different combination of influencing factors (Di Perna et al., 2011; Figueiredo et al., 2016; Hamdy et al., 2017; Makantasi and Mavrogianni, 2016; Stazi et al., 2015; van Hooff et al., 2014). Although CIBSE TM52 is for the UK climate, similar approaches are used in different climates (de Dear et al., 2020; Rahif et al., 2021).

In summary, for natural ventilation buildings, using adaptive thermal comfort models with metrics of overheating hours and/or degree-hours is the mainstream method of overheating assessment.

Table 2.1: The ASHRAE scale of thermal sensations (ANSI/ASHRAE, 2013a).

Descriptor	Cold	Cool	Slightly cool	Neutral	Slightly warm	Warm	Hot
Code	-3	-2	-1	0	1	2	3

Table 2.2: Commonly indoor overheating criteria standards of the year released. T_{op}: operative temperature, T: air temperature.

Standards	Indoor variable	Criteria of overheating	Threshold	Metric	Studies applying the criteria
CIBSE Guide A (2006)	T_{op}	For dwellings: Living areas: 1% annual occupied hours over 28 °C Bedroom: 1% annual occupied hours over 26 °C	Fixed	Hours	(Makantasi and Mavrogianni, 2016; Mavrogianni et al., 2014; McLeod et al., 2013; Ridley et al., 2014)
Housing Health and Safety Rating System (2006)	T	Temperatures exceeding 25°C	Fixed	-	(McLeod and Swainson, 2017; Morgan et al., 2017)
The passive house planning package (PHPP) (2007)	T	Temperatures exceeding 25°C for more than 10% of the year	Fixed	Hours	(Morgan et al., 2017; Ridley et al., 2014)
Standard Assessment Procedure (SAP) (2012)	T	< 20.5°C: not significant; 20.5°C to 22.0°C: Slight; 22.0°C to 3.5°C: medium; ≥ 23.5°C: high	Fixed	-	(Tillson et al., 2013)
CIBSE TM52 (2013)	T_{op}	Adaptive thresholds based on the equation of Nicol and Humphreys (2010)	Adaptive	Hours and degree hours	(Fletcher et al., 2017; McGill et al., 2017; Mulville and Stravoravdis, 2016; Ridley et al., 2014; Tabatabaei Sameni et al., 2015; Vellei et al., 2017; Virk et al., 2015)
CIBSE Guide A (2015)	T_{op}	Not exceeding 25 °C for more than 5% of occupied hours and 28°C for more than 1% of occupied hours	Fixed	Hours	(Morgan et al., 2017; Mulville and Stravoravdis, 2016)
		As CIBSE TM 52			

2.1.2. Heat stress assessment

When body temperature increases, the central regulation of human body will increase heat dissipation by transporting some portion of venous blood that stores excess metabolic heat to the skin to induce sweating (Lim, 2020). However, in hot environments and particularly during physical work, the function of central regulation of body temperature will be challenged, and may be eventually lost as it moves to uncommendable heat stress (Cheung et al., 2000; Taylor, 2000). Clinical syndromes due to heat stress include heat stroke, heat exhaustion, heat syncope, and heat cramps, which can lead to death if not treated properly (Kilbourne, 1996; Kovats and Hajat, 2008).

Various heat stress indices are developed to combine the complex environmental variables into single indices, and quantify the stress of the thermal environment on the human body (Beshir and Ramsey, 1988). In general, heat stress indicators can be empirical and analytical (or rational) indices (Beshir and Ramsey, 1988; Brake and Bates, 2002). Empirical indices are developed from field experiments and generally expressed in terms of some environmental parameter (e.g. temperature-like indices) instead of physiological parameters (Brake and Bates, 2002). While analytical indices are physiological parameters (e.g. sweat rate and core temperature) obtained by analysing the heat balance of the human body. Examples of the empirical indicator and analytical indicator are the Wet-bulb globe temperature (WBGT) used in ISO 7243 (2017) and predicted heat strain (PHS) used in ISO 7933 (2004). Although criticised as oversimplified, empirical indices are widely used in studies assessing the heat stress, especially climate or building modelling studies as empirical indices only require commonly available environmental parameters (Buzan et al., 2015; Oleson et al., 2015).

Heat stress indices are developed for conditions with risk of heat-related disorders, e.g., mines, factories and military training (Macpherson, 1962). However, with the climate change and increase in deadly extreme heat event, heat stress indices are gradually gaining attention for residential use (Holmes et al., 2016). Currently, heat stress indices are less commonly used for indoor overheating assessments compared to thermal comfort approaches, and usually focus more on extreme cases, e.g. power outages during heatwaves (Baniassadi et al., 2018; O'lenick et al., 2020; Phadke et al., 2019). Heat stress indices usually come with thresholds to define different warning levels, e.g., WBGT has thresholds at which the core temperature will reach 38 °C (ISO, 2017). With these thresholds, the indoor overheating risk can be also assessed with the same overheating hours and degree-hours approach as used with thermal comfort thresholds (Baniassadi et al., 2018). Additionally, the resiliency to extreme heat of the building can be assessed with the number of hours it takes from power outage to the first time reaching the heat stress threshold (Baniassadi et al., 2019)

It should be noted that most indices have been developed for use within certain combinations and ranges of environmental and other factors, and should not be used uncritically in environments and contexts for which they were not intended (Budd, 2008; Macpherson, 1962). Considering that like the steady-state thermal comfort model, most heat stress indices are developed with experimental data from climate chambers, they can have the same limitation that the indicator may not be suitable for naturally ventilated buildings and different climates.

2.2. Factors influencing indoor overheating

2.2.1. Urban impacts on buildings

The local climate condition surrounding the building directly influence the indoor thermal environment. For common naturally ventilated buildings, ways of heat transfer between indoor and outdoor include the conduction through the building envelope, convection at the building surfaces, ventilation through openings and radiation between the building and external surfaces. The heat conduction is influenced by the heat exchanges on the outside building surface, including the short- and long-wave radiation and convective flux exchange with outside air (U.S. Department of Energy, 2020b). And the natural ventilation can be driven by wind or buoyancy, which are influenced by the outdoor wind speed and indoor-outdoor air temperature differences.

Due to the different land covers and high-intensity human activities, the climate in the urban area is largely different from it in the rural area, and the climate can vary among neighbourhoods inside the city. Buildings in urban areas experience different risks of indoor overheating based on neighbourhood climate, building construction, and socio-economic factors of the residents. Urban factors influencing indoor thermal environment are summarised in Fig. 2.1 (Oke et al., 2017; Tang et al., 2021):

- **Street geometry**: the urban morphology affects the radiation and airflow. Due to the overshadowing from surrounding buildings, the solar heat gain on urban buildings is smaller than isolated buildings. However, the larger view factors to surrounding buildings with high surface temperatures can lead to more trapped longwave radiation. In the dense urban area, the average canopy wind speeds are lower than the rural area, which leads to lower wind-driven natural ventilation rate for buildings and less convention heat loss on building external surfaces.
- **Building fabric**: common building materials like the cement, asphalt and bricks are impervious and have high heat capacities. These will lead to larger heat storage and less evaporation, and lead to higher night temperatures than rural areas, and can increase nocturnal indoor overheating risks.

- **Human activities** (e.g. traffic and space heating/cooling): the intense human activities in cities release anthropogenic heat, and lead to higher air temperatures.

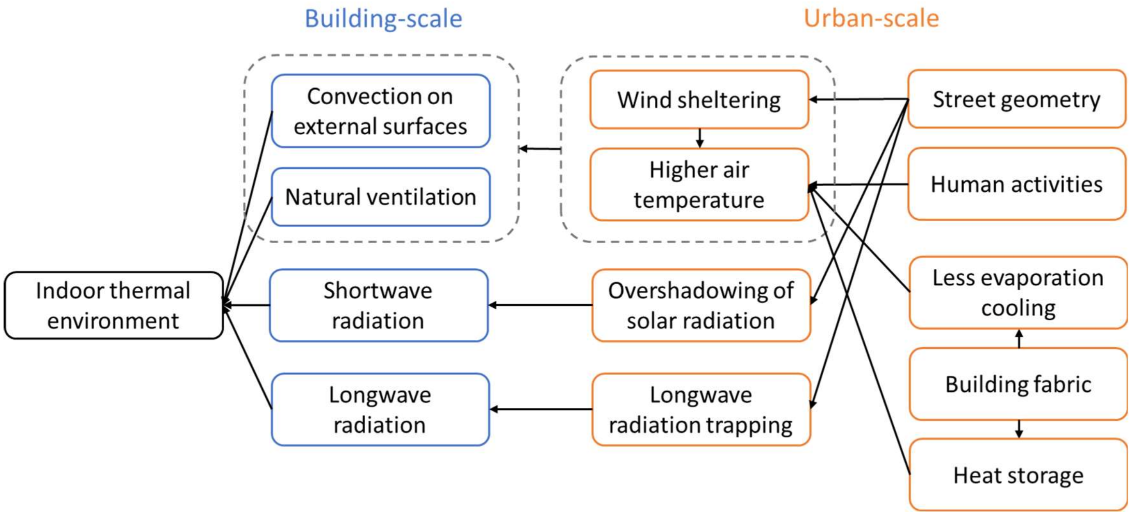

Fig. 2.1. Influences of urban factors on the indoor thermal environment.

2.2.2. Building factors in the urban context

The indoor overheating is a direct result from various sources of heat gain and ways of heat release. As mentioned in the previous section, sources of heat include the short- and long-wave radiation on the building facets, solar gain though windows, high outdoor air temperatures and internal heat gains. Thermal resistance of the building envelope can influence the processes of indoor-outdoor heat transfer (Fosas et al., 2018; McLeod et al., 2013; Porritt et al., 2011). Ventilation and other building characteristics, like the orientation and location (e.g. top floor), can also influence the indoor thermal environment (Dengel et al., 2016). Here we summarise the major factors considered to influence the indoor thermal environment and hence overheating risks based on literature (Fosas et al., 2018; Mavrogianni et al., 2014; McLeod et al., 2013; Taylor et al., 2014). Also, we consider the urban impacts on the effects of building factors.

2.2.2.1. Natural ventilation

Sensitivity study by Fosas et al. (2018) shows that natural ventilation is the most important factor related to indoor overheating. It is commonly agreed that limited ventilation rate could largely increase the indoor overheating risk, no matter what criteria were applied (Chvatal and Corvacho, 2009; Di Perna et al., 2011; Mavrogianni et al., 2014; Porritt et al., 2011; Psomas et al., 2016). European studies found that when windows were closed during the whole day, the maximum indoor operative temperature would rise around 5 °C to 8 °C and the mean indoor operative temperature would increase around 1 °C to 3 °C (Hamdy et al., 2017; Mavrogianni et al., 2014), while the percentage of overheating hours during summer can be up to 60 % higher than dwellings with always-open windows (Chvatal and Corvacho, 2009; Di Perna et al., 2011). Psomas et al. (2016) simulated dwellings located in four European cities with fixed ventilation rates and found reducing the air change rate from 1.5 to 0.5 would increase the overheated hours by 8% to 20%, depending on the climate, construction types and thresholds.

Although higher ventilation and infiltration rates are preferred in mild climates for passive cooling, it is reported by Baniassadi et al. (2018) that for very hot climates (e.g. Phoenix, US in their case), increased infiltration rate for buildings would further exacerbate overheating. The main reason is the continuously high outdoor temperature during both daytime and night-time. As the infiltration is uncontrolled, this highlights the importance of applying adaptive ventilation strategies, as the cooling effect of always-open windows largely depends on the climate.

To make full use of the passive ventilation cooling, most studies considered window rules in building simulations, which allow windows to be open under the outdoor temperature is low (e.g. at night). Multiple studies have suggested that night ventilation is one of the most effective passive cooling strategy for buildings in hot-humid climates (Doctor-Pingel et al., 2019; Gamero-Salinas et al., 2021; Jamaludin et al., 2014; Kubota et al., 2009; Ran and Tang, 2018; Zune et al., 2021). In hot climates where daytime outdoor air temperature is high, closing window may improve the indoor thermal comfort. For example, Ratnaweera and Hestnes (1996) found that during a typical hot day in Sri Lanka, closing windows during daytime could reduce the maximum air temperature by 1.7 °C.

Natural ventilation largely depends on the variable outdoor climate and the resultant changing driving forces. Hence, it needs to be assessed in different conditions. The natural ventilation potential of urban and rural areas also varies with the local-scale climate. Considering these impacts, assessing buildings in the urban environment using rural weather data will cause biases. A detailed review of natural ventilation potential assessment is given in Chapter 4, which suggests that there is a need for improving approaches to calculate natural ventilation potential when considering the local-scale climate.

2.2.2.2. Radiative heat exchange

Solar radiation is one of the main sources of indoor heat gain, therefore solar control measures are important to mitigate the indoor overheating. Common solar control measures include external and internal shading (e.g., overhang, external shutters, internal blinds, curtains) and reflective building envelope (e.g. solar reflective paint on roof and walls, solar control glazing) (Porritt et al., 2012). Overhangs above windows could reduce the peak indoor air temperature by 0.6 °C on a typical hot day according to simulation by Ratnaweera and Hestnes (1996). Cool roof are found to be more effective in tropical climates in reducing the indoor cooling energy demand than in other climates (Rawat and Singh, 2022), and modelling by Zingre et al. (2015) suggests that white paint (albedo = 0.74) on roof and walls could reduce the peak indoor air temperature by 2.4 °C on a typical sunny day in Singapore. Singh et al. (2008) found that for buildings in Mumbai, using solar control glazing windows with reflective film coating could reduce the predicted percentage of dissatisfied (PPD) of indoor thermal comfort by 47% compared to clear double-glazing windows. Here we consider the overhang, white paint on the roof and walls, and solar control glazing with low solar heat gain coefficients (SHGC) as measures related to solar control.

Buildings in the urban environment are usually surrounded by other buildings, which provides solar shading. Li and Wong (2007) found that for a surrounded building, the annual cooling energy use can be reduced by 7.3% compared to an isolated building. Pisello et al. (2014) reported that the solar gain through windows of the lower floors for the surrounded building could be 78% less than the isolated building. Taylor et al. (2014) suggested that shading effect from surrounding buildings statistically contributed to the larger differences in indoor overheating risks between climates due to different solar altitudes. Therefore, the solar shading from surrounding building cannot be ignored when assessing the indoor overheating risks for urban buildings.

In addition to short-wave radiation, the urban buildings also have larger longwave radiation exchanges with surrounding buildings (Oke et al., 2017), However, the impact of longwave radiation on building thermal environment is usually ignored or approximated (see detailed review in Chapter 2), which can cause biases. In this thesis we will investigate the calculation of longwave radiation and their impacts on indoor overheating risks.

2.2.2.3. Insulation

Insulation can be installed in roof or external walls to prevent heat transferring between indoor and outdoor spaces. For air-conditioned buildings, envelops with good thermal resistance could prevent heat loss in winter and/or heat gain in summer, thereby reduce energy consumption. However, the impact of insulation on free-running buildings can be bi-directional and influenced by other factors, since it may prevent heat releasing to outdoor environment as well. For example, Chvatal and Corvacho (2009) found that for building in Évora, Portugal, decreasing external wall U-value from 0.91 W $m^{-2}K$ to 0.2 W $m^{-2}K$ would increase the indoor overheating hours in summer if the window solar heat gain coefficient (SHGC) is larger than 0.32 but decrease if SHGC < 0.32. Baniassadi et al. (2018) compared the impact of updated version of local building codes in different U.S. cities, and found that higher insulation and air tightness levels could exacerbate indoor heat stress for buildings in relatively cooler cities like Albuquerque and Boise during summer power outages, but mitigate the heat stress in very hot climate like Phoenix. Studies by Fosas et al. (2018) and Makantasi and Mavrogianni (2016) highlighted the importance of sufficient ventilation in preventing increased overheating risks due to added insulation. Porritt et al. (2012) compared the internal and external insulation of walls and found that internal insulation could increase the overheating degree-hour by 14% and external insulation could decrease it by 49% during a nine-day heatwave in London. These indicate that the effect of insulation is linked to other factors including the climate, solar control, ventilation and thermal mass. Insulation can work better as a passive cooling intervention in hot climates as it prevents the inward heat conduction through building envelopes. However, precautions should be taken to minimise the heat gain for the indoor space, e.g. solar heat gain through windows. For buildings in tropical climate, it is suggested that less wall insulation should be used compared to buildings in cold climate to reduce the cooling energy use (Zune et al., 2021). Nevertheless, Ratnaweera and Hestnes (1996) found that for a Colombo dwelling on a typical day in December, adding 100 mm thick polystyrene to the asbestos roof could reduce the maximum air temperature by 0.2 °C as it prevented heat on the roof transferred to the interior.

Considering the impacts of different factors on the effect of insulation, how would insulation influence the indoor overheating risks in different local-scale climates needs further studies.

2.2.2.4. Other factors

Building types and the window orientation are also influencing the indoor thermal environment. According to prior studies, the building type with the lowest indoor overheating risk is the ground floor of multi-storey buildings like flats, as results of the low ground temperature and less area exposed to the sun (Hamdy et al., 2017). While those building types that have large roof area, like single-facing top floor flats without cross ventilation and single-storey bungalows, have higher overheating risk than other building types (Gupta and Gregg, 2013; Mavrogianni et al., 2012; Oikonomou et al., 2012). The north orientation is widely accepted as having the lowest indoor overheating risk for rooms in northern hemisphere (Figueiredo et al., 2016; Psomas et al., 2016), but there is no consensus for other orientations (Makantasi and Mavrogianni, 2016; Porritt et al., 2011). It should be noted that there is a large number of diversities existing in building designs, e.g. the building size, the arrangement and area of each room, etc. Thus, the normalisation of building types and orientation is challenging.

2.3. Building energy simulation in the urban context

The emergence of building energy simulation (BES) is for use to appraise options for change in terms of relevant issues from human health and comfort, through energy demand reduction, to sustainable practices (Clarke, 2001). In recent years, there are various BES tools developed (e.g. EnergyPlus (U.S. Department of Energy, 2020a), TRNSYS (TRNSYS, 2009), DeST (Yan et al., 2008), IES-VE (Integrated Environmental Solutions, 2018)) to dynamically simulate the building thermal characteristics, heating/cooling loads and operation energy consumption.

Considering differences between urban and rural climates, when modelling urban buildings, the urban impacts should be considered. In current studies, there are different approaches to consider urban climate in building simulation. EnergyPlus is a free BES tool that is well evaluated and widely used to assess building energy performance (Chan, 2011; Liu et al., 2015; Ciancio et al., 2018; Yang et al., 2019) and overheating risks

(Demanuele et al., 2012; Mavrogianni et al., 2012; Oikonomou et al., 2012; Virk et al., 2015; Hwang et al., 2017). As an open-source tool, EnergyPlus has been combined with different urban climate models to simulate the urban impacts on building performance. Bueno et al. (2011) coupled EnergyPlus and a urban canopy model Town Energy Balance (TEB) (Masson, 2000) by providing external building surface temperature to EnergyPlus, but did not consider influence of urbanised wind speed on ventilation. Yang et al. (2012) coupled EnergyPlus with a computational fluid dynamics (CFD) based microclimate model Envi-met (Bruse, 2004), which provides outdoor variables including air temperatures and relative humidity, and calculated radiation and convection fluxes to EnergyPlus. However, the impact of urbanised wind was only considered in external building surface convection, but not building ventilation. Also, the CFD-based model can be computationally expensive (e.g. 3-day run taking 168 hours on PC). Ramponi et al. (2014) modelled the natural ventilation potential of a urban building by using the urbanised air temperature and modified wind pressure coefficients, but did not consider full urban impacts on the building like the longwave radiation exchanges. Miller et al. (2018) coupled EnergyPlus with a urban energy model CitySim (Robinson et al., 2009), which only estimated the heat emission from surrounding buildings to modify outdoor temperatures, but did not consider the wind and radiation components. Therefore, there is a need for an approach to consider the complete urban impacts in building energy simulation while balancing the computational cost.

Since the processes of urban characteristics contributing to the surface energy balance is complex, the best way to study these processes individually is by using urban land surface models (ULSMs) (Best and Grimmond, 2015). There are many ULSMs existing, ranging from simple bulk representations of the surface to those considering the complete energy balance at various levels within the urban canyon (e.g. Fig. 1 of Best and Grimmmond (2015)). Comprehensive comparisons of these models had addressed gaps of lacking well-modelled latent heat flux, and suggested that having multiple models combined could give more accurate results (Grimmond et al., 2011, 2010). To fill the gap, the Surface Urban Energy and Water Balance Scheme (SUEWS) was therefore developed (Järvi et al., 2011).

In this study, the state-of-art model SUEWS (Järvi et al., 2011; Sun et al., 2020; Sun and Grimmond, 2019; Tang et al., 2021; Ward et al., 2016) is combined with EnergyPlus in this study to predict the indoor overheating risks for urban buildings. SUEWS uses surface characteristics and climate forcing data to simulate both energy and water fluxes, and then derive local-scale environmental parameters (Järvi et al., 2011; Ward et al., 2016). SUEWS is selected to be used in this study is because of its main advantages (Järvi et al., 2011, 2014; Ward et al., 2016; Ao et al., 2018; Kokkonen et al., 2018): 1) it provides vertical profiles of outdoor climate variables that can be used in EnergyPlus; 2) it only requires limited input data that can be relatively easily obtained; 3) it is a combination of multiple sub-models based on parameterisation to achieve balance between accuracy and computational cost; 4) it has been evaluated across different climates globally (e.g. Järvi et al. 2011, Ward et al. (2016), Table 3 of Lindberg et al. (2018), Tang et al. (2021). However, as a one-dimensional model that only account for vertical variations of variables, SUEWS simplifies some features of the building geometry. Therefore, the combination of SUEWS and EnergyPlus needs some work to better account for the impact of urban characteristics on buildings.

2.4. Summary

Based on the literature review, following research gaps are addressed:

- Indoor overheating risks of residential buildings have been extensively studies around the world, but few studies have sufficiently considered the impact of urban climate. Impacts of some building factors on indoor overheating may be influenced by the local-scale climate. For example, it is found that the effect of insulation on indoor thermal environment largely depends on the outdoor climate. Similarly, urban areas may have lower or higher natural ventilation potential compared to rural areas due to differences in the air temperature and wind speed.
- BES tools are typically developed for isolated building simulations. When modelling urban buildings, different urbanised variables should be considered, including the outdoor air temperature, humidity, wind speed, short- and long-wave radiations. Previous studies have made efforts to combine EnergyPlus with urban-scale models, but none of them have fully considered all urban impacts on buildings. In particularly, the calculation of longwave radiation exchange between buildings and natural ventilation affected by urban wind fields are lacked in most studies. In addition, among these approaches, CFD-based models like ENVI-met can provide

more accurate results but are computationally expensive, therefore not suitable for modelling in large spatial and temporal scales. There is a need of an approach that can fully consider urban impacts in BES, while balancing the computational cost.

To fill the gaps, this work combines the urban-scale model SUEWS and building-scale model EnergyPlus to assess the indoor overheating risks for urban buildings with improved methods of longwave radiation and natural ventilation calculation. Fig. 2.2 summarises the workflow of the thesis.

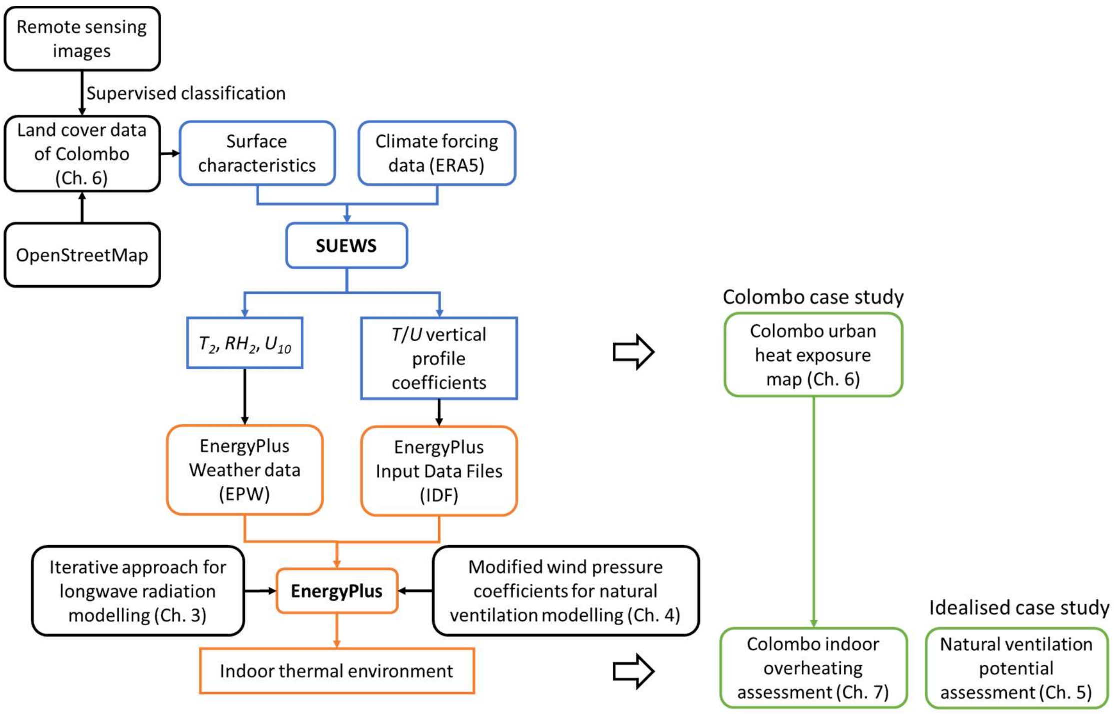

Fig. 2.2. Workflow of the thesis. T_2: 2 m air temperature; RH_2: 2 m relative humidity; U_{10}: 10 m wind speed.

Chapter 3 Impact of inter-building longwave radiative exchanges on building energy performance and indoor overheating

This chapter proposes a novel 'spin-up' approach for calculating inter-building longwave radiation in EnergyPlus, and investigates its impact on building energy performance and indoor overheating.

This chapter has been published as a journal paper: **Xie, X.**, Luo, Z., Grimmond, S., Sun, T., Morrison, W., 2022. Impact of inter-building longwave radiative exchanges on building energy performance and indoor overheating. Building and Environment, 209, 108628.

I conducted the research, wrote the first draft, and created the figures. Z. Luo and S. Grimmond provided guidance on the conception and structure of the paper, interpretation of the findings, and editing of the text. Additionally, W. Morrison provided observation data for model evaluation.

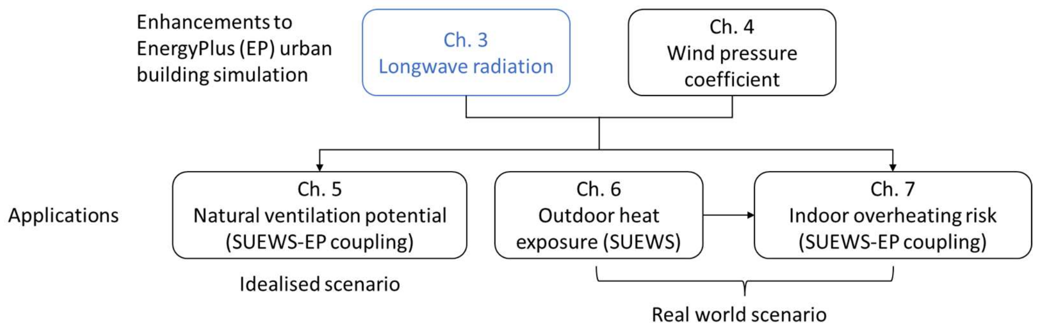

Nomenclature

F	View factor with subscripts (e.g. $boi \rightarrow a$: boi to air)
subscripts	
a	air
adj	adjacent
boi	building of interest
g	ground
sky	sky
T	Temperature (K)
subscripts	
a	Typical meteorological year (TMY) air temperature
adj	external surface of adj buildings
boi	external surface of boi
iso	external surface of isolated building

op	indoor operative (mean of air and radiant) temperature
α	albedo - external building facet
λ_P	plan area fraction

3.1. Introduction

The indoor thermal environment and cooling/heating energy consumption of buildings are affected by the local microclimate, including changes in longwave radiation from the surroundings. Longwave radiative exchange plays an important role in the urban heat island (Oleson et al., 2011), the urban energy balance (Oke, 1982), and in turn influences building energy performance (Santamouris et al., 2001). Ignoring longwave radiative exchanges with the surroundings in building energy simulations, can cause energy consumption to be overpredicted in winter and underpredicted in summer in mid-latitude cities (Bouyer et al., 2011).

Typically, building energy simulation (BES) tools are developed for isolated buildings and focus on the internal rather than external longwave radiation exchange (Allegrini et al., 2012; Evins et al., 2014) as obtaining both the external surface temperatures of the surroundings and the view factors in real urban areas is challenging (Yang et al., 2012; Evins et al., 2014). BES longwave radiative exchanges between buildings are either pre-calculated using an urban climate model (e.g., TEB (Bueno et al., 2011), ENVI-met (Yang et al., 2012) and CitySim (Miller et al., 2018)), or indoor radiation schemes have been applied to surrounding external facets (so-called "false zone", e.g. Vallati et al. (2018) and Allegrini et al. (2016) in TRNSYS). Both approaches have been restricted to simple geometries (e.g. symmetric and low-rise street canyons) (Evins et al., 2014).

Commercial software (e.g. TRNSYS) by definition has more restricted availability than open-access software. Free, open-source BES tools (e.g. EnergyPlus) tend to be well evaluated and widely used to assess building energy performance (Chan, 2011; Liu et al., 2015; Ciancio et al., 2018; Yang et al., 2019) and overheating risks (Demanuele et al., 2012; Mavrogianni et al., 2012; Oikonomou et al., 2012; Virk et al., 2015; Hwang et al., 2017). Urban climate studies using EnergyPlus have addressed different sources of air temperature (e.g. Chan, 2011; Ciancio et al., 2018; Salvati et al., 2017; Yang et al., 2019), but very few consider longwave radiative exchanges from adjacent buildings (Evins et al., 2014; Luo et al., 2020).

Three approaches are used to address longwave radiative exchanges between buildings with EnergyPlus according to our mini-review (Table 3.1). By default (#1, Table 3.1), the surface temperature of both the ground and adjacent buildings are assumed to be equal to the air temperature from weather data input. However, typically, air temperature has a smaller range than surface temperatures. In practise, roofs have the largest range (Morrison et al., 2020, 2021) and walls are warmer during both the day and night (e.g. summer in London: south wall peak 15 °C warmer (cf. canopy air temperature peak), minimum 3 °C warmer (Morrison et al., 2020, 2021)). Also, the timing of the peak temperatures differs with air being later than facet surface temperatures apart from the east facet (e.g. peak air temperature around 4 hours later than the south wall peak surface temperature on a summer day in London (Morrison et al., 2020, 2021)). Hence, using air rather than facet surface temperatures to derive longwave radiation is biased. This method assumes the view factors of the ground and adjacent buildings are equal to the residual of the sky (and further split into sky and air) view factors.

A second method (Evins et al. (2014), #2, Table 3.1) assigns surface temperatures of the building of interest (*boi*) to adjacent (*adj*)buildings. All buildings are assumed to have the same height. First, the *boi* wall temperatures are determined assuming it is isolated (*iso*). Second, these are assigned to the corresponding *adj* building (e.g., east-facing wall → east-facing wall). This neglects radiative exchanges for adjacent buildings.

In the third method (#3, Table 3.1), a new EnergyPlus sub-module allows view factors and *adj* facet surface temperatures to be supplied from an external source. Luo et al. (2020) assume the *adj* is isolated, therefore ignore the building density (i.e. plan area fraction) influence on surface temperature. They account for the real setting view factors by using Monte Carlo ray tracing. Although, the siting assumptions and view factors (e.g. values, methods) can be changed between applications, a more fundamental constraint is that the surface temperature data are a static time series that does not dynamically respond during the simulation.

Here, our aims are:

(1) to improve EnergyPlus' ability to account for longwave radiation from surrounding buildings impact on the external facets of a building of interest,

(2) to assess the impacts these model changes to simulated building surface temperature, building heating/cooling demand and indoor thermal environment (indoor overheating hours and degree-hours),
(3) to assess if these impacts are influenced by building density and/or climate,
(4) to assess if the impacts are sufficient to be regarded as an improvement to EnergyPlus simulation outcome.

Table 3.1: Methods used in EnergyPlus (E+) to calculate longwave radiation. View factor (F) are determined using ray-tracing with #3 using the Monte Carlos method (section 3.2.2 and Appendix 1). The temperatures of the ground (T_g) are assigned the Typical meteorological year (TMY) air temperature (T_a) in all three cases but the external surface of *adj* buildings (T_{adj}) are assigned different temperature between the three.

#	Urban geometry	View factors *(F)* considered	T_{adj}	Remarks	References
1	*boi* with *adj* buildings	$F_{boi\rightarrow sky}$; $F_{boi\rightarrow a}$ $F_{boi\rightarrow g} + F_{boi\rightarrow adj} = 1 - (F_{boi\rightarrow sky} + F_{boi\rightarrow a})$	T_a	default	Kesten et al. (2012), Oikonomou et al. (2012), Ramponi et al. (2014), Gracik et al. (2015), Han et al. (2017), Salvati et al. (2017), Vartholomaios (2017), Martinopoulos et al. (2018), Lima et al. (2019), Boccalatte et al. (2020)
2	Street canyon	$F_{boi\rightarrow sky}$ and slope of the building surface $F_{boi\rightarrow adj}$ for the street canyon	$T_{boi,iso}$	Needs: $F_{boi\rightarrow adj}$, T_{adj}	Evins et al. (2014)
3	A real case	$F_{boi\rightarrow adj}$ $1 - F_{boi\rightarrow adj} = F_{boi\rightarrow sky} + F_{boi\rightarrow a} + F_{boi\rightarrow g}$	$T_{adj,iso}$	Needs: $F_{boi\rightarrow adj}$, T_{adj}	Luo et al. (2020)

3.2. Methods

To compare inter-building longwave radiative exchange using the available methods in EnergyPlus, the building of interest (*boi*) is simulated assuming either it is isolated (*iso*) or with adjacent (*adj*) buildings at different densities and climates. To undertake this work, we use an idealised neighbourhood (3 × 3 aligned single-zone-buildings). EnergyPlus Version 9.4 (U.S. Department of Energy, 2020a) is used.

3.2.1. Building energy simulation setup in EnergyPlus

In this study we use the reference building BESTEST Case 600 from ANSI/ASHRAE Standard 140-2011 (ANSI/ASHRAE, 2011) for the analyses. This lightweight construction building (thermal properties are summarized in Table 3.2) is 8 m wide x 6 m long x 2.7 m tall, with no interior partitions, and two 2 m x 3 m windows on the south-facing wall. An ideal load system is assumed with a winter heating setpoint of 20 °C and summer cooling setpoint of 27 °C. The ventilation rate is 0.5 air change per hour (ACH). The internal heat load is constant at 200 W and assumed to be 100% sensible heat. To compare indoor overheating risks, the free-running building BESTEST Case 600 FF is used. Unlike Case 600, there is no mechanical heating or cooling system but everything else is the same (e.g. ventilation rate remains 0.5 ACH).

When the *boi* has adjacent buildings, they are all identical (Fig. 3.1). Given its replicability and generalisability, this idealised building has been widely used in neighbourhood-scale building energy simulation studies (e.g. #1, Table 3.1) (Liu et al., 2015). Building densities, characterised by the plan area fraction (λ_P), are varied (0.1, 0.3, 0.6) to cover a range found in real cities (Grimmond and Oke, 1999a). The *adj* buildings modify the radiative exchanges. View factors (F) between the *boi* surfaces and *adj* surfaces are calculated with Monte Carlo ray-tracing method (Howell et al., 2010) (Section 3.2.2). TMY (typical meteorological year) data (ASHRAE, 2001) for three cities with similar longitude but different latitudes are chosen, hence different daylengths and climates are investigated: London (51.15° N, 0.18° W), Aberdeen (57.20° N, 2.22° W) and Marseille (43.45° N, 5.23° E). The 10-min timestep simulations are used to assess convergence of the surface temperature but hourly sample are analysed.

Table 3.2: Main features of construction elements from ANSI/ASHRAE (2011), with the normal incidence window albedo given modified by incident angle (Arasteh et al., 2009).

Element	**Materials**	**U-value**	**α**	**ε**
Walls	Plasterboard, fiberglass quilt, wood siding	0.514	0.4	0.9
Roof	Plasterboard, fiberglass quilt, roof deck	0.318	0.4	0.9
Floor	Timber flooring, insulation	0.039	0.4	0.9
Windows	Double-pane glass	3.0	0.078	0.9

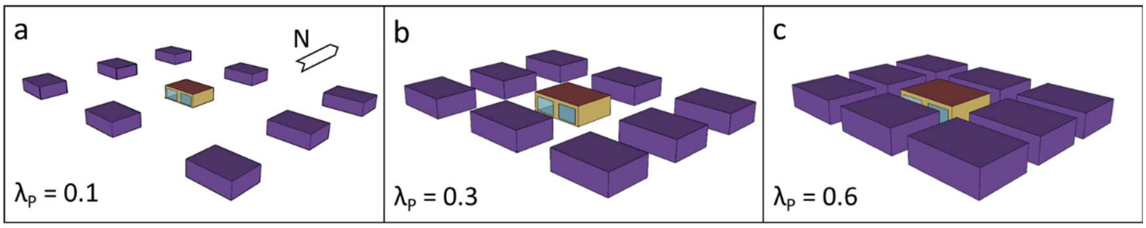

Fig. 3.1. Building of interest (*boi*) is in the centre of eight adjacent buildings (*adj,* purple), with different plan area fractions (λ_P): (a) 0.1, (b) 0.3, and (c) 0.6.

3.2.2. Inter-building longwave radiation exchange

The longwave radiative exchange between surfaces depends on surface temperature, spatial relations between surfaces and surroundings, and material properties of the surfaces (U.S. Department of Energy, 2020c). In the absence of more detailed information, the EnergyPlus default setting assumes (U.S. Department of Energy, 2020c): the ground is flat; the external surface temperature is equal to air temperature in the weather data input; all surfaces (including the ground) are opaque grey bodies; have isotropic emissivity; have uniform surface temperatures; no longwave reflection occurs; and across a sphere the total view factor (=1) from a building surface consists of only sky, ground, and buildings (U.S. Department of Energy, 2020b).

Previously, EnergyPlus obtains surface temperature data for an adjacent building (T_{adj}) from (Fig. 3.2): (1) TMY air temperature (T_a) (#1, Table 3.1), or (2) calculated surface temperatures for an isolated building (T_{iso}) (#2,3, Table 3.1). However, neither represents conditions where *adj* buildings are also influenced by other buildings in the neighbourhood. In this study, we determine the *adj* surface temperature using the Luo et al. (2020) sub-module. However, as Luo et al. (2020) originally used static surface temperatures, we investigate the impact of building surface temperatures used on model spin-up on the results as this is important in urban areas (Best and Grimmond, 2014). Luo et al. (2020) uses static surface temperature time series of which does not update after each iteration. In our new method, we spin-up the model by updating the building surface temperature from the previous run, until the EnergyPlus convergence criteria are met. Since EnergyPlus cannot calculate the external ground surface temperatures, they remain equal to TMY air temperatures (i.e. the default setting in EnergyPlus).

For example, if the building of interest (*boi*) surface temperatures are obtained from an *adj* building that is isolated (T_{iso}) after *i* iterations (indicated as $boi_{adj\leftarrow iso,i}$), this involves the following steps (Fig. 3.2): (1) EnergyPlus is run for the entire year to obtain boi_{iso} (isolated *building of interest*) surface temperature T_{iso} at each time step; (2) T_{iso} is assigned to the *adj* buildings to initialise them by facet (e.g. surface temperature of N wall of boi_{iso} is assigned onto the N wall of *adj* buildings as a yearlong EnergyPlus schedule file in csv format, and so as for other three facets.) All buildings are identical; (3) EnergyPlus is re-run to obtain the surface temperatures of $boi_{adj\leftarrow iso}$ for the year; (4) Repeat Step (2), surface temperatures of $boi_{adj\leftarrow iso}$ are assigned to $boi_{adj\leftarrow iso,1}$ as T_{adj}; and,

(5) so on for each i with convergence assessment made for each wall facet. For external surface temperatures of each facet, this convergence criteria is 0.01 °C (Winkelmann, 2001). Iteration stops when the annual mean bias error (MBE, Section 3.2.4) between the current and previous iteration of each facet is within ±0.01 °C. Similar procedures are applied for $boi_{adj \leftarrow a,i}$ with T_a used for initialisation.

In these simulation, although other variables (e.g. air temperature, wind) that are also impacted by the surroundings (Tang et al., 2021), they do not vary from their original TMY values at each time step.

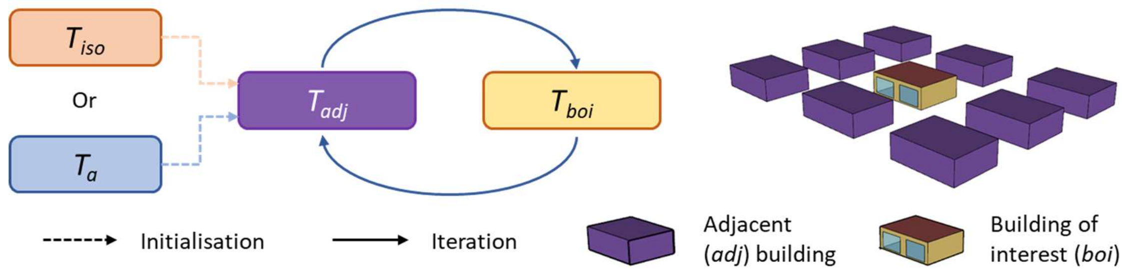

$boi_{adj \leftarrow iso}$	T_{adj} from T_{iso}	$boi_{adj \leftarrow iso,i}$	i^{th} iteration after $boi_{adj \leftarrow iso}$
$boi_{adj \leftarrow a}$	T_{adj} from T_a	$boi_{adj \leftarrow a,i}$	i^{th} iteration after $boi_{adj \leftarrow a}$

Fig. 3.2. Simulation workflow for different cases with T_{iso} or T_a used as the initial T_{adj}. In subsequent iteration T_{adj} is used to calculate T_{boi}, and T_{boi} used for T_{adj} in the next simulation.

If T_a is assigned to *adj* buildings ($boi_{adj \leftarrow a}$), the default EnergyPlus view factor calculation method is used. As ground and *adj* buildings are assumed to have the thermal characteristics of air (U.S. Department of Energy, 2020c), the *boi* surface to non-sky surfaces view factor is obtained by subtracting the sky view factor from 1. It is assumed that the sky longwave radiance distribution is isotropic.

When surrounding buildings exist, EnergyPlus calculates the sky view factor for 144 points (6 zeniths x 24 azimuths) evenly distributed across the sky dome. The view factor is the fraction of building external surfaces receiving points (4 points per facet, the rectangular area is defined by its length and width) relative to the 144 sky dome points (U.S. Department of Energy, 2020d).

For the $boi_{adj \leftarrow iso}$ we follow Luo et al. (2020) and use a Monte Carlo ray-tracing approach from the building surface (Howell et al., 2010):

$$F_{1\to 2} = \frac{A_2}{n}\sum_{i=1}^{n}\frac{\cos\theta_1\cos\theta_2}{\pi r^2}H_{block} \quad (3.1)$$

where *n* is the number of pairs of randomly points on surfaces 1 and 2, A_2 the area of surface 2, *r* the ray length, *θ* is the angle between the ray and the surface normal, H_{block} indicates if the ray is blocked by other surfaces (= 0, obstructed) or not (= 1). In this study, we find *n* = 3000 to be sufficient by comparing the Monte Carlo method to analytical results (Appendix 1).

With view factors to *adj* building surfaces determined, the sky and ground view factors are given by the residual ($1 - \sum F_{adj}$). As all buildings in the neighbourhood are the same size, $F_{boi\to g}$ and $F_{boi\to sky}$ are equal. To reduce computational cost, we assume each *adj* building facet has uniform surface temperatures independent of material variations (e.g. glass, concrete) (Evins et al., 2014; Luo et al., 2020). Impact of this simplification has been analysed and the surface temperature difference is suggested to be smaller than 0.2 °C (Appendix 2).

3.2.3. Building heating/cooling load and overheating risk

Heating and cooling loads are calculated for Ideal Loads Air System with 100% efficiency (U.S. Department of Energy, 2020e) and setpoints of 20 °C for heating in winter and 27 °C for cooling in summer. The indoor overheating risk within free-running buildings is assessed based on the degree hours (Zhang et al., 2006; Porritt et al., 2011, 2012) exceeding indoor operative temperature thresholds of CIBSE Guide A (CIBSE, 2006) (28 °C for the living area and 26 °C for the bedroom). Given the single-zone *boi*, we split the day based on occupancy into night ('bedroom', 23:00 to 7:00) and day ('living room', 07:00-23:00) (Porritt et al., 2012). The CIBSE overheating thresholds, determined for the UK climate, may not be directly applicable to other climates, however, we use them in all climates (i.e. including Marseilles) for consistency in the comparisons.

3.2.4. Analysis metrics

Mean absolute error (MAE) and mean bias error (MBE) are used to assess the difference in surface temperatures between iterations:

$$MAE = \frac{1}{N}\sum_{j=1}^{N}\left|y_j - x_j\right| \quad (3.2)$$

$$MBE = \frac{1}{N}\sum_{j=1}^{N}\left(y_j - x_j\right) \quad (3.3)$$

where y_j and x_j are data from two cases at instance j, and N is the number of values analysed (e.g. a year with 10-min timestep, $N = 52560$). The distribution of hourly surface temperature variances between iterations is analysed in Section 3.3.1.

The normalised mean bias error is used in multiple guidelines for uncertainty analysis of building energy simulation programmes (Ruiz and Bandera, 2017):

$$nMBE = \frac{1}{N}\frac{\sum_{j=1}^{N}(y_j - x_j)}{\bar{x}_j} \times 100\% \qquad (3.4)$$

In this study, we use nMBE to compare the hourly load variance between different cases. The ASHRAE Guideline 14 (ASHRAE, 2014) sets the uncertainty limits for building energy simulation programmes as nMBE within ±10% for hourly data.

For annual energy demand and overheating degree hour comparisons, the percentage difference is calculated as the ratio of difference between cases to the base case.

3.2.5. Evaluation of longwave radiative exchange with observations

To evaluate the longwave radiative calculations, surface temperature observations (Morrison et al., 2021, 2018) conducted at the Comprehensive Outdoor Scale Model (COSMO) test site (Kanda et al., 2007) are used. The 100 m × 50 m site has 32 × 16 aligned arrays of 1.5 m cubic concrete blocks (0.1 m wall thickness, $\lambda_P = 0.25$). The long axis is oriented 49° west of true north.

Surface brightness temperatures were measured with two Optris PI160 LWIR cameras (Optris GmbH, Germany) facing north (Fig. 3.3a) and south. The measurements for a predominantly clear-sky day (2nd August 2014) are selected for evaluation. The experimental setup is reproduced in EnergyPlus consists of 3 × 3 array of concrete cubes all with the same size and thickness (0.1 m dense concrete wall, conductivity = 1.63 W m^{-1}K^{-1}, density = 2300 kg m^{-3}, specific heat = 1000 J kg^{-1}K^{-1} (CIBSE, 2006)). EnergyPlus simulations of brightness temperatures are compared to the observations (Fig. 3.3b,c) by treating the concrete blocks as blackbodies (i.e. by assuming emissivity = 1 in EnergyPlus simulations). The weather data used in the EnergyPlus simulations are measured at the site or nearby (Morrison et al., 2021, 2018).

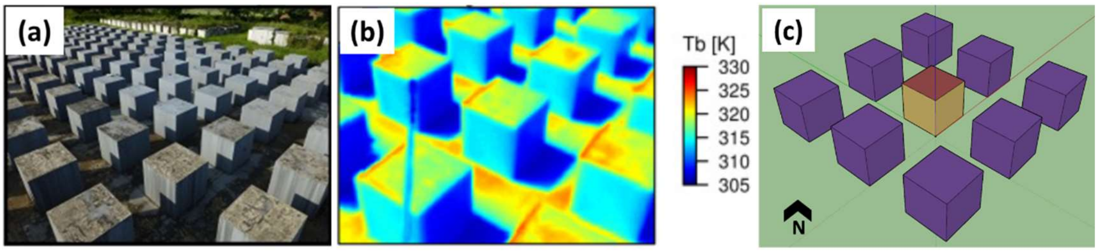

Fig. 3.3. Comprehensive Outdoor Scale Model (COSMO) test site in Japan (a) view near the north-viewing longwave infrared camera location, (b) brightness temperature (T_b) from the north-viewing camera at 2nd August 2014 10:00 local standard time, (c) model geometry used in EnergyPlus. Sources (a,b): Morrison et al. (2018).

3.3. Results

3.3.1. Impact of iteration on surface temperature

First, we assess if using an iterative approach (model spin up) to obtain external building surface temperature of surrounding buildings could impact the model surface temperature (Fig. 3.4). In all test cases, the mean bias error (MBE) indicates that there is a difference in surface temperature (i.e. MBE is not 0 °C) between the first and second iteration.

As neighbourhood density impacts both the shortwave and longwave radiative exchanges; for example, shadows and receipt of longwave radiation are very different with adjacent buildings (cf. isolated building), we assess if the impact of interactions varies with plan area fraction (λ_P). The number of iterations needed to meet the surface temperature convergence criteria (<0.01 °C) increases with urban density. At the lowest building density considered (λ_P = 0.1, Fig. 3.1) only two iterations are needed, increasing to three for λ_P = 0.3, and five when λ_P = 0.6 (Fig. 3.4). This is expected as the building of interest (*boi)* becomes increasingly influenced by the surroundings. At λ_P = 0.6, both the south-facing and north-facing walls of $boi_{adj\leftarrow iso,i}$ require more iterations to converge than other facets as they have largest difference between the initial and final surface temperatures. In addition to MBE, the distribution of surface temperature differences between $boi_{adj\leftarrow a,4}$ and $boi_{adj\leftarrow a,5}$ at λ_P = 0.6 are shown in Fig. 3.5. For the north-facing wall with the largest difference, there are 93.6% of time steps within the convergence criteria of ±0.01°C, while for other facets the fraction is higher than 99%.

Second, we consider the impact of source of the initial surface temperatures values (i.e. $boi_{adj\leftarrow iso.i}$ and $boi_{adj\leftarrow a.i}$). The difference between the two sources is large for the first iteration, up to 1.15 °C in the dense neighbourhood (λ_P = 0.6), but negligible in the low-density neighbourhood (λ_P = 0.1). Obviously, with each iteration their difference decreases (Fig. 3.4, 3.6) indicating that by updating T_{adj} it can modify an initial common value independent of the initial surface temperature chosen. As $boi_{adj\leftarrow iso,5}$ and $boi_{adj\leftarrow a,5}$ have very similar surface temperatures, hereafter three representative cases are analysed:

(i) $boi_{adj\leftarrow a}$ using the default EnergyPlus method ('base');

(ii) $boi_{adj\leftarrow iso}$ following Luo et al. (2020) (no iteration); and

(iii) $boi_{adj\leftarrow a,5}$ the most realistic case with initialisation from TMY air temperature and five iterations.

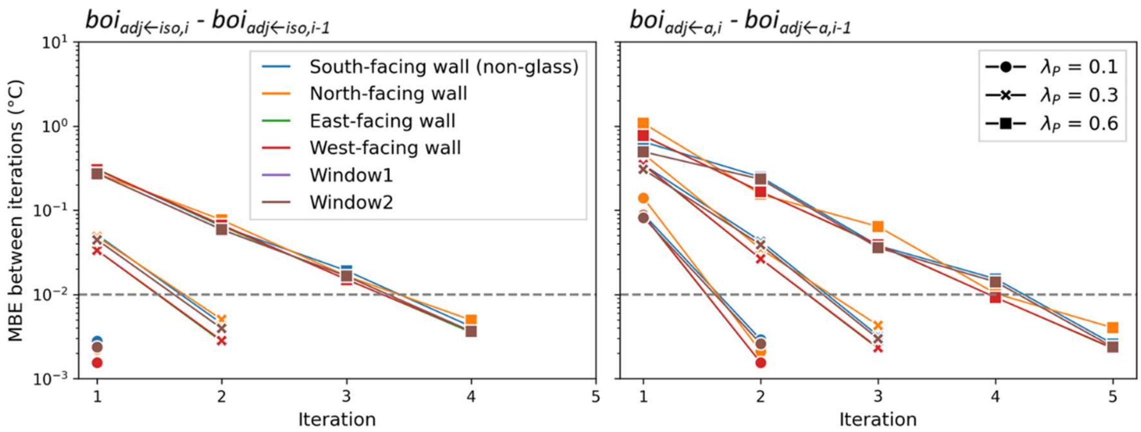

Fig. 3.4. Annual mean bias error (MBE, section 3.2.4; 10-min timestep, N=52560) determined using the external building surface temperature of the previous iteration (Fig. 3.2) for different facets (colour) in London with three plan area fractions (λ_P) (marker) and two initial *adj* surface temperatures (columns) with convergence criteria (0.01 °C, dashed line). Seasonal MBE and annual MAE are shown in section Appendix 3.

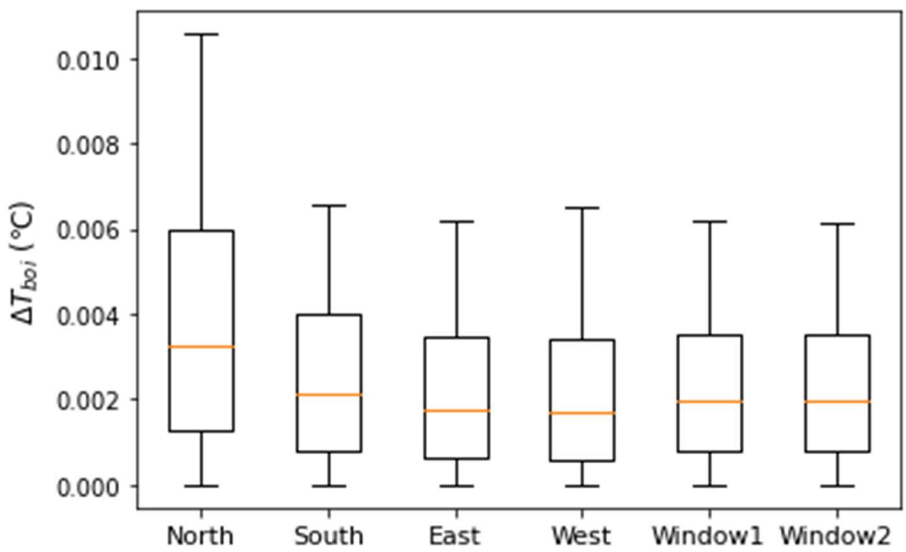

Fig. 3.5. Distribution of facet surface temperature differences (10-min timestep, N=52560) between $boi_{adj\leftarrow a,5}$ and $boi_{adj\leftarrow a,4}$ at λ_P = 0.6 with interquartile range (box), median (horizontal line) and 5th and 95th percentiles (whiskers).

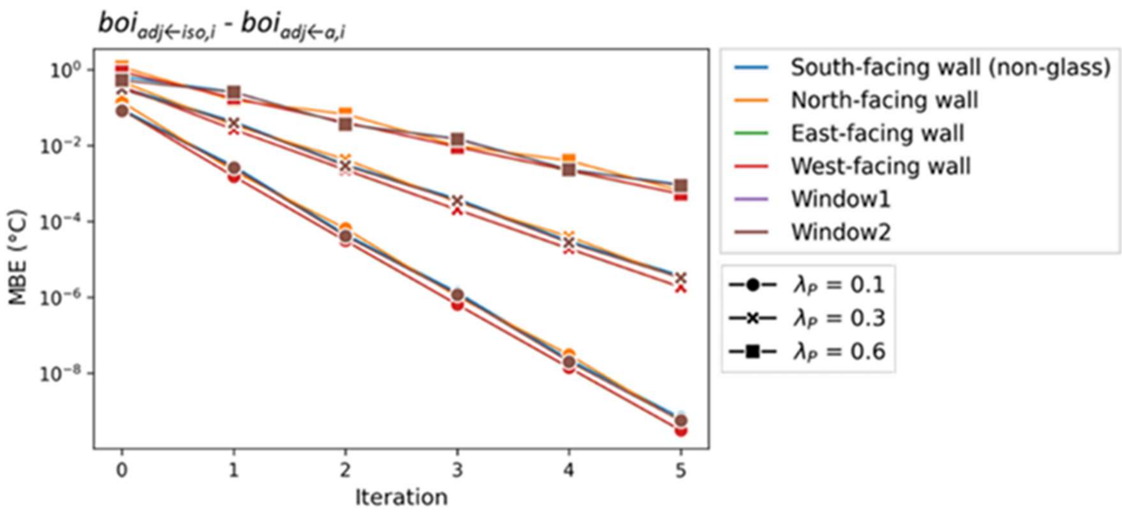

Fig. 3.6. As Fig. 3.4, but with different initial surface temperatures for different facets (colour) and plan area fractions (λ_P) (marker). Iteration 0 is $boi_{adj\leftarrow iso} \rightarrow boi_{adj\leftarrow a}$. Seasonal MBE and annual MAE are shown in Section Appendix 4.

3.3.2. Evaluation of simulated brightness temperatures with observations

The EnergyPlus simulated brightness surface temperatures using the above three methods can capture the main trend of observed diurnal pattern in an urban context (λ_P = 0.25, Fig. 3.3) (Fig. 3.7). The proposed improvement ($boi_{adj\leftarrow a.5}$) results are more similar to the observations than the default method ($boi_{adj\leftarrow a}$). $boi_{adj\leftarrow a,5}$ brightness temperatures are slightly larger (0.1 °C in average) than $boi_{adj\leftarrow iso}$ in this area because of the relatively low λ_P. It is expected that such difference will be much obvious when λ_P is high. This will be discussed in section 3.3.3.

The simulated surface temperatures are impacted by the ground surface temperature being set to the same as air temperature, whereas it will have a larger range: warmer during the day and depending on view factors cooler/warmer at night (e.g. summer in London: impervious ground peak 10 °C warmer (cf. canopy air temperature peak), minimum 3 °C warmer (Morrison et al., 2020)). Therefore, assigning the air temperature to the ground can potentially underpredict the longwave radiation received by building external walls, and hence underpredict the wall surface temperatures.

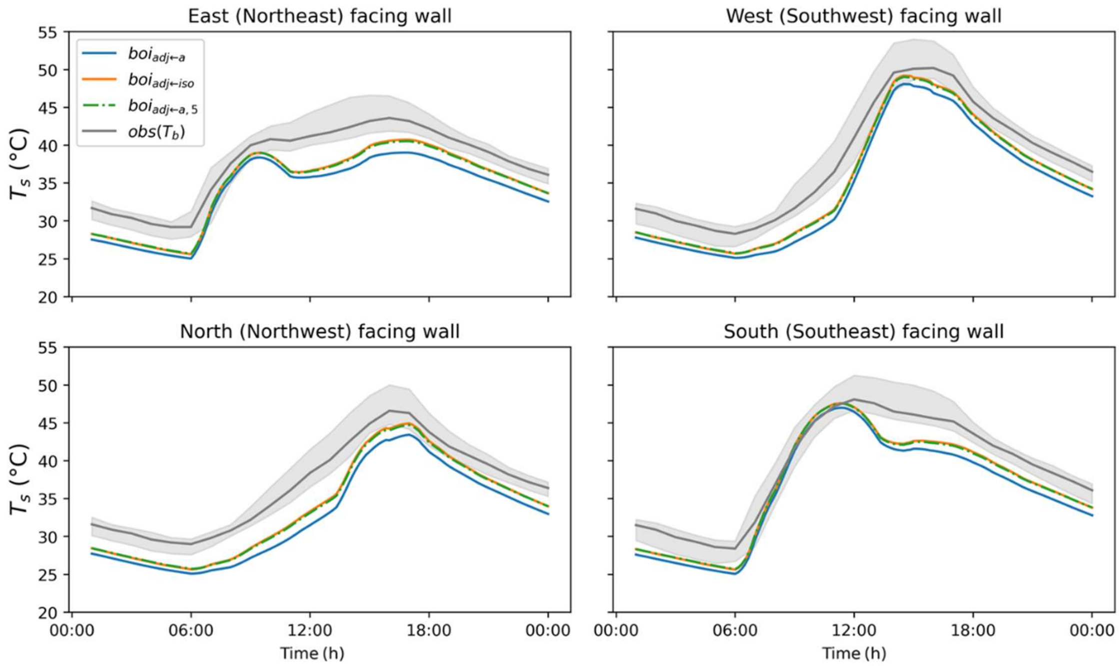

Fig. 3.7. Comparison of simulated (assuming emissivity = 1, 10-min) and observed (hourly median, line) brightness temperatures (5th and 95th percentiles: shading) at the COSMO site (Fig. 3.3) on 2nd August 2014. Observations are data from Morrison et al.'s Fig. 10c (2018).

3.3.3. External wall (opaque part) surface temperature in London

The longwave radiative calculation method selected (Section 3.3.1) changes the external building surface temperature diurnal cycle by facet orientation (Fig. 3.8a-f: north facing wall, g-x: south-facing wall - non-glass part). As expected, peak differences occur near solar noon, and when external surface temperatures are warmer than air temperature (Morrison et al., 2020, 2021).

The neighbourhood density impacts the *boi* external building surface temperatures. The smallest differences between methods occurs for the lowest-density ($\lambda_P = 0.1$) neighbourhood. These differences are smaller at night (0.8 °C) than during the day (3 °C) in summer (Fig. 3.8c), and varies less in the winter (night=1 °C; day=1.5 °C, Fig 8f) for the north-facing wall. The south-facing wall surface temperature differences are smaller, but the median difference at midday is still as large as 2 °C in summer (Fig. 3.8i) and 1.2 °C in winter (Fig. 3.8l). This suggests the default method ($boi_{adj \leftarrow a}$, #1, Table 3.1) in EnergyPlus introduces biases to the surface temperature in dense urban areas at London's latitude. As the external building surface temperature is an important variable in EnergyPlus-related coupling (Zhang et al., 2013), such biases can result in further uncertainties.

The diurnal temporal pattern differs among the three methods, for example, timing of the surface temperature peak. In winter the north-facing wall (λ_P = 0.6) surface temperature assigned from isolated building to *adj* buildings ($boi_{adj \leftarrow iso;}$ cf. $boi_{adj \leftarrow a}$) peaks later than the one after five iterations using the air temperature initially ($boi_{adj \leftarrow a,5}$; cf. $boi_{adj \leftarrow a}$) (Fig. 3.8f). The south-facing wall of the *iso* building is heated by the sun, surface temperatures continue to increase for a longer period after noon, and leads to more longwave radiation exchange for the *boi* north-facing wall. While for $boi_{adj \leftarrow a,5}$, south-facing wall of the *adj* building becomes shaded around noon, so the longwave radiation starts to decrease earlier than for $boi_{adj \leftarrow iso}$.

Daytime in winter, the north-facing wall surface temperature difference between $boi_{adj \leftarrow iso}$ and $boi_{adj \leftarrow a}$ is higher than for the other facet orientations for the denser areas (λ_P = 0.3 and 0.6; Fig. 3.8e, f). With the lower solar altitude in winter, much less direct solar radiation is received by the south-facing wall in denser neighbourhoods. Thus, the difference in south-facing wall (non-glass area) surface temperature between shaded and isolated buildings becomes much larger and further influences the longwave radiation calculated. This difference is more evident on days with larger fluxes (e.g. 75th percentile) than the median (Fig. 3.8f), because of the high frequency of winter cloudy periods (in the London TMY data) which reduces the solar radiation differences between isolated and surrounding buildings. Whereas on a clear winter day (30th December, i.e. at the 75th percentile), a large diurnal cycle of $boi_{adj \leftarrow iso}$ occurs (Fig. 3.9). During the midday hours, the $boi_{adj \leftarrow iso}$ surface temperature is greater than $boi_{adj \leftarrow a,5}$ by 2 °C. This does not occur for the south-facing wall, as the opposite *adj* north-facing walls are less influenced by the solar radiation compared to *adj* south-facing wall.

The night-time surface temperature from the $boi_{adj \leftarrow iso}$ method is cooler overall than when the $boi_{adj \leftarrow a,5}$ method is used, because of the lack of nocturnal longwave trapping. The underprediction is largest when λ_P = 0.6. These surface temperature differences are up to 0.6 °C.

View factors calculated by the EnergyPlus default method (i.e. as in $boi_{adj \leftarrow a}$) and Monte Carlo ray-tracing method (i.e. used in the following iterations) may introduce uncertainties. To address such impact, similar comparisons (as Fig. 3.8) are made in Fig. 3.10 but with surface temperatures of $boi_{adj \leftarrow a}$ simulated with the updated method (input T_{adj} and view factors independently). Results suggest that comparing with the updated view factor calculating method for $boi_{adj \leftarrow a}$, the default method by EnergyPlus tends to underpredict surface temperatures of $boi_{adj \leftarrow a}$. Such underpredictions are greater at λ_P = 0.3 and 0.6, which are up to 0.3 °C and 0.5 °C in median, respectively. The increase in surface temperatures of $boi_{adj \leftarrow a}$ hence reduces difference between it and the other two cases ($boi_{adj \leftarrow iso}$ and $boi_{adj \leftarrow a,5}$), especially at night due to the relatively smaller differences, but variations between spin-up ($boi_{adj \leftarrow a,5}$) and non-spin-up ($boi_{adj \leftarrow iso}$ and $boi_{adj \leftarrow a}$) methods still exist.

In summary, the $boi_{adj \leftarrow iso}$ method causes large differences in wall surface temperatures compared to the method with the most iterations/spin-ups ($boi_{adj \leftarrow a,5}$). These differences are most evident at night and in the winter near noon.

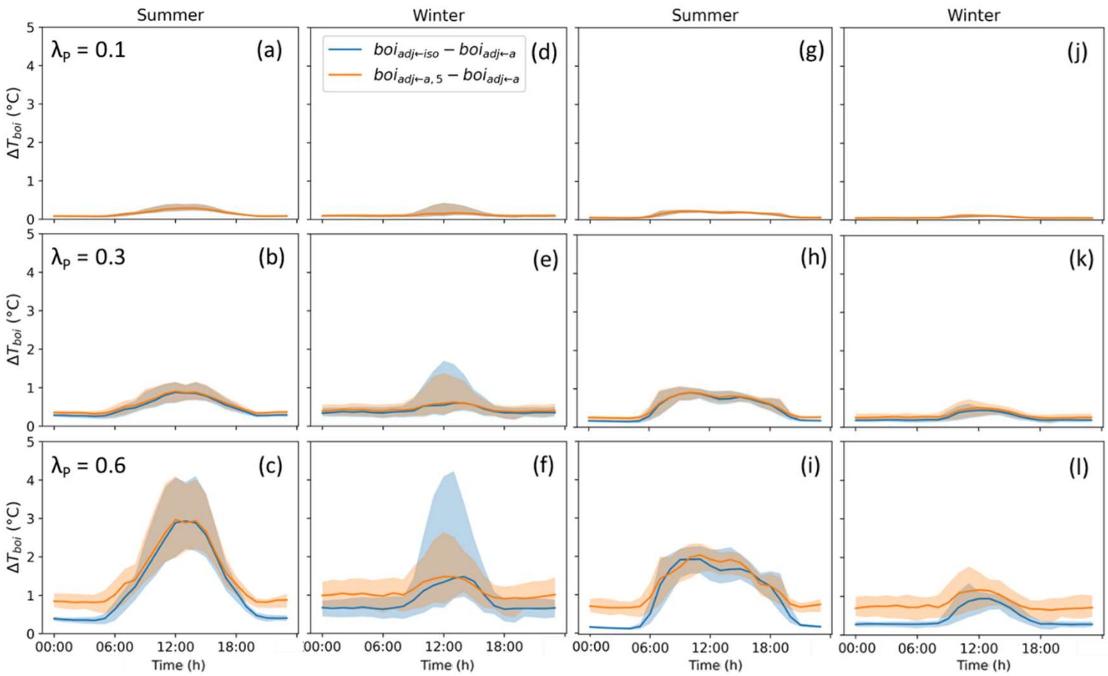

Fig. 3.8. Median diurnal cycle (lines) and inter-quartile ranges (shading) of (a-f) north-facing and (g-l) south-facing wall (non-glass part) surface temperature differences (hourly) using $boi_{adj \leftarrow iso}$ and $boi_{adj \leftarrow a,5}$ or $boi_{adj \leftarrow a}$ in summer (JJA) and winter (DJF) in London for plan area fractions **(a,d,g,j)** λ_P=0.1, (**b,e,h,k**) λ_P=0.3, (**c,f,i,l**) λ_P=0.6.

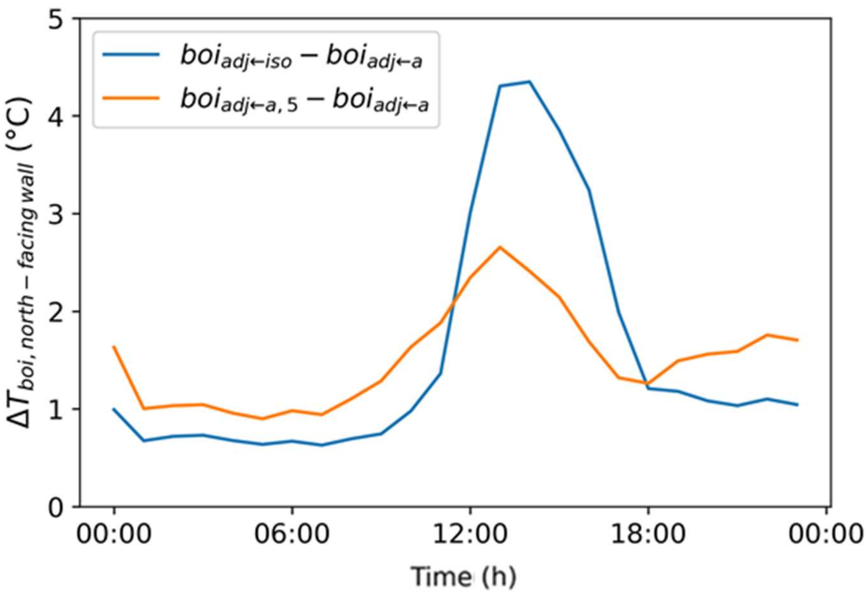

Fig. 3.9. London (λ_P = 0.6) clear winter day (30th December) diurnal differences in hourly north-facing wall surface temperature relative to $boi_{adj\leftarrow a}$ when using $boi_{adj\leftarrow iso}$ and $boi_{adj\leftarrow a,5}$.

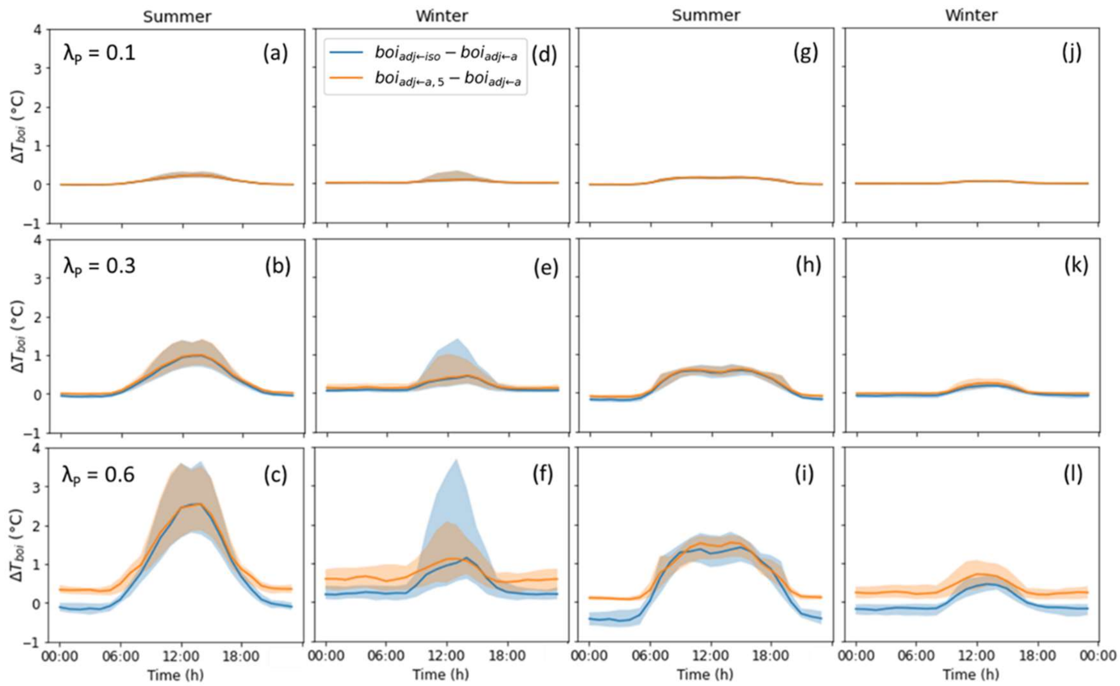

Fig. 3.10. As Fig. 3.8, but with $boi_{adj\leftarrow a}$ calculated with updated view factors.

3.3.4. Impact of longwave radiation method on building energy demand in London

Choice of longwave radiative exchange method (Table 3.1) impacts the annual cooling and heating energy demands. Simulations for London neighbourhoods with different λ_P show differences in energy demand, relative to base case ($boi_{adj\leftarrow a}$), to increase with λ_P (Table 3.3). The annual cooling energy demand is predicted to be larger using $boi_{adj\leftarrow iso}$

(cf. $boi_{adj \leftarrow a}$) by 12.4% (13% for $boi_{adj \leftarrow a,5}$), whereas annual heating energy demand is lower (cf. $boi_{adj \leftarrow a}$) by 3.1% (5% for $boi_{adj \leftarrow a,5}$) at $\lambda_P = 0.6$.

These differences are large compared to previous studies. For example, Evins et al.(2014) 's study in Geneva (unspecified λ_P) predicts a 5.1% increase in cooling energy and 3.5% decrease in heating energy ($boi_{adj \leftarrow a}$ to $boi_{adj \leftarrow iso}$). Similarly for Chicago (λ_P unknown), Luo et al. (2020) report a 0.2% - 3.2% increase in cooling energy and 0.2% - 3.6% decrease in heating energy (#1 to #3, Table 3.1). While Bouyer et al. (2011) model longwave radiation in an urban context (unspecified λ_P) in Lyon using a CFD-thermoradiative coupling with their own building energy model. They obtain a larger impact (19.1% increase in building cooling energy and 9.3% decrease in heating energy) possibly due to the different simulation methods, building models and settings (e.g., building of interest - 7-stories located in a dense neighbourhood with large window-to-wall ratio - 66.7% glazing area on all facets). Also by using CFD, the local wind can be modified by the neighbourhood, which will further influence the surface temperatures and building energy consumption. While in our study the influence of neighbourhood on wind is not considered in this study, but is included in other work of us (Tang et al., 2021 , Chapter 5 and 7).

This suggests neglecting neighbourhood characteristics' (λ_P) influence on inter-building longwave radiation simulations (Table 3.3) may result in important differences in energy demand predictions. The EnergyPlus default longwave radiative exchange method is suitable for buildings in areas with $\lambda_P < 0.1$ as the longwave radiation from *adj* buildings is relatively small, but not if simulating building thermal energy performance in a relatively denser urban area (e.g., $\lambda_P > 0.3$). The $boi_{adj \leftarrow iso}$ method tends to underpredict the annual cooling demand but overpredict the heating demand.

Diurnal cycles of cooling and heating loads difference are shown in Fig. 3.11. Consistent with the building external surface temperature pattern (Fig. 3.8, 3.9), the peak cooling load of $boi_{adj \leftarrow a}$ is the smallest and the heating load the highest. Similarly, peak load differences between the other two methods and the default method increase with λ_P. The heating load differences in the afternoon are closer to 0 at $\lambda_P = 0.1$ and 0.3 (Fig. 3.11b, d), because the more open neighbourhoods receive more solar radiation allowing the indoor air temperature to be above the heating setpoint (no heating is required). When $\lambda_P = 0.6$ (Fig. 3.11f), heating is needed during the whole day in winter in all cases, creating larger differences. In the densest neighbourhood (λ_P = 0.6), the peak cooling load difference between $boi_{adj\leftarrow a,5}$ and $boi_{adj\leftarrow a}$ could be as high as 4 W m^{-2} in summer (median), which is comparable to the internal heat gain of 4.17 W m^{-2} used in these simulations. In winter, the median difference is larger than 1 W m^{-2}. Here, the nMBE (see section 3.2.4) is calculated with the hourly differences of cooling/heating load of $boi_{adj\leftarrow iso}$ and $boi_{adj\leftarrow a,5}$ (cf. $boi_{adj\leftarrow a}$). When λ_P = 0.6, hourly cooling load of both $boi_{adj\leftarrow iso}$ and $boi_{adj\leftarrow a,5}$ nMBE are around 12% in summer (not shown), and for winter heating load are -4% and -2%, respectively. The summer values clearly exceed the ASHRAE 10% uncertainty limits (section 3.2.4). Hence, using the EnergyPlus default longwave radiative exchange method could introduce a non-negligible bias into the simulated loads.

Table 3.3: (a) Annual cooling and heating energy demand and (b) percentage variation comparing with $boi_{adj\leftarrow a}$; (c) nMBE (section 3.2.4) of hourly load comparing with $boi_{adj\leftarrow a}$ in London for different λ_P.

		(a) Energy demand (kWh)			(b) Percentage variation (%)		(c) nMBE (%)	
	λ_P	$boi_{adj\leftarrow a}$	$boi_{adj\leftarrow a.5}$	$boi_{adj\leftarrow iso}$	$boi_{adj\leftarrow a.5}$	$boi_{adj\leftarrow iso}$	$boi_{adj\leftarrow a.5}$	$boi_{adj\leftarrow iso}$
Cooling	0.1	55.4	55.9	55.9	0.9	0.9	1.0	1.0
	0.3	46.0	47.8	47.7	3.8	3.6	4.0	3.9
	0.6	24.9	28.1	28.0	13.0	12.4	12.3	12.0
Heating	0.1	94.6	94.2	94.2	-0.5	-0.4	-0.3	-0.3
	0.3	96.9	95.0	95.3	-2.0	-1.6	-1.4	-1.2
	0.6	107.3	101.9	104.0	-5.0	-3.1	-3.7	-2.3

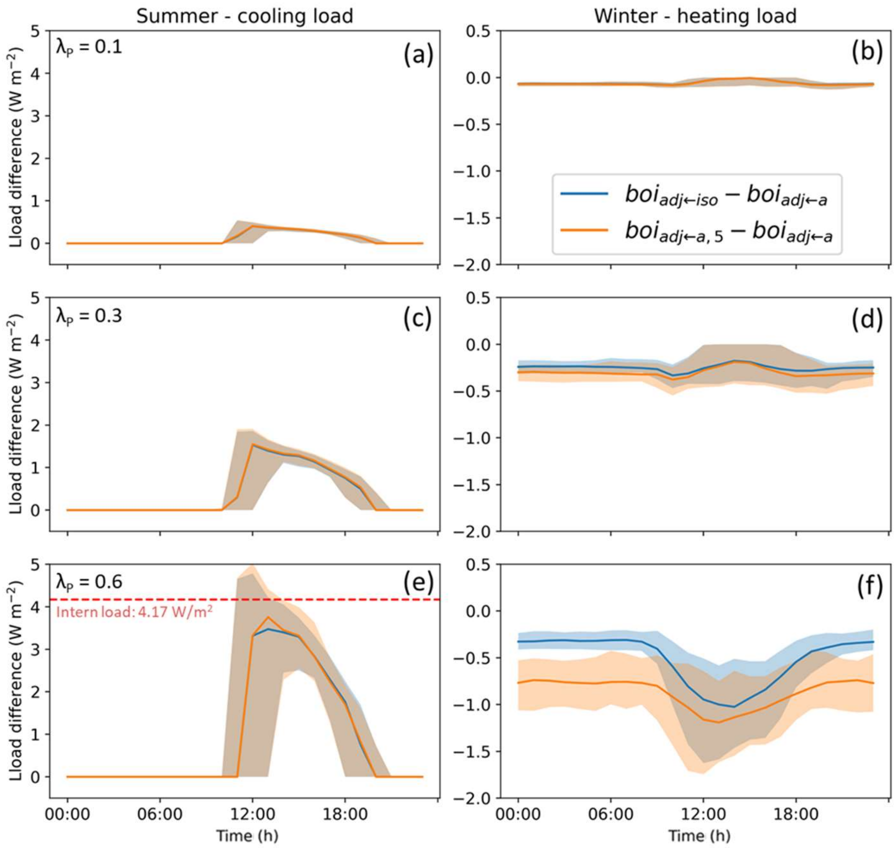

Fig. 3.11. Median diurnal cycle (lines) and inter-quartile range (shading) of hourly cooling load differences in summer (JJA) and heating load differences in winter (DJF) from $boi_{adj \leftarrow a}$ (default method) in London for plan area fraction (**a,b**) λ_P=0.1, **(c,d)** λ_P=0.3, (**e,f**) λ_P=0.6. (**e**) internal load (red dashed line) provides a reference for comparison. **(b,d)** winter for λ_P = 0.1 and 0.3. All differences are < 0 because indoor temperatures are warmer than the setpoint, so heating system is not used.

3.3.5. Indoor overheating risk in London

To assess the impact on indoor overheating risk, we use the annual overheating degree hours above 26 °C and 28 °C (section 3.2.3) as the metric for our reference building in free-running condition in London (section 3.2.1). A building in a low-density neighbourhood (λ_P = 0.1) receives more shortwave radiation (than denser neighbourhoods) and therefore the overheating degree hours are larger (Table 3.4) given the other meteorological parameters (i.e., TMY weather data) are the same.

In the densest neighbourhood (λ_P = 0.6), the predicted overheating degree hours for $boi_{adj \leftarrow a,5}$ are higher during the both the day (18 %, time period defined in section 3.2.3) and night (43%, Table 3.4) when using the $boi_{adj \leftarrow a,5}$ (cf. $boi_{adj \leftarrow a}$). These biases are large and comparable to effects of increasing external wall insulation (Porritt et al. 2012). Porritt et al. (2012) identified increasing external wall insulation as one of most effective interventions for mitigating overheating, as it could reduce the degree hours for living rooms (> 28°C) by 20-22% and bedrooms (> 26 °C) by 49–51% in the UK climate. The $boi_{adj \leftarrow iso}$ method tends to underpredict the overheating risk (cf. $boi_{adj \leftarrow a,5}$), especially at night (12% less when λ_P = 0.6) as it cannot capture the effect of nocturnal longwave radiation trapping between buildings.

Another overheating criteria, maximum indoor operative temperature (T_{op}) (section 3.2.3), set by BS EN 15251 (BSI, 2007) and CIBSE TM52 (CIBSE, 2013), can be assessed based on diurnal cycles (Fig. 3.12). The median differences in T_{op} ($boi_{adj \leftarrow a,5}$ cf. $boi_{adj \leftarrow a}$) are 1.3 °C in summer. These are as large as the overheating risk assessment classes defined in BS EN 15251 (BSI, 2007) of 1 °C. Thus, the choice of longwave radiation method may lead to an overheating risk level misclassification. With night-time differences reaching 0.8 °C, and this period of the day overheating will become more critical than daytime for free-running buildings if occupants are indoors and unable to take adaptive interventions (e.g., open windows) when sleeping (Anderson et al., 2013).

As the discrepancy between existing methods ($boi_{adj\leftarrow a}$ and $boi_{adj\leftarrow iso}$) is large, it is especially critical to use the iterative/spin-up inter-building longwave calculating method when assessing indoor overheating risk in cities.

Table 3.4: London with different λ_P. simulated (a) annual overheating degree hours and (b) percentage variation (cf. $boi_{adj\leftarrow a}$, defined in section 3.2.4). Day (7:00 to 23:00, defined in section 3.2.3) and night (23:00 to 7:00) and indoor operative temperature thresholds are 28 °C (day) and 26 °C (night) (CIBSE, 2006).

	λ_P	(a) Overheating degree hours			(b) Percentage variation (%)	
		$boi_{adj\leftarrow a}$	$boi_{adj\leftarrow a.5}$	$boi_{adj\leftarrow iso}$	$boi_{adj\leftarrow a.5}$	$boi_{adj\leftarrow iso}$
Day	0.1	16949	17147	17144	1.2	1.1
	0.3	14261	15045	14990	5.5	5.1
	0.6	7948	9398	9191	18.2	15.6
Night	0.1	602	619	619	2.8	2.8
	0.3	506	575	567	13.6	12.0
	0.6	314	450	411	43.3	31.0

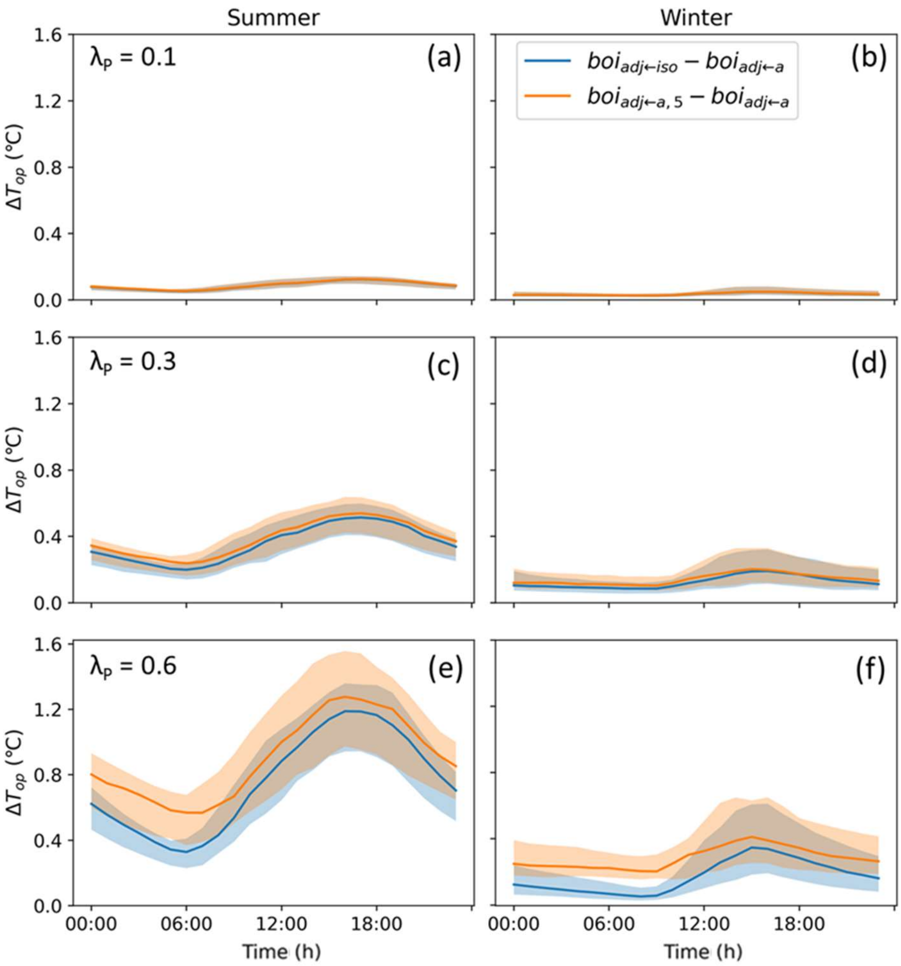

Fig. 3.12. As Fig. 3.11, but indoor operative temperature T_{op} differences.

3.3.6. Impact of latitude

To consider if these results vary with latitude and therefore solar altitude, we simulate a transect North (Aberdeen) and South (Marseille) of London. As the densest neighbourhood ($\lambda_P = 0.6$) has the largest differences, we only present the simulations for $\lambda_P = 0.6$.

3.3.6.1. North-facing wall surface temperature

As the north-facing wall surface temperature is most influenced by the increased inter-building longwave radiative exchange (section 3.3.3, Fig. 3.8), we select this for analysis. The surface temperature differences (Fig. 3.13) are generally larger for lower latitudes (i.e., Marseille > London > Aberdeen). The median midday simulated surface temperature using $boi_{adj \leftarrow a,5}$ are 2 °C warmer (cf. $boi_{adj \leftarrow a}$) in Aberdeen and 3 °C in Marseille in summer; whereas in winter these increases are slightly smaller (1.2 and 2.4 °C, respectively). The nocturnal surface temperature differences are smaller between methods.

Thus, latitudinal variations in shortwave radiation impact the inter-building longwave exchange. As lower latitudes can have higher solar altitudes, the *adj* south-facing wall receives more solar radiation allowing higher surface temperature at noon. Therefore, the directly opposite *boi* north-facing wall receives more longwave radiation, increasing its surface temperature.

In winter, there is a large increase in midday surface temperatures for the $boi_{adj \leftarrow iso}$ method used for London and Marseille, as the shortwave radiation at lower latitudes increases the difference between south-facing wall surface temperature of the isolated building (used as T_{adj} of $boi_{adj \leftarrow iso}$) and air temperature (used as T_{adj} of $boi_{adj \leftarrow a}$) (Terjung and O'Rourke, 1981).

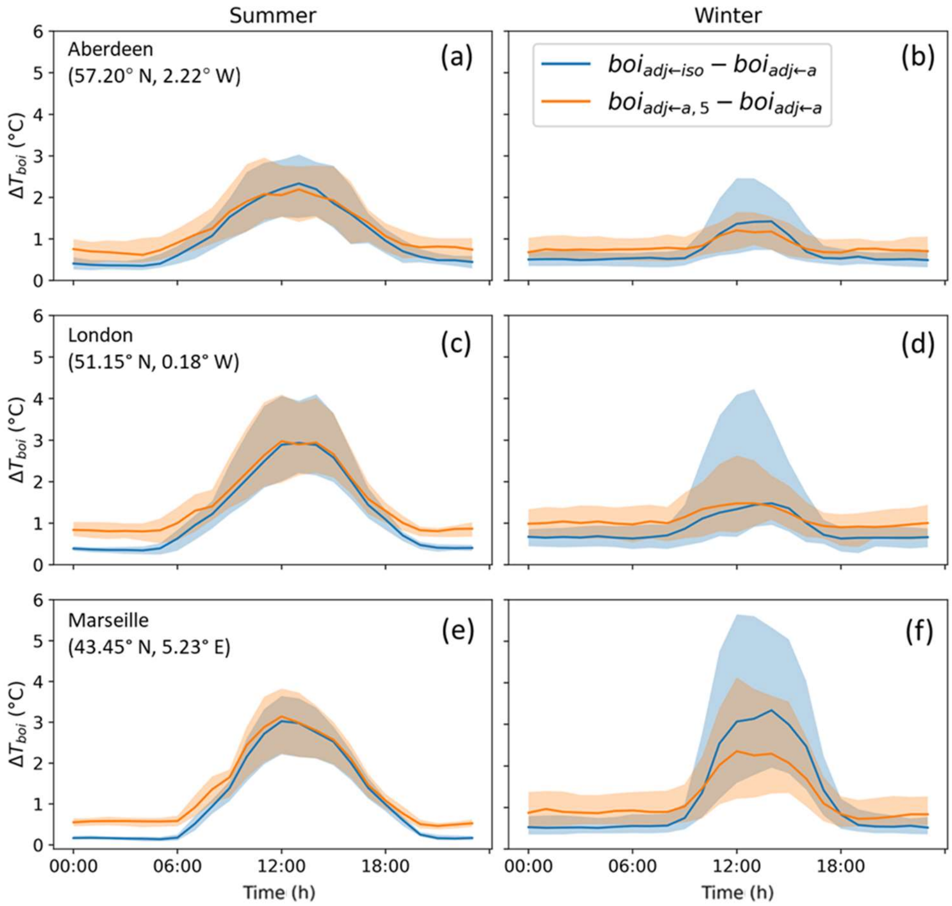

Fig. 3.13. As Fig. 3.8, but north-facing wall surface temperature differences (hourly) in three locations: (a,b) Aberdeen, (c,d) London, (e,f) Marseille for $\lambda_P = 0.6$.

3.3.6.2. Cooling/heating demand

As the latitude decreases, annual cooling energy demand difference between the $boi_{adj←a,5}$ and $boi_{adj←a}$ methods decreases (17% to 9%, Table 3.5) while difference in heating demand increases (4% to 6%). Whereas, the trend in absolute difference in energy demand is the opposite (Table 3.5: annual cooling demand increases from 1.7 (Aberdeen) to 5.8 kWh (Marseille) and heating decreases (5.2 to 3.7 kWh). Relative differences in energy demand are commonly compared (e.g. Evins et al., 2014; Luo et al., 2020), but as absolute consumption impacts both cost and carbon emission, it should not be neglected.

Diurnal median peak cooling load differences between methods ($boi_{adj←a,5}$ and $boi_{adj←a}$) occur in around the mid-day and increase with decreasing latitude from 3 to 4.5 W m^{-2} (Fig. 3.14) and the equivalent peak heating load differences are also larger (0.8 to 1.2 W m^{-2}) and appearing during the similar period (except Marseille). In Marseille, a fluctuation near mid-day impacts the heating when the indoor air temperature exceeds the heating setpoint (no heating is required). These trends of differences are consistent with diurnal cycle of cooling and heating loads, and hence are potentially influences by building-related settings. For instance, lowering the cooling setpoint and raising the heating setpoint can expand the period of HVAC system operation and may potentially increase the absolute differences in energy demand. Orientation of windows affect the time period when the indoor space is exposed to direct sunlight as well as the intensity, therefore influences the cooling/heating loads (Raftery et al., 2014). Other building envelope features (e.g. insulation, thermal mass and wind-to-wall ratios) will have an impact but are beyond the scope of this study.

As shown in Table 3.5, summer hourly cooling load nMBE for $boi_{adj \leftarrow a.5}$ and $boi_{adj \leftarrow iso}$ (cf. $boi_{adj \leftarrow a}$) in both Aberdeen and London are exceeding the ASHRAE ±10% uncertainty limit (section 3.2.4). This demonstrates the bias of simulated cooling (heating) load with EnergyPlus default longwave radiative exchange method is larger for higher (lower) latitudes.

Table 3.5: As Table 3.3, but for locations at three latitudes. Percentage variation is related to the base value (cf. $boi_{adj \leftarrow a}$).

		(a) Energy Demand (kWh)			(b) Percentage variation (%)		(c) nMBE (%)	
	$\lambda_P = 0.6$	$boi_{adj \leftarrow a}$	$boi_{adj \leftarrow a.5}$	$boi_{adj \leftarrow iso}$	$boi_{adj \leftarrow a.5}$	$boi_{adj \leftarrow iso}$	$boi_{adj \leftarrow a.5}$	$boi_{adj \leftarrow iso}$
Cooling	Aberdeen	10.0	11.7	11.7	17.1	17.3	15.3	15.4
	London	24.9	28.1	28.0	13.0	12.4	12.3	12.0
	Marseille	61.2	67.0	66.6	9.4	8.8	8.3	7.8
Heating	Aberdeen	129.2	124.0	125.7	-4.1	-2.7	-2.7	-1.7
	London	107.3	101.9	104.0	-5.0	-3.1	-3.7	-2.3
	Marseille	59.8	56.1	57.6	-6.2	-3.7	-5.4	-3.5

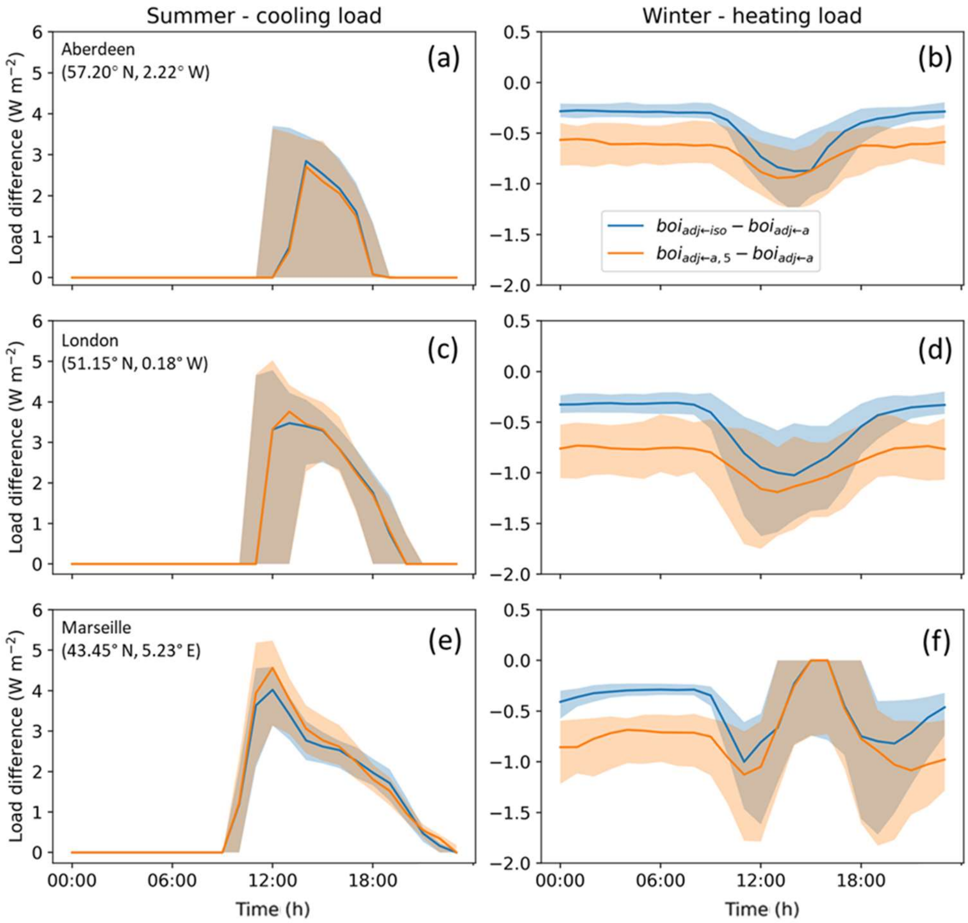

Fig. 3.14. As Fig. 3.13 but cooling/heating load differences. In winter, Marseille's differences are all less than 0 because of indoor temperatures being warmer than the setpoint, so heating system is not used.

3.3.6.3. Overheating risk

The annual overheating degree hours (Table 3.6), have a similar trend to the cooling energy demand (Table 3.5) with larger relative differences in Aberdeen because of the lower base value (60% at night, cf. 43% in London, 20 % in Marseille). The absolute difference in overheating degree hours is the largest in Marseille (Table 3.6). Diurnal median operative temperature differences (Fig. 3.15) indicate the default method tends to underestimate the peak, especially at lower latitudes. Summer median difference in peak increase from 1 °C in Aberdeen to 1.35 °C in Marseille (Fig. 3.15). As a bias of 1 °C can cause overheating risk misclassification (section 3.3.4), even in Aberdeen the default method underestimation should not be ignored.

Table 3.6: As Table 3.4, but for three locations. Percentage variation is related to the base value (cf. $boi_{adj \leftarrow a}$).

		(a) Overheating degree hours			(b) Percentage variation (%)	
		$\mathrm{boi}_{\mathrm{adj}\leftarrow\mathrm{a}}$	$\mathrm{boi}_{\mathrm{adj}\leftarrow\mathrm{a.5}}$	$\mathrm{boi}_{\mathrm{adj}\leftarrow\mathrm{iso}}$	$\mathrm{boi}_{\mathrm{adj}\leftarrow\mathrm{a.5}}$	$\mathrm{boi}_{\mathrm{adj}\leftarrow\mathrm{iso}}$
Day	Aberdeen	2491	3102	3050	24.5	22.4

	London	7948	9398	9191	18.2	15.6
	Marseille	22258	25093	24666	12.7	10.8
Night	Aberdeen	39	62	619	60.1	46.5
	London	314	450	411	43.3	31.0
	Marseille	2814	3387	3216	20.4	14.3

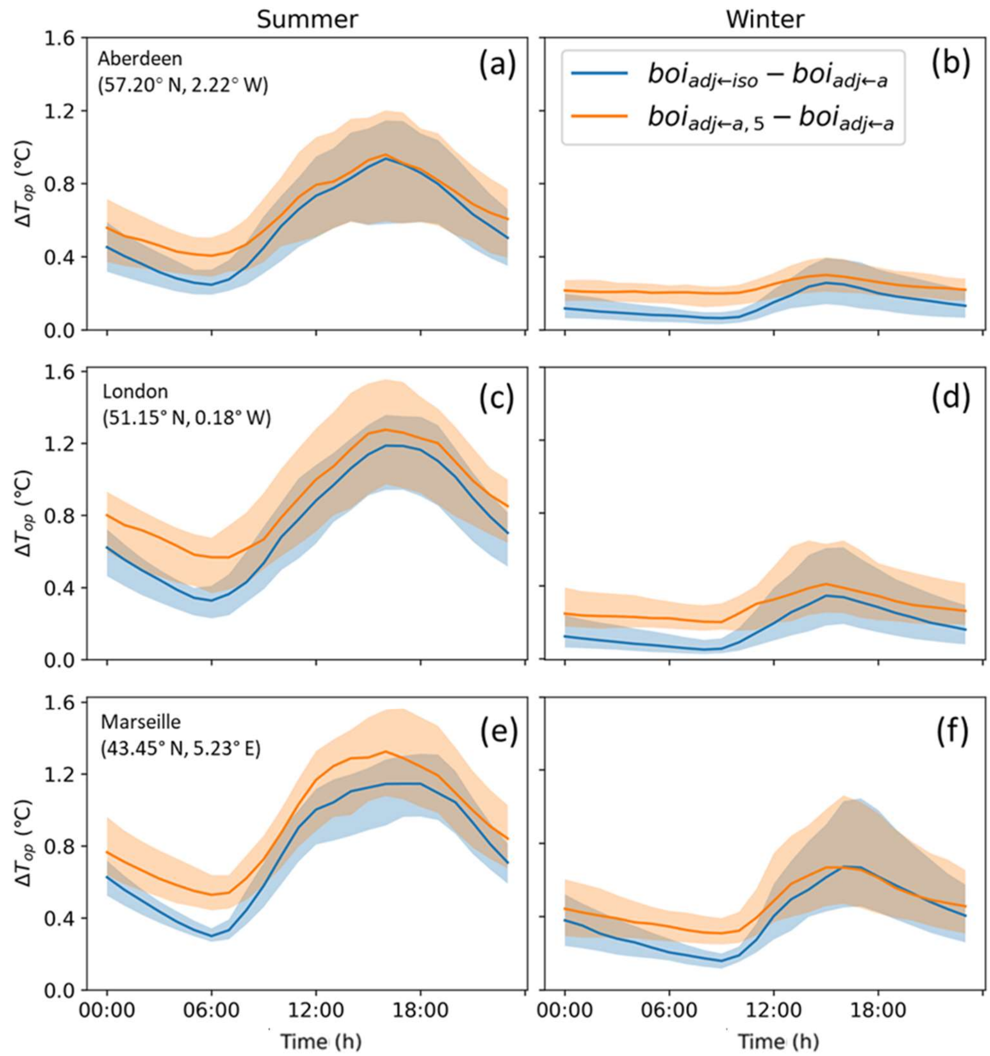

Fig. 3.15. As Fig 3.12, but indoor operative temperature differences (hourly) in three locations: (**a,b**) Aberdeen, (**c,d**) London, (**e,f)** Marseille for $\lambda_P = 0.6$.

3.4. Discussion

Prior work documented the importance of considering external longwave radiation in building energy simulations (Bouyer et al., 2011; Evins et al., 2014; Luo et al., 2020), but did not assess plan area ratios of different neighbourhoods. We apply an iterative/spin-up approach to the widely-used building energy simulation tool (i.e., EnergyPlus) to better determine the impacts of longwave radiative exchanges between buildings and further improve usability of the tool. One advantage of our proposed approach is that it does not require extra external data inputs apart from the supply of view factors, which can be calculated in a variety of ways (e.g., Howell et al., 2010). Thus, the approach can be easily and widely applied to assess the impact of the urban setting on building internal and external thermal conditions and energy performance.

Our findings extend current understanding of external longwave radiation on buildings by considering changes in urban plan area density and latitude. As denser neighbourhoods have larger building view factors, rather than sky, the longwave radiative fluxes between buildings are greater. Solar altitudes are larger for lower latitudes, which causes less shading on external building surfaces and higher surface temperatures, hence emitting greater longwave radiation. Therefore, differences in all metrics (e.g. energy demand and indoor overheating risk) compared to the default EnergyPlus option are found to be more evident in denser neighbourhoods. This indicates that the benefits gained from the updated approach may be particularly important for buildings located in dense neighbourhoods and low latitudes. As the urban population growth is expected to be greater at lower latitudes (United Nations, 2019) with increasing neighbourhood densities, our approach has a large potential to ensure more sustainable designs in these regions if taken into account.

However, in our present work we use idealised neighbourhoods with identical buildings. In many neighbourhoods that may be reasonable but where there is a heterogenous mix of buildings, the surface temperature of adjacent buildings could be calculated by treating them as isolated individuals (Luo et al., 2020), as we find this bias to be smaller than the EnergyPlus default option. However, further improvement is needed for dense heterogenous neighbourhoods in low latitudes. Currently, the ground surface temperature is not updated (i.e. remains the same as air temperature from TMY inputs), this should be further explored in the future. Furthermore, we only consider one building type, many design options will have an impact (e.g. envelope features, building heights) on the outdoor variables and feedback to the indoor thermal environment in various ways, therefore could also be explored in future research.

3.5. Conclusions

Using EnergyPlus, the surface temperature for an adjacent building can be simulated using the air temperature provided (e.g. TMY) or from an isolated building if simulating inter-building longwave radiative exchange. If these air temperature data are observations are based on standard WMO rural climate settings, they will not represent the urban climate properly (Tang et al., 2021; WMO, 2018). We conclude that none of the existing EnergyPlus methods allow realistic simulations if the building of interest (*boi*) is within a neighbourhood surrounded by other buildings. Here, we propose a model spin-up approach to account for adjacent buildings surface temperatures. When compared to existing methods to determine inter-building longwave radiative exchange, the surface temperature, building energy demand and overheating risks in various plan area fractions and climates are impacted. Key conclusions are:

- At least five iterations/spin-up are needed when simulating the inter-building longwave radiative exchange in EnergyPlus, especially in dense neighbourhoods (λ_P = 0.6). With sufficient iterations, the initial adjacent building surface temperature chosen no longer matters.
- Comparing the default EnergyPlus longwave radiative exchange method (assigning air temperature to adjacent building surfaces) to the spin-up method we propose:
    - Differences in metrics are small for low density neighbourhoods (λ_P = 0.1) but increase to unignorable for denser neighbourhoods (λ_P = 0.3 and 0.6).
    - Median external building surface temperature is underpredicted by up to 3 °C, which could become even larger with lower latitudes.
    - Annual cooling energy demand is underpredicted (up to 17%) and heating energy demand overpredicted (up to 6%) varying with climates when λ_P = 0.6. For lower latitudes, the absolute difference in peak cooling and heating loads are larger.
    - Annual overheating degree hours are underpredicted in the day (up to 25%) and night (60%) (λ_P = 0.6). Lower latitudes have larger absolute differences, but the relative differences tend to decrease. The median indoor operative temperature is underestimated, with larger impacts at lower latitudes (up to 1.4 °C).
- Using isolated building surface temperatures for adjacent buildings in a neighbourhood, nocturnal wall surface temperature is underpredicted (up to 0.6 °C). The winter north-facing wall temperature is largely overpredicted (~2 °C). Annual

cooling demand is underpredicted (up to 0.6%) and heating overpredicted (up to 2.5%). Overall, indoor overheating risk is underpredicted, especially at night (up to 13.6%).

Chapter 4 Use of wind pressure coefficients to simulate natural ventilation and building energy for isolated and surrounded buildings

This chapter explores the issue of incorrectly used wind pressure coefficients in building energy simulations, and evaluate the resulting biases in various scenarios. Methods for modifying wind pressure coefficients in these scenarios are also proposed.

This chapter has been published as a journal paper: **Xie, X.**, Luo, Z., Grimmond, S., Blunn, L., 2022. Use of wind pressure coefficients to simulate natural ventilation and building energy for isolated and surrounded buildings. Building and Environment, 230, 109951.

I conducted the research, wrote the first draft, and created the figures. Z. Luo, S. Grimmond, and L. Blunn provided guidance on the paper's structure, interpretation of the findings, and editing of the text.

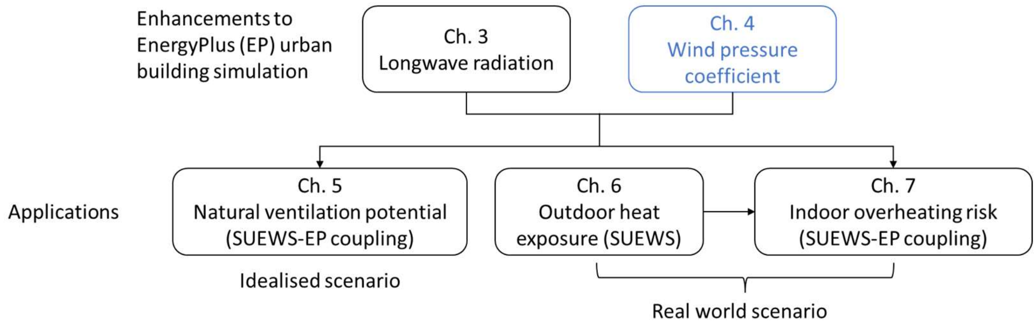

Nomenclature

A	Opening area (m^2)
C_d	Discharge coefficient of the opening
C_p	Wind pressure coefficient
C_{pl}	Wind pressure coefficient based on the (local) opening height
C_{pr}	Wind pressure coefficient based on the (reference) roof height
H	Roof height (m)
q_w	Wind-driven ventilation rate ($m^3\ s^{-1}$)
P_w	Wind pressure (Pa)
U	Wind speed ($m\ s^{-1}$)
z	Opening height (m)
α	Wind profile exponent
δ	Height where a constant mean gradient wind speed is assumed to occur (m)
λ_P	Plan area fraction

ρ Outdoor air density (kg m^{-3})

subscripts

ref	Reference in the wind tunnel experiment
EP	EnergyPlus
free	Free stream wind
met	Reference in the meteorological observation site
r	Undisturbed rural wind
u	Disturbed urbanised wind
WT	Wind tunnel

4.1. Introduction

Wind pressure coefficients (C_p) are key inputs for natural ventilation calculation in building energy simulations (BES) and multi-zone airflow models (e.g. AirflowNetwork (AFN) in EnergyPlus (EnergyPlus-AFN) (U.S. Department of Energy, 2020f), MacroFlo in IES-VE (Integrated Environmental Solutions, 2018), CONTAM and COMIS linkages with TRNSYS (TRNSYS, 2009)). C_p is the nondimensional ratio of wind pressure on the building surface to the dynamic pressure in the upstream undisturbed flow (Akins and Cermak, 1976) but is defined differently depending on the height of free stream dynamic pressure (Akins et al., 1979):

$$C_{pr}(z) = \frac{P_W(z)}{0.5\ \rho\ U_{free}^2(H)} \qquad (4.1)$$

where H is a *reference* height (m, building roof/eave height), and alternatively the *local* opening height z (m) is used (Akins et al., 1979):

$$C_{pl}(z) = \frac{P_W(z)}{0.5\ \rho\ U_{free}^2(z)} \qquad (4.2)$$

where $P_w(z)$ is the wind pressure (Pa) measured on the building facet at height z (m), U_{free} is the wind speed (m s^{-1}) in the upstream undisturbed flow at H or z, and ρ is the outdoor air density (kg m^{-3}) which is assumed constant. Typically, C_p is calculated as the average value across the entire building facet facing the flow (i.e. surface mean).

C_p is widely applied in studies of natural ventilation potential (Costanzo et al., 2019; Luo et al., 2007; Tan and Deng, 2017; Yang et al., 2005), cooling energy savings (Lim et al., 2017; Park and Lee, 2020; Ramponi et al., 2014b; Schulze and Eicker, 2013), indoor thermal comfort and overheating (Heracleous and Michael, 2018; Mavrogianni et al., 2014; Schünemann et al., 2021; Stazi et al., 2017), and other applications like the solar chimney (Sung et al., 2013) and windcatcher (Sadeghi et al., 2020). Commonly the C_p

data sources used in BES (Table 4.1) are from (Cóstola et al., 2009): primary sources (e.g., full-scale experiments, wind tunnel experiments and CFD simulations for a specific building of interest); and secondary sources (e.g. databases with generic building archetypes derived often from wind tunnel experiments). In databases (Table 4.1), C_{pr} rather than C_{pl} data are provided and are the default values used in BES.

C_p data, together with the reference wind conditions, are regarded as the major sources of uncertainties in multi-zone airflow models (Axley, 2007; Belleri et al., 2014). Therefore, applying C_p data correctly is important for more accurate estimation of natural ventilation rates. C_p data are dependent on many factors including the height of free stream dynamic pressure measured and the vertical wind profile which is modified by the surrounding buildings (Liddament, 1986; Swami and Chandra, 1987). However, these dependencies are often overlooked in BES, which could cause biases. Here we focus on EnergyPlus, as it is one of the most widely used open-source BES tools. Our aim is to critically explore potential biases of EnergyPlus-AFN simulation in three comparative C_p application scenarios (Fig. 4.1).

Scenario 1: In EnergyPlus the surface averaged C_{pr} ($\overline{C_{pr}}$) data are usually used with wind speed at the opening height $U_{free}(z)$. This is inconsistent (Eq. 4.1 cf. Eq. 4.2) and can cause biases since $U_{free}(z)$ should be used with the surface averaged C_{pl} ($\overline{C_{pl}}$) (Fig. 4.1a). EnergyPlus options allow the use of either provided (Akins et al., 1979; Swami and Chandra, 1987) or user-supplied C_p data. In the latter case, the user also needs to indicate the height the C_p values are for (i.e., opening or reference), with the EnergyPlus default (i.e., if not modified) being the opening height (U.S. Department of Energy, 2020g). If the provided default C_p values are used, the opening height will be used (not explicitly stated in U.S. Department of Energy (2020b) but found in the source code (EnergyPlus, 2022) and mentioned by Gimenez et al. (2018), Schulze and Eicker (2013) and Toesca et al. (2022). Hence, the provided $\overline{C_{pr}}$ value is used with wind speed at the opening height (z) instead of the reference roof height (H). This inconsistency between $\overline{C_{pr}}$ and freestream wind speed will cause biases in the wind pressure calculations if not corrected. Given this, we review current studies for choosing C_p if modelling natural ventilation in buildings using EnergyPlus-AFN (Table 4.2). Typically, if the detailed C_p settings are not mentioned, the supplied default $\overline{C_{pr}}$ values are assumed to be used. Of the studies stating the C_p settings (fully or partly), only four (Albuquerque et al., 2020;

Belmans et al., 2019; Bre and Gimenez, 2022; Toesca et al., 2022) of 27 (Table 4.2) use the correct combination of C_p and free stream wind speed (i.e. $\overline{C_{pr}}$ with $U_{free}(H)$ or $\overline{C_{pl}}$ with $U_{free}(z)$). The other studies (where both C_p and U_{free} are clear) all use $\overline{C_{pr}}$ with $U_{free}(z)$. Thus, this common bias (23 of 27 studies) caused by using $\overline{C_{pr}}$ with $U_{free}(z)$ needs to be assessed.

Scenario 2: $\overline{C_{pr}}$ is defined using pressure and wind profiles from wind tunnel or CFD studies. If the wind profile in building energy models have systematic differences compared to the wind profile used to derive the pressure coefficients, then using the unmodified $\overline{C_{pr}}$ data will cause systematic errors in predicted pressure values (Fig. 4.1b). $\overline{C_{pl}}$ is calculated with the wind speed at the same height as the wind pressure, so is not a function of the wind profile (Akins and Cermak, 1976; Swami and Chandra, 1987), and is directly applicable in BES with a different wind profile from the one used to derive $\overline{C_{pl}}$ in the wind tunnel or CFD study. However, this does not apply to $\overline{C_{pr}}$ because it is based on the wind speed at a reference height (Fang and Sill, 1995; Yang et al., 2008). For example, it is possible for different wind profiles to have the same wind speed at the reference height H. Neglecting differences in vertical wind profiles can cause biases. Potentially, this is a large problem as $\overline{C_{pr}}$ is widely used (Table 4.1, 4.2), and wind profiles in BES are normally different from the C_p source experiment wind profiles especially when using the secondary sources (11 of 27 studies in Table 4.2). When the wind profiles for both the $\overline{C_{pr}}$ source and the BES are known, the $\overline{C_{pr}}$ data can be modified appropriately.

Scenario 3: If BES are combined with urbanised wind speed from urban canopy models, the free stream wind C_p values should be also accounted for the influence of the surrounding buildings (Fig. 4.1c). With increasing attention on urbanization and the impact of urban climate on building performance, efforts have been made to integrate BES with urban land surface or canopy models, such as combining EnergyPlus with Surface Urban Energy and Water Balance Scheme (SUEWS) (Järvi et al., 2011; Tang et al., 2021) and the Vertical City Weather Generator (VCWG) (Moradi et al., 2022). Urban canopy models can modify meteorological variables to better account for the impact of buildings on local climate which will influence wind pressure calculation. For example, SUEWS provides a mean neighbourhood vertical profile of wind speed (Tang et al., 2021; Theeuwes et al., 2019). This differs from the undisturbed wind used in Eq. 4.1 and 4.2 which are default weather data inputs in EnergyPlus. In this case, C_p values need to be corrected if the local wind speed is used (Fig. 4.1c). This has been largely overlooked in existing urban-building coupling energy simulation studies (e.g., use of C_p for surrounded case and disturbed local wind speed as reviewed by Johari et al. (2020)).

The objectives of this study are to: (1) quantify the bias arising from using inconsistent reference height and wind pressure coefficient combinations; (2) assess the bias arising from the inconsistence of approaching wind profiles between BES and the source deriving the wind pressure coefficients; and (3) discuss the correction of wind pressure coefficients when combining building energy simulation tools and urban climate models.

Table 4.1: Summary of commonly used databases (DB#) of wind pressure coefficients (C_p) in building energy simulations (BES) either using reference height (C_{pr}) or the local height (C_{pl}). $\overline{C_{pr}}$ and $\overline{C_{pr}}$ refer to surface averaged C_{pr} and C_{pl} data, respectively. *C_{pl} data are also calculated but not used in ASHRAE *Handbook of Fundamentals* (ASHRAE, 2005) and EnergyPlus (U.S. Department of Energy, 2020f). In places information is not given (NG). Examples of where the data source are used in a BES tool as a default. Modified after Cóstola et al. (2009).

DB#	C_p Source	Type	Wind profiles in wind tunnel experiments	Sheltering effects	BES Default
1	Akins et al. (1979)	$\overline{C_{pr}}$ and $\overline{C_{pl}}$*	Provided	Isolated	EnergyPlus for high-rise buildings
2	AIVC by Liddament (1986)	$\overline{C_{pr}}$	NG	Isolated, semi-exposed or sheltered (λ_P are not given)	IES-VE and DesignBuilder (DesignBuilder, 2022)
3	Swami and Chandra (1987)	$\overline{C_{pr}}$	NG	Isolated, correction coefficients for ventilation rate	EnergyPlus for low-rise buildings
4	TPU (2007)	$\overline{C_{pr}}$	Provided	λ_P from 0.1 to 0.6	Used as external source

Table 4.2: Summary of types of C_p data and wind speed height used in EnergyPlus and Airflow Network (AFN) studies. All C_p values are surface averaged values. Following Cóstola et al. (2009), sources are either primary (1°) from wind tunnel (WT) experiments and computational fluid dynamics (CFD) simulations, or secondary (2°) from published databases (DB, with references to Table 4.1 indicated by #) or analytical tools for generic building archetypes. EnergyPlus-AFN studies that do not indicate the C_p method used, are assumed to use pre-provisioned C_{pr} values with wind speed at the opening height *z*. *H* refers to the reference building height. Sometimes information is not given (NG).

Reference	C_p		$\overline{C_{pr}}$ or $\overline{C_{pl}}$	Free stream wind speed height
	Source	Type		
Botti et al. (2022)	2°	DB#3	$\overline{C_{pr}}$	*z*
Bre and Gimenez (2022)	1°	CFD	$\overline{C_{pr}}$	*H*
Guo et al. (2022)	1°	CFD	NG	NG
Toesca et al. (2022)	2°	UrbaWind (2022)	$\overline{C_{pr}}$	*H*
Dogan and Kastner (2021)	1°, 2°	CFD, DB#3	$\overline{C_{pr}}$	*z*
Saif et al. (2021)	2°	DB#2	$\overline{C_{pr}}$	NG
Sakiyama et al. (2021)	2°	DB#3	$\overline{C_{pr}}$	*z*
Song et al. (2021)	1°	WT	$\overline{C_{pl}}$	NG
Albuquerque et al. (2020)	1°	CFD	$\overline{C_{pr}}$	*H*
Raji et al. (2020)	1°	WT	NG	NG
Sadeghi et al. (2020)	1°	WT	$\overline{C_{pr}}$	NG
Bayraktar and Ok (2019)	1°	WT	NG	NG
Belmans et al. (2019)	1°	CFD	$\overline{C_{pl}}$	*z*
Gimenez et al. (2018)	1°	CFD	$\overline{C_{pr}}$	*z*
Kim et al. (2018)	2°	DB#3	$\overline{C_{pr}}$	*z*
Short et al. (2018)	1°	CFD	NG	NG
Southall (2018)	2°	DB#3	$\overline{C_{pr}}$	*z*
Van Nguyen and De Troyer (2018)	2°	C_p Generator (Knoll et al., 1996)	$\overline{C_{pr}}$	NG
Bre et al. (2016)	2°	DB#3	$\overline{C_{pr}}$	*z*
Sorgato et al. (2016)	2°	C_p Generator (Knoll et al., 1996)	$\overline{C_{pr}}$	NG
Belleri et al. (2014)	1°	WT	NG	NG
Ramponi et al. (2014b)	1°	WT	$\overline{C_{pr}}$	NG
Joe et al. (2013)	1°	CFD	$\overline{C_{pr}}$	NG
Schulze and Eicker (2013)	2°	DB#2	$\overline{C_{pr}}$	*z*
You et al. (2013)	1°	CFD	$\overline{C_{pr}}$	NG
Carrilho Da Graça et al. (2012)	1°	CFD	NG	NG
Olsen and Chen (2003)	1°	CFD	$\overline{C_{pr}}$	NG

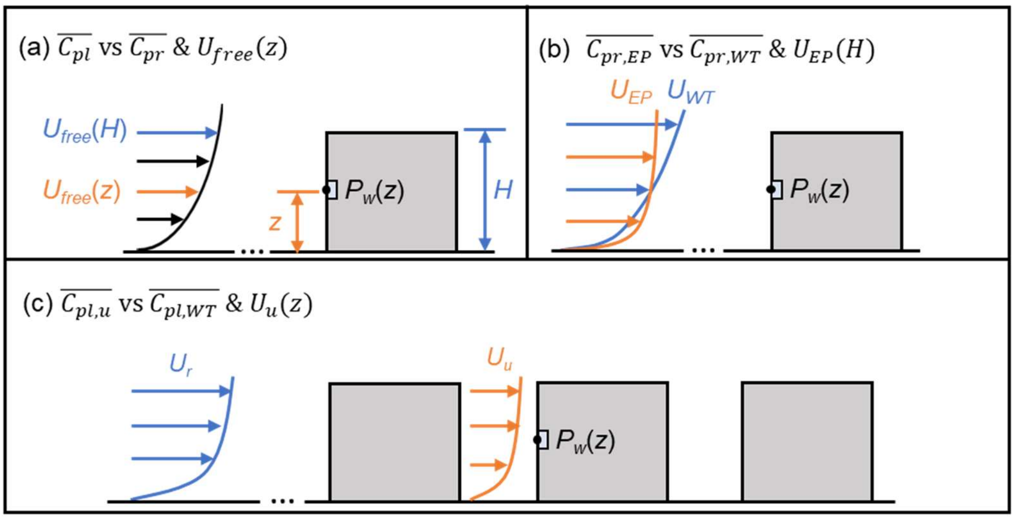

Fig. 4.1. Three scenarios (Section 4.1) to determine wind pressure coefficients (C_p) all assume they are surface-averaged ($\overline{C_{pl}}$ or $\overline{C_{pr}}$) but with different wind profiles (U): (a) *Scenario 1* are calculated with free stream wind speed at the opening height ($U_{free}(z)$), (b) *Scenario 2:* $\overline{C_{pr}}$ is derived from wind tunnel (WT) wind profile ($\overline{C_{pr,WT}}$) or from the EnergyPlus (EP) building energy simulation ($\overline{C_{pr,EP}}$); and (c) *Scenario 3:* $\overline{C_{pl}}$ is based on disturbed urbanised (u) wind speed ($\overline{C_{pl,u}}$) rather than an undisturbed free stream wind speed ($\overline{C_{pl,WT}}$).

4.2. Methods

To analyse the use of wind pressure coefficients in building energy simulation (BES), we use the BES tool EnergyPlus v9.4 (U.S. Department of Energy, 2020a) with Airflow Network (AFN) for ventilation rate calculation, and urban land surface model SUEWS (Järvi et al., 2011; Ward et al., 2016) to simulate urban wind profiles. The wind pressure coefficient (C_p) data are obtained from the Tokyo Polytechnic University's aerodynamic database for low-rise buildings (TPU, 2007) under isolated and surrounded scenarios.

A two-storey reference building (Fig. 4.2a) based on ASHRAE Case 600 (ANSI/ASHRAE, 2011) is simulated for the Shanghai weather conditions in 2018 (SUEWS outputs forced with ERA5 (Hersbach et al., 2020) for three settings:

(1) a rural, isolated (Fig. 4.2a)

(2) a neighbourhood with plan area fraction $\lambda_P = 0.3$ (Fig. 4.2b)

(3) a neighbourhood with plan area fraction $\lambda_P = 0.6$ (Fig. 4.2c).

Each floor of the building has a 3 m × 2 m window on the north and south facing walls, of which the upper 1/3 area hinged and openable to 20° for cross ventilation. For consistency with weather data, the building envelope thermal characteristics are set using the current local Shanghai building code (MoHURD, 2015). This has overall heat transfer coefficients (U-values) of 0.39 W m^{-2} K^{-1} for the roof, 0.54 W m^{-2} K^{-1} for the external wall, 0.46 W m^{-2} K^{-1} for the floor, and 1.77 W m^{-2} K^{-1} for the windows. All windows are assumed to have 15% openable area and a discharge coefficient (C_d) of 0.61.

We calculate the natural ventilation rate, indoor overheating risk and energy saving potential. For the naturally ventilated mode, all windows are always open. The overheating risk is assessed using the Category II Chinese adaptive thermal model comfort corresponding to 75% satisfaction (MoHURD, 2012). For the southern zone (i.e., applicable for Shanghai) the upper (T_{max}) and lower temperature limits (T_{min}) are (MoHURD, 2012):

$$\begin{cases} T_{max} = 0.73T_{rm} + 12.72 & (18℃ \leq T_{max} \leq 30℃) \\ T_{min} = 0.91T_{rm} - 3.69 & (16℃ \leq T_{min} \leq 28℃) \end{cases} \qquad (4.3)$$

where the running mean outdoor temperature T_{rm} is:

$$T_{rm} = (1-k)(T_{od-1} + kT_{od-2} + k^2T_{od-3} \cdots + k^6T_{od-7}) \qquad (4.4)$$

where k is a constant between 0 and 1, with 0.8 used as recommended (Nicol and Humphreys, 2002), and T_{od-n} is the daily mean outdoor temperature n days ago (°C).

The air-conditioning mode follows the Code for Thermal Design of Civil Building recommendation of heating (18 °C) and cooling (26 °C) setpoints (MoHURD, 2016). Windows can be open if air-conditioning is off and outdoor temperature is lower than indoor temperature. The cooling energy saving is calculated as the difference between the energy demand in hybrid mode (natural ventilation together with air conditioning) and fully air-conditioned mode.

The indoor overheating metrics are hours and degree hours exceeding the upper limits of temperatures (T_{max}) (Porritt et al., 2012). Local outdoor weather data required for EnergyPlus simulations for the two neighbourhoods are generated using SUEWS with the vertical profiles option of air temperature, relative humidity, and wind speed (Tang et al. (2021). Air temperature and wind profiles evaluations using observations at three sites have reasonable accuracy (Tang et al., 2021; Theeuwes et al., 2019). For the neighbourhood cases, solar shading and inter-building external longwave radiative exchanges are also considered (Chapter 3).

The normalised mean bias error (nMBE) assessment metric is used to compare two cases (x; y) for each of the three scenarios (Section 4.1, Fig. 4.1):

$$nMBE = \frac{1}{N}\frac{\sum_{i=1}^{N}(y_i - x_i)}{\bar{x_i}} \cdot 100\% \qquad (4.5)$$

where x_i is the results from a consistent combination of C_p and level of U, and y_i is the results from the inconsistent combination of these for each hour i in the year (total of N = 8760 hours). The ASHRAE-14 Guideline (ASHRAE, 2014) acceptable uncertainty limits for building energy simulation programmes is set as the nMBE needs to be within ±10% for hourly data.

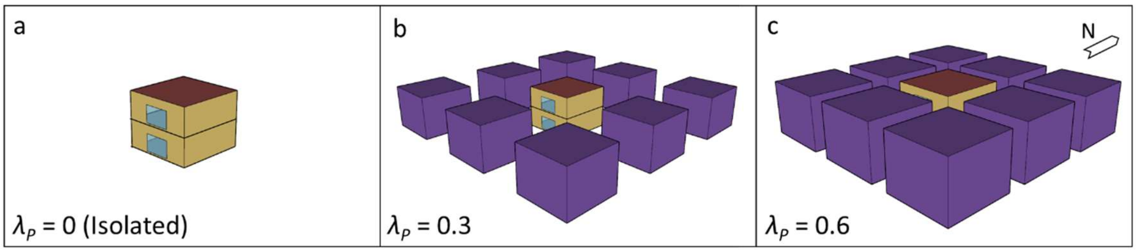

Fig. 4.2. A reference building (8 m (L) × 8 m (W) × 6.4 m (H)) is simulated using EnergyPlus in: (a) a rural (isolated) site, and in neighbourhoods with a plan area fractions λ_P = (b) 0.3 and (c) 0.6.

4.3. Results

4.3.1. C_{pl} & $U_{free}(z)$ vs C_{pr} & $U_{free}(z)$ for an isolated building

First, we need to derive a relation between surface averaged C_{pl} ($\overline{C_{pl}}$) and C_{pr} ($\overline{C_{pr}}$). To obtain the surface averaged C_p over the facet one can either calculate C_p at several locations and average, or define $\overline{C_{pl}}$ as the constant value that gives the correct total wind pressure over the facet (Akins and Cermak, 1976). The latter is analogous to Santiago and Martilli's (2010) approach used for vertically distributed drag modelling of urban canopies, where the surface-averaged drag coefficient is the value giving the correct total drag over the building facet.

Akins and Cermak (1976) suggested the differences between these two techniques are minimal, so we assume surface averaged C_p calculated with both methods are the same. We take the correct total wind pressure approach, which is defined by rearranging Eq. 4.1 or 4.2 for $P_w(z)$ and integrating over the facet. For the pressure coefficient defined with velocity at the local opening height (Eq. 4.2) one finds:

$$\overline{C_{pl}} = \frac{\int_0^H P_w(z)dz}{\int_0^H 0.5\rho U_{free}^2(z)dz} \quad (4.6)$$

and for the pressure coefficient defined with velocity at the building height (Eq. 4.1) one finds:

$$\overline{C_{pr}} = \frac{\frac{1}{H}\int_0^H P_w(z)dz}{0.5\rho U_{free}^2(H)} \quad (4.7)$$

By only integrating over height it has been assumed that C_p variations in the horizontal can be neglected or that $P_w(z)$ has first been horizontally averaged across the facet. The approach is practical since velocity profiles in building energy models normally have vertical variation, so horizontal variation of C_p is not included.

To get the same average wind pressure over the building facet $\frac{1}{H}\int_0^H P_w(z)dz$, one can combine Eq. 4.6 and 4.7 so that:

$$\overline{C_{pl}} \cdot \frac{1}{H}\int_0^H 0.5\rho U_{free}^2(z)dz = \overline{C_{pr}} \cdot 0.5\rho U_{free}^2(H) \quad (4.8)$$

which after rearranging becomes:

$$\overline{C_{pl}} = \overline{C_{pr}} \cdot \frac{0.5\rho U_{free}^2(H)}{\frac{1}{H}\int_0^H 0.5\rho U_{free}^2(z)dz} = \overline{C_{pr}} \cdot \frac{U_{free}^2(H)}{\frac{1}{H}\int_0^H U_{free}^2(z)dz} \quad (4.9)$$

To find $\overline{C_{pl}}$, values for $\overline{C_{pr}}$ and an equation for the wind speed are required. $\overline{C_{pr}}$ data from the TPU (2007) database are used. Commonly in wind tunnel experiments (e.g. TPU (2007)), a power law is used to describe the undisturbed wind speed at height z:

$$U_{free}(z) = U_{\mathrm{ref}}\left(\frac{z}{z_{\mathrm{ref}}}\right)^{\alpha} \quad (4.10)$$

where U_{ref} is the reference wind speed at height z_{ref} defined within the experiment, and the exponent α is an empirically derived coefficient. The vertically averaged wind speed is given by:

$$\frac{1}{H}\int_0^H U_{free}^2(z)dz = \frac{1}{H}\int_0^H \left(U_{\mathrm{ref}}\left(\frac{z}{z_{\mathrm{ref}}}\right)^{\alpha}\right)^2 dz = \frac{U_{\mathrm{ref}}^2 H^{2\alpha}}{\mathrm{z}_{ref}^{2\alpha}(2\alpha+1)} \quad (4.11)$$

Substituting Eq. 4.10 and 4.11 into Eq. 9:

$$\overline{C_{pl}} = \overline{C_{pr}} \frac{U_{\mathrm{ref}}^2\left(\frac{H}{z_{\mathrm{ref}}}\right)^{2\alpha}}{\frac{U_{\mathrm{ref}}^2 H^{2\alpha}}{\mathrm{z}_{ref}^{2\alpha}(2\alpha+1)}} = \overline{C_{pr}}(2\alpha + 1) \quad (4.12)$$

Using Eq. 4.12 with $\overline{C_{pr}}$ data from the TPU database (vertical profiles of original C_{pr} data are shown in Supplementary Material Fig. A5.1a), the results for an isolated reference building are given in Table 4.3, as are the $\overline{C_{pl}}$ data. EnergyPlus is used with the power law velocity profile that is the same as in the wind tunnel experiment in the TPU database assuming a suburban terrain and an exponent α of 0.2. EnergyPlus simulations are conducted for Shanghai in 2018 under naturally ventilated and mechanical cooling/heating modes as described in Section 4.2. The normalised mean bias errors (nMBE) for the ventilation rate, indoor overheating risks and cooling/heating energy demand are calculated between $\overline{C_{pl}}$ & $U_{free}(z)$ and $\overline{C_{pr}}$ & $U_{free}(z)$.

The $\overline{C_{pr}}$ with $U_{free}(z)$ underpredicts the annual air change per hour (ACH) ventilation rate (Fig. 4.3), with a nMBE of -15.5% (i.e., exceeding the ASHRAE-14 acceptable limit of ±10%). The annual overheating hours and degree hours are overpredicted by 11.9% and 12.9%, respectively. Such differences in overheating are found to largest during three consecutive heatwave days (13 to 15 July 2018, Fig. 4.4). During this period the $\overline{C_{pr}}$ & $U_{free}(z)$ case overpredicts the overheating hours and degree hours by 19.5% and 12.4%, respectively. Given the smaller ventilation rate, the nMBE in cooling energy saving is -10.5%, again exceeding the ASHRAE-14 limit. This suggests confusing $\overline{C_{pl}}$ with $\overline{C_{pr}}$ should be avoided when modelling ventilation rates and indoor overheating risks of naturally ventilated buildings, as well as the resultant cooling energy saving.

Table 4.3: Surface-averaged wind pressure coefficients based on the reference height *H* ($\overline{C_{pr}}$) and opening height *z* ($\overline{C_{pl}}$) by wind angle related to the facet (0° is when wind is normal to the facet). $\overline{C_{pr}}$ is obtained from the TPU (2007) database. $\overline{C_{pl}}$ is calculated by substituting $\overline{C_{pr}}$ into Eq. 4.12.

	0°	45°	90°	135°	180°
$\overline{C_{pr}}$	0.66	0.35	-0.57	-0.56	-0.28
$\overline{C_{pl}}$	0.92	0.49	-0.80	-0.79	-0.40

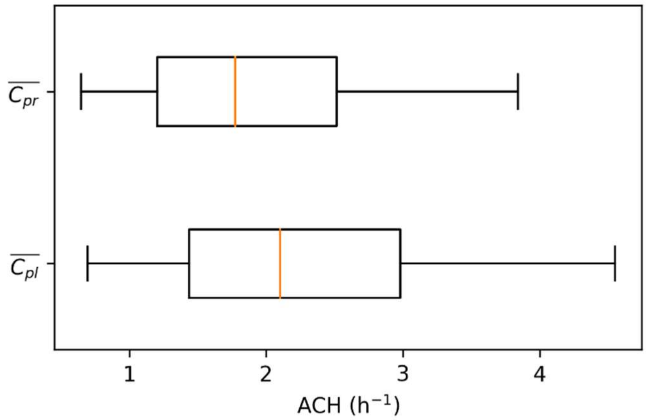

Fig. 4.3. Distribution of annual ACH (air change per hour, N = 8760) calculated with surface averaged wind pressure coefficients based on the opening height z ($\overline{C_{pl}}$) and reference height H ($\overline{C_{pr}}$), with interquartile range (box), median (orange line) and 5th and 95th percentiles (whiskers).

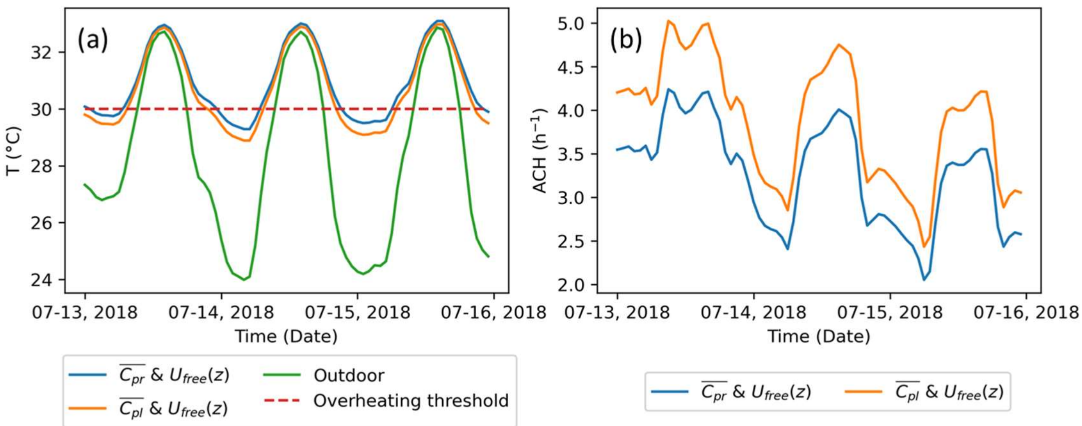

Fig. 4.4. Diurnal changes during three-day heatwave (13 - 15 July 2018) period in Shanghai for the upper floor (Fig. 4.2a) (a) indoor air temperatures, and (b) ventilation rates in ACH when calculated using the $\overline{C_{pl}}$ and $\overline{C_{pr}}$. i.e., $\overline{C_{pl}}$ & $U_{free}(z)$ vs $\overline{C_{pr}}$ & $U_{free}(z)$.

4.3.2. C_{pr} with wind profiles: wind tunnel vs outdoor

Swami and Chandra (1987) and Akins et al. (1979) suggest $\overline{C_{pl}}$ is not a function of the wind profile given it is based on the wind at the opening height z, which is the same as pressure measurement height. After further testing (section Appendix 6), the results suggest that $\overline{C_{pl}}$ independence on wind profile exponent α is acceptable.

However, $\overline{C_{pr}}$ obviously depends on the wind profile. Therefore, when the wind profile in the building energy simulation is different from the wind tunnel experiment where the C_p data are derived, $\overline{C_{pl}}$ can be used directly without further corrections. If only undisturbed wind speed at height H is available (e.g., TMY (typical meteorological year) wind speed data at 10 m), the $\overline{C_{pr}}$ values should be corrected. The EnergyPlus outdoor wind profile module determines the approaching wind speed profile U(z) as (ASHRAE, 2005):

$$U(z) = U_{met}\left(\frac{\delta_{met}}{z_{met}}\right)^{\alpha_{met}}\left(\frac{z}{\delta}\right)^{\alpha} \qquad (4.13)$$

It is calculated with the wind speed measured at a meteorological station U_{met} (i.e., weather data input). Standard World Meteorological Organisation (WMO) wind speed measurement height (z_{met}) is 10 m above ground level (WMO, 2017). δ refers to the height where the vertical gradient of wind speed is assumed to become constant (Tang et al., 2021). Typical values are given in ASHRAE (2005) for different terrain types For an isolated building in open country terrain $\alpha = \alpha_{met} = 0.14$ and $\delta = \delta_{met} = 270$ m.

Following Eq. 4.8, assuming $\overline{C_{pl}}$ data from the TPU database can be used directly (i.e. $\overline{C_{pl,WT}} = \overline{C_{pl,EP}}$) the average wind pressure on the building facet (Fig. 4.4) is calculated as

$$\frac{1}{H}\int_0^H P_w(z)dz = \overline{C_{pl,WT}} \cdot \frac{0.5\rho}{H}\int_0^H U_{EP}^2(z)dz = \overline{C_{pr,EP}} \cdot 0.5\rho U_{EP}^2(H) \qquad (4.14)$$

and upon rearranging one finds

$$\overline{C_{pr,EP}} = \overline{C_{pl,WT}} \cdot \frac{\frac{1}{H}\int_0^H U_{EP}^2(z)dz}{U_{EP}^2(H)} \qquad (4.15)$$

And similar to Eq. 4.12:

$$\overline{C_{pl,WT}} = \overline{C_{pr,WT}}(2\alpha_{WT} + 1) \qquad (4.16)$$

$$\overline{C_{pr,EP}} = \frac{\overline{C_{pl,WT}}}{2\alpha_{EP}+1} = \overline{C_{pr,WT}} \cdot \frac{2\alpha_{WT}+1}{2\alpha_{EP}+1} \qquad (4.17)$$

where $\overline{C_{pr,EP}}$ and $\overline{C_{pl,EP}}$ are used with the EnergyPlus wind speed (U_{EP}), and $\overline{C_{pr,WT}}$ and $\overline{C_{pl,WT}}$ are obtained in the wind tunnel experiment.

To quantify the bias from neglecting the impact of vertical wind profile on C_{pr}, we model the isolated reference building in EnergyPlus, and calculate the ventilation rate, indoor overheating risks and cooling energy demand with both modified $\overline{C_{pr,EP}}$ and unmodified $\overline{C_{pr,WT}}$ obtained from the TPU database directly (Table 4.4). In the TPU database the wind profile exponent is $\alpha_{WT} = 0.2$. The default EnergyPlus wind profiles exponents (α_{EP}) are 0.14, 0.22 and 0.33, for open, rough and urban terrain (ASHRAE, 2005), respectively.

Results (Fig. 4.5) show there are biases if unmodified $\overline{C_{pr,WT}}$ is used along with varying α_{EP}. When $\alpha_{EP} < \alpha_{WT}$, $\overline{C_{pr,WT}}$ is smaller than $\overline{C_{pr,EP}}$, hence the ventilation rate is underpredicted when using $\overline{C_{pr,WT}}$. At $\alpha_{EP} = 0.14$, the nMBE in ACH is -4.5%, which is within the acceptable range of ASHRAE-14. The annual indoor overheating hours and degree hours are overpredicted by 2.3% and 3.7%, respectively. During the heatwave (13 to 15 July 2018) the overpredictions slightly increase to 8.0% and 4.4%. nMBE in cooling energy saving is -3.3%. With $\alpha_{EP} = 0.22$ and 0.33, the ventilation rates are overpredicted resulting in underpredicted overheating risks and overpredicted cooling energy saving (Fig. 4.5). Although all the biases are smaller than the ±10% ASHRAE-14 limit, they would increase in rougher terrain as the wind profile exponent increases.

Table 4.4: Surface-averaged wind pressure coefficients from the wind tunnel experiment ($\overline{C_{pr,WT}}$) (TPU, 2007) and corrected with Eq. 4.17 ($\overline{C_{pr,EP}}$). The wind angles are related to the surface (0° refers to wind blowing perpendicular to the facet).

	α	0°	45°	90°	135°	180°
$\overline{C_{pr,WT}}$	0.2	0.66	0.35	-0.57	-0.56	-0.28
$\overline{C_{pr,EP}}$	0.14	0.72	0.38	-0.62	-0.61	-0.31
	0.22	0.64	0.34	-0.55	-0.54	-0.27
	0.33	0.56	0.30	-0.48	-0.47	-0.24

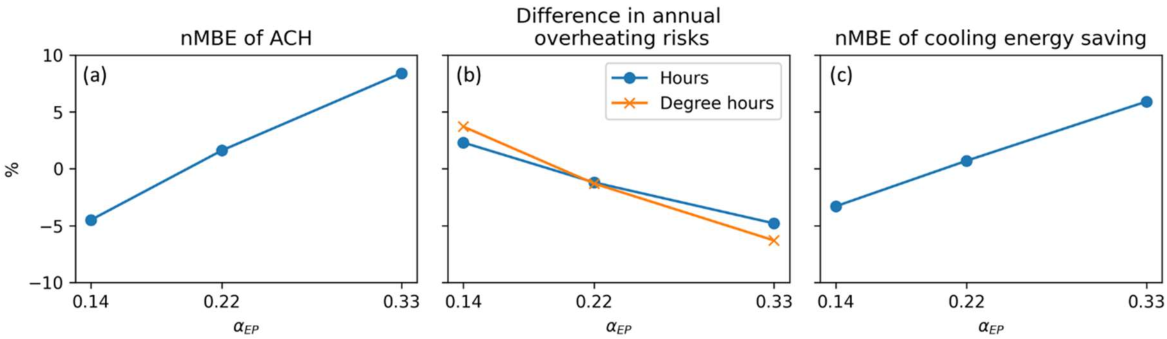

Fig. 4.5. Normalized mean bias errors (nMBE) linked to using unmodified $\overline{C_{pr,WT}}$ from the wind tunnel experiment compared to modified $\overline{C_{pr,EP}}$ for three EnergyPlus wind profiles exponents (*α_{EP})* for (a) ventilation rate in ACH, (b) difference in annual overheating risks and (c) cooling energy saving.

4.3.3. Wind pressure coefficients for urban climate models

When local outdoor weather data are derived from urban climate models, the influence of the neighbourhood buildings are considered, but when calculating building facet wind pressure an 'undisturbed' flow is assumed in Eq. 4.1 and 4.2. For example in SUEWS, the horizontally averaged neighbourhood wind speed is calculated for the roughness sublayer (RSL) based on a modified MOST (Monin–Obukhov similarity theory) approach (Theeuwes et al., 2019). Similar methods are used in other models like the Vertical City Weather Generator (Moradi et al., 2022). The advantages of using RSL wind are in calculating convective heat transfer on building surfaces and single-sided ventilation. But the cross-ventilation calculation will be biased if the urbanised wind speed is not used with corrected C_p values.

In SUEWS, the undisturbed wind profile can be modelled with an open rural setting (U_r), and the disturbed RSL wind profile can be modelled using different urban settings (U_u). To get the average wind pressure across the building facade:

$$\frac{1}{H}\int_0^H P_w(z)dz = \overline{C_{pl,WT}} \cdot \frac{0.5\rho}{H}\int_0^H U_r^2(z)dz = \overline{C_{pl,u}} \cdot \frac{0.5\rho}{H}\int_0^H U_u^2(z)dz \tag{4.18}$$

$$\overline{C_{pl,u}} = \overline{C_{pl,WT}} \cdot \frac{\int_0^H U_r^2(z)dz}{\int_0^H U_u^2(z)dz} \tag{4.19}$$

where $\overline{C_{pl,u}}$ is the corrected wind pressure coefficient for use alongside with the RSL wind (U_u) assuming the vertical profiles of U_u and U_r have the power law format of Eq. 4.13. Details of obtaining power law vertical profiles of U_u and U_r applicable for use with EnergyPlus are given in Tang et al. (2021). Eq. 4.19 can be re-written as:

$$\overline{C_{pl,u}} = \overline{C_{pl,WT}} \cdot \frac{U_r^2(10)H^{2\alpha_r}\delta_u^{2\alpha_u}(2\alpha_u+1)}{U_u^2(10)H^{2\alpha_u}\delta_r^{2\alpha_r}(2\alpha_r+1)} \tag{4.20}$$

Since the RSL wind have lower velocities than the undisturbed wind, $\overline{C_{pl,WT}}$ values need to be scaled to larger magnitudes ($\overline{C_{pl,u}}$) to obtain the same wind pressure. To quantify the biases of using the disturbed RSL wind speed U_u with $C_{pl,WT}$, we consider two idealised neighbourhoods with aligned buildings in EnergyPlus with plan area fractions of λ_P = 0.3 and 0.6, with the surface-averaged C_p values given in Table 4.5 (original $C_{pr,WT}$ vertical profiles are shown in Fig. A5.1b, c).

For the neighbourhood with a λ_P of 0.3, using $\overline{C_{pl,WT}}$ with the RSL wind $U_u(z)$ largely underpredicts the ventilation rate, with an annual nMBE of -19.0%, exceeding the ASHRAE-14 acceptable uncertainty limits. The annual indoor overheating hours and degree hours are overpredicted by 5.9% and 13.2%, respectively. During the heatwave (13 to 15 July 2018), the indoor overheating hours difference is 0, because in both cases the indoor air temperature exceeds the maximum temperature threshold throughout (Fig.

4.6a), but the overprediction in degree hours increases to 18.4%. The nMBE in cooling energy saving is -14.0%.

Additionally, the ventilation rate is simulated with $\overline{C_{pl,WT}}$ and the free stream wind $U_r(z)$ to evaluate Eq. 4.18. Results (Fig. 4.7), as expected, suggest that using $\overline{C_{pl,WT}}$ with $U_r(z)$ and $\overline{C_{pl,u}}$ with $U_u(z)$ give very similar results (nMBE = 0.8%). The small differences are possibly due to the buoyancy-driven ventilation dominating, since the wind speed input to EnergyPlus is also used for calculations of both convection and indoor air temperature.

Generally for the $\lambda_P = 0.6$ neighbourhood, the biases are slightly smaller (cf. $\lambda_P = 0.3$) because of the lower wind speeds. The nMBE for the ventilation rate is -16.2%, while the annual indoor overheating hours and degree hours are overpredicted by 4.7% and 9.0%, respectively. However, during the heatwave (Fig. 6b) when ventilation rates are small, differences in overheating hours become 20.3%. The nMBE in cooling energy saving is -9.6%.

In summary, when modelling naturally ventilated buildings using urbanised wind speeds, correcting the C_p data correspondingly is important. Increasing λ_P can lead to slightly smaller annual biases, but during heatwaves when the natural ventilation rates are small, larger biases can be seen.

Table 4.5: Surface-averaged wind pressure coefficients from the wind tunnel experiment ($\overline{C_{pr,WT}}$) (TPU, 2007), calculated with Eq. 4.12 ($\overline{C_{pl,WT}}$) and corrected with Eq. 4.20 ($\overline{C_{pl,u}}$) for urbanised wind (U_u) for two plan area fractions ($\lambda_P = 0.3$ and 0.6) for different wind angles (0° refers to wind blows perpendicular to the facet).

		0°	45°	90°	135°	180°
$\lambda_P = 0.3$	$\overline{C_{pr,WT}}$	0.15	0.05	-0.22	-0.24	-0.16
	$\overline{C_{pl,WT}}$	0.21	0.07	-0.31	-0.34	-0.22
	$\overline{C_{pl,u}}$	0.34	0.11	-0.51	-0.55	-0.37
$\lambda_P = 0.6$	$\overline{C_{pr,WT}}$	-0.13	-0.09	-0.17	-0.20	-0.21
	$\overline{C_{pl,WT}}$	-0.18	-0.13	-0.24	-0.28	-0.29
	$\overline{C_{pl,u}}$	-0.66	-0.46	-0.86	-1.02	-1.07

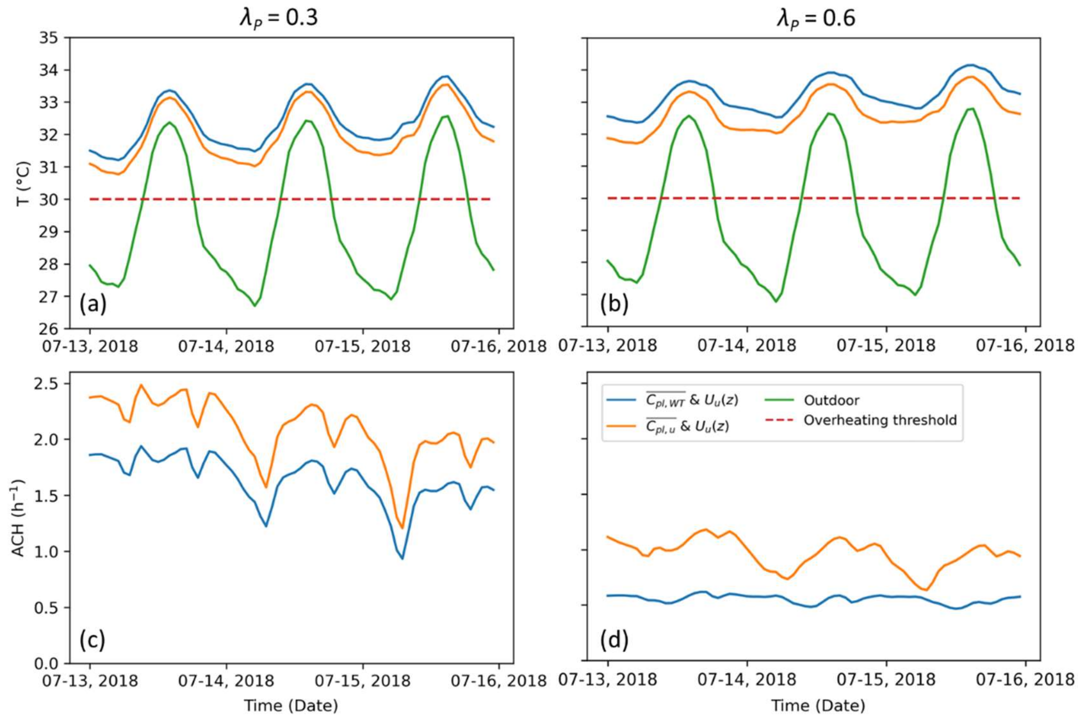

Fig. 4.6. As Fig. 4.4, but using surface-averaged wind pressure coefficients from wind tunnel experiments ($\overline{C_{pl,WT}}$) (TPU, 2007) and corrected with Eq. 4.20 ($\overline{C_{pl,u}}$) at for two neighbourhoods when λ_P is (a, c) 0.3 and (b, d) 0.6, for (a, b) air temperature and (c, d) ventilation rate in ACH.

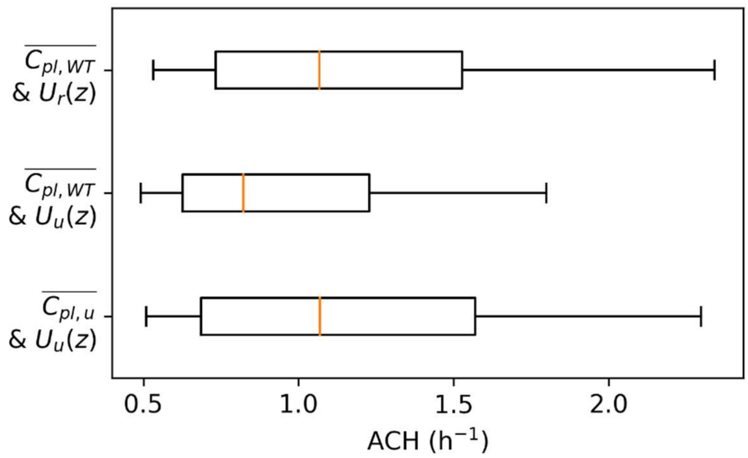

Fig. 4.7. As Fig. 4.3, but for modelling ventilation rate (as ACH) with three combinations of $\overline{C_{pl}}$ and $U(z)$. $\overline{C_{p,WT}}$ & $U_r(z)$ and $\overline{C_{p,u}}$ & $U_u(z)$ give the similar results but vary slightly due to differences in buoyancy-driven ventilation, whereas assuming $\overline{C_{p,WT}}$ & $U_u(z)$ is inconsistent and therefore biased.

4.4. Discussion

There are various assumptions and approximations made for C_p to simplify the calculation of wind pressure on building facets that can cause various uncertainties. Some of these have been assessed previously, such as those linked to the surface averaged values and different data sources (Cóstola et al., 2010; Ramponi et al., 2014a). Most common sources of C_p data provide surface averaged values based on the reference height ($\overline{C_{pr}}$), rather than being based on the opening height ($\overline{C_{pl}}$). Given the definition (Eq. 4.7), $\overline{C_{pr}}$ data needs to be corrected in some circumstances, but this appears to have been overlooked in most existing studies. In this study we explore three scenarios to quantify biases from inconsistent combination of C_p value and wind speed.

In each scenario we find critical differences, which impact the resulting predictions especially of ventilation rates and indoor overheating risks for naturally ventilated buildings. These findings confirm that natural ventilation rate calculations are sensitive to the C_p and wind data used. Notably, we revise the relation between the $\overline{C_{pr}}$ and $\overline{C_{pl}}$ that has often been neglected in building energy simulations. Our results demonstrate the importance of modifying C_p data for wind conditions, including the wind speed height, wind profile and terrain surface type (e.g. extensive grass – 'undisturbed', neighbourhoods at different λ_P – 'disturbed' or 'urbanised').

There are limitations in our work. Although surface averaged C_p data are widely used, their errors (cf. local C_p data) are assumed relatively smaller if openings are located in the facet centre instead of edges where extreme values occur (Cóstola et al., 2010). Hence, we only consider windows located in the centre of each facet. We consider only one climate type, but expect that relative results should be similar across different climates, as found by Ramponi et al. (2014a). Future work could evaluate a wider range of climates and different building geometries (e.g., gable and hip roofs).

4.5. Conclusions

Wind pressure coefficients are widely used in building energy simulations (BES) to calculate the ventilation rate. However, wind pressure coefficients may be used inappropriately given their assumptions and simplifications. Users obtain them from datasets that most commonly have a fixed *reference* height H (hereafter C_{pr}) but some use a *local* opening height z (hereafter C_{pl}). From analysis of three typical scenarios, we conclude these impacts are critical especially when simulating natural ventilation rates, indoor overheating and cooling energy saving. By using surface averaged C_{pr} ($\overline{C_{pr}}$) data in BES directly in Shanghai climate, biases can potentially lead to:

(1) if using free stream wind speed at z in EnergyPlus, rather than the velocity at H

- nMBE = -15.5% in predictions of ventilation rate, 11.9% for indoor overheating hours and 12.9% for overheating degree hours, and -10.5% for cooling energy saving

(2) if using wind profiles that differ from the wind tunnel and CFD studies used to derive the pressure coefficients

- relatively small errors (nMBE of ventilation rate of up to 8.4%), but these may increase when there are greater differences between wind tunnel experiment and BES wind profile exponents

(3) if using urbanised wind speeds, but $\overline{C_{pr}}$ is calculated based on free stream wind speeds

- large errors in ventilation rates (nMBE of up to -19.0%), indoor overheating risks (differences in annual hours and degree hours of up to 5.9% and 13.2%, respectively) and cooling energy saving (nMBE of up to -14.0%) when two different neighbourhoods (λ_P = 0.3 and 0.6) are considered.

Furthermore, all of these biases increase during heatwave periods.

Clearly these biases should be considered when simulating the impact of natural ventilation using building energy simulation tools. To improve the accuracy of natural ventilation rate prediction in BES we recommend:

- C_p data should be used with the free stream wind speed at a consistent height, i.e. reference height H for $\overline{C_{pr}}$, or local opening height z for $\overline{C_{pl}}$. For power law wind profiles, $\overline{C_{pr}}$ and $\overline{C_{pl}}$ can be interconverted with Eq. 4.12.

- As the wind profile in BES could be different from the ones in wind tunnel and CFD studies where $\overline{C_{pr}}$ are derived, care is needed with which C_p data are used. $\overline{C_{pl}}$ this can be used directly, but not for $\overline{C_{pr}}$ data. The latter should be corrected based on wind profiles in the BES and the wind tunnel/CFD studies (e.g., Eq. 4.17).

- When BES use urbanised wind speed (i.e., not 'undisturbed'), C_p data should be corrected to account for the relation between undisturbed free stream and urbanised wind (Eq. 4.19).

Chapter 5 Predicting natural ventilation potential in idealised urban neighbourhoods across Chinese climate zones

Building energy simulations typically use rural weather data, which is not representative of urban areas where most buildings are located. In the previous two chapters, methods were proposed to improve EnergyPlus's ability to simulate urban buildings. This chapter demonstrates the application of the improved SUEWS-EnergyPlus method in idealised scenarios, specifically predicting natural ventilation potential (NVP) in buildings located in three urban neighbourhoods in five Chinese cities with different climate zones. The aim is to highlight the importance of considering the neighbourhood or local-scale climate when assessing NVP and to demonstrate a method to improve the accuracy of NVP predictions using EnergyPlus in urban areas.

This chapter is written in the format of a journal paper, with Xie, X., Luo, Z., Grimmond, S., Sun, T. as authors. As the primary author, I conducted the research, wrote the first draft, and created the figures, while Z. Luo, S. Grimmond, and T. Sun provided guidance on the conception and structure of the paper, interpretation of the findings, and text editing.

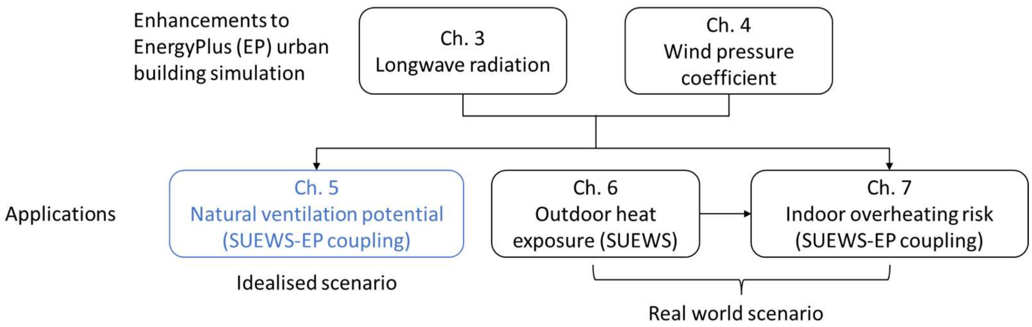

5.1. Introduction

The Paris Agreement calls on countries to cut carbon emissions to meet the target of limiting global warming to preferably 1.5 °C compared to pre-industrial levels (UN, 2015). In 2019, carbon emissions from the operation of buildings accounted for 28% of total global energy-related carbon emissions (UNEP, 2020). Although in China building operation contributes to 21.6 % of national carbon emissions (CABEE, 2021), China's building energy consumption is expected to continue to rise with urbanisation and climate change. Thus, it is important but challenging to improve energy efficiency.

Natural ventilation is a key passive cooling strategy used to achieve low-carbon building design. It reduces energy consumption, and improves occupants' health, comfort, and productivity (Emmerich et al., 2001). As the effectiveness of natural ventilation depends on the outdoor weather conditions, these impacts need to be assessed.

Natural ventilation potential (NVP) is defined as the possibility (or probability) of achieving acceptable indoor thermal comfort and air quality through natural ventilation alone (Luo et al., 2007). It has been studied worldwide using different methods and metrics (Table 5.1), but assessing NVP can be difficult due to its sensitivity to factors such as weather, climate, building design, and the surrounding environment (Yin et al., 2010).

Climate-based approaches provide broad geographic NVP variations using outdoor air temperature and wind speed (Wang and Malkawi, 2019), for use in the early design stage when detailed building information is unavailable (outdoor data analysis, Table 5.1). For example, Chen et al.'s (2017) global analysis using typical meteorological year (TMY) data found temperate climates (e.g. subtropical highland, Mediterranean) tend to have larger NVP compared to more extreme climates (e.g. tropical, subarctic). Humidity has also been identified as being important when assessing NVP in hot-humid climates (Causone, 2016).

Using building energy simulation tools (e.g. EnergyPlus (U.S. Department of Energy, 2020a), TRNSYS (2009), DeST (Yan et al., 2008), IES-VE (Integrated Environmental Solutions, 2018)) NVP assessments can account for building design elements (building simulation, Table 5.1) including impacts such as the internal heat gain, building envelope, occupancy schedule and ventilation pattern. Building energy simulation tools have proven ability to accurately simulate indoor thermal environments, if detailed and accurate input data are provided (Anđelković et al., 2016; Royapoor and Roskilly, 2015).

Originally (and typically) building energy simulation tools treat buildings as being isolated, using weather data input acquired from meteorological stations located in open country. However, the climate in urban areas is known to differ from surrounding rural areas due to various aspects of the urban environment potentially affecting natural ventilation (Oke et al., 2017a). Under wind-driven ventilation conditions the airflow pattern is influenced by surrounding buildings modifying the wind pressure on building facades (van Hooff and Blocken, 2010; Yang et al., 2008; Zhang et al., 2005). Whilst buoyancy-driven ventilation is affected by warmer outdoor air temperatures caused by the canopy layer urban heat island effect (WMO, 2023), which is a result of the building fabric affecting heat storage and waterproofing (Grimmond et al., 1986; Grimmond and Oke, 1999a), anthropogenic heat release from human activities (Allen et al., 2011; Sailor, 2011), trapped longwave radiation (Xie et al., 2022) and reduced wind speed (WMO, 2023).

Considering these impacts, assessing buildings in the urban environment using rural weather data will cause biases. Some have accounted for urban climate in building energy simulation (Frayssinet et al., 2018; Johari et al., 2020), with most assessing urban buildings NVP using computational fluid dynamic (CFD) models (Table 5.1) to obtain air flow (Toparlar et al., 2017). However, CFD methods are dependent on the meteorological boundary conditions and the building morphology details, and their high computational costs make them unsuitable for long-term and large-scale simulations. Long-term modelling using EnergyPlus has accounted for urban climate, by modifying weather data using a simple urban heat island scenario that considers the air temperature only, so natural ventilation cooling energy savings can be simulated (Ramponi et al., 2014). However, their urban heat island prediction only considers a fixed UHI magnitude, which does not account for neighbourhood density (or plan area fraction), and thus may not fully represent the local climate. Tong et al. (2017) accounted for local atmospheric conditions on NVP for super high-rise buildings using Monin-Obukhov similarity theory (MOST) approach. However, MOST applies in the inertial sublayer (a layer that begins 2 to 5 times above the mean canopy height) if present but not in the roughness sublayer (Grimmond and Oke, 1999b; Theeuwes et al., 2019). Also, the analysis did not consider inter-buildings impacts such as radiation and canopy layer urban heat island.

In this study, we propose a more practical method to simulate natural ventilation potential (NVP) of buildings in urban settings that combines the urban land surface model SUEWS (Järvi et al., 2011) and the building simulation tool EnergyPlus (U.S. Department of Energy, 2020a). The objectives are to: (1) improve EnergyPlus's ability to predict NVP in the urban environment, (2) analyse impacts of urban climate on the NVP, and (3) investigate how NVP changes with neighbourhood plan area fraction of buildings and climate.

Table 5.1: Summary of studies on natural ventilation potential (NVP) by date. Weather data source: open - standard rural meteorological station; urban - on-site observation or CFD modelling. NVP Metric: NV-hours - natural ventilation hours; PDPH - pressure difference Pascal hours; NVCE – natural ventilation cooling effectiveness (Yoon et al., 2020), ratio of actual ventilation heat loss rate to required ventilation heat loss rate. NV criteria: T - air temperature, U -wind; RH - relative humidity. Method of NVP calculation: OutMet – outdoor meteorological data, BS - Building simulation, OuInMet - Outdoor/indoor data analysis.

City Location	NVP Method	Effective NV criteria				BS tool	Weather data	NVP Metric	Urban Met	Reference
		T	*U*	*RH*	Others					
Townsville, Australia	OutMet	√	√	√		-	Open	Number of occasions		(Aynsley, 1999)
Multiple China	BS	√	√			Own model	Open	PDPH		(Yang et al., 2005)
Athens, Greece	OutMet	√	√		Noise, pollution	-	Urban	No metrics - Method development	*T, U*	(Ghiaus et al., 2006)
Multiple China	BS	√	√			Own model	Open	NV-hours, PDPH		(Luo et al., 2007)
Basel, Switzerland	OuInMet	√	√		Noise, pollution	-	Urban	NV-hours	*T, U*	(Germano, 2007)
Multiple China	BS	√				Own model	Open	NV-hours		(Yao et al., 2009)
Multiple China	BS	√	√	√		Own model	Open	NV-hours		(Yin et al., 2010)
Vejle, Denmark	BS	√				EnergyPlus	Open	NV-hours		(Oropeza-Perez and Østergaard, 2013)
Multiple Europe	OuInMet	√	√			-	Open	NV-hours		(Faggianelli et al., 2014)
Multiple China	BS	√		√		DeST and CFD	Urban	Mean ventilation rate	*T, RH*	(Li and Li, 2015)
Multiple India	BS	√	√			TRNSYS	Open	PDPH		(Patil and Kaushik, 2015)
Multiple US	BS	√				EnergyPlus	Open	Target air change rate		(Hiyama and Glicksman, 2015)
State College, US	BS	√	√			IES-VE	Open	NV-hours		(Cheng et al., 2016)
Multiple Global	OutMet	√		√		-	Open	NV-hours		(Causone, 2016)
Multiple China	BS	√		√	Pollution	EnergyPlus	Open	NV-hours		(Tong et al., 2016)
Multiple US	OutMet	√	√	√		-	Urban	NV-hours	*T, U, RH*	(Tong et al., 2017)
Multiple Europe	BS	√			Pollution	EnergyPlus	Open	NV-hours		(Martins and Carrilho Da Graça, 2017)
Multiple Global	OutMet	√	√			-	Open	NV-hours		(Chen et al., 2017)
Multiple Australia	BS	√				TRNSYS	Open	NV-hours		(Tan and Deng, 2017)
Multiple Spain	BS	√		√		DesignBuilder	Open	NV-hours		(Pesic et al., 2018)
Multiple North America	BS	√				Own model + CFD	Open	NV-hours		(Cheng et al., 2018)

Boston, US	BS	√	√			Own model + CFD	Urban	NV-hours	*T, U*	(Wang and Malkawi, 2019)
Multiple China	BS	√				EnergyPlus	Open	NV-hours		(Chen et al., 2019)
Chongqing, China	BS	√			Pollution	EnergyPlus + CFD	Urban	NV-hours	*T*	(Costanzo et al., 2019)
Multiple US	BS	√	√			EnergyPlus	Open	NVE		(Yoon et al., 2020)
Chambéry, France	BS	√	√			EnergyPlus	Open	NV-hours		(Sakiyama et al., 2021)

5.2. Methods

To study the impact of urban climate on building natural ventilation potential (NVP), we couple the local-scale land surface model Surface Urban Energy and Water Balance Scheme (SUEWS) v2021a (SuPy v2021.11.20) (Järvi et al., 2011; Sun et al., 2020; Sun and Grimmond, 2019; Tang et al., 2021; Ward et al., 2016) and the building energy simulation tool EnergyPlus v9.4 (U.S. Department of Energy, 2020a). Representative cities from five different climate zones in China are selected to consider the climate variations.

5.2.1. Urban microclimate modelling

The urban surroundings could affect the natural ventilation of a building of interest (Fig. 5.1) in multiple ways (Fig. 5.2) by directly impacting the driving potential of NV (buoyancy force and wind-driven force). Specifically, the street geometry in urban areas can result in a decrease in wind speed, leading to a reduction in wind-driven natural ventilation rate. The urban heat island can lead to smaller temperature differences between indoor and outdoor air, which can reduce the buoyancy-driven natural ventilation rate. Here we use an urban wind profile, which requires the use of modified wind pressure coefficients based on differences between free-stream and urban wind profiles in Energy Plus (Xie et al., 2023).

SUEWS is used to model three idealised neighbourhoods (Fig. 5.1) that have different plan area densities but the same initial climate forcing data. The simulated energy and water balance fluxes are used to diagnose local-scale meteorological variables for the three neighbourhoods which are provided to EnergyPlus as the weather data for the building energy simulations. SUEWS performance has been extensively evaluated and applied in different climates globally (e.g. Table 3 of Lindberg et al. (2018); Table 1 of Sun and Grimmond (2019)).

SUEWS allow each neighbourhood to have varying amounts of seven land cover types: paved, buildings, deciduous trees/shrubs, evergreen trees/shrubs, grass, bare soil and water. This allows realistic intra-city land cover variations, between different cities. For simplicity, here we assume neighbourhoods consist of buildings and grass (i.e., two typical but contrasting surface types), so vegetation's influence (e.g., evapotranspiration) is considered but more complicated impacts, such as trees/shrubs influence on wind (Kent et al., 2018) and radiation (Morrison et al., 2018) are not included. Our three neighbourhoods are:

(a) *rural* (Fig. 5.1a): is a large area covered with 100% grass, hence the isolated building area is negligible

(b) *medium density* (Fig. 5.1b): has buildings covering 30% of the area (plan are fraction λ_P = 0.3) and grass covering 70%

(c) *high density* (Fig. 5.1c): has λ_P =0.6 and grass in the remaining 40% of the area

The SUEWS neighbourhood population density is consistent with the EnergyPlus building occupancy (Section 5.2.2).

The Design Standard for Energy Efficiency of Public Buildings (MoHURD, 2015) splits China into five climate zones (Table 5.2). Using European Centre Reanalysis version 5 (ERA5) (Hersbach et al., 2020) meteorological data is available globally with a spatial resolution of 0.125° and temporal resolution of a hour. As natural ventilation cooling for buildings is particularly important during hot periods, we select 2018, the year with the warmest Northeast Asia summer (JJA) mean near-surface air temperature between 1979 and 2018 (Xu et al., 2019) for simulation. The three neighbourhoods are simulated in one city for each of the five climates (Table 5.2), assuming human activities do not vary between the regions. One ERA5 grid located in centre of the city is used. Note the ERA5 data do not account for urban land cover in the reanalysis but do assimilate meteorological data with cities (Tang et al., 2021). The vegetation cover assigned to the grid is representative of local conditions (Hersbach et al., 2020).

To drive SUEWS the meteorological data in the inertial sub layer or constant flux layer are needed. This layer is located above the roughness sub layer (RSL). Within the RSL individual roughness element influences the air flow, while above that it becomes blended and provides a neighbourhood or local scale response. The RSL extends from ground to a depth of approximate 2 to 5 times of mean roughness element height (i.e. buildings and trees) (Oke et al., 2017b), where the building are located and most human activities occur. Thus, SUEWS requires a forcing height of at least 32 m above ground as the mean building height is 6.4 m. ERA5 data at this height is obtained with environmental lapse rates assumed, as detailed in Appendix B in Appendix B of Tang et al. (2021). However, since the ERA5 data may have different altitudes from the actual city centre, the forcing heights for each climate are different, ranging from 32 m to 108 m. The forcing height is determined by the city's altitude, with higher altitude cities having a larger forcing height. For example, Kunming has an altitude of 1892 m, but the lowest available ERA5 data altitude is 2000 m.

Building energy simulation of natural ventilation potential, requires wind speed *U*, temperature *T* and relative humidity *RH* in the RSL. Here we use the SUEWS-RSL module to obtain the environmental variables. SUEWS-RSL calculates vertical profiles of these variables with a RSL corrected MOST (Monin-Obukhov Similarity Theory) approach (Harman and Finnigan, 2008, 2007; Theeuwes et al., 2019), while accounting for varying atmospheric stability, roughness characteristics and turbulent heat fluxes (Tang et al., 2021; Theeuwes et al., 2019). Evaluation of the SUEWS-RSL *U* and *T* profiles against observations in three global cities, suggest an acceptable accuracy (Tang et al., 2021; Theeuwes et al., 2019).

The SUEWS-RSL generated local weather data, includes *T* and *RH* at 2 m above ground (T_2 and RH_2), *U* at 10 m (U_{10}), and vertical profiles of *T* and *U* within the RSL (Fig. 5.2). The supplied T_2, RH_2 and U_{10} as well as other climate data (e.g., incoming solar radiation from ERA5) are formatted as a EnergyPlus weather file (.epw). The SUEWS-RSL wind profile is passed to EnergyPlus via input files (.idf) by replacing the power law coefficients with values derived from the SUEWS-RSL data.

In EnergyPlus solar shading from adjacent buildings (purple, Fig. 5.1) are simulated as 'shading objects'. The longwave radiative exchanges between the reference building and adjacent buildings are calculated with an iterative approach (Chapter 3). Impacts of other urban factors like the heat storage and the anthropogenic heat are simulated with SUEWS and reflected in the outdoor air temperature (Fig. 5.2).

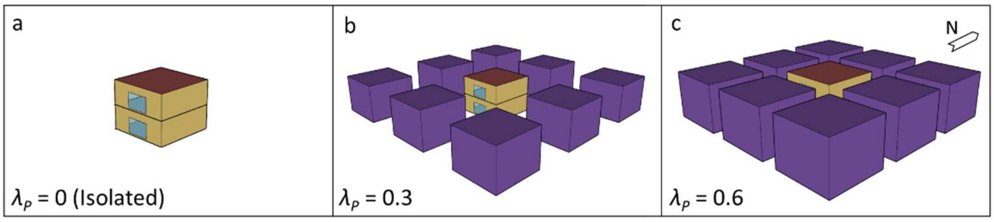

Fig. 5.1. Reference building (8 m × 8 m × 6.4 m) is simulated (EnergyPlus) after the weather data is simulated (SUEWS) for three neighbourhoods: (a) a rural (isolated), and two city neighbourhoods with plan area fractions (λ_P) of (b) 0.3 and (c) 0.6.

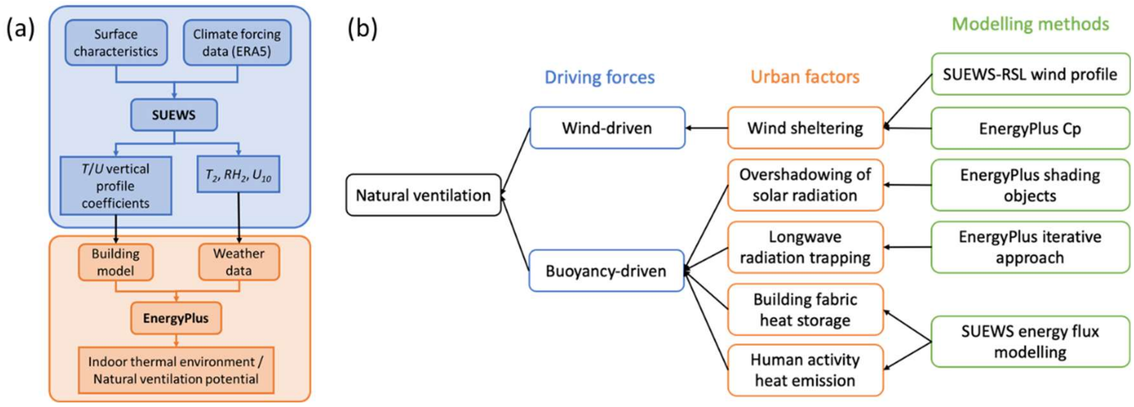

Fig. 5.2. SUEWS-EnergyPlus (a) overview of the workflow integration (Tang et al., 2021), and (b) urban factors influencing the natural ventilation and modelling methods.

5.2.2. Building characteristics

To compare the NVP, a two-storey building model (Fig. 5.1a) based on ASHRAE Case 600 (ANSI/ASHRAE, 2011) is developed in EnergyPlus. The 8 m wide × 8 m long × 6.4 m tall, building has no interior partitions. There are two windows on each floor, one on the south-facing and one on the north facing-wall to provide natural ventilation. All four windows are 2 m × 3 m. A simplified residential occupancy (2 people on each floor, 125.6 W person^{-1}, occupied all-day) and internal heat gain (lighting: 6 W m^{-2}, equipment: 4.3 W m^{-2}) are assumed (Xiong et al., 2019). The simulated reference building is assigned the Design Standard for Energy Efficiency of Public Buildings (MoHURD, 2015) thermal characteristics appropriate for each climate zone (Table 5.2).

For the NVP analysis, we consider both cross and single-sided ventilation (only south-facing windows open). All windows are assumed to have 15% openable area and discharge coefficient (C_d) of 0.61. For the cooling energy savings calculation, an ideal load system is assumed with a heating setpoint of 18 °C and cooling setpoint of 26 °C based on the recommendation of the Code for Thermal Design of Civil Building (MoHURD, 2016).

Table 5.2. Building thermal characteristics and specific city simulated in each climate zones in China. SHGC: solar heat gain coefficient. Modified from Tong et al. (2016).

City	Climate zone	U-value (W m^{-2} K^{-1})				SHGC
		Roof	External wall	Ground floor	Window	Window
Harbin	Very cold	0.25	0.35	0.25	1.76	0.68
Beijing	Cold	0.39	0.46	0.46	1.77	0.37
Shanghai	Cold winter hot summer	0.39	0.54	0.46	2.3	0.32
Kunming	Temperate	0.44	0.72	1.32	2.4	0.2
Guangzhou	Warm winter hot summer	0.44	0.72	1.32	2.4	0.2

5.2.3. Natural ventilation models

To simulate the cross ventilation the Airflow Network (AFN) model within EnergyPlus is used (U.S. Department of Energy, 2020b). The AFN has been evaluated and widely used for natural ventilation calculations (Johnson et al., 2012). The AFN airflow rate is calculated using the pressure difference across openings, with the standard orifice flow equation. The wind-driven ventilation rate V_w is (Awbi, 2003):

$$V_w = C_d A \sqrt{\frac{2\Delta P_w}{\rho_0}} \quad (5.1)$$

where C_d is the discharge coefficient of opening, A is the effective opening area (m^2), ρ_0 is the outdoor air density (kg m^{-3}) and ΔP_w is the wind pressure difference across opening (Pa). The wind pressure at the opening height is (Awbi, 2003):

$$P_w = 0.5\rho_0 C_p U_{free}^2 \quad (5.2)$$

where C_p is the surface-averaged wind pressure coefficient, and U_{free} is the upstream undisturbed flow at the opening height.

As C_p values are influenced by the building geometry, surrounding conditions and wind profile and direction (Grosso, 1992), it is important to use the appropriate C_p values as it impacts the accuracy of the building natural ventilation simulation in an urban environment. In this study, TPU *Aerodynamic Database of Non-isolated Low-Rise Buildings* (TPU, 2007) C_p data from wind-tunnel experiments for buildings with different geometries and surrounding conditions are used. As the TPU C_p database is for free-stream wind measured in wind tunnel experiments, we modified these using the SUEWS-RSL wind speeds and profile as shown in Xie et al. (2023).

Although it is widely accepted that cross ventilation usually achieves much larger ventilation rate, it is less practical than single-sided ventilation for urban buildings where isolated rooms are common (Zhong et al., 2022). The single-sided ventilation model, based on the mixing layer theory (Warren, 1977; Warren and Parkins, 1984), is used. This has been evaluated in wind-tunnel and full scale experiments (Gough et al., 2020; Yamanaka et al., 2006). The wind-driven ventilation rate (V_w, m^3 s^{-1}) is calculated with:

$$V_w = 0.1AU \quad (5.3)$$

From Bernoulli principles, the buoyancy-driven ventilation rate (V_b) is calculated with:

$$V_b = \frac{C_d A}{3}\sqrt{g h_{opening}\frac{\Delta T}{T}} \qquad (5.4)$$

where g is the gravitational acceleration, $h_{opening}$ the height of the opening, ΔT temperature difference across the opening. The total ventilation rate (V_t) is the quadrature sum of the wind and stack air flow components (U.S. Department of Energy, 2020c):

$$V_t = \sqrt{V_w^2 + V_b^2} \qquad (5.5)$$

5.2.4. Analysis metrics

In this study, the natural ventilation hours (NV-hour) and the cumulative air change rate (ACH-hour) are used to quantify the natural ventilation potential (NVP).

The NV-hour, the most common NVP metric (Table 5.1), is the number of hours per year when natural ventilation can fulfil both the air quality and thermal comfort requirements (Luo et al., 2007; Yin et al., 2010). ASHRAE Standard 62.1 (ANSI/ASHRAE, 2013) defines the required minimum outdoor airflow rate (V_R) for a residential space as a function of the number of people occupying (N_p) the floor area (A_f, units: m^2) as:

$$V_R = 0.0025N_p + 0.0003A_f \qquad (5.6)$$

In this study, as each floor has $N_p = 2$ and $A_f = 64$ m^2, $V_R = 0.0242$ m^3 s^{-1} (≈ 0.425 ACH).

For free-running building thermal comfort assessment, we use the Chinese adaptive thermal comfort models provided in the *Evaluation Standard for Indoor Thermal Environment in Civil Buildings* (MoHURD, 2012) for 75% satisfaction (or Category II). These specify an upper (T_{UL}) and lower indoor operative temperature limit (T_{LL}) by zone, with the northern (very cold, cold, Table 5.2):

$$\begin{cases} T_{UL,N} = 0.73T_{rm} + 15.28 & (18℃ \le T_{UL,N} \le 30℃) \\ T_{LL,N} = 0.91T_{rm} - 0.48 & (16℃ \le T_{LL,N} \le 28℃) \end{cases} \qquad (5.7)$$

and southern zones (cold winter hot summer, temperate, warm winter hot summer, Table 5.2):

$$\begin{cases} T_{UL,S} = 0.73T_{rm} + 12.72 & (18℃ \le T_{UL,S} \le 30℃) \\ T_{LL,S} = 0.91T_{rm} - 3.69 & (16℃ \le T_{LL,S} \le 28℃) \end{cases} \qquad (5.8)$$

This uses a seven day (n = 7) running mean of the outdoor air temperature (T_{rm}):

$$T_{rm} = (1-k)(T_{od-1} + \alpha T_{od-2} + \alpha^2 T_{od-3} \cdots + \alpha^6 T_{od-7}) \qquad (5.9)$$

where k is a constant between 0 and 1, with 0.8 as recommendation (Nicol and Humphreys, 2010), and $T_{od\text{-}n}$ is the daily mean outdoor air temperature for n days ago (°C).

As higher ventilation rates may prevent sick building syndrome symptoms and reduce potential airborne infection risk (Sundell et al., 2011), we also determine the ACH-hour, or cumulative air change rate during the NV-hour period. This is similar to pressure difference Pascal hours (PDPH) (Yang et al., 2005). Although both aim to quantify availability of natural driving forces, ACH-hour is more directly linked to amount of ventilation.

Cooling energy saving (Q_{saving}) is also determined (Tong et al., 2016):

$$Q_{saving} = Q_{window\_closed} - Q_{window\_open} \tag{5.10}$$

The is the difference in energy demand between a fully air-conditioned building (i.e. windows always closed, Q_{window_closed}) and a hybrid-controlled building with windows open (Q_{window_open}) when the indoor air temperature can vary between the heating and cooling set points (18 to 26 °C) while the air conditioning system is turned off. The air-conditioning system setting are given in section 2.1.

In summary (Fig. 5.3), three metrics are determined from analysis of simulations for five climates and for three neighbourhoods with different plan area fractions (λ_P) and two ventilation types. Thus, a total of (5 × 3 × 2 =) 30 cases are simulated.

We use mean the bias error (MBE) to assess the difference between SUEWS-RSL and modified EnergyPlus wind profiles (Eq. 5.12, Table 5.3 coefficients):

$$MBE = \frac{1}{N}\sum_{i=1}^{N}(y_i - x_i) \tag{5.11}$$

where y_i and x_j are EnergyPlus and SUEWS-RSL wind speeds at each timestep, and N is the number of values analysed (i.e. a year with hourly timestep, $N = 8760$).

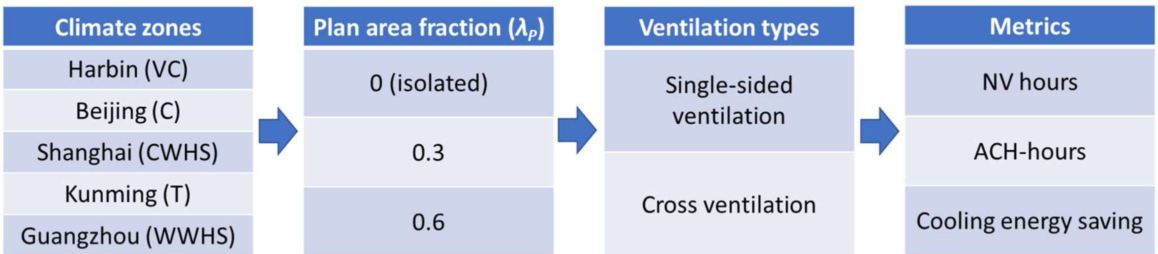

Fig. 5.3. Variables and metrics analysed in this study. See Fig. 5.1 and Table 5.2 for more details.

5.3. Results

5.3.1. Outdoor climate

First, we assess differences in modelled local environmental variables for the neighbourhoods with different plan area fractions (*λ_P)* and in different climate zones (Fig. 5.3).

Modelled outdoor air temperature at 2 m (T_2) in denser neighbourhoods (larger λ_P, green Fig. 5.4) have warmer monthly values and greater variation than at the rural site in all five climates (blue, Fig. 5.4). Annual mean differences in T_2 between cases with λ_P of 0.6 and 0 vary between 0.8 °C in Guangzhou and 1.6 °C in Kunming. This difference is indicative of the canopy layer urban heat island effect.

Whereas the monthly variation of SUEWS-RWL modelled wind speed at 10 m (U_{10}) decrease as λ_P increases (Fig. 5.5). The annual mean differences ($\Delta\lambda_{P\ 0.6\rightarrow 0}$) are smallest in Beijing (0.6 m s^{-1}) to and larges in Harbin (1.1 m s^{-1}). These results are qualitatively similar to previous CFD studies considering outdoor velocity and λ_P (e.g. Mei et al. (2017)).

Vertical wind profiles (Fig. 5.6) derived SUEWS-RSL are used to calculate the EnergyPlus power-law parameters (*δ, α,* Table 5.3)(ASHRAE, 2005):

$$U_z = U_{10}\left(\frac{\delta_{ref}}{10}\right)^{\alpha_{ref}}\left(\frac{z}{\delta}\right)^{\alpha} \qquad (5.12)$$

where the meteorological station boundary layer depth (δ_{ref}) and exponent (α_{ref}) are obtained as the default settings in EnergyPlus for open terrain (U.S. Department of Energy, 2020d).

To assess the mean bias error (MBE) for the EnergyPlus wind profiles when using the Table 5.3 coefficients (hereafter EP-RSL profiles), we use the original SUEWS-RSL vertical wind profiles data which varying because of the different forcing heights; (5 to 8 vertical levels for $\lambda_P = 0$; 9 levels at $\lambda_P = 0.3$ and 0.6) as the baseline (Fig. 5.7). As the SUEWS-RSL wind profile does not assume a power law and varies with stability (Tang et al., 2021; Theeuwes et al., 2019), biases still exist in EP-RSL profiles. The biases are larger for climates with stronger wind speeds (e.g. Harbin). When $\lambda_P = 0$, the EP-RSL profiles underpredicts the median wind speeds by up to 0.35 m s^{-1}, especially around 2 m above ground level. For $\lambda_P = 0.3$ the EP-RSL MBE_{median} are smaller ($\leq$ 0.2 m s^{-1}), as are

λ_P = 0.6 cases. As the MBE$_{median}$ become better (smaller) with height within the canopy layer (> 3.2 m), we focus analysis on the upper floor natural ventilation potential and energy saving. Future work could directly use the RSL wind profile within EnergyPlus after rewriting the appropriate code. This is beyond the scope of this study.

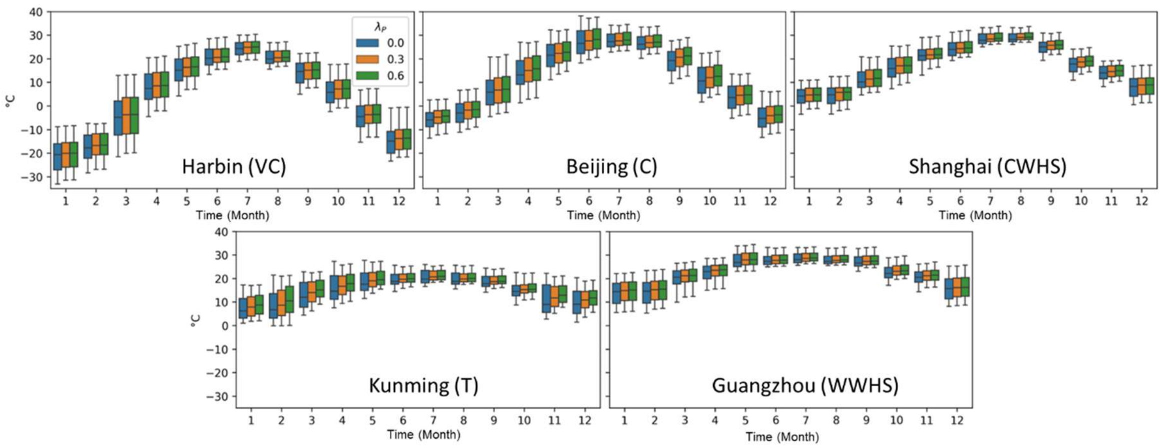

Fig. 5.4. Monthly distribution (hourly) of modelled outdoor air temperature at 2 m agl for three plan area fraction of buildings (λ_P, Fig. 5.1; colours) and five climates (Table 5.2), with interquartile range (box), median (horizontal line) and 5th and 95th percentiles (whiskers).

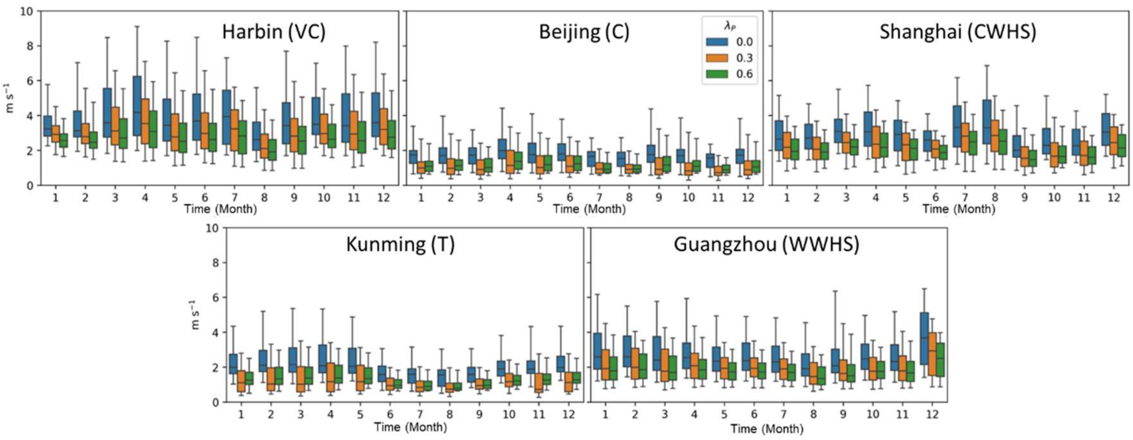

Fig. 5.5. As Fig. 5.4, but wind speed at 10 m agl.

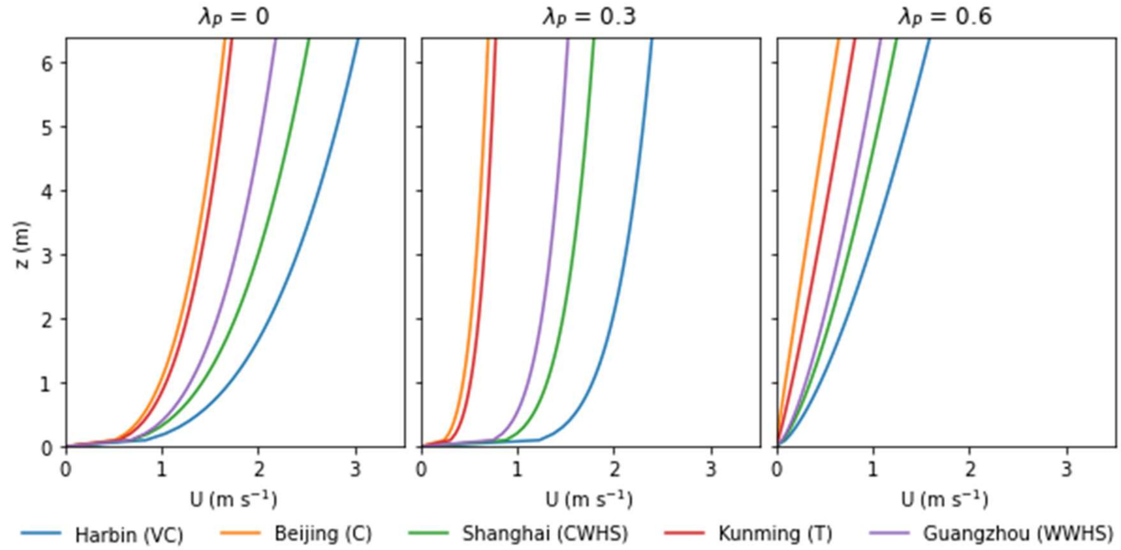

Fig. 5.6. Vertical wind profiles for three different λ_P and five climates (colour) calculated with annual median 10 m wind speeds and coefficients (Table 5.3) derived from the SUEWS-RSL results (EP_{RSL}) within the canopy layer (building height= 6.4 m).

Table 5.3: Wind power law (Eq. 5.12) coefficients derived from SUEWS-RSL model output for each climate and neighbourhood.

	Exponent α					Boundary layer depth δ (m)				
λ_P	Harbin (VC)	Beijing (C)	Shanghai (CWHS)	Kunming (T)	Guangzhou (WWHS)	Harbin (VC)	Beijing (C)	Shanghai (CWHS)	Kunming (T)	Guangzhou (WWHS)
0	0.31	0.28	0.31	0.27	0.28	40.41	37.88	37.34	46.62	46.93
0.3	0.16	0.25	0.17	0.22	0.17	380.44	125.28	322.01	149.76	320.19
0.6	0.67	1.02	0.68	0.86	0.68	25.96	16.16	25.11	16.65	24.87

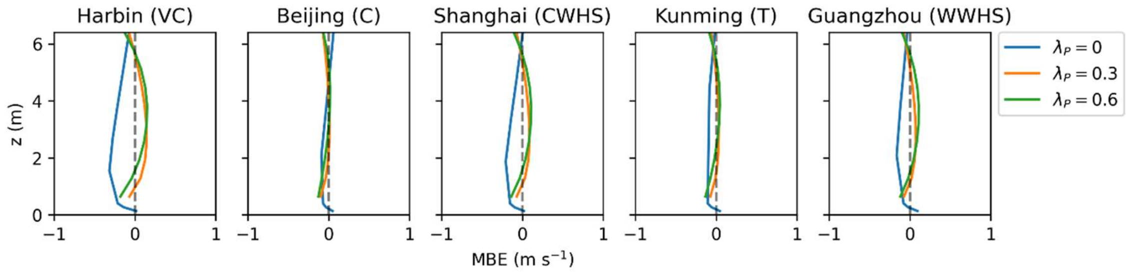

Fig. 5.7. Annual mean bias error (MBE) for wind speed calculated at hourly timestep but vertical resolution (Δz) that varies (from 0.13 m with varying Δz for $\lambda_P = 0$; from 0.64 m with $\Delta z = 0.64$ m for $\lambda_P = 0.3$ and 0.6) to 6 m above ground level; where SUEWS-RSL (x, Eq. 5.11) and EP-RSL wind profiles (y, Eq. 5.11; using Eq. 5.12, and Table 5.3 coefficients) for three λ_P (colour) and five climates.

5.3.2. Natural ventilation potential (NVP)

5.3.2.1. Natural ventilation hours (NV-hour) of cross ventilation

Cross ventilation monthly percentage of NV-hours across the five climates (Table 5.2) and three λ_P classes (Fig. 5.1) are generally larger for upper floor room (Fig. 5.8). With windows always opened, the minimum ventilation rate requirement of 0.425 air change per hour (ACH) (section 2.4) can be fulfilled during most of the year (Fig. 5.8). Although the Beijing neighbourhood with λ_P = 0.6 has the lowest wind speeds, there are only 23 hours within the year that do not meet the ventilation rate criteria. Thus, differences in NV-hours are mostly influenced by the thermal comfort criteria. As a result, warm climates (Guangzhou, Kunming, Shanghai) have more annual total NV-hours than cold climates (Harbin, Beijing), since there is very limited NV potential for cold climates in winter (Fig. 5.8).

Influences of λ_P on NV-hours vary across climates (Fig. 5.8). In terms of the annual total, the building in the λ_P = 0 rural neighbourhood has the most annual NV-hours in hot climates like Guangzhou. While for low-medium density λ_P = 0.3, warm winter hot summer climates like Shanghai have the most annual NV-hours. Dense urban neighbourhoods (λ_P = 0.6) have the most annual NV-hours in cold northern zones including Harbin and Beijing, and the mild climates like Kunming. This can be explained by the air temperature distribution (Fig. 5.5) as dense neighbourhoods (λ_P = 0.6) tend to have higher outdoor temperatures (in their regional climate), which is beneficial in cool climates for thermal comfort, and vice versa. The annual differences in NV-hours between λ_P = 0 and λ_P = 0.6 is largest in Kunming (1545) which is more than twice the difference to the next largest (Harbin, 753). The others are smaller again Guangzhou (587), Shanghai (254), and smallest in Beijing (201).

The λ_P has a greater impact on nocturnal NV-hours than daytime (Fig. 5.8), linked to the larger night-time temperature differences (Fig. 5.4). During cool months there are larger proportion of daytime NV-hours, but the nocturnal NV-hours increases with λ_P to a greater extent (e.g. nocturnal NV-hours increase by 33.9% while daytime increase by 13.2% from λ_P = 0 to 0.6 during March in Kunming). While in warm months, nocturnal NV-hours are reduced more with the increase of λ_P (e.g. nocturnal NV-hours decrease by 35.3% while daytime increase by 16.3% from λ_P = 0 to 0.6 during July in Guangzhou).

Generally, the dependence of NV-hours change with λ_P is highly related to climate and seasons (Fig. 5.9). In summer, very cold climates (e.g. Harbin) have an increase in NV-hours with λ_P (10% λ_P = 0.6 c.f. λ_P = 0), while the opposite occurs in hot summer climates regions (-43% λ_P = 0.6 c.f. λ_P = 0 in Guangzhou). Whereas in the temperate climate (e.g. Kunming) λ_P has negligible impact on NV-hours, as temperatures have both small variations and are usually pleasant for indoor thermal comfort (Fig. 5.8). In winter, NV-hours increase with λ_P in all regions due to cooler outdoor air temperatures, but the increase is small in regions with cold winter and little natural ventilation potential including Harbin, Beijing and Shanghai. During the spring/autumn transition seasons, the NV-hours tend to increase with λ_P in most climates associated with the relatively mild outdoor climate except Guangzhou, where the warm climate causes the indoor air temperature to exceed the upper limit of thermal comfort in late spring (May) and early autumn (September) (Fig. 5.8).

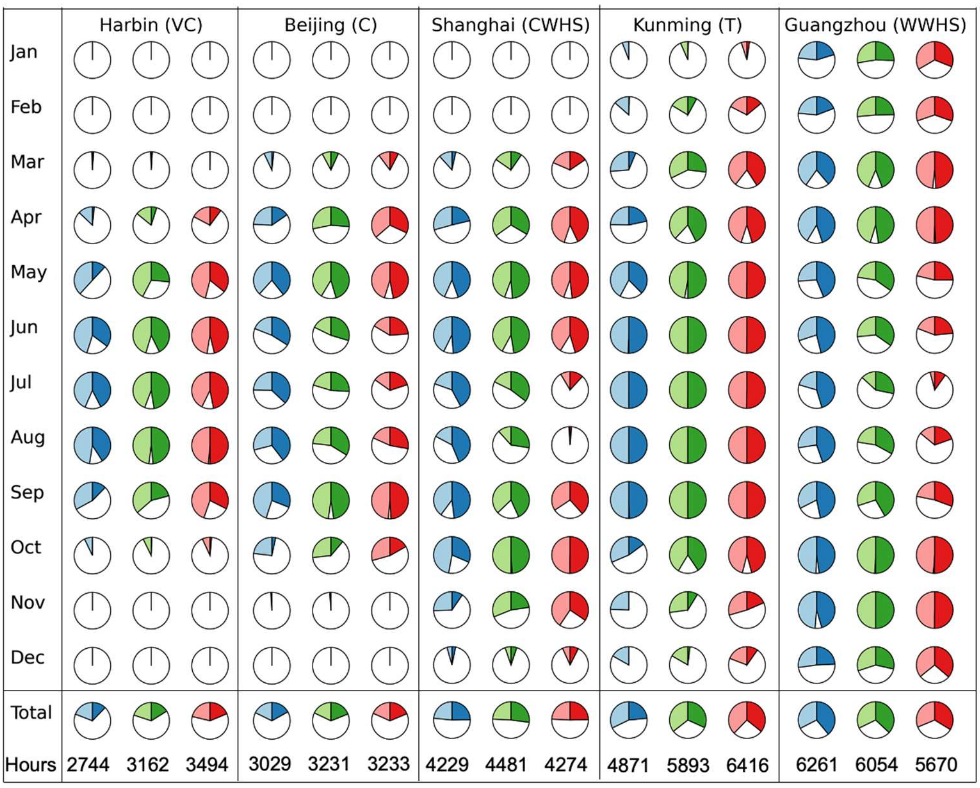

Fig. 5.8. Upper floor cross ventilation as percentages of NV-hours (relative to total hours in the period for five climates (columns), three neighbourhoods (λ_P colours, blue: 0; green: 0.3; red: 0.6) and different time intervals (rows: monthly and annual, time of day (pie chart half): left daytime (7:00 to 19:00), right night-time (19:00 to 7:00)).

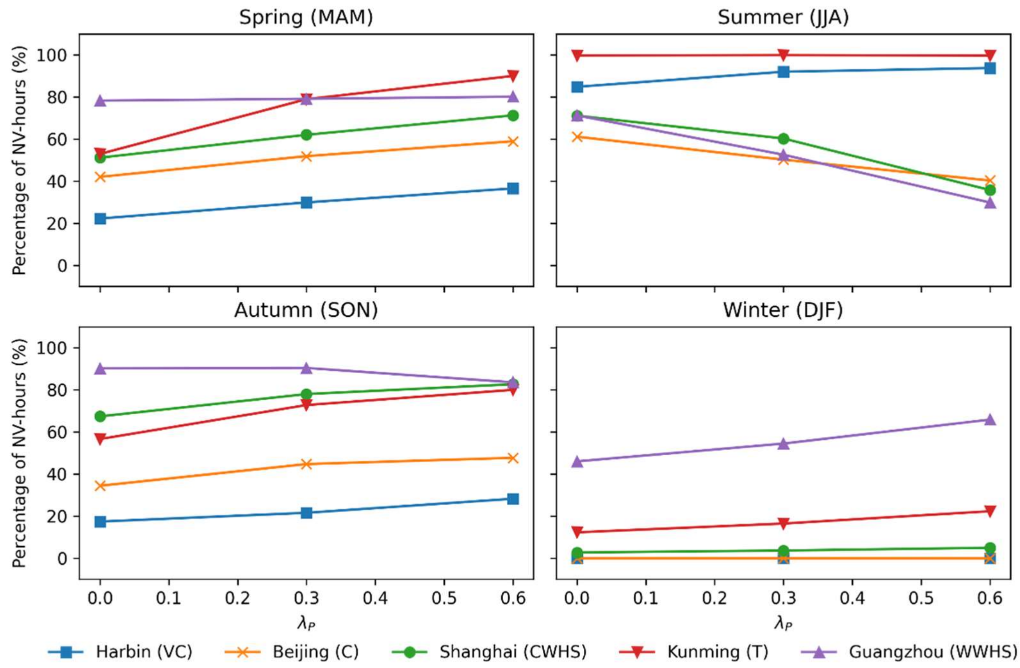

Fig. 5.9. Seasonal upper floor with cross ventilation (percentage of possible hours) in five climates (colour) for three λ_P (marker).

5.3.2.2. ACH-hours of cross ventilation

The air exchange rates can enhance the NV benefits for air quality purposes. The annual variability in ACH (hourly) during NV period (Fig. 5.10) is the largest when buildings are sited in open areas ($\lambda_P = 0$) because of the higher variability of wind speed (Fig. 5.5, 5.7), with median ACH between 10.8 (Beijing) and 20 (Harbin). As λ_P increases the median ACHs become smaller ($\lambda_P = 0.3$: 4.9 (Beijing) and 10.1 (Harbin); $\lambda_P = 0.6$: 2.6 (Beijing) and 3.0 (Harbin)).

The annual cumulative ACH-hours differs from NV-hours with λ_P variations. As ACH-hours largely depend on wind speeds and ACH-hours decrease with λ_P in all climates (Fig. 5.11), the inter-climate variations are smaller (Fig. 5.11). Given the large number of annual NV-hours, buildings in areas with a λ_P of 0 and 0.3 in Guangzhou and $\lambda_P = 0.6$ in Kunming have the most ACH-hours (cf. to buildings in the same λ_P neighbourhoods but different climates). While Beijing has the least annual ACH-hours for all λ_P due to low both ventilation rate and NV-hours.

The seasonal variations in ACH-hours are also influenced by both NV-hours and ventilation rates (Fig. 5.12). In transition seasons (spring/autumn), Guangzhou's climate has the largest ventilation potential in both ACH-hours and NV-hours (Fig. 5.9) benefiting from appropriate air temperatures and wind speeds, while Kunming's ranking drops due to the low ventilation rates. In summer, high wind speeds and mild summer temperatures make Harbin the climate with the most ACH-hours. The ranking of ACH-hours in winter remains consistent with the NV-hours.

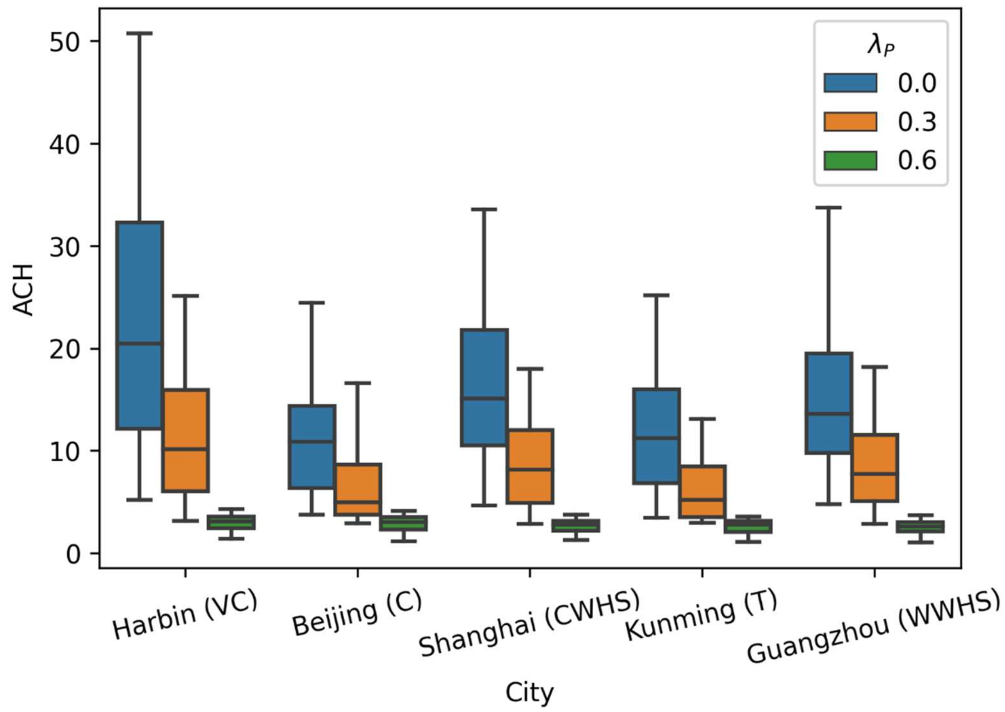

Fig. 5.10. Annual variability in air changes per hour (ACH) when the upper floor cross ventilation (NV-hour >0) through the year for five climates and three λ_P (colours) with interquartile range (box), median (horizontal line) and 5th and 95th percentiles (whiskers).

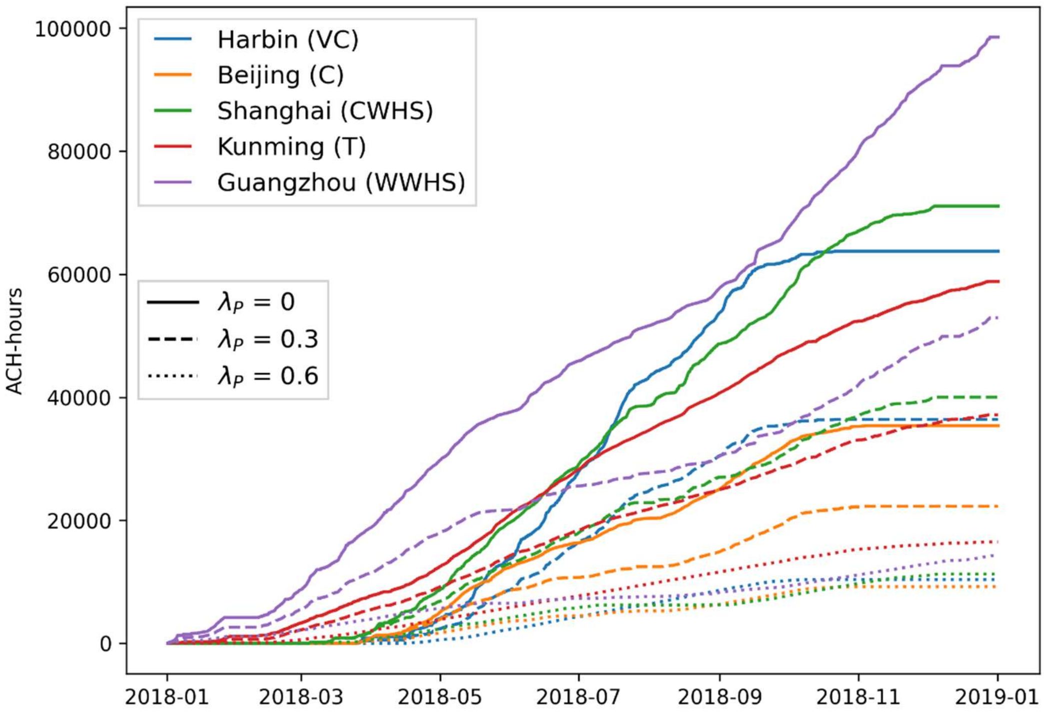

Fig. 5.11. Annual cumulative ACH-hours of the upper floor with cross ventilation across different climates (colour) and λ_P (line style).

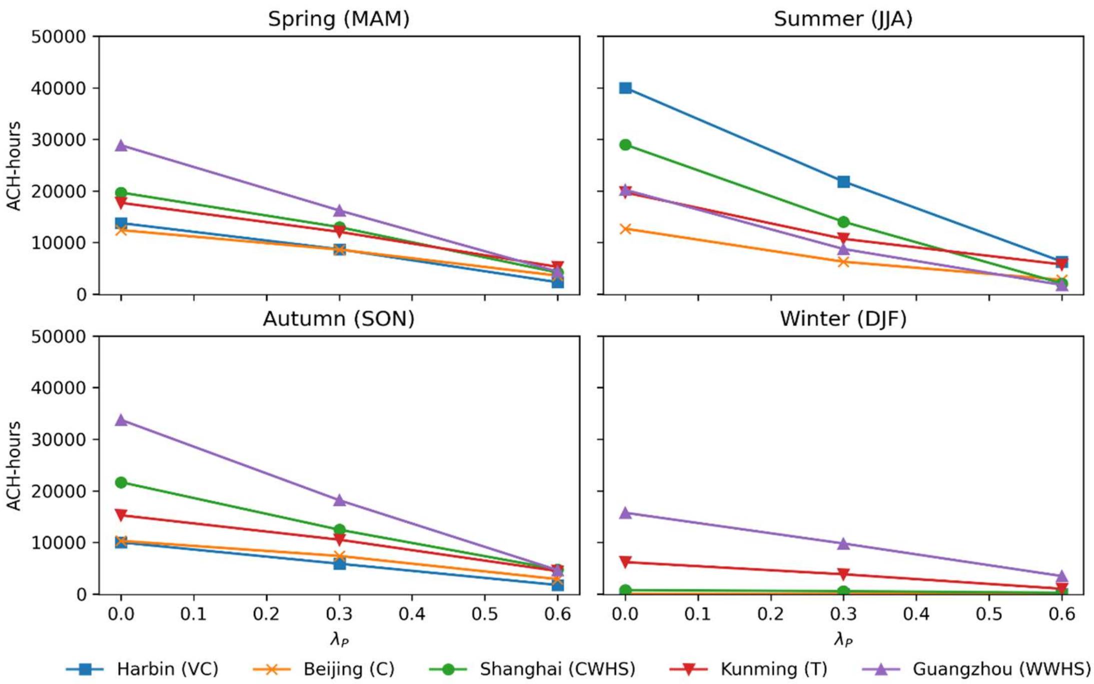

Fig. 5.12. As Fig. 5.9, but ACH-hours.

5.3.2.3. Single sided ventilation

To assess NVP differences between cross ventilation and single-sided ventilation we focus on Shanghai as similar conclusions are drawn for the other cities. Ventilation rates are largely less for single-sided ventilation (cf. cross ventilation) (Fig. 5.13) with annual median ACH reducing from 15.1/8.2/2.7 (cross ventilation) to 3.9/2.9/2.1 (single-sided ventilation) across the three plan area densities (λ_P = 0/0.3/0.6). This also implies that the single-sided ventilation is as effective as cross ventilation for buildings located in dense urban areas. Although the ventilation rates are reduced, the annual minimum ventilation rate for the single-sided ventilation building even for λ_P = 0.6 (0.59 ACH), still meets the requirement of indoor air quality. Therefore, in Shanghai the natural ventilation potential is mainly influenced by thermal comfort criteria only. However, we do not consider the impact of outdoor air pollution (i.e., assuming outdoor air is unpolluted).

The reduced ventilation cooling potential with single-sided ventilation causes median indoor air temperature to increase by 0.9/0.8/0.2 °C for λ_P = 0/0.3/0.6 (Fig. 5.13). The seasonal percentage of NV-hours with single-sided ventilation therefore increases by up to 10.6 % (λ_P = 0) during spring and autumn, but decreases by up to 14.7 % (λ_P = 0.3) in summer (cf. cross ventilation) (Fig. 5.14). The ACH-hours are higher with cross ventilation in all conditions due to the higher ventilation rate, and differences between ventilation modes decreases as λ_P increases (Fig. 5.15).

Generally, the single-sided ventilation leads to lower ventilation rates across λ_P, and reduce the natural ventilation potential in magnitude. The changing pattern of NVP with λ_P is similar to cross ventilation.

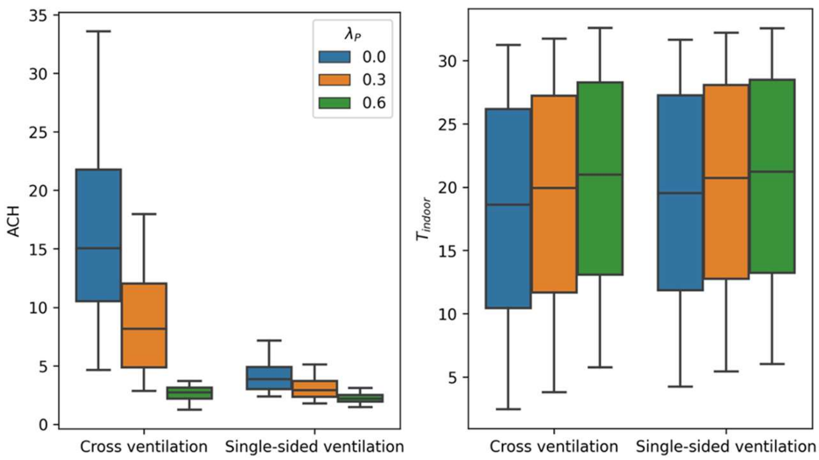

Fig. 5.13. As Fig. 5.10, but for Shanghai for two ventilation modes and (b) upper floor indoor air temperature.

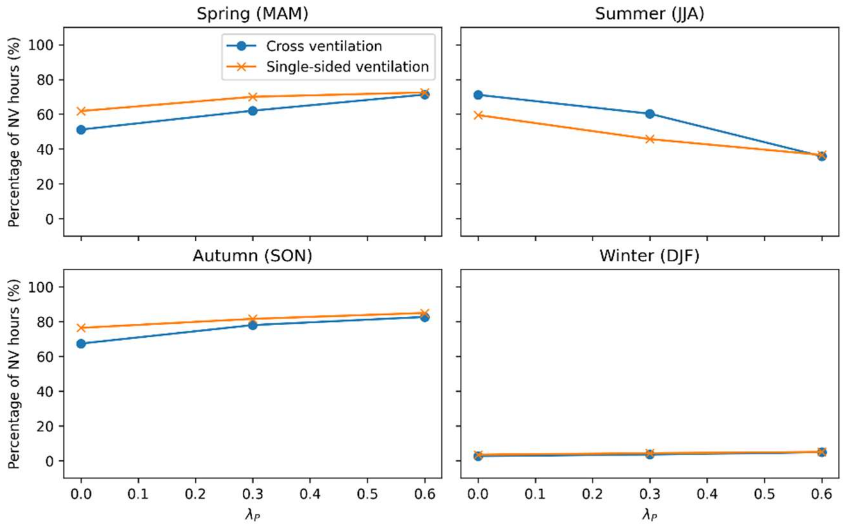

Fig. 5.14. As Fig. 5.9, but for two ventilation modes in Shanghai.

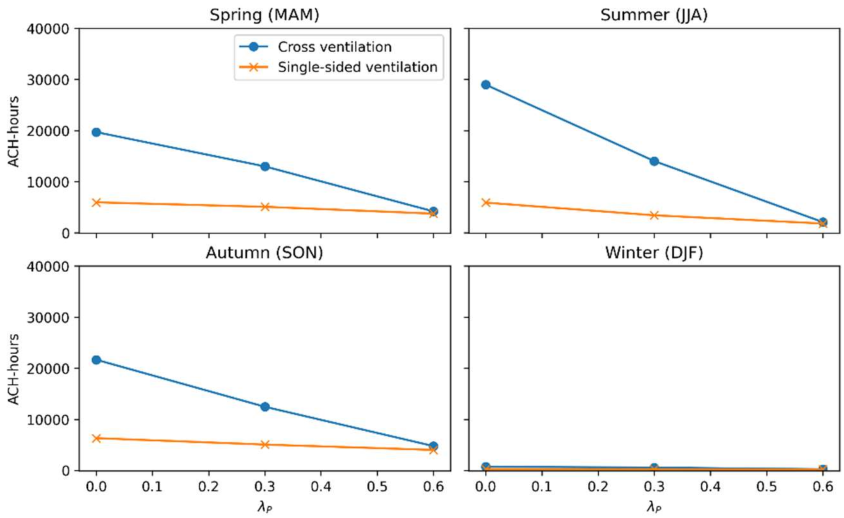

Fig. 5.15. As Fig. 5.14, but in ACH-hours.

5.3.3. Cooling energy saving

The cooling energy saving is calculated as the difference in cooling energy demand between a building with air-conditioning only and hybrid ventilation (air-conditioning plus natural ventilation). Therefore, the cooling energy saving amount is linked with the effectiveness of natural ventilation cooling (Eq. 5.10). Cooling energy saving is expected to be larger for climates and neighbourhoods with lower outdoor air temperatures and higher wind speeds. Hence, in all climates the cooling energy saving decreases as λ_P increases (Fig. 5.16). For cross ventilation, such decreases are smallest in Kunming, as the climate is mild and temperature variation is small, making natural ventilation cooling available most of the time. For the other climates the cooling energy saving between building densities (λ_P) are similar (Harbin: 8% to Beijing: 12.5%).

Our results differ slightly from Ramponi et al. (2014)'s nocturnal ventilation cooling energy saving study of three European cities. They suggest inter-λ_P differences are largely influenced by the climate, with natural ventilation cooling energy saving dropping by 20% in cool but windy Amsterdam, while in warmer less windy Milan (2 %) and Rome (13 %) reductions are less. Differences may arise from their different approach, as their outdoor air temperatures and wind speeds are independent of λ_P (only Cp values changed), and longwave radiative exchanges are not considered. The last may be critical as increased λ_P can result in more trapped longwave radiation, increasing building cooling demand (Xie et al. 2022). Our work highlights the importance of a holistic consideration of the complex interaction between urban climate and building performance.

Compared to cross ventilation, single-sided ventilation has less cooling energy savings due to lower wind speeds. The trends across climates are similar, despite slightly smaller inter- λ_P variations (6.5% to 8.1% excluding Kunming).

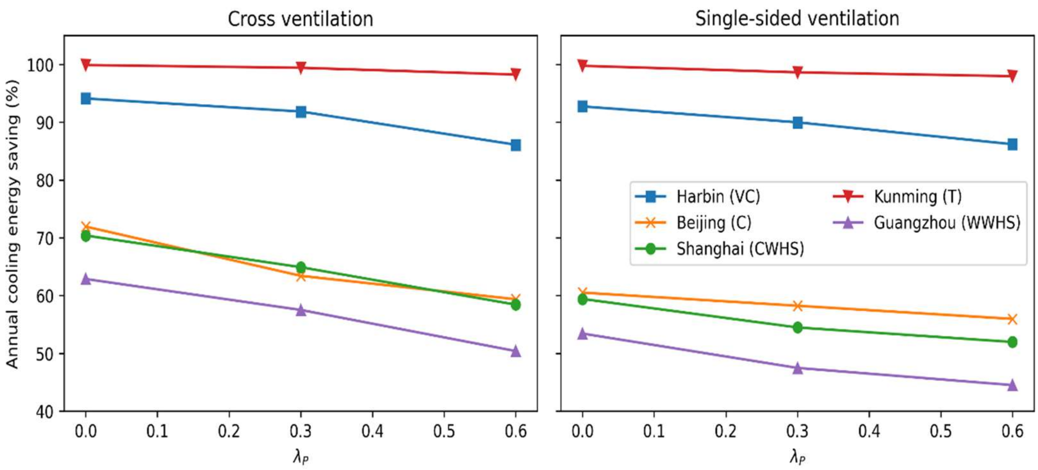

Fig. 5.16. As Fig. 5.9 but for annual cooling energy saving (Eq. 5.10, percentages) for two ventilation modes.

5.4. Discussion and conclusions

Although NVP across China's climate zones has been assessed previously, given the large dependence on research approach, climate data and building model used, the results vary (Luo et al., 2007; Tong et al., 2016; Yang et al., 2005; Yao et al., 2009). The effects of urban climate are rarely fully considered due to data availability, or use of computationally expensive CFD limiting conditions analysed. In this study we combine the urban land surface model SUEWS and building energy simulation tool EnergyPlus to assess the natural ventilation potential of buildings in different Chinese climate zones and neighbourhoods with different plan area fractions (λ_P). Our approach (cf. CFD) has practical advantages, including both simpler model set-up and lower computational cost. The SUEWS model only requires some commonly available surface characteristics and meteorological forcing data. A year long run for one neighbourhood normally takes around 1 minute (PC) which is around 1 million times less than CFD-based approaches (e.g. 3-day run taking 168 hours on PC by Yang et al. (2012)). Therefore, our approach can be applied for quick estimates of natural ventilation potential and cooling energy saving in larger scales (e.g. intra-city neighbourhoods) for longer time periods. Also, the outputs by SUEWS can be used as boundary conditions for CFD simulation.

We find that climate, plan area fraction and season combine to impact the NVP. Our findings improve current understanding and design of NVP of urban buildings from a local climate perspective. Local climate in denser areas have been shown to reduce NVP due to warmer outdoor air temperatures on several summer days in Basel (cf. the rural area) (Germano, 2007) and reduced wind speeds from increasing λ_P ($0 \rightarrow 0.2$) reducing annual mean wind-driven ventilation rate by up to 35% (Li and Li, 2015). Given these studies, our findings further suggest that under different conditions, increasing the λ_P can either increase or decrease the NVP. For example, in summer, when the λ_P increases from 0 to 0.6, NV-hours increase by around 10% in Harbin (very cold) but decrease by around 43% in Guangzhou (warm winter hot summer). However, a critical disadvantage of urban areas is the low wind speeds, which leads to lower ventilation rates (e.g. Harbin: annual median ventilation rate reduced by 50% at λ_P =0.3 and 85% at λ_P =0.6). Hence, we should consider both NV-hours and ACH-hours. It is also found that single-sided ventilation can be as effective as cross ventilation in dense urban areas due to the low wind speed regardless of the metric used.

Our approach offers a quick assessment of NVP for buildings in the urban environment. We model idealised neighbourhoods with simplified building models based on relevant observations and standards, although we acknowledge that real cities are more complex. Our findings should be representative of similar climates and neighbourhoods, but future studies could focus on more detailed information on neighbourhoods in real cities where the variance in NVP might be greater. Existing evaluations suggest that the SUEWS model has acceptable accuracy, although the Cp values should be changed with building geometry. We have only considered buildings and grass in our study and have ignored the impact of trees, which could modify the wind field (Kent et al., 2018) and radiative fluxes (Morrison et al., 2018) and affect the natural ventilation of nearby buildings. Although trees can be modelled in SUEWS and considered as shading objects in EnergyPlus (e.g. Hsieh et al., 2018), to modify wind pressure coefficients on nearby building facets, measurements or CFD simulations are still necessary. Therefore, our approach can be extended with additional data. Additionally, air and noise pollution, which could be high in dense urban areas, may further reduce NVP (as noted in Table 5.1), but this is beyond the scope of this study and could be considered in future work.

Chapter 6 Temporal and spatial population-based heat exposure in Colombo, Sri Lanka: impact of 2035 urban development plan and mitigation strategies

The previous chapter discussed the use of SUEWS and EnergyPlus to simulate the natural ventilation cooling potential in idealised neighbourhoods in different Chinese climate zones and highlighted the importance of considering local-scale climate for building energy simulation. This method also forms the basis for this and subsequent chapters, where we extend our understanding of the impact of local-scale climate on outdoor and indoor overheating risks in real world scenarios.

This chapter specifically examines the effect of local-scale climate on outdoor population-based heat exposure in Colombo, Sri Lanka, using SUEWS. The objectives of this chapter are to: (1) understand the spatial and temporal patterns of population heat exposure across Colombo and its surrounding areas, (2) investigate changes in heat stress for a future urban development scenario, and (3) evaluate the effectiveness of mitigation measures in reducing heat stress.

This chapter is written in form of a paper. I performed the research, wrote the first draft, and prepared all the figures. The co-authors, Z. Luo and S. Grimmond (supervisors), provided advice on structuring the paper, interpreting findings, and editing the text. The anthropogenic heat data used in SUEWS modelling is submitted for review as: Blunn, L., **Xie, X.**, Grimmond, S., Luo, Z., Sun, T., Perera, N., Ratnayake, R., Emmanuel, R., 2022. Spatial and temporal variation of anthropogenic heat emissions in Colombo, Sri Lanka. Submitted to Urban Climate, Oct 2022. In this submission, I contributed to creating the land cover data of Colombo, which is also used for SUEWS modelling in this and subsequent chapters.

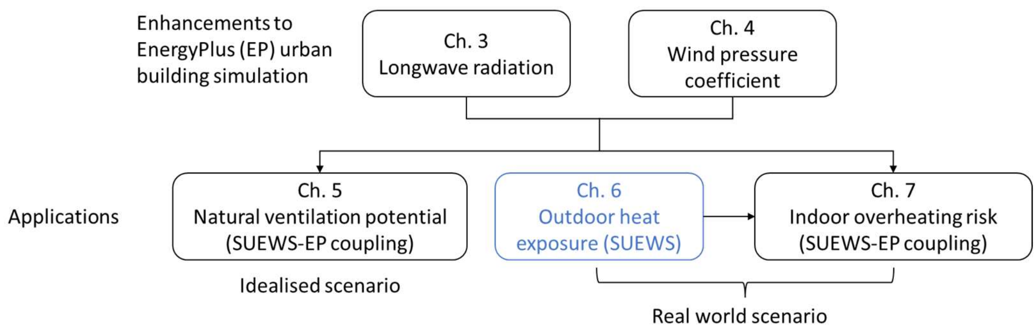

6.1. Introduction

Research interest regarding heat exposure in South Asia has grown rapidly in recent years, spurred by a series of deadly heatwaves, such as the 2015 event that caused around 3500 deaths in the region (ESCAP, 2015). More recently, in 2022, India and Pakistan experienced their hottest April since 1900, affecting over a billion people (Mogul et al., 2022). South Asia is projected to experience increasingly frequent and intense heatwaves. In particular, Sri Lanka has experienced some of the largest temperature changes in the region in recent decades (Sharma et al., 2022). By the end of the century (cf. 1990) projected changes in Sri Lanka include: increase in annual mean air temperature of 3.7 °C; increase in number of heatwave days per year from 25 days to around 250 days (WHO, 2016); and maximum wet-bulb temperature exceeding the survivability threshold of 35 °C (and over most of South Asia) (Im et al., 2017). These changes are predicted to increase heat-related mortality among individuals over the age of 65 by about 20 times (WHO, 2016).

The proportion of Sri Lanka's population living in urban areas was 18.5% in 2018, with a projected increase to 31.6% by 2050 (United Nations, 2018). However, urban areas typically have higher heat exposure risks than rural areas, particularly during periods of intense canopy layer urban heat island (CL-UHI) effects (Kovats and Hajat, 2007; Oudin Åström et al., 2011). Heatwaves can exacerbate this phenomenon, with factors such as increased solar radiation, greater anthropogenic heat from air conditioning systems, enhanced evaporation in rural areas and increased heat storage (Kong et al., 2021; Li and Bou-Zeid, 2013; Ramamurthy and Bou-Zeid, 2017). Therefore, during periods of extreme heat, densely populated urban areas face greater risks than rural regions.

High temperatures during extreme heat events (Green et al., 2019; Oudin Åström et al., 2011; Rocklöv et al., 2014) and intense UHI (Heaviside et al., 2016; Huang et al., 2020; Tan et al., 2010; Taylor et al., 2015) can increase heat-related morbidity and mortality. Exploring potential impacts of the CL-UHI on human health can assist decision makers with developing policies and measures to mitigate the health hazards faced by urban residents. This requires a understanding of the actual thermal patterns of heat exposure for the population, which cannot be achieved solely by analysing the distribution of canopy layer air temperature (Dong et al., 2020).

In Sri Lanka, a regional-scale early warning system of heatwave risk is operated by the Disaster Management Centre (Disaster Management Centre, 2022). However, to address the health risks faced by vulnerable populations and develop effective community-level action plans, it is important to understand the spatial pattern of heat exposure risk within cities. While studies have assessed outdoor thermal comfort in Sri Lanka cities like Colombo (Johansson and Emmanuel, 2006; Simath and Emmanuel, 2022), these studies rely on on-site weather observations and do not provide a comprehensive understanding of the intra-city heat exposure pattern. In fact, studies on intra-city population heat exposure in tropical and South Asian cities remain limited (Chew et al., 2021; Kong et al., 2021). Therefore, our study aims to narrow this gap by analysing the neighbourhood-scale heat exposure risks and linking them to the population in Colombo. The methodology we develop in this study can be applied to other cities facing similar challenges.

In the field of outdoor thermal environment and heat exposure risk analysis, climate models at various scales are frequently used (Kong et al., 2021). In this study, we employ the land surface model SUEWS to simulate the microclimate at a local scale in Colombo, Sri Lanka, and evaluate the risks of heat exposure for the population. Our objectives are: (1) to understand the spatial and temporal pattern of population heat exposure across the city of Colombo and surrounding areas; (2) to explore the changes in heat stress for a future urban development scenario; and (3) to assess the impact of mitigation measures on heat stress.

6.2. Methods

This study is focused on the city of Colombo (6°55'N, 79°51'E), which is the commercial capital and largest city in Sri Lanka with a population of approximately 1 million (Patankar, 2017). Colombo is located on the west coast of Sri Lanka (Fig. 6.1) and has a tropical rainforest climate (Köppen climate type *Af*) (Beck et al., 2018). It has no seasonal variations in air temperature or humidity, with rainfall year-round (Perera and Emmanuel, 2018), and low wind speed during March to April and October to November (Emmanuel and Johansson, 2006).

In this study we use SUEWS-RSL (Tang et al., 2021) to simulate the heat exposure pattern across the study area (section 6.2.1). Model outputs are evaluated with observations from the Colombo meteorological station (WMO code: 43466, CLB in Fig. 6.1) and Ratmalana meteorological station (WMO 43467, RML in Fig. 6.1). 3-hourly temperature/moisture/wind data from the NOAA Integrated Surface Database (ISD) (Smith et al., 2011) are available for both sites, and daily maximum/minimum air temperatures from Global Historical Climatology Network daily (GHCNd) (Menne et al., 2012) are available for CLB.

Schoetter et al. (2015) defines a heat wave as at least three consecutive days with daily maximum temperatures exceeding the 98th percentile based on long-term temperature records. Using this definition, we focus on a 6-day heatwave from Feb 23 to 28, 2020 based on ERA5 data (see section 6.2.1.2) of 2010-2020, during when heat alerts have been issued by the Disaster Management Centre of Sri Lanka (Disaster Management Centre, 2022).

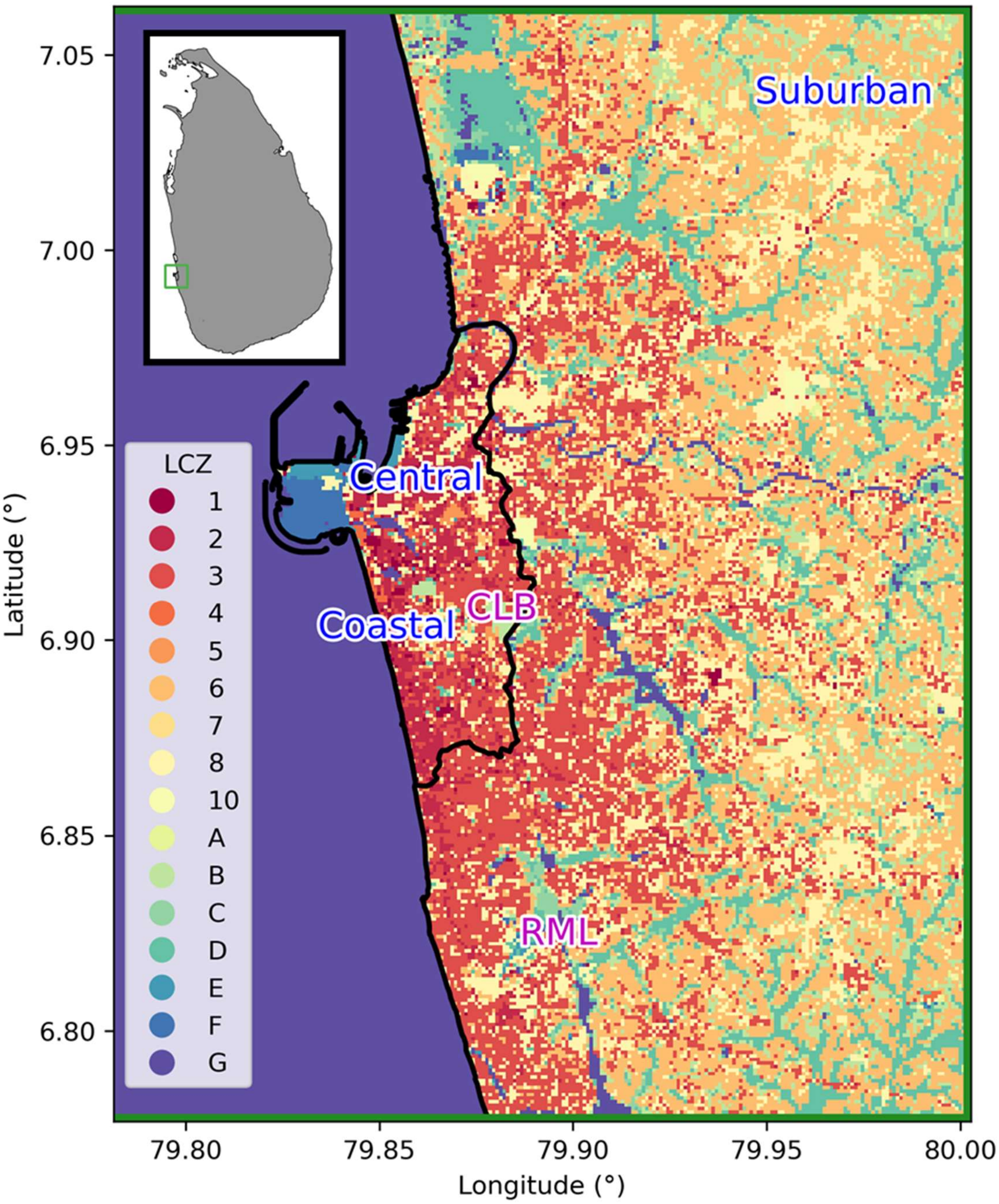

Fig. 6.1. Sri Lanka (inset) with location Colombo shown, and the local climate zones (LCZ) (100 m resolution) (Perera and Emmanuel, 2018) for the Colombo Municipal Council (CMC) (black boundary) and the surrounding area. Two World Meteorological Organization (WMO) stations (red) are located in this region (Colombo: WMO 43466; Ratmalana: WMO 43467). Locations of focused neighbourhoods (Section 3.2) indicated in blue. Definitions of LCZs can be found in Table 2 of Stewart and Oke (2012).

6.2.1. Urban climate modelling

6.2.1.1. Model overview

We use the Surface Urban Energy and Water Balance Scheme (SUEWS) v2021a/SuPy 2022.8.5 (Järvi et al., 2011; Sun et al., 2020; Sun and Grimmond, 2019; Ward et al., 2016) to model the climate variables across Colombo. SUEWS uses seven surface types: paved, buildings, evergreen trees/shrubs, deciduous trees/shrubs, grass, bare soil and water.

The model calculates surface energy exchanges of multiple grids at the neighbourhood/local scale constrained by the surface energy balance (Oke, 1987):

$$Q^* + Q_F = Q_H + Q_E + \Delta Q_S \qquad (6.1)$$

where Q^* is the net all-wave radiation, Q_F is the anthropogenic heat flux, Q_H and Q_E are turbulent sensible and latent heat fluxes, and ΔQ_S is the net storage heat flux. One major advantage of SUEWS is the balance between the simplicity and accuracy (Järvi et al., 2011, 2014; Ward et al., 2016; Ao et al., 2018; Kokkonen et al., 2018). The model only requires commonly measured meteorological variables and surface cover characteristics that can be relatively easily obtained. From the sub-models options, we use the Net All-wave Radiation Parameterization (NARP) for radiative fluxes (Loridan et al., 2011; Offerle et al., 2003), Objective Hysteresis Model (OHM) for storage heat flux estimation (Grimmond et al., 1991; Grimmond and Oke, 1999b, 2002), the Penman-Monteith equation adjusted for urban areas for latent heat flux calculation (Grimmond and Oke, 1991), and the roughness sublayer (RSL) module for near-surface wind, temperature and humidity profiles diagnostics (Tang et al., 2021; Theeuwes et al., 2019). The model has been extensively evaluated in different climates globally (Table 3 of Lindberg et al. (2018); Table 1 of Sun and Grimmond (2019)), and reported to provide generally acceptable outputs.

Here we use the surface diagnostics of air temperature, moisture and wind speed from the SUEWS-RSL module. In this application it assumes horizontally homogeneous surfaces both above and below the roughness sub-layer (RSL). It uses Monin-Obukhov Similarity Theory (MOST) (Brutsaert, 2005) above the RSL (i.e. within the inertial sub-layer, ISL) and a modified-MOST RSL parametrisations (Harman and Finnigan, 2008, 2007; Theeuwes et al., 2019) to calculates the diagnostic profiles in the surface layer based on the climate forcing data above the blending height. The conventional MOST approach is only applicable to models exchanges of momentum and scalars in the ISL above the RSL (Roth and Oke, 1995; Wood et al., 2010). Corrections are required within RSL. The SUEWS-RSL module, near-surface diagnostics are calculated assuming MOST only when the RSL is very shallow (e.g. open grass) otherwise the RSL parametrisations are applied. Theeuwes et al. (2019) evaluated the SUEWS-RSL approaches with observations in central areas of Basel and Gothenburg, reporting reasonable wind profile predictions. More recently, Tang et al. (2021) evaluate the temperature profile at an urban site in central London, suggesting an slight underestimation in mean absolute error (MAE) of 0.93 °C. Since the SUEWS-RSL module assumes a homogeneous area and provides horizontally averaged outputs, such bias is considered acceptable.

6.2.1.2. Land cover characteristics

Land cover data are needed for SUEWS modelling. The spatial analysis (Fig. 6.2) is undertaken to obtain six land cover types (building, paved, trees, grasses, bare soil and water) fractions and morphology (Table A7.1).

An iterative process is employed which first uses the Semi-Automatic Classification Plugin (SCP) (Congedo, 2021) in QGIS (QGIS Development Team, 2022) and a clear sky Sentinel-2 multiband (20 m resolution) satellite image (ESA, 2018) taken on 20 February 2020 covering the study area (Fig. 6.1). The SCP algorithm training involved visual inspection of high-resolution satellite imagery (Google, 2022) at 60 samples across the Sentinel-2 image, allowing SCP to generate the first version of a land cover map (LCv1).

To improve LCv1 additional data are used:

- Buildings – Colombo Municipal Council (CMC) building footprints and number of storeys (Blunn et al., 2022a) are used to derive the volumes with heights obtained by assuming the 3 m minimum storey height regulation (UDA, 2018) plus 1 m to account for roof height.
- Roads (paved) – To determine the area of roads the OpenStreetMap (OpenStreetMap contributors, 2021) roads are used. By inspection of Google Earth imagery (Google, 2022) at 10 random locations per road class (24 classes)

the road width of each class is estimated. To avoid areal overestimation, the class minimum width is used with the OpenStreetMap line features.

- Trees and grass – OpenStreetMap's 16 vegetation types in Colombo do not include scattered vegetation (e.g. street trees). After inspecting imagery (Google, 2022) the 16 classes are assigned to our two classes (Table A7.2). The SCP identified scattered vegetation is retained.
- Bare soil – OpenStreetMap railways are classified as bare soil.
- Water – OpenStreetMap has 'large open water' (e.g. lakes, rivers, and pools) polygons, and narrow waterways (e.g. canals and streams) as lines. To obtain areas for the latter, the same approach as roads is used.

These data are used to update the LCv1 based on the following order of assumed accuracy: (1st) buildings, (2nd) land cover derived from OpenStreetMap, and (3rd) SCP LCv1 results. Paved fraction is equal to the sum of road fraction and the remaining unclassified areas, based on visual inspection of ESA. This version is LCv2.

To improve the estimate of building fraction beyond the CMC area, within the CMC area bootstrapping is applied to obtain a plan area fraction relation between CMC building footprints and SCP data (Appendix 8). This relation is applied to correct the SCP data outside the CMC. To extend the building height information beyond the CMC, within the CMC mean building heights are calculated for local climate zones (LCZs), as mapped by Perera and Emmanuel (2018) (Fig. 6.1), and assigned beyond the CMC using the LCZ map (Blunn et al., 2022b). Definitions of LCZs can be found in Table 2 of Stewart and Oke (2012).

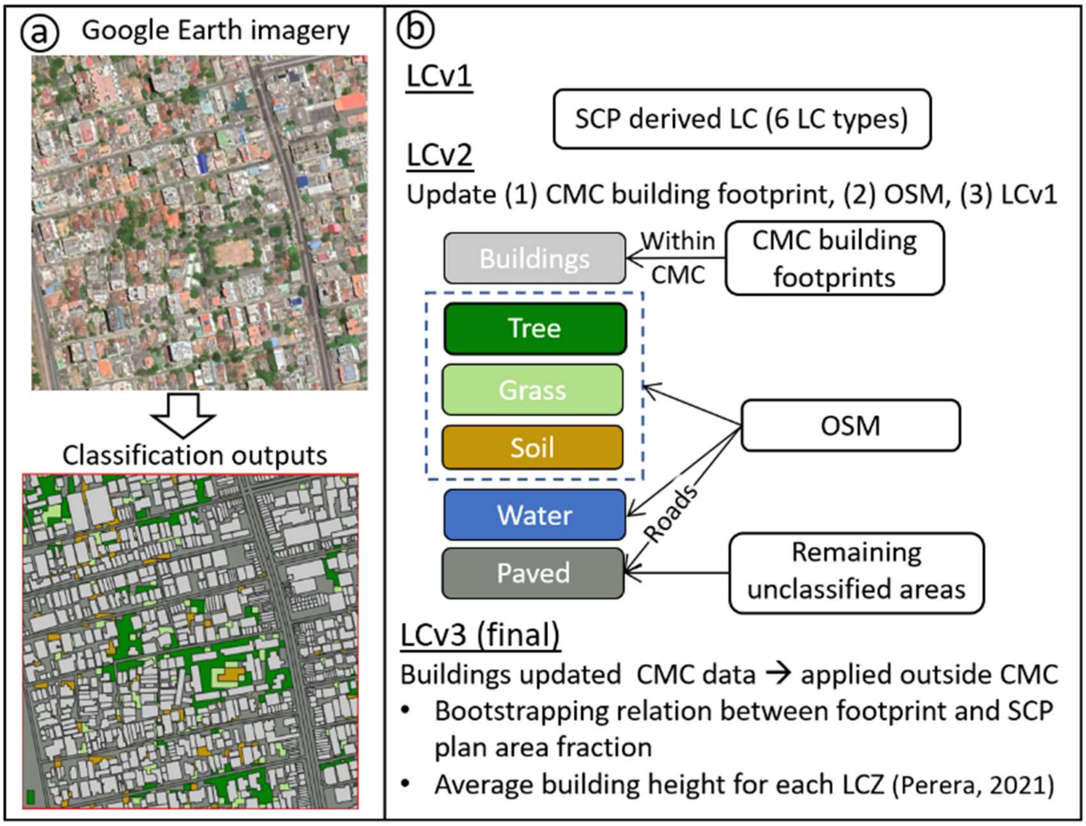

Fig. 6.2. Land cover fraction calculation (a) example outputs and (b) procedures.

6.2.1.3. Input data preparation

The daytime and night-time divisional population data are obtained from the divisional secretariats' census in 2012 (Department of Census & Statistics, 2012) and downscaled into 500 m grids based on the building volume calculated from land cover data in Section 6.2.1.2 (Fig. 6.3). During weekdays the population is assumed to linearly change between 04:00–10:00 and 16:00–22:00 based on timing of trips to and from work in the Western Province (Fig. 3.1.23 of JICA (2014)). It is assumed that no commuting occurs on weekends, so the population density remains equal to the night-time population. The population and land cover data are used to calculate the anthropogenic heat diurnal profiles for each grid and input to SUEWS. More details of population data processing and anthropogenic heat calculation can be found in Blunn et al. (2022b).

To force SUEWS, climate data above the roughness layer is required to exclude the local influence. Here we use data of European Centre Reanalysis version 5 (ERA5) (Hersbach et al., 2020), available at 0.125° × 0.125° resolution at hourly intervals for 1979 to present, downscaled to the model time-step (5-min). The inverse distance weighting approach (Shepard, 1964) is used to downscale ERA5 data to SUEWS grids, as shown in Fig. 6.4. The forcing data show spatial distribution of higher air temperatures in the north and lower in the south because of mountainous areas to the east and southeast (Lobelia, 2022).

Model spin-up is important for land surface models to initialise the soil moisture state, which can have a substantial impact on urban land surface model performance (Best and Grimmond, 2014). The model spin-up usually requires multiple years' run prior to the period of interest. However, in our study there are nearly 3000 grids in total, and performing spin-up for each grid can be very time-consuming. Therefore, we bin the built-up fractions and vegetation fractions with the interval of 0.1 for all grids, and categorise them into 28 groups. From each group we select one grid that with built-up and vegetation fractions closest to the median values in the group. SUEWS is run from 2010 for all selected grids, allowing nine years' spin-up prior to the study periods in 2020. The initial conditions of soil moisture and vegetation states are assigned to grids in the same group. The remaining non site-specific parameters, e.g. heat storage, surface conductance and albedo related variables are obtained from Ward et al (2016) and Omidvar et al. (2022).

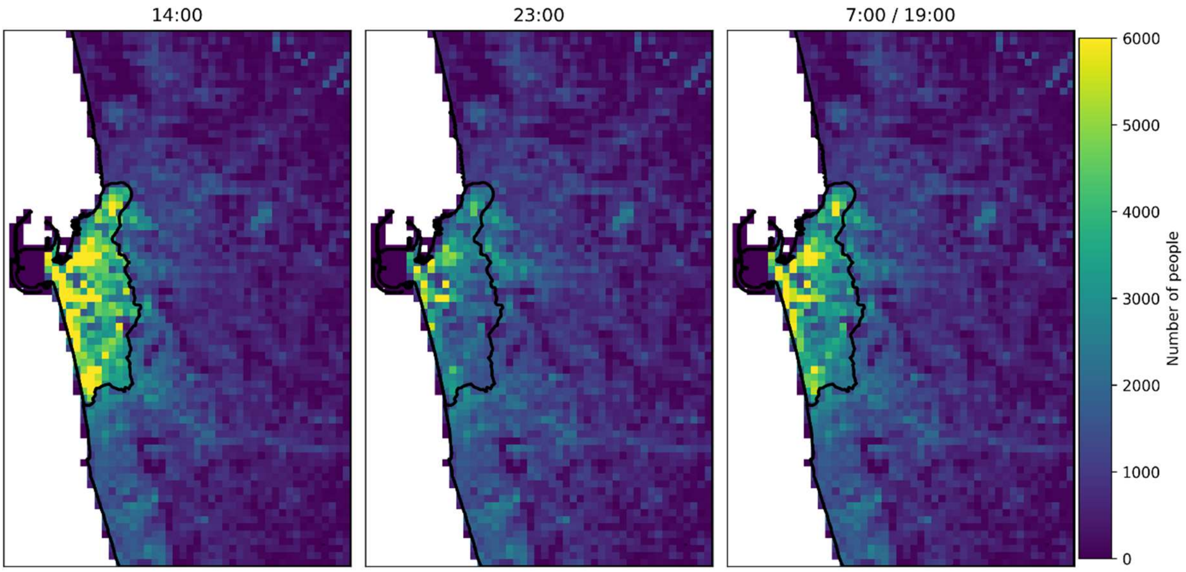

Fig. 6.3. Population (grid cell resolution 500 m) at three different local times on weekdays (a)14:00, (b) 23:00 (c_ 07:00 and 19:00. Modified from Blunn et al. (2022b).

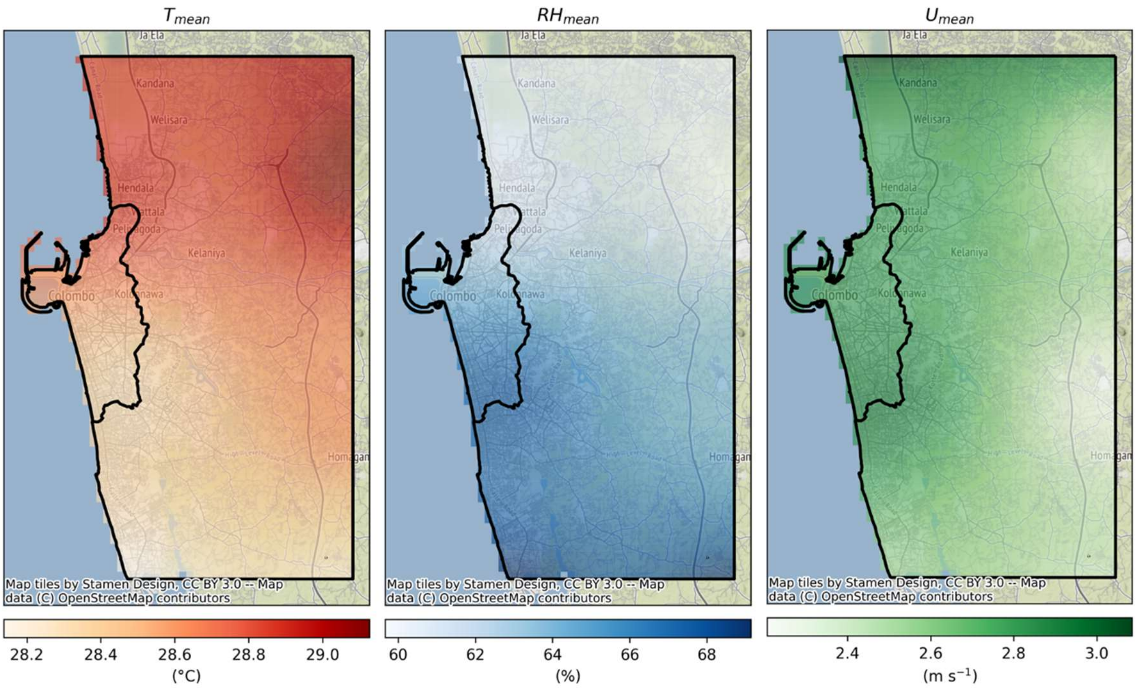

Fig. 6.4. Colombo region 23 – 28 February 2020 mean air temperature, relative humidity and wind speed from ERA5 (spatial resolution: 0.125°) (Hersbach et al., 2020) forcing data downscaled to SUEWS grid resolution of 500 m.

6.2.2. Heat exposure indices

In addition to air temperature, there are numerous indices for assessing heat stress (e.g. Epstein and Moran's (2006) Fig. 3, Buzan et al.'s (2015) Fig. 1). These require various meteorological variables and are applicable for different situations. Here, we consider indices: (1) developed for outdoors; (2) have heat stress thresholds for public guidance; (3) regarded to be reliable (physiologically and/or epidemiologically); and (4) feasible meteorological variables (e.g. SUEWS output: air temperature, humidity, wind speed). The following three indices meet these criteria, with recommendations in literature reviews and comparative studies (Auliciems and Szokolay, 2007; Barnett et al., 2010; Blazejczyk et al., 2012; Buzan et al., 2015; d'Ambrosio Alfano et al., 2011; Epstein and Moran, 2006; Roghanchi and Kocsis, 2018):

First, the Heat Index (I_H units:°C), a temperature-like index, is one of the most used heat exposure indicators globally (Brooke Anderson et al., 2013), including both the Sri Lankan Department of Meteorology (Disaster Management Centre, 2022) and the US National Weather Service (2022) for heat alert. Rothfusz's (1990) polynomial fit to Steadman's apparent temperature table (Steadman, 1979a) which models the human body heat balance. The adult (either sex) is assumed to be 1.7 m tall, weigh 67 kg, be wearing long trousers with a short sleeve shirt, and be walking outdoors in a shaded area at 1.4 m s^{-1} (Steadman, 1984, 1979a, 1979b) with a wind speed of 2.57 m s^{-1} (5 knots) (Rothfusz, 1990). The equation (Blazejczyk et al., 2012):

$$I_H = c_1 + c_2T + c_3RH + c_4T \cdot RH + c_5T^2 + c_6RH^2 + c_7T^2RH + c_8T \cdot RH^2 + c_9T^2RH^2 \quad (6.2)$$

requires the pedestrian level (i.e. 2 m) air temperature (*T;* °C), relative humidity (RH; %) and constants (c_i Table A9.1). Corrections are made under certain circumstances (e.g., if RH < 15 % or RH> 85 %). Absolute thresholds exist for heat-health alerts based on the effect on the human body (Fig. 6.1) (Disaster Management Centre, 2022; National Weather Service, 2022).

Discomfort Index (I_D; units °C) has been in use for one of the longest periods (Epstein and Moran, 2006). It is the average between T and wet-bulb (T_w units °C) temperature (Israel Meteorological Service, 2022; Tennenbaum et al., 1961):

$$I_D = 0.5T + 0.5T_w \quad (6.3)$$

The T_w can be determined using T and RH using (Stull (2011):

$$T_w = T \cdot \tan^{-1}(0.151977 \cdot (RH + 8.313659)^{0.5}) + \tan^{-1}(T + RH) - \tan^{-1}(RH - 1.676331) + 0.00391838 \cdot RH^{1.5} \times \tan^{-1}(0.023101 \cdot RH) - 4.686035 \quad (6.4)$$

Combining dry- and wet-bulb temperatures (Eq. 6.3) originates from the US air-conditioning industry's cooling degree days calculation (Thom, 1959). The Israeli Defence Forces modified it to measure heat load (Tennenbaum et al., 1961) and is used by the Israel Meteorological Service (2022) and European climate services (Gidhagen et al., 2020). The heat load thresholds (Fig. 6.1) are based on field and clinical observations of exertional heat stroke patients in Israel (Shapiro and Seidman, 1990). Israel Meteorological Service (2022) defines the discomfort intensity as the difference between the actual I_D and the threshold of 22 °C. The index is valid both physiologically (linked to sweat rate (Tennenbaum et al., 1961)) and epidemiologically (correlated with summer mortality (Tout, 1980)). It has been used to assess the heat exposure risks in warm-humid climates (e.g. Atlanta, US (Baniassadi et al., 2019), Putrajaya, Malaysia (Md Din et al., 2014)). Although a relatively simple index, it is correlated with the more advanced wetblub globe temperature (WBGT) (Epstein and Moran, 2006) index adopted as an ISO standard 7243 (ISO, 2017).

Humidex (I_{HD}, units: °C), used by Meteorological Service of Canada for heat warnings (Environment and Climate Change Canada, 2019), is a modification of I_D (d'Ambrosio Alfano et al., 2011) by Masterson and Richardson (1979) with the intent of representing a perceived equivalent temperature for the average person:

$$I_{HD} = T + 0.5555\left(6.11e^{\left(5417.753\times\left(\frac{1}{273.15}-\frac{1}{273.15+T_{dp}}\right)\right)} - 10\right) \tag{6.5}$$

where e is the Euler's number (≈ 2.71828) and the dewpoint temperature (T_{dp}, units: °C) here determined using Lawrence (2005):

$$T_{dp} = \frac{243.04\times\left(ln\left(\frac{RH}{100}\right)+\frac{17.625\times T}{243.04+T}\right)}{17.625-\ \left(\frac{RH}{100}\right)-\frac{17.625\times T}{243.04+T}} \tag{6.6}$$

This index agrees well with the comfort zone of human body especially at high humidity (i.e. > 60%) (Roghanchi and Kocsis, 2018) but it may underestimate heat stress risk in hot-dry conditions (i.e., T > 36 °C and specific humidity < 10 g kg^{-1} (RH < 27.25%)) (d'Ambrosio Alfano et al., 2011). Barnett et al. (2010) epidemiological analysis of 107 US cities mortality data for 1987–2000 found this index performed better than others, especially in the humid subtropical south-eastern region. These suggests it is suitable for heat stress assessment in hot-humid climates, and can provide different warning levels (Table 6.1).

The differences in humidity impacts on the heat stress indices are evident, as are their critical health thresholds (Fig. 6.5). When T is constant (e.g. 30 °C), an increase in RH (e.g. 30 to 40 %) I_H increase is smaller (i.e. 1 °C) than for the same size RH increase at high values (e.g. 70 to 80 % leads to a 3 °C increase in I_H). I_H becomes more sensitive at higher T and RH. However, the impact of RH increases on I_D are smaller as RH increases (i.e. less sensitive to high humidity). Given its development in a hot-arid climate, further study is needed to determine its suitability for hot-humid climates like Sri Lanka. I_D has only three thresholds (Table 6.1), which may be linked to its original application (i.e. military training) with assumed higher intensity activity. The I_{HD} 'feels-like' temperature index, has a similar range to I_H (Table 6.1), but is more sensitive to changes in RH at lower T (cf. I_H) but unvarying with RH for a fixed *T*. For example, as 10 % change in RH is increases I_{HD} by 2 °C when T is 26 °C (cf. I_{HD} by 3 °C when T is 34 °C). The first heat-health thresholds are similar for I_{HD} and I_D, suggesting caution once T is 25 °C if RH reaches 60 %. But the thresholds differ between next two levels with a T of 35 °C and RH = 30 % classified as caution for I_{HD} but extreme caution for I_H. Whilst the danger thresholds are similar (Table 6.1), with T of 31 (33) °C and RH of 80 (60) %.

Table 6.1: Levels of warning for three indexes used with threshold values (units: °C). Colours show the levels of comparable thresholds of different indices based on their health outcomes (Blazejczyk et al., 2012; Schwingshackl et al., 2021).

Thresholds	Levels	Warning
	Caution	**Heat Index *I_H*** (Disaster Management Centre, 2022; National Weather Service, 2022)
27-32	Caution	Fatigue possible with prolonged exposure and activity. Continuing activity could result in heat cramps.
32-41	Extreme	Heat cramps and heat exhaustion possible.
41-54	Danger	Heat cramps and heat exhaustion are likely; heat stroke possible.
>54	Extreme danger	Heat stroke imminent
	Heat load	**Discomfort Index *I_D*** (Epstein and Moran, 2006; Shapiro and Seidman, 1990; Tout, 1980)
22-24	Light	Slight feeling of heat.
24-28	Moderate	Caution needed during physical work outdoors. Physical work performed with some difficulties
> 28	Severe	Dangerous to engage in physical effort outdoors. Body temperature cannot be maintained during physical work. High risk for heat illness.
	Discomfort	**Humidex *I_{HD}*** (d'Ambrosio Alfano et al., 2011; Environment and Climate Change Canada, 2019; Masterson and Richardson, 1979)
30-40	Some	Tone down or modify certain types of outdoor exercise
40-45	Great	Reduce all unnecessary physical activity. Avoid exertion.
45-54	Dangerous	Heat stroke possible.
>54	Heat stroke	Imminent

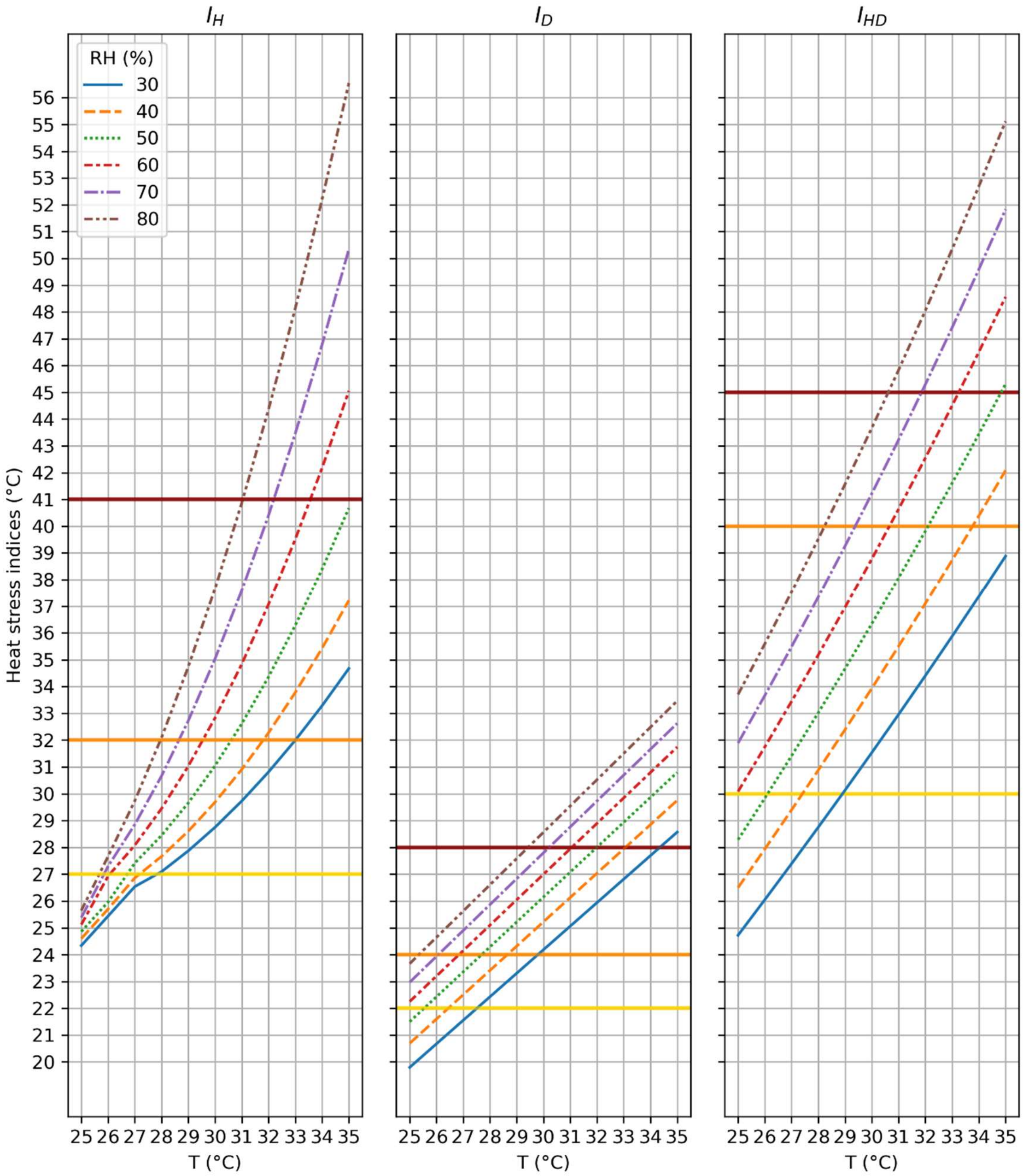

Fig. 6.5. Heat stress values with air temperatures and relative humidity for (a) **Heat Index I_H**, (b) **Discomfort Index I_D** and (c) **Humidex I_{HD}** . Bold horizontal lines show Table 6.1 thresholds.

6.2.3. Urban development scenarios

The Colombo Core Area Development Plan (CCADP) (Rathnayake et al., 2020) for 2035 has development scenarios for the Colombo Municipal Council (CMC). It is assumed that the urban local climate zones (LCZs) become more developed by 2035 with LCZ 1 to 3 becoming LCZ 1 (compact high-rise), LCZ 4 to 10 becoming LCZ 3 (compact low-rise), and the non-urban LCZs remain unchanged (Fig. 6.6) (Scenario #1,Table 6.2). Land cover fractions, mean building heights and anthropogenic heat fluxes (Blunn et al., 2022b) for each LCZ type in CMC are based on 2020 data, and projected to 2035 scenario. The 100 m × 100 m LCZ grids are resampled to 500 m × 500 m for SUEWS simulations. Scenario #1has changes in urban morphology but no changes in climate.

We also consider two Colombo potential mitigation approaches (Simath and Emmanuel, 2022) (Table 6.2): (1) increasing the albedo of paved surfaces from 0.10 to 0.27 and building albedo from 0.12 to 0.35 (i.e. with light colour paint) (Jandaghian and Berardi, 2020; Kalkstein et al., 2022; Oke et al., 2017); and (2) increasing tree cover extent by 25 % with a corresponding reduction in paved surfaces (Grimmond, 2007; Heaviside et al., 2017; Kalkstein et al., 2022). Note here we only assume the idealised condition, as in reality paved areas like roads cannot be fully removed.

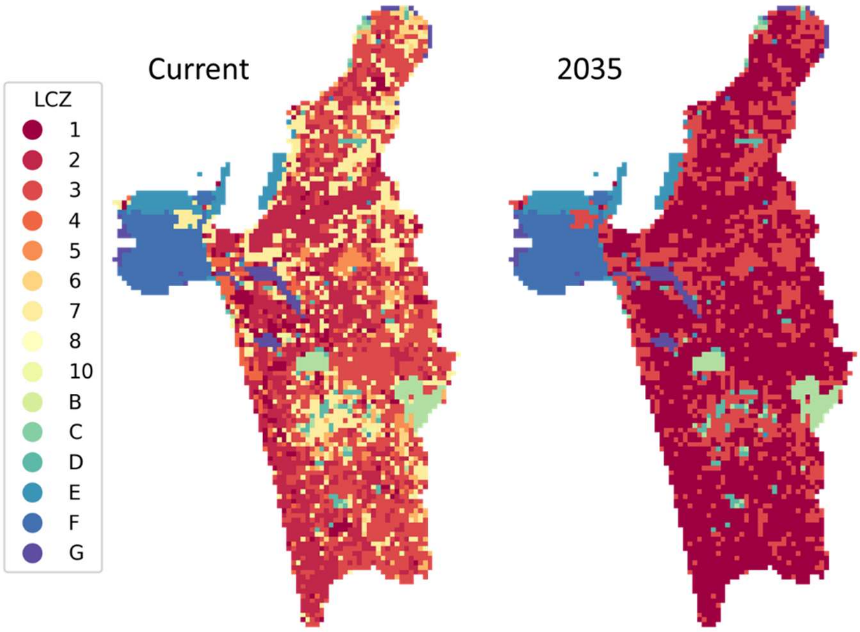

Fig. 6.6. Local climate zones of CMC (Fig. 6.1) in current (Perera and Emmanuel, 2018) and 2035 (Rathnayake et al., 2020). Definitions of LCZs can be found in Table 2 of Stewart and Oke (2012).

Table. 6.2: Modelling scenarios for the CMC 2035 development (Jandaghian and Berardi, 2020; Kalkstein et al., 2022; Oke et al., 2017).

#	Scenario	Changes made
1	2035 base case	LCZ 1-10: → LCZ 1 and 3. LCZ A-G: unchanged
2	Increase albedo	Albedo: Building : 0.12 → 0.35; Paved: 0.10→ 0.27
3	Replace paved with tree cover	Tree cover increase 25% by paved surface reduction. Per grid-cell

6.3. Results

6.3.1. Model evaluation

The modelled weather variables and heat exposure metrics are compared to observations at two meteorological stations (CLB, WMO 43466; RML, WMO 43467; Fig. 6.1) for the heat wave period (Fig. 6.7). The daily maximum and minimum air temperatures are well captured (Fig. 6.7a), but the nocturnal air temperatures tend to be underpredicted by up to 1.5 °C in the median at night. Modelled diurnal patterns with a large inter-quantile range are highly dependent on the forcing data, which differs from local observations. Generally, air temperatures are underpredicted (MAE ≤1.1 °C at both sites, Fig. 6.2) with results similar to a London evaluation (Tang et al., 2021) (MAE = 0.93 °C). Modelled relative humidity (Fig. 6.7b) generally agree with observations. Modelled wind speeds (Fig. 6.7c) diurnal patterns are dependent on the forcing data but capture differences between the two sites.

Modelled heat-health indices agree well with observations (i.e. derived values using observations) in the morning but are more biased in the afternoon and at night. However, as the minimum and maximum air temperatures are well modelled (Fig. 6.7a) the indices biases at these times are expected to be smaller. Also, differences between the meteorological variables of the two sites are calculated to show the biases in inter-site variations. (Fig. 6.3). MAEs in ΔI_H, ΔI_D and ΔI_{HD} are 0.86 °C, 0.49 °C and 0.87 °C, respectively, and MBEs are all within ±0.1 °C. These suggest that modelled relative differences between different sites have smaller errors compared to modelled variables at each individual site.

These errors may arise from uncertainties of model parameters due to lack of local coefficients for surface conductance coefficients and heat storage. We do not account for variability of tree height (5 m). These will impact the SUEWS-RSL temperature and wind speed modelling. Simulations will capture local-scale climate but lack details of individual point sensors which are at a smaller scale, which is acceptable.

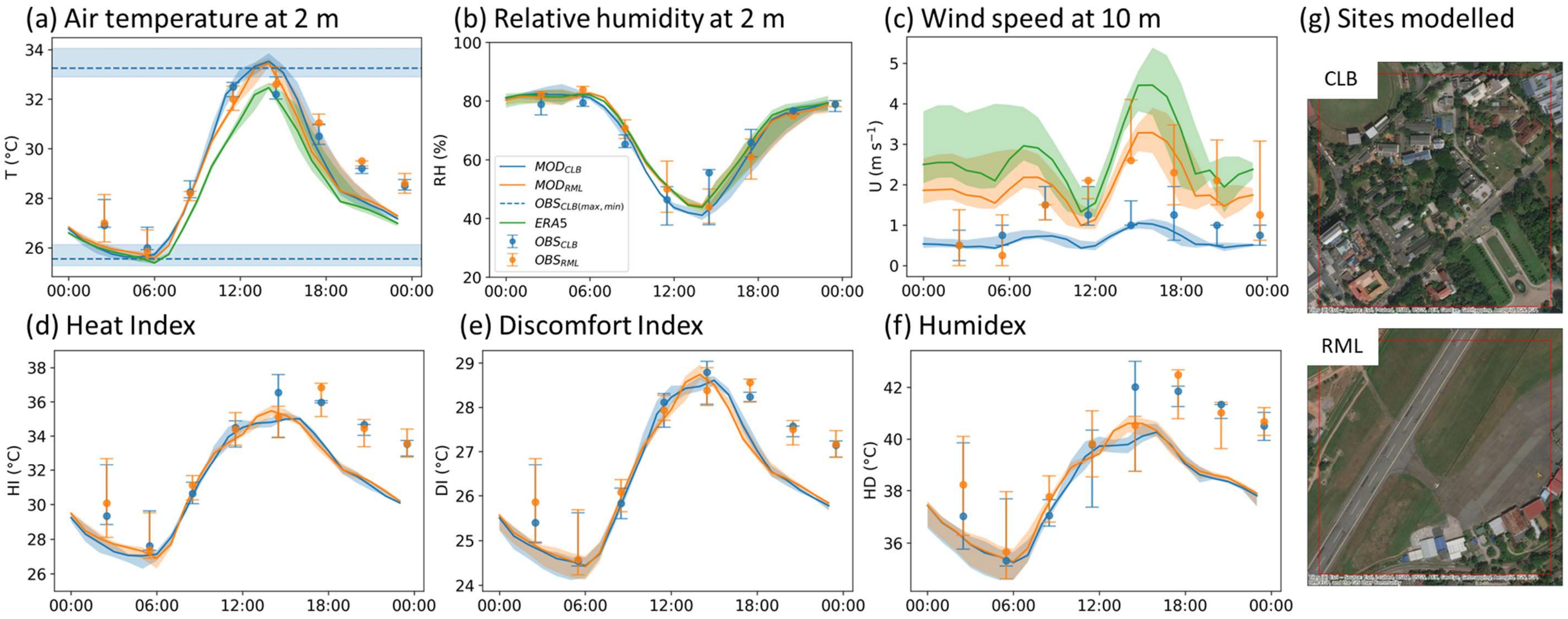

Fig. 6.7. Comparison for 23 to 28 February 2020 of modelled (MOD, hourly) and observed (OBS, 3-hourly) median and interquartile range of (a) air temperature at 2 m above ground level (agl) (forcing data (ERA5), hourly), (b) relative humidity at 2 m agl, (c) wind speed at 10 m agl, (d) 2 m heat index, (e) discomfort index and (f) humidex determined for (g) Colombo meteorological station (CLB, WMO 43466, Fig. 6.1)) and Colombo International Airport Ratmalana meteorological station (RML, WMO 43467, Fig. 6.1) (g) 500 m × 500 m grid cell simulated with SUEWS (Imagery: July 2020 Source: Esri, (2022)). Source of observations: 3-hourly - NOAA Integrated Surface Database (Smith et al., 2011), CLB daily maximum/minimum air temperatures - Global Historical Climatology Network daily (Menne et al., 2012).

Table. 6.3: Mean absolute error (MAE) and mean biased error (MBE) between modelled and observed hourly (N = 46) variables at two sites 23 to 28 February 2020 (N = 46). Differences between the meteorological variables of the two sites are calculated to show the biases in inter-site variations.

Site		T (°C)	RH (%)	U (m s^{-1})	I_H (°C)	I_D (°C)	I_{HD} (°C)
CLB	MAE	1.10	6.59	0.61	2.00	0.80	1.85
	MBE	-0.63	0.41	-0.43	-1.64	-0.58	-1.20
RML	MAE	1.03	5.42	1.13	1.96	0.85	1.81
	MBE	-0.74	0.79	1.00	-1.55	-0.64	-1.23
		ΔT (°C)	ΔRH (%)	ΔU (m s^{-1})	ΔI_H (°C)	ΔI_D (°C)	ΔI_{HD} (°C)
CLB - RML	MAE	0.53	4.82	1.44	0.86	0.49	0.87
	MBE	0.11	0.38	-0.67	-0.09	-0.04	0.06

6.3.2. Spatial distribution of heat stress indices

The variability of heat indices during the diurnal cycle of the heatwave period (23 to 28 February 2020) is analysed at four specific times: (a) 07:00 when people begin their morning commute; (b) 14:00 when peak air temperature is expected; (c) 19:00 when people are commuting home; and (d) 23:00 when people are going to bed (Blunn et al., 2022a).

The spatial distributions of air temperature and relative humidity at these times (Fig. 6.8) are controlled by the forcing data (Fig. 6.4) and local characteristics. Despite the warmer air temperatures in the north (Fig. 6.4), the more built-up coastal areas tend to be warmer (~0.3 °C) than the northeast rural area (Fig. 6.1) at 7:00 and 23:00. However, this nocturnal urban heat island intensity (UHII) between the CMC and inland rural areas is relatively smaller when compared to other hot-humid cities, e.g. nocturnal UHII around 2 °C during a heatwave in Singapore (Chew et al., 2021), which is due to the lower background forcing temperatures (around 1 °C lower in average in the CMC) (Fig. 6.4) and relatively small anthropogenic heat compared to other low-latitude cities (annual average 11.7 W m^{-2} for LCZ 1 in CMC (Blunn et al., 2022a), compared to annual 85 W m^{-2} for commercial area in Singapore (Quah and Roth, 2012)). At 14:00, rural and suburban areas in the north and northeast have higher air temperatures with the largest difference of around 1.8 °C across the study area. At 19:00, the temperature distribution largely follows the forcing pattern (Fig. 6.8) and the variations in local scale are small, as founded in the model evaluation (Fig. 6.7). The spatial distribution of relative humidity generally follows the forcing data with some variations due to local scale climates.

The heat stress indices at these times (Fig. 6.9) have similar spatial distributions to air temperature (Fig. 6.8), but with some obvious differences among indices. At 7:00, all three indices have similar distributions with higher values in the south, with differences up to around 0.7 °C (I_H), 0.4 °C (I_D) and 1.0 °C (I_{HD}) compared to the north. At 14:00, the spatial variations are the largest, which are 1.2 °C (I_H), 0.8 °C (I_D) and 0.9 °C (I_{HD}) across the whole study area. I_H and ID have similar patterns as the air temperature, while I_{HD} is more sensitive to the relative humidity, therefore higher in the south. Such differences are more obvious at 19:00, when I_{HD} is high in the south coast and lower in the northwest. The differences are up to 0.5 °C (I_H), 0.3 °C (I_D) and 0.8 °C (I_{HD}). This shows differences in the weighting of humidity component in heat stress indices. At 23:00, all three indices show similar patterns with CMC and southern coastal areas have higher values, with differences of 0.6 °C (I_H), 0.4 °C (I_D) and 1.2 °C (I_{HD}). This suggests that air temperature alone is not a good indicator for assessing heat stress in the hot-humid climate. Variations between the sensitivity of different heat stress indices to humidity are also reported in other studies. For example, Oleson et al. (2015) found that during summer middays Huston (hot-humid) had higher I_{HD} than Phoenix (hot-arid) but lower I_H and I_D. Although without validation one cannot determine which index is superior, this shows the importance of selecting index suitable for the climate.

Thresholds of different heat stress indices should be comparable based on their health outcomes (Fig. 6.1) (Blazejczyk et al., 2012; Schwingshackl et al., 2021). Spatial distributions of these heat stress warning levels (Fig 6.10) show large differences among indices. I_H has the largest variation in warning levels during the day. At 7:00 the suburban and rural areas in the northeast have no heat stress risks, and at 14:00 the whole study area is beyond the level of extreme caution. At 19:00, only CMC and surrounding urban areas are still at the extreme caution level. And at 23:00 the whole region is at the level of caution. It should be noted that I_H assumes a pedestrian level wind speed of 2.57 m s^{-1}, which is generally higher than the observed and modelled wind speeds (Fig. 6.7), therefore the actual heat stress may be underestimated. I_D, however, identifies the study area with higher risks during the day. At 7:00 the most areas are already classified as extreme caution, and at 14:00 it is raised to danger, suggesting high risks for heat illness. In contrast, I_{HD} has the smallest variation in warning levels. During the day all areas are beyond the level of caution, but at 14:00 only some areas with high air temperatures and relative humidity are classified as in extreme caution.

In summary all three indicators suggest the entire study area is at risk of heat stress during the heat wave period. The highest risk occurs during the daytime when air temperatures are high, especially areas inside the CMC and its east related to high both temperatures and relative humidity. In these areas people may experience heat related cramps and exhaustion, with the recommendation exertion from outdoor physical activities should be avoided. In the evening, heat stress risk levels are lower except in the built-up CMC area, where similar risks as at midday continue. Heat stress risk at night is further reduced, with rural areas no longer at risk (based on I_H), while built-up areas may experience thermal discomfort.

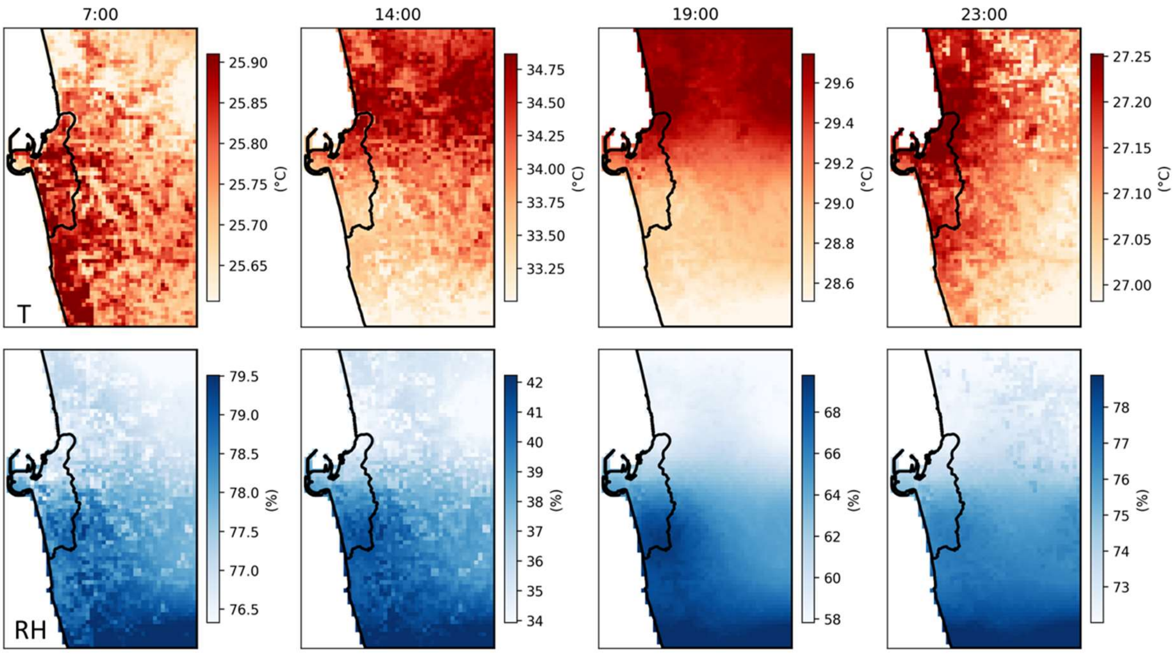

Fig. 6.8. Spatial distribution of modelled mean 2 m (a-d) air temperature (T) and (e-h) relative humidity (RH) during the heatwave (23 to 28 February 2020) at four local times (a, e) 07:00. (b.f) 14:00, (c,g) 19:00, and (d,h) 23:00.

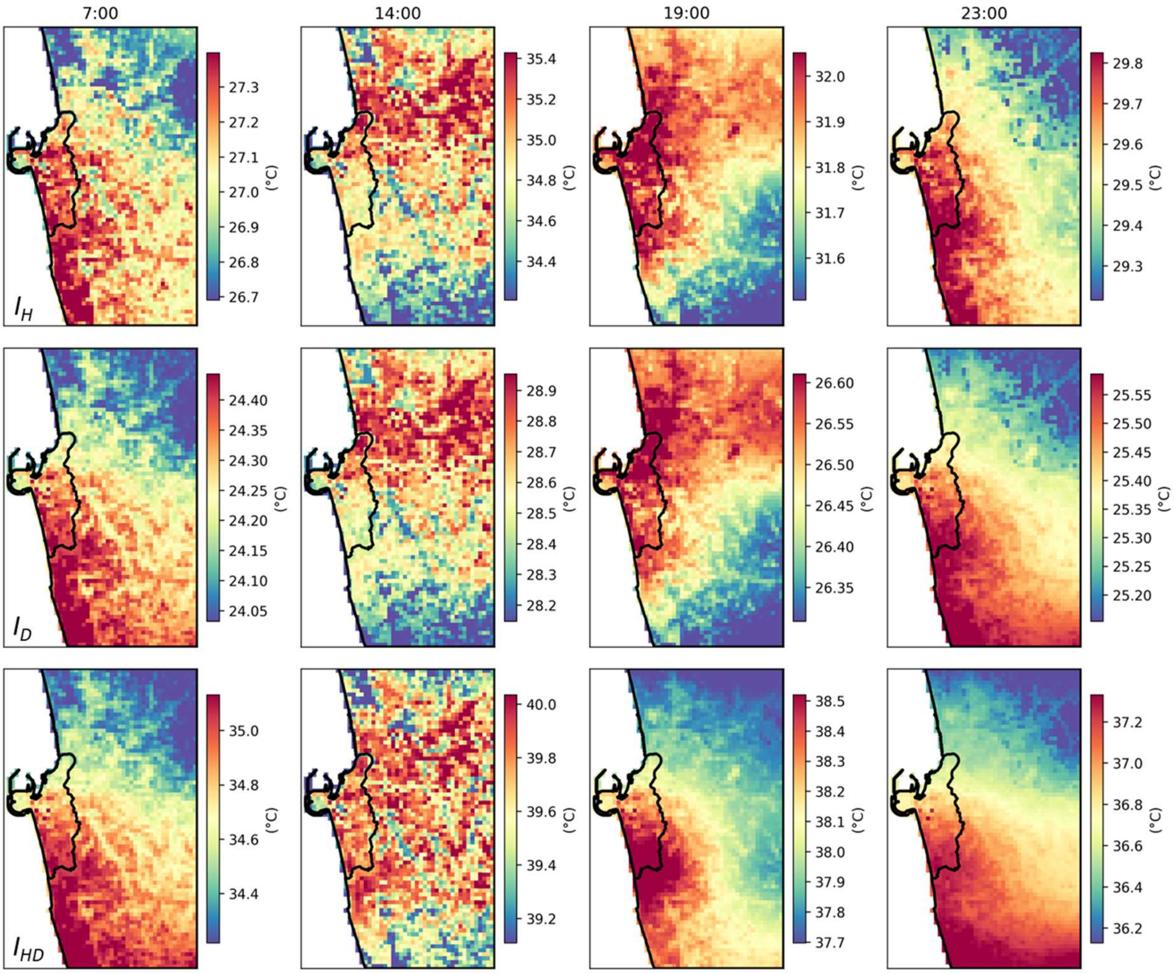

Fig. 6.9. As Fig. 6.8, but heat stress indices.

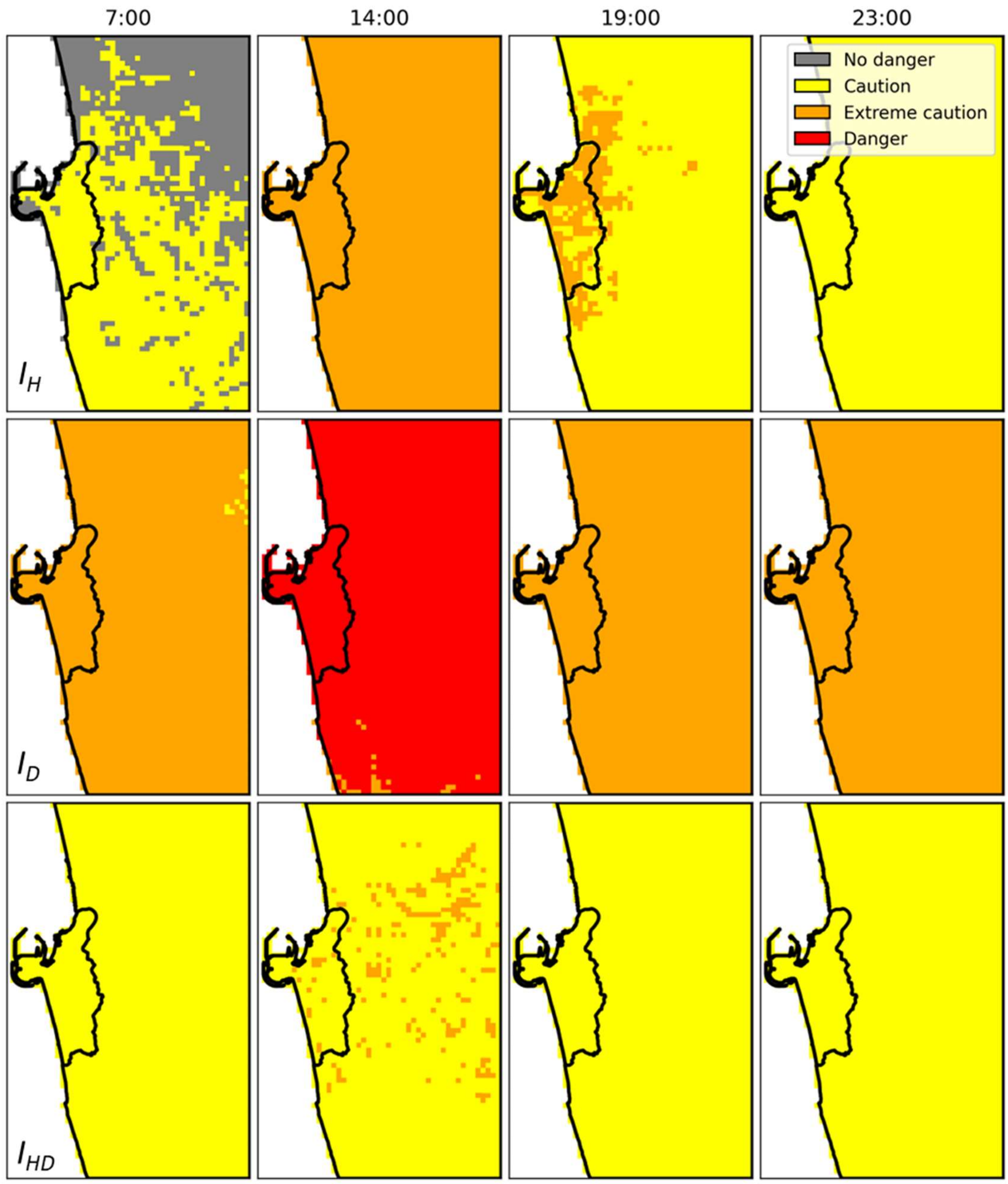

Fig. 6.10. Spatial distribution of warning levels of each heat stress index at different time of the day based on Fig. 6.9. Definitions of thresholds are in Table 6.1.

6.3.3. Population exposed to heat

It is critical to account for the population to understand the heat stress risks faced by citizens and provide targeted warnings and guidance. The hotspots in the study area, with both high heat stress risks (> caution level) and dense population (Fig. 6.11), are similar for the most critical areas in the CMC and the densely populated coastal areas, but spatially vary by time of day. The higher risk areas are in the south in the morning, move northward during the day, and back southward at night. Hence, the highest daytime combined population and heat exposure risk occurs in the northern less populated areas, although most of the population works in the CMC, while at night and early morning when there are fewer people in the warmer urban area when the heat exposure is highest.

To better understand the level of heat stress risks faced by citizens, the percentage of the population in the study area at the different heat stress levels for each index by time of the day (Fig. 6.12) is explored. Although 40% of the area is not within a critical I_H threshold (Fig. 6.9), 80% is exposed to the caution threshold. At 19:00, I_H extreme caution covers 11% of the area (Fig. 6.9), but mostly the CMC with 35% of the population. At 14:00, the I_{HD} extreme caution linked to high temperatures or high humidity simultaneously covers a large area, including the less urbanized east, with only 13% of the population.

The six heatwave days' total degree-hours exceeding the minimum heat stress threshold (Fig. 6.13) indicate I_H and I_D have similar hotspot spatial distributions across the CMC and surrounding populated areas, both north and south. While the I_{HD} hotspots are mainly in the south linked to the higher I_{HD} values. For all three, the degree-hours increase with building fraction (Fig. 6.13b), despite I_{HD} being lower in areas where building cover is 50 to 60% because these are mostly in the northern CMC, with lower RH and therefore I_{HD} values.

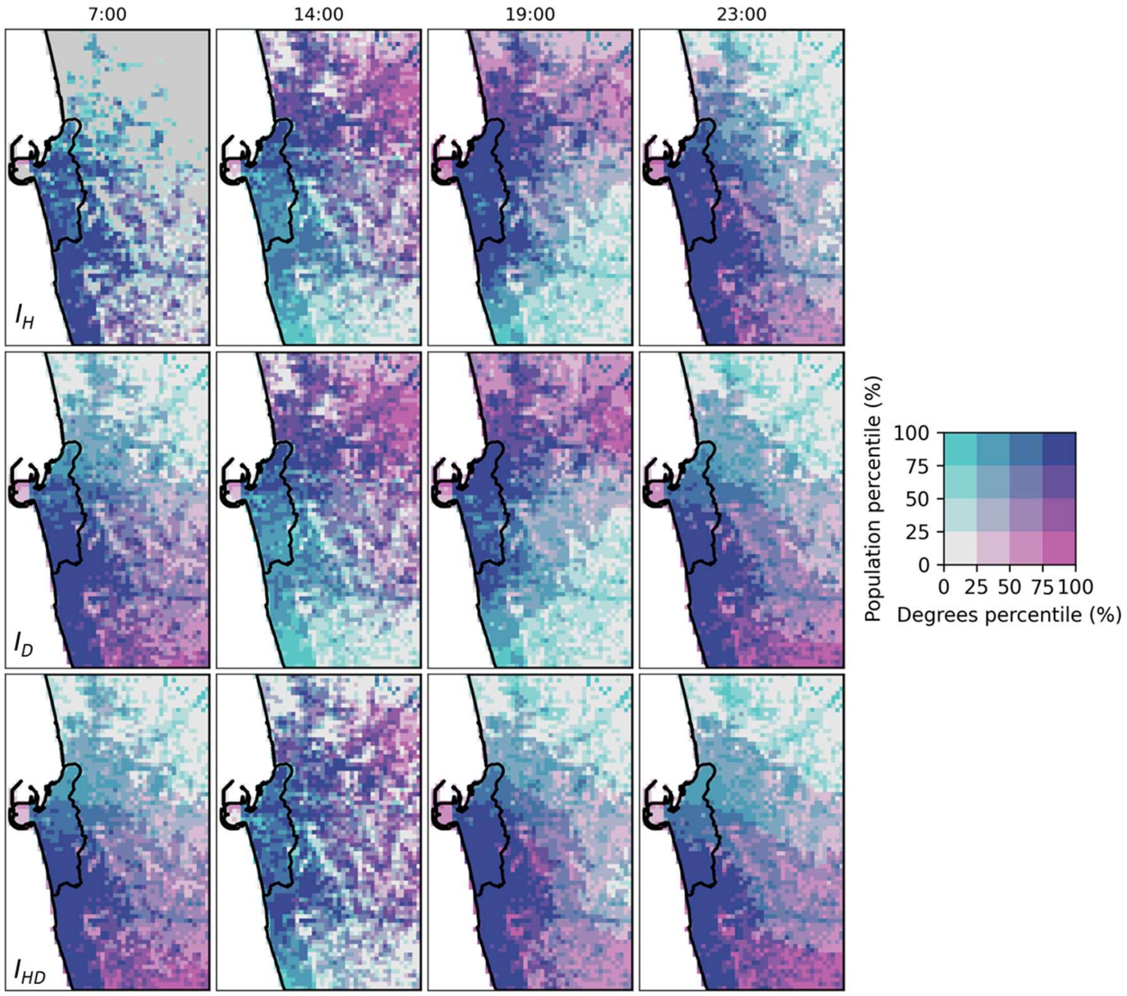

Fig. 6.11. Spatial distribution of population (cyan) and number of degrees exceeding the lowest threshold of different heat stress indices in Table 6.1 (pink) in percentile at different time of the day during the heatwave (23 to 28 February 2020). Areas not exceeding heat stress thresholds are grey.

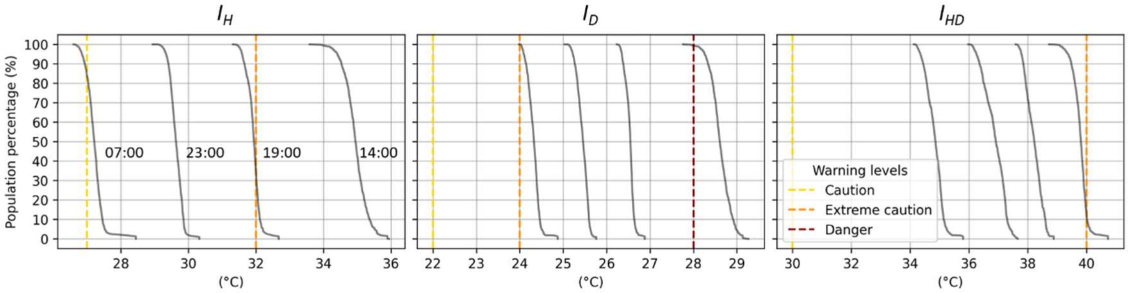

Fig. 6.12. Percentage of population as a function of heat stress indices at different time of the day during the heatwave (23 to 28 February 2020).

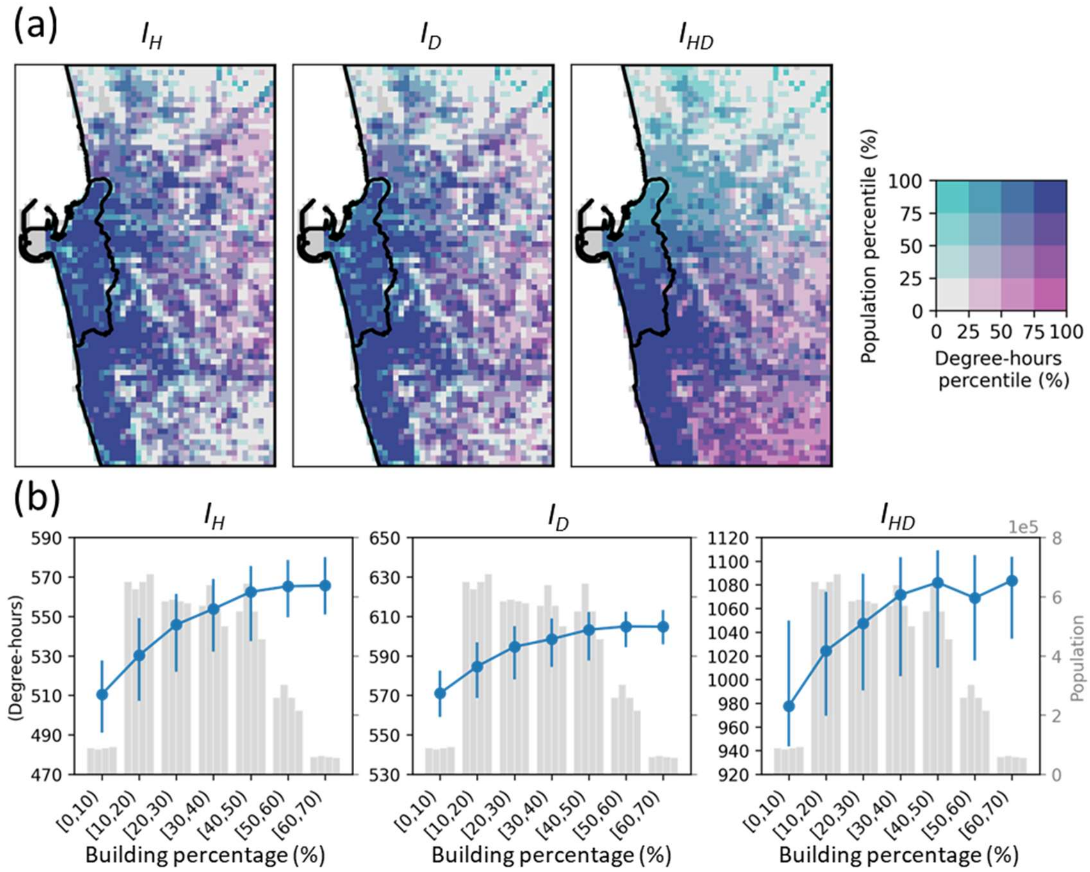

Fig. 6.13. (a) As Fig. 6.11, but total degree-hours exceeding the minimum thresholds during the heatwave (23 to 28 February 2020), and (b) total degree-hours as a function of plan area building coverage (blue) and population (grey bars) at (left to right) 7:00, 14:00, 19:00, 23:00.

6.3.4. Densely populated neighbourhoods

We explore three areas with population > 75th percentile of the region at daytime (14:00) and nocturnal (23:00) and their I_H values (Fig. 6.1).

The "central" CMC neighbourhood has mostly low-rise commercial and residential buildings (mean building height = 6.6 m) that cover 72% or the plan area (Fig. 6.14a). It is warm during both the day and night (I_H > 75th percentile at 14:00 and 23:00). The "suburban" Kadawatha neighbourhood in northeast Colombo (Fig. 6.14b) has small business, industrial and residential buildings (mean building height = 6.3 m) that only cover 13% of the plan area, whilst vegetation cover is large (78%). Here is high I_H during the day (I_H > 75th percentile at 14:00) but low at night (I_H < 25th percentile at 23:00). A CMC mid- to high-rise commercial and residential buildings (mean building height = 14.6 m) neighbourhood has 45 % plan area with building (Fig. 6.14c) is cooler during the day but warm at night (I_H < 25th percentile at 14:00 and > 75th percentile at 23:00).

Diurnal variability is driven by the background forcing data and local-scale influences. The central neighbourhood has consistently warmer air temperatures linked to typical urban influences: large buildings reducing the wind speed and the albedo, but storing more heat during the day (and releasing it at night), and emitting more anthropogenic heat. The suburban neighbourhood has a warmer background forcing data (Fig. 6.4), but the low heat storage and high evapotranspiration make it cooler at night. For the coastal neighbourhood, the urban effects also exist, but the influence of heat storage is more significant, leading to lower daytime temperatures and higher nocturnal temperatures.

The central neighbourhood is always beyond the I_H caution level at night and exceeds the I_{HD} extreme caution level during the daytime. It has continuously higher cumulative degree-hours of heat stress indices compared to the other two sites (Fig. 6.16). As the suburban neighbourhood has the lowest RH, it has lower heat stress indices, especially I_{HD}. The high RH at the costal neighbourhood makes it to have higher heat stress indices and surpass the dense neighbourhood in I_{HD} at night. Therefore, residents of the central or dense urban areas should be more cautious about nocturnal heat stress than suburban residents. While in the daytime, people work or live in the suburban area should also pay close attention to the influence of high temperatures as those in the dense urban area.

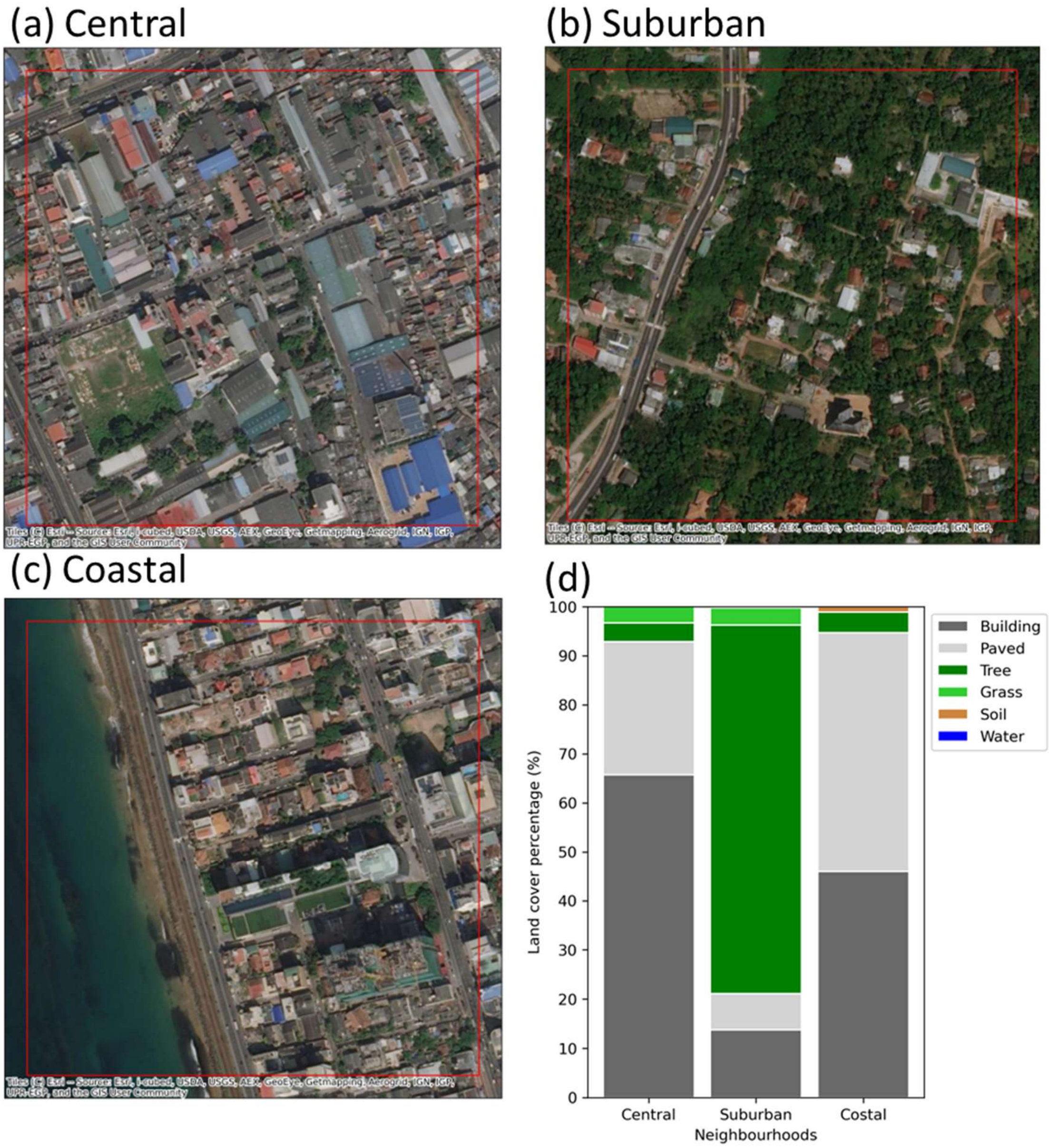

Fig. 6.14. Details of (a-c) three neighbourhoods (red box 500 m x 500 m) and (d) land cover. Note for the coastal land cover the ocean is excluded. Source: Imagery July 2020 (Esri, 2022).

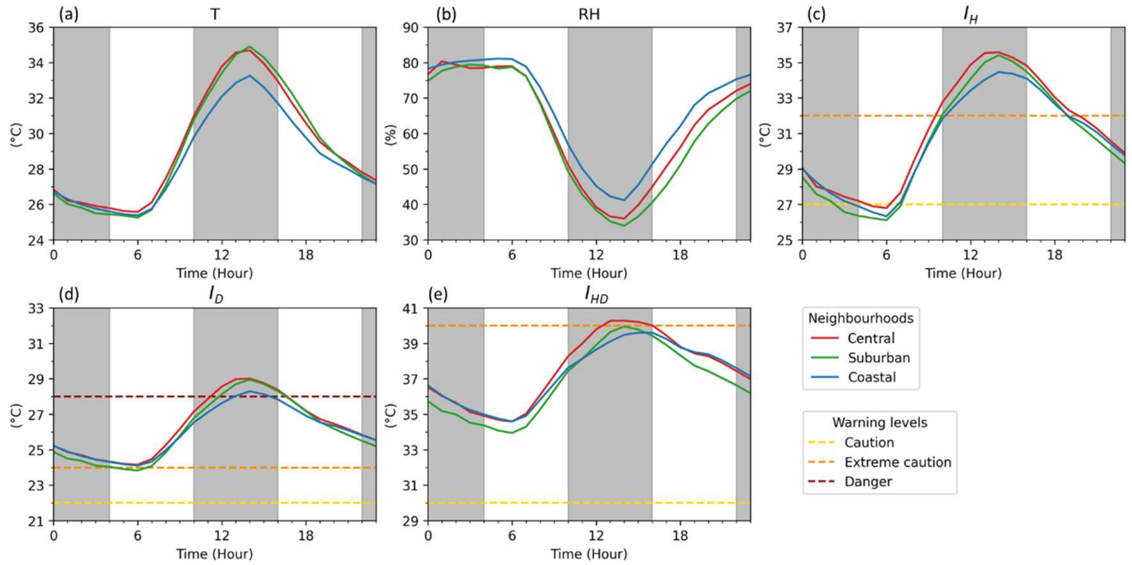

Fig. 6.15. Three neighbourhoods 6 days heatwave (23 to 28 February 2020) average hourly (a) 2 m air temperature (b) 2 m relative humidity, (c - e) Heat Index, Discomfort Index and Humidex at 2 m.

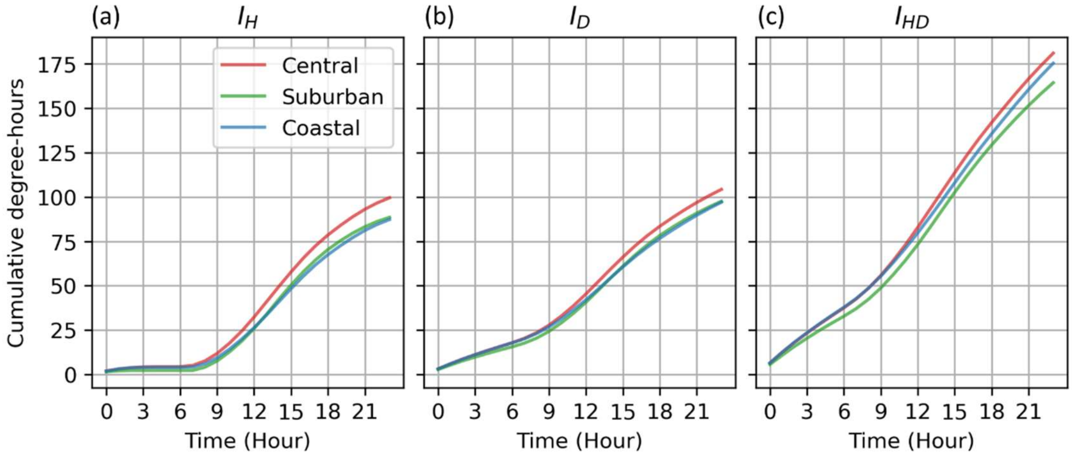

Fig. 6.16. Three neighbourhoods (Fig. 6.14) 6 days heatwave (23 to 28 February 2020) cumulative degree-hours exceeding minimum thresholds (see Table 6.1) for (a) Heat Index, (b) Discomfort Index and (c) Humidex at 2 m.

6.3.5. Future scenarios and mitigation

Beyond current conditions, it is important to prepare for future conditions such as expected urban development by 2035 (section 6.2.3). Heat stress indices are expected to increase (cf. 2020 under heat wave conditions) by up to around 0.8 °C (Fig. 6.17) with median increases in 0.14 °C (I_H) to 0.07 °C (I_D) in the CMC area (Fig. 6.18). These increases will lead to larger percentage of population in the study area exposed to higher heat stress. For I_H - caution, 5% more are exposed (i.e. to 97 %) at 7:00, and I_H-extreme caution increases from 70 % to 97 % at 19:00. Similarly, I_{HD} - extreme caution increases from 10 % to 45 % at 14:00.

To help reduce these effects by increasing the albedo of built-up surfaces (including all building and paved areas) can reduce the net all-wave radiation and air temperature. Compared to the 2035 base case, increasing albedo will reduce the median of the heat stress indices by 0.03 °C (ID) to 0.06 °C (I_H). At midday when the shortwave radiation is the largest, the air temperature can be reduced by up to 0.23 °C, and heat stress indices median reduced by 0.15 °C (ID) to 0.26 °C (I_H). These are consistent with Geletič et al.'s (2020) increase of built-up surface albedo (+0.25) in Prague and Brno reducing daily mean air temperature by 0.2 °C. In this study, the increases in albedo will reduce the heat stress exposure risks especially during the daytime, resulting in the population in extreme caution decrease from 45 % to 25 % with I_{HD} at 14:00 (Fig. 6.19).

Increasing tree cover by 25 % (at the expense of paved areas) increases the median of the heat stress indices by 0.006 °C (ID) to 0.03 °C (I_{HD}). Indices with temperature-humidity indices, are impacted by evapotranspiration from adding trees as the dry-bulb temperature is lowered (median: ≤0.05 °C) but the relative humidity increases (median: ≤ 0.5 %). This is consistent with Kalkstein et al.'s (2022) air temperature 0.4 °C reduction but dewpoint temperature increase ~3.2 °C (≈ 5 % RH) at midday during a Los Angeles heatwave assuming a 150% increase in tree cover (replaced land cover type is not given). As Los Angeles has a hot-dry climate, I_H is less sensitive to humidity. As expected, trees are not a sensible mitigation approach in hot-humid climates. However, it trees provide micro-scale shade (McPherson et al., 1997; Simath and Emmanuel, 2022; Tan et al., 2016), which is not captured in this neighbourhood (or local-scale) study. Radiative modelling at the pedestrian scale level can provide heat stress indices such as mean radiant temperature (Thorsson et al., 2007) and the Universal Thermal Climate Index (UTCI) (Blazejczyk et al., 2012).

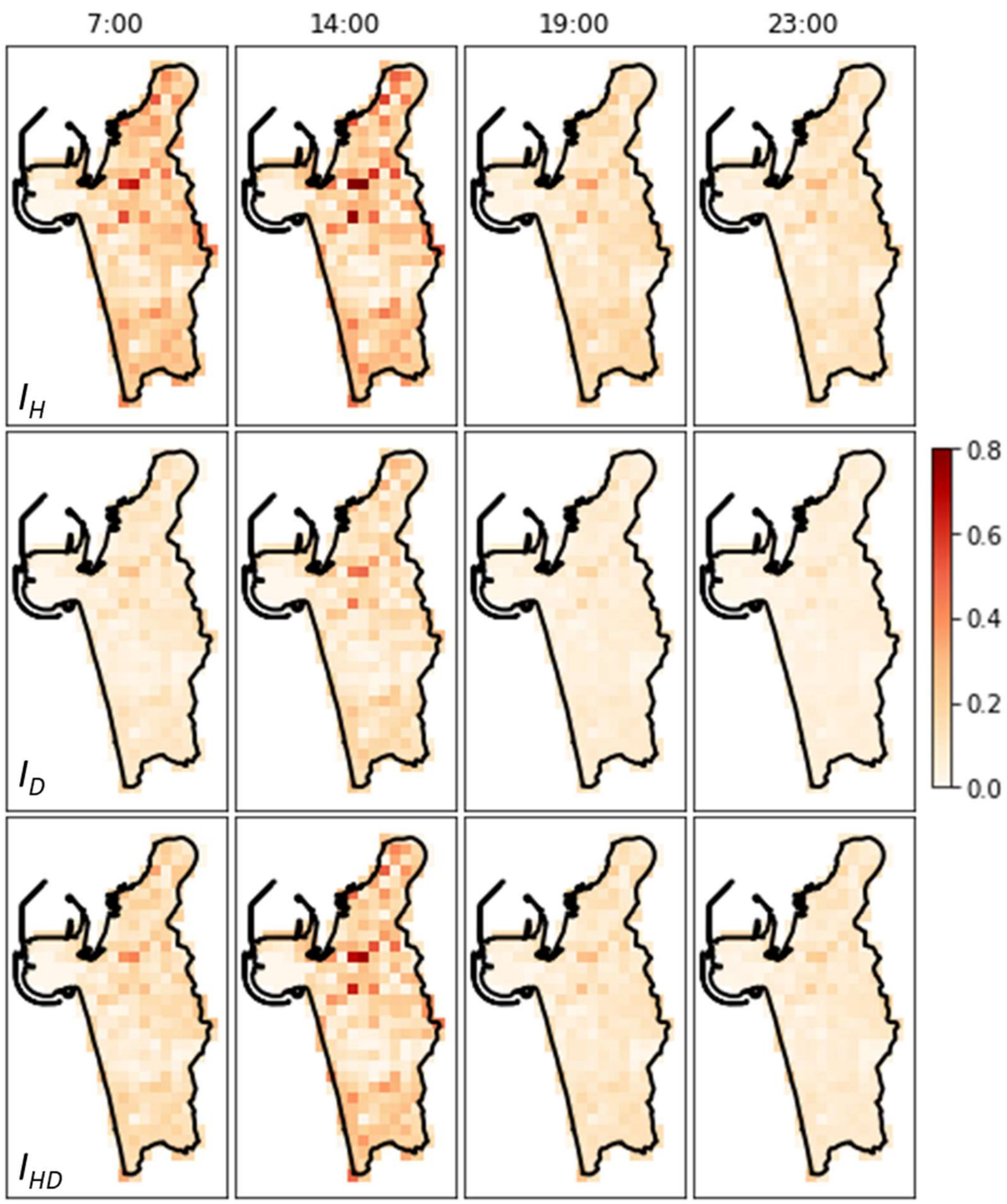

Fig. 6.17. As Fig. 6.9, but increases in heat stress indices in 2035 CMC development scenario (Fig. 6.5) compared to 2020 scenario.

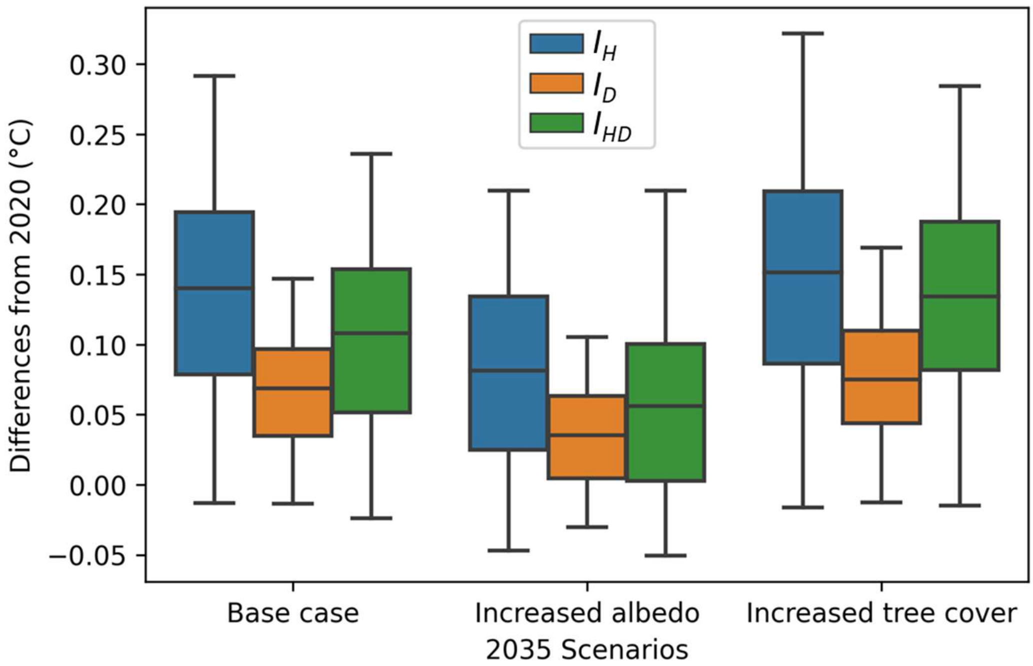

Fig. 6.18. Variability of heat stress indices differences (averaged during the 23 to 28 February 2020 heatwave period across the 291 grids) between 2035 development scenarios compared to 2020 (current) scenario with interquartile range (box), median (horizontal line) and 5th and 95th percentiles (whiskers).

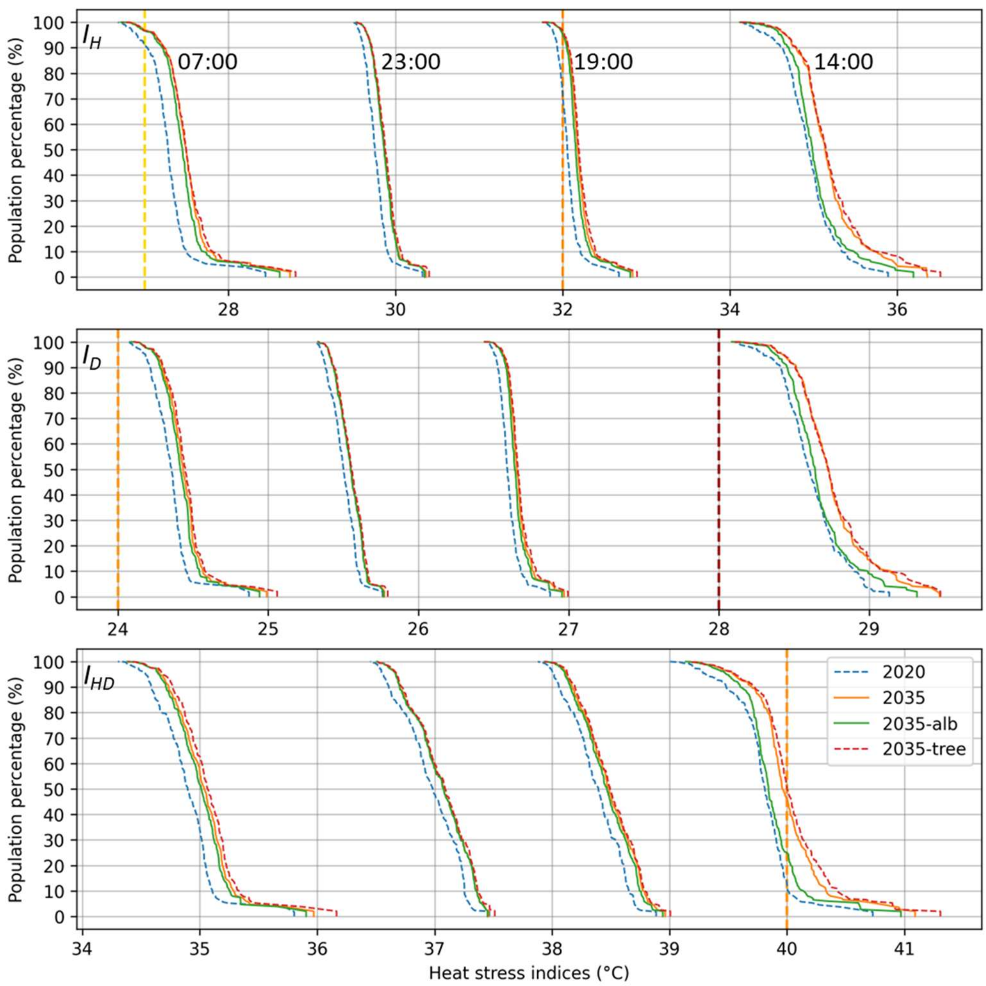

Fig. 6.19. As Fig. 6.12, but for CMC in three future scenarios. 2035: 2035 base scenario, 2035-alb: increased albedo scenario, 2035-tree: increased tree cover scenario (Table 6.2).

6.4. Discussion

Global warming combined with the UHI make urban dwellers likely to be at higher risk of heat exposure especially during extreme heat events. Understanding the intra-city spatial and temporal variation of population heat exposure can help with creating more targeted community level warnings and action plans. However, currently these are very limited in the global South tropical cities (e.g., Colombo, Sri Lanka and neighbouring in South Asia) where data and resource are scarce. In this study we use SUEWS to model the local-scale climates in Colombo to analyse outdoor population-based heat exposure risks. SUEWS requires easy-to-obtain input data and has relatively low computational cost, making it widely usable for different locations and scenarios (actual or planned) or coupled with models at different scales.

Our findings extend the current understanding of heat exposure patterns in tropical cities, and highlight the importance of including the influence of humidity in heat stress assessments for the hot-humid climate. The spatial and temporal dynamics of heat stress indices and population help to identify hotspots that require special attention during extreme heat events. It can also be combined with the individual's daily locations for personalised assessments. For example, a person working in a neighbourhood that is hot by day and cool by night and living in a neighbourhood that is warm by night will experience higher risks than those who stay in the same neighbourhood for the whole day. Analyses of future urban development scenarios can support long-term urban planning. Widely proposed mitigation approaches such as increasing albedo is found to help reduce the heat stress risks, but increasing tree covers is not ideal at the neighbourhood scale but may have net benefit at the micro-scale from shading effect. This could be further studied through more detailed simulations of canopy layer radiation in the future (Stretton et al., 2022). Climate change may increase heat exposure risks results reported in this work. Analysing the effectiveness of different mitigation measures can help reduce costs.

The three heat stress indices have different spatial distribution and threshold definitions, with the Discomfort Index (I_D) being less sensitive to high humidity but narrower thresholds. The Humidex is more sensitive to humidity even at lower air temperatures and has a large range between caution and extreme caution thresholds. Without local health data, we cannot determine which index is superior, but using a climate- and purpose-suitable heat stress index is critical (Brake and Bates, 2002; Cheng et al., 2019; Di Napoli et al., 2019; Schwingshackl et al., 2021). The temperature-humidity indices used are easy to use but, unlike UTCI and WBGT, which use more meteorological variables (i.e., wind speed and radiation) that act synergistically (Katavoutas and Founda, 2019). This could be also achieved through improved radiation modelling as mentioned above and could be done with SUEWS modelling in future works.

6.5. Conclusions

Using SUEWS, the local-scale temporal and spatial patterns of heat exposure of the population during a heatwave period in Colombo, Sri Lanka, are explored using three heat stress indices: Heat Index (I_H), Discomfort Index (I_D) and Humidex (I_{HD}). The largest spatial difference is found at 14:00 (local time) varying between 1.2 °C(I_H) and 0.8 °C (I_D), at night (23:00) the spatial range is 1.2 °C (I_{HD}) when the relative humidity is high. Although differences occur between indices threshold, during most of the heat wave period the study region is above the lowest heat stress warning. I_D classifies 98 % of the population to be exposed to "danger" level at midday (cf. up to the lower "extreme caution" for the other indices). Hotspots are evident in areas of large population, notably in the Colombo Municipal Council and surrounding coastal urban areas. Some inland areas can be overheated during the day but overall cooler at night.

Simulating the Colombo Municipal Council in 2035 development scenario, evidence of increases in heat stress indices (≤ 0.8 °C) suggest an additional 35 % of population will experience higher risks at midday with the higher I_{HD} index. Increasing the built-up (building and paved) surface albedo can reduce this 2035 risk by 15% (i.e. only 15 % net population exposed). Increasing tree cover by 25 % increases humidity and therefore heat stress risk so is inappropriate in a hot-humid climates. Note microscale shading effects from trees are not considered but would need to be balanced between scales as the humidity effect would remain.

This highly resolved tempo-spatial heat stress mapping of a South Asian tropical cities can provide guidance for urban planners, policy makers as well as individuals to deal with extreme climate conditions. The experience can be used by other cities with similar climates and development status. Future work could include: using more detailed population data to understand the heat exposure of specific vulnerable groups; use of SUEWS coupled to meso-scale weather model (e.g. WRF) to give feedbacks allow better forecasts and early warnings, and EnergyPlus for indoor heat exposure assessment.

Chapter 7 Indoor overheating risks of residential buildings in different neighbourhoods in Colombo, Sri Lanka

Building on the previous chapter's use of SUEWS to evaluate outdoor heat exposure in Colombo, this chapter extends the analysis by using the improved SUEWS-EnergyPlus method to assess indoor overheating risks in a typical Colombo urban dwelling during a heatwave period. The study considers various neighbourhood-scale climates and occupancy profiles, and evaluates passive cooling interventions under different conditions. The aim is to highlight the importance of considering local-scale climate and in building energy simulation for mitigating indoor overheating risks.

The chapter is presented in the form of a paper, with me as the primary author responsible for conducting the research, drafting the paper, and creating the figures. My co-authors, Z. Luo and S. Grimmond, provided guidance on structuring the paper, interpreting the results, and editing the text.

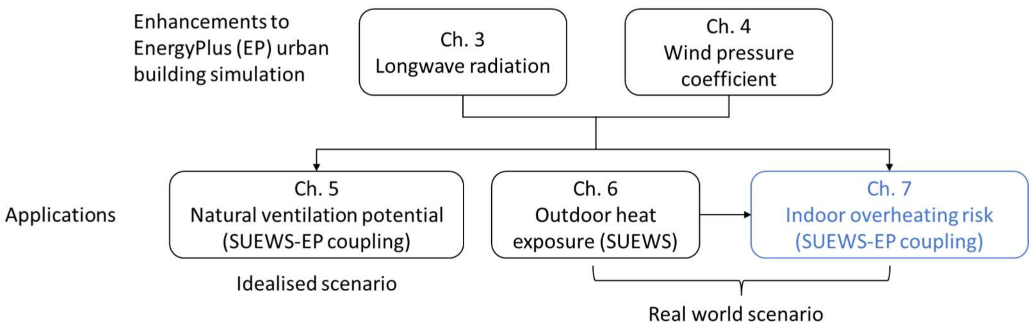

7.1. Introduction

The average temperature increase in South Asian countries is projected to exceed 2 °C by 2050 compared to 2000 (Ahmed and Suphachalasai, 2014), which will increase the risk of heat exposure. In Sri Lanka, air-conditioners are popular in purpose-built apartments (90% AC ownership in 2018), but rare in houses (5% AC ownership for single-storey houses and 10% for multi-storey houses) that account for 85% of the total dwellings (Sri Lanka Ministry of Environment, 2019). Measurements and surveys indicate that Sri Lankan buildings without air-conditioners can have high indoor overheating risks. For example, air temperatures in office buildings in Colombo were measured up to 42 °C on a typical hot sunny day in 2017 (Rajapaksha, 2020). This suggests that most households in Sri Lanka need to rely on passive cooling measures to protect themselves from overheating risks.

Colombo (6°54'N, 79°52'E) is the commercial capital and most populated city of Sri Lanka (Department of Census & Statistics, 2012). It is located in a tropical rainforest (*Af*) Köppen climate (Beck et al., 2018) or an ASHRAE extremely hot-humid (0A) climate (ANSI/ASHRAE, 2019), with high air temperature and humidity throughout the year and little seasonal variation (Emmanuel and Johansson, 2006). Dwellings in these areas are at higher risk of indoor overheating due to the canopy layer urban heat island (Hwang et al., 2020). Therefore, improving the indoor thermal environment of naturally ventilated dwellings in urban areas requires consideration of the urban setting.

Indoor overheating risks for naturally ventilated dwellings in different tropical regions have been extensively studied (Gamero-Salinas et al., 2021; Kubota et al., 2009; Tong et al., 2019; Zune et al., 2021). However, research on indoor overheating and passive cooling strategies for Sri Lankan dwellings considering the urban neighbourhood microclimate is limited. A TRNSYS modelling study of a typical Colombo dwelling room found the roof insulation, overhang and enhanced natural ventilation could help to reduce the indoor air temperatures (Ratnaweera and Hestnes, 1996), but without considering the outdoor microclimate. The modelled impact of a courtyard on a dwelling's natural ventilation suggests that with a warmer air temperature in the courtyard than outside, airflow through the building from outside to the courtyard could provide better cooling than airflow in the opposite direction (Rajapaksha et al., 2003). To extend the current understanding of Sri Lankan indoor overheating risks, we assess the indoor overheating risks of a single-family archetype dwelling in two Colombo neighbourhoods (central and suburban) by combining the urban land surface model SUEWS and the building energy simulation tool EnergyPlus. Our objectives are to: (1) assess overheating risks in a typical Colombo urban dwelling during a heatwave period, considering different neighbourhood-scale climates and occupancy profiles; (2) compare and evaluate passive cooling interventions for these dwellings in different conditions.

7.2. Methods

To assess the indoor overheating risks and mitigation approaches in different Colombo neighbourhoods, an archetype dwelling is simulated in different neighbourhood settings by combining the local-scale land surface model Surface Urban Energy and Water Balance Scheme (SUEWS) v2021a/SuPy 2022.8.5 (Järvi et al., 2011; Sun et al., 2020; Sun and Grimmond, 2019; Tang et al., 2021; Ward et al., 2016) and the building energy simulation tool EnergyPlus v9.4 (U.S. Department of Energy, 2020a).

7.2.1. Urban climate modelling

SUEWS is used to simulate the city of Colombo and surrounding regions (Fig. 7.1a) with a spatial resolution of 500 m during a heatwave period (23 to 28 February 2020) (Chapter 6). Two neighbourhoods with a midday air temperature above the 75th percentile during the heatwave period for the entire study area are chosen for indoor overheating simulations. The 'central' neighbourhood has a building percentage of 64% and an average building height of 6.46 m. The 'suburban' neighbourhood has a building fraction of 13% and an average building height of 6.28 m (refer to Section 6.3.4). Section 6.2.1 presents the SUEWS model setup and evaluation.

The SUEWS roughness sublayer module (SUEWS-RSL) generates air temperature, relative humidity, and wind speed vertical profiles, which are then provided to EnergyPlus. The SUEWS-EnergyPlus simulation workflow is described in detail in Section 5.2. The 2 m air temperature (T_2) and relative humidity (RH_2) and the 10 m wind speed (U_{10}) are provided to EnergyPlus via the weather input (.epw) file. The SUEWS-RSL vertical wind profile is incorporated into EnergyPlus via input files (.idf) by substituting the power law coefficients with values derived from the SUEWS-RSL data. The EnergyPlus wind profile equation, as defined by ASHRAE (2005), is used in this process:

$$U_z = U_{10}\left(\frac{\delta_{ref}}{10}\right)^{\alpha_{ref}}\left(\frac{z}{\delta}\right)^{\alpha} \qquad (7.1)$$

where the meteorological station boundary layer depth (δ_{ref}) and exponent (α_{ref}) are the EnergyPlus default for open terrain (U.S. Department of Energy, 2020b). To obtain the equivalent site values (δ, α) for the central and suburban neighbourhoods, the SUEWS-RSL wind profile results are fitted to Eq. 7.1. Here the fitted values for the central neighbourhood values are α = 0.43 and δ = 100.3 m, while for the suburban neighbourhood they are 0.30, and 64.3 m, respectively (Fig. 7.2b).

During the heatwave period of 23 to 28 February 2020, the median diurnal cycle of T_2 was modelled for the central and suburban neighbourhoods. The results indicate that the suburban neighbourhood was 0.4 °C warmer during midday and 0.6 °C cooler at night compared to the central neighbourhood, which demonstrates the influence of both neighbourhood- and regional-scale climates. More information about this can be found in Section 6.2.1.3.

Wind pressure coefficients (C_p) from the Tokyo Polytechnic University database (TPU, 2007) are used to simulate natural ventilation with EnergyPlus-AFN. The TPU database provides data for buildings in neighbourhoods with different plan area fractions (λ_P). To ensure consistency with the TPU database, λ_P values of 0.6 (central) and 0.1 (suburban) are used in EnergyPlus simulations (Fig. 7.3). The simulation accounts for the differences in view factors (Chapter 3) and wind pressure coefficients for the building facets (Chapter 4, Appendix 11).

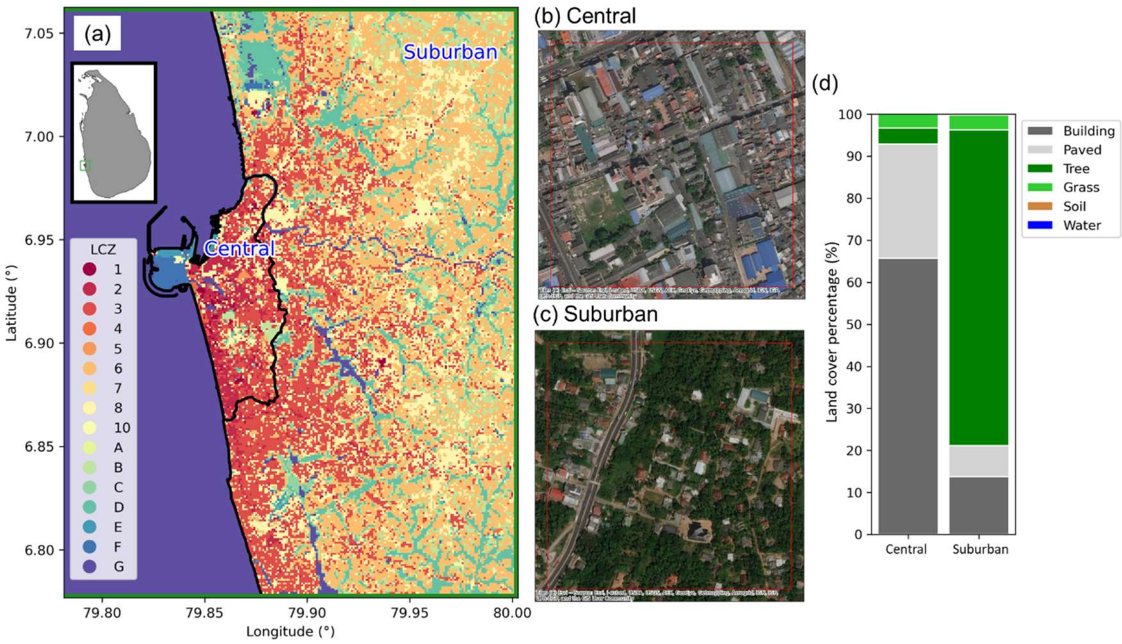

Fig. 7.1. Colombo region (a) locations of the two neighbourhoods (blue) on local climate zone map (Table 2 of Stewart and Oke (2012)) (data source: Perera and Emmanuel (2018). (b, c) aerial view July 2020 of the two neighbourhoods (red box) (sources: Esri (2022), and (d) land cover percentages (see section 6.3.4).

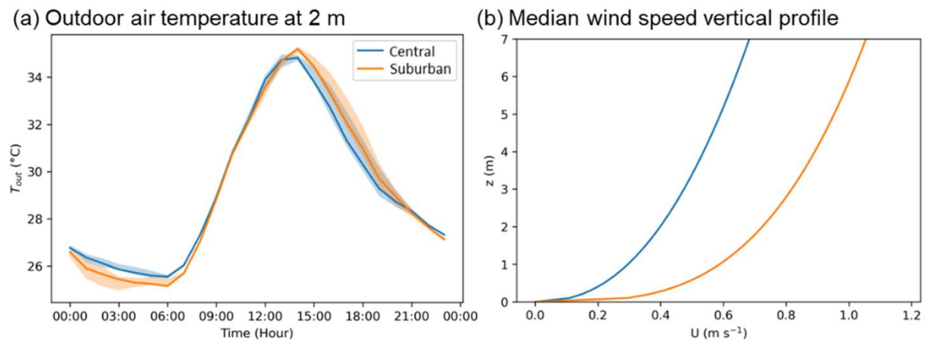

Fig. 7.2. Heatwave period (23 to 26 February 2020) condition for two neighbourhoods (Fig. 7.1) (a) hourly median (lines) and inter-quartile range (shading) T_2, and (b) median vertical wind profiles using coefficients derived from the SUEWS-RSL layer (building height= 6 m).

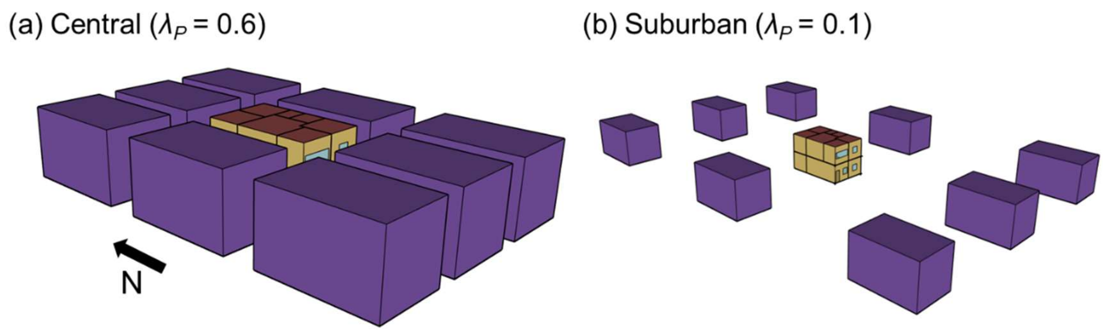

Fig. 7.3. Building archetype simulated (EnergyPlus) using (SUEWS) weather data for two neighbourhoods: (a) central (plan area fraction λ_P = 0.6) and (b) suburban (λ_P = 0.1).

7.2.2. Dwelling archetype simulation

The typical Sri Lankan dwelling is a single-family detached house (Department of Census & Statistics, 2012), which we simulate in this study (Fig. 7.4) with building geometry adapted from Halwatura and Jayasinghe (2007). The house has three bedrooms, which is the most common configuration in Sri Lankan households (about 30%) (Department of Census & Statistics, 2012). The building materials are based on the Census of Population and Housing 2012 (Department of Census & Statistics, 2012), which indicates that brick walls (53.1%), cement floors (72.5%), and asbestos roofs (64.6%) are the most prevalent in Colombo. We obtained detailed information on the construction and thermal characteristics of the building envelope (Table 7.1) from various sources (ASHRAE, 2005; Emmanuel, 2004; Ratnaweera and Hestnes, 1996; Sri Lanka Sustainable Energy Authority, 2021).

Two occupancy patterns are considered in this study: (1) a family with two working adults and two children, and (2) an elderly couple. The family leaves the house at 7:00 on weekdays for work or school and returns at 17:00, based on a survey by Pathirana and

Halwatura (2020). During weekends, the family stays at home for the entire day. The elderly couple is assumed to be at home all the time. As no detailed room-wise occupancy data is available, schedules and heat gains are assumed based on previous studies (Mavrogianni et al., 2014; Porritt et al., 2012) and presented in Appendix 10. Internal heat gains from lighting and equipment are assumed to be 5 W m^{-2} (Pathirana et al., 2019) and 4 W m^{-2} (Liu et al., 2017), respectively..

Surveys report that 85 % of households in Sri Lanka tend to close windows at night (Halwatura and Jayasinghe, 2007), which is traditional and practised for security reasons (Ratnaweera and Hestnes, 1996). However, there is no detailed information on window opening during the daytime. In Hyderabad, India, a survey during the monsoon season in 2008 showed that more than 50% of households closed windows during the daytime when the outdoor air temperature was high (Indraganti, 2010). Therefore, it is assumed that windows are closed during the daytime when no one is home. The effective openable area of all windows is assumed to be 25%, in accordance with local regulations (Urban Development Authority of Sri Lanka, 2020), while all doors except bedroom and bathroom doors remain open. Natural ventilation is simulated using the AirflowNetwork (AFN) module of EnergyPlus. For this archetype with brick walls, an infiltration rate of 1 ACH is assumed, based on previous studies (Bandara et al., 2011; Ratnaweera and Hestnes, 1996).

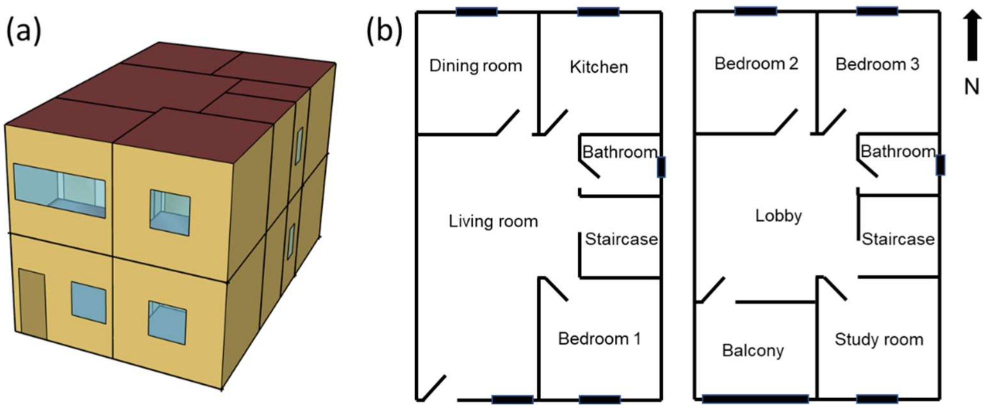

Fig. 7.4. (a) Dwelling archetype and (b) layouts of ground (left) and first (right) floor.

Table 7.1: Building envelope construction material and U-values. Data are from various sources (ASHRAE, 2005; Emmanuel, 2004; Ratnaweera and Hestnes, 1996; Rawat and Singh, 2022; Sri Lanka Sustainable Energy Authority, 2021). SHGC: solar heat gain coefficient. U-value: overall heat transfer coefficient.

	Construction (inside to outside)	U-value ($W\ m^{-2}\ K^{-1}$)
External wall	12.5 mm plasterboard, 200 mm brick (albedo = 0.3, emissivity = 0.9)	3.29
Internal wall	12.5 mm plasterboard, 100 mm brick, 12.5 mm plasterboard	3.69
Roof	20 mm ceiling tile, air gap, 6 mm dark coloured asbestos-cement sheet (albedo = 0.2, emissivity = 0.9)	1.91
First floor	40 mm cement screed, 100 mm concrete, air gap, 20 mm ceiling tile	1.31
Ground floor	40 mm cement screed, 200 mm concrete	4.67
Windows	Double glazing with 6 mm clear glass and 12 mm air gap (timber frame). SHGC = 0.73	2.95
Doors (external)	25 mm insulation board with metal surface cover	1.20
Doors (internal)	25 mm wood	6.00

7.2.3. Indoor overheating metrics

Currently there is no consensus definition for indoor overheating. International standards state the risk of indoor overheating can be assessed either with adaptive thermal comfort models (ANSI/ASHRAE, 2013a; CIBSE, 2013) or heat stress indices (ISO, 2017, 2004).

Adaptive thermal comfort equations provide indoor comfort temperatures derived based on field surveys of thermal comfort and measurements of indoor and outdoor temperatures (Nicol et al., 2012). The overheating thresholds for adaptive equations are usually determined based on 80% occupant acceptability (ANSI/ASHRAE, 2013a; CIBSE, 2013). However, such thresholds are for thermal comfort, not heat-related health.

Heat stress indices can be categorised into empirical and analytical indices. Empirical indices (e.g. wet bulb globe temperature (WBGT) (ISO, 2017)) are developed based on experiments, while analytical indices (e.g. predicted heat strain (PHS) (ISO, 2004)) are derived from thermal balance equations of the human body.

As the adaptive thermal comfort is the most used approach for indoor overheating assessment in international standards (ANSI/ASHRAE, 2013a; CIBSE, 2013; MoHURD, 2012), in this study we consider the adaptive thermal comfort equation for the local climate to assess the risk of indoor overheating. Since there are no adaptive thermal comfort equations specific to Sri Lanka, we will refer to studies in southern India, which has a similar hot-humid climate and is geographically close. The adaptive thermal comfort equation developed by Indraganti et al. (2013) is based on field studies in naturally ventilated buildings in Chennai and Hyderabad (in southern India):

$$T_{comf} = 0.26T_{rm} + 21.4 \qquad (7.2)$$

where the running mean outdoor temperature T_{rm} is (Nicol and Humphreys, 2010):

$$T_{rm} = (1 - k)(T_{od-1} + kT_{od-2} + k^2T_{od-3} \cdots + k^6T_{od-7}) \qquad (7.3)$$

where k is a constant between 0 and 1, with 0.8 used as recommended (Nicol and Humphreys, 2010), T_{od-n} is the daily mean outdoor temperature n days ago (°C).

The overheating threshold of adaptive thermal comfort equations is usually based on the percentage who indicate "satisfactory". For example, the UK standard (CIBSE, 2013) defines the overheating threshold as the indoor operative temperature at which 80% of occupants feel comfortable, and the Chinese standard defines it as 75% satisfaction (MoHURD, 2012). For Eq. 7.2, Indraganti et al. (2013) reported that 70% satisfaction was found at 2 °C higher than T_{comf}. Therefore, we take T_{comf} + 2 °C as the overheating threshold (T_{max}):

$$T_{max} = 0.26T_{rm} + 23.4 \qquad (7.4)$$

7.2.4. Interventions for passive cooling

Passive cooling approaches for buildings can be classified into two categories: solar and heat protection, such as shading and reflective coating, and heat dissipation techniques, such as heat sinks and natural ventilation (Santamouris et al., 2007; Santamouris and Kolokotsa, 2013). However, some of these methods may not be practical due to cost or the hot-humid climate in Colombo (Bhamare et al., 2019). In this study, we focus on practical approaches that are relatively easy to apply in Colombo dwellings, including solar control, natural ventilation, and insulation (Ratnaweera and Hestnes, 1996).

Solar radiation is high in low-latitude regions, making solar control measures important. External and internal shading, such as overhangs, external shutters, internal blinds, and curtains, and reflective building envelope, such as solar reflective paint on roofs and walls and solar control glazing, are common solar control measures (Porritt et al., 2012). Overhangs above windows, which are common in Sri Lanka, have been shown to reduce peak indoor air temperature by 0.6 °C on a typical hot day (Ratnaweera and Hestnes, 1996). Cool roofs are more effective in tropical climates than in other climates in reducing the indoor cooling energy demand due to the high solar angles (Rawat and Singh, 2022). White paint on roofs and walls with an albedo of 0.74 has been simulated to reduce peak indoor air temperature by 2.4 ℃ on a typical sunny day in Singapore (Zingre et al., 2015). In Mumbai, solar control glazing with a reflective coating is estimated to reduce indoor thermal comfort, measured as 'predicted percentage dissatisfied' (PPD), by 47% compared to clear double-glazing windows (Singh et al. (2008). In this study, we simulate three solar control measures: overhang, white paint on roofs and walls, and solar control glazing with low solar heat gain coefficients (SHGC).

Night ventilation is a widely recommended passive cooling strategy for buildings in hot-humid climates (Doctor-Pingel et al., 2019; Gamero-Salinas et al., 2021; Jamaludin et al., 2014; Kubota et al., 2009; Ran and Tang, 2018; Zune et al., 2021). However, in hot climates with high daytime outdoor air temperature, closing windows during the day may improve indoor thermal comfort. For example, Ratnaweera and Hestnes (1996) suggest that closing windows during the daytime could reduce the maximum air temperature by 1.7 ℃ on a typical hot day in Sri Lanka.

Insulation is not typically considered a passive cooling solution (Santamouris and Kolokotsa, 2013), but it can help reduce indoor overheating risk under certain conditions. Insulation can be applied to the roof and/or external walls to prevent heat transfer between indoor and outdoor spaces. Good thermal resistance of building envelopes can help save energy by reducing heat loss in winter and heat gain in summer for air-conditioned buildings. However, the impact of insulation on free-running buildings can be bi-directional and influenced by other factors, since it may prevent heat from releasing to the outdoor environment as well. For instance, Chvatal and Corvacho (2009) estimated that reducing the external wall U-value from 0.91 to 0.2 W m-2 K in Évora (Portugal) would increase the indoor overheating hours in summer if the window solar heat gain coefficient (SHGC) is larger than 0.32, but decrease if SHGC < 0.32. Updated local building codes in different U.S. cities suggest that higher insulation and air tightness levels can exacerbate indoor heat stress for buildings in relatively cooler cities like Boise during summer power outages but mitigate heat stress in very hot climates like Phoenix (Baniassadi et al., 2018). Fosas et al. (2018) and Makantasi and Mavrogianni (2016) highlight the importance of adequate ventilation in preventing increased overheating risks resulting from adding insulation. Porritt et al. (2012) compared the effects of internal and external insulation of walls during a nine-day heatwave in London and found that internal insulation could increase overheating degree-hours by 14%, while external insulation could decrease it by 49%. Therefore, the effect of insulation is linked to several factors such as climate, solar control, ventilation, and thermal mass. Insulation can be more effective in hot climates as it prevents inward heat conduction through the building envelope, but precautions should be taken to minimize heat gain by the indoor space, such as solar heat gain through windows. In tropical climates, it is suggested that less wall insulation should be applied to reduce cooling energy use (Zune et al., 2021). However, Ratnaweera and Hestnes (1996) found that adding 100 mm thick polystyrene to the asbestos roof of a Colombo dwelling reduced the maximum air temperature by 0.2 °C on a typical day in December, as it prevented heat transfer from the roof to the interior. Therefore, in this study, we only consider roof insulation as a potential passive cooling measure.

In summary, we assess passive cooling interventions (Table 7.2) in two different neighbourhoods. This includes both accepted and debatable options for hot-humid climates.

Table 7.2: Passive cooling interventions simulated using the materials and thermal characteristics based on various sources (Halwatura and Jayasinghe, 2008; Porritt et al., 2012; Singh et al., 2008).

Intervention	*Description*
Overhang	Overhang above windows – 1 m deep
White paint	White colour paint on roof and walls (albedo = 0.74)
Solar control (SC) glazing	Solar-control glazing with reflective film coated (SHGC = 0.1, U-value = 1.95)
Night ventilation	Windows opened at night (21:00 to 5:00)
Roof insulation	Roof insulation – 100 mm expanded polystyrene

7.3. Results

7.3.1. Indoor overheating risks of the base cases in different neighbourhoods

We focus on the overheating risk analysis in different conditions, in the two rooms occupied for the longest duration during the day (living room) and night (bedroom). As bedroom 2 on the first floor with a west-facing wall is found to be warmest among the three bedrooms in the archetype building (Fig. 7.4), we select this bedroom for analysis.

During a heatwave period, diurnal changes of indoor operative temperatures (average of air and mean radiant temperatures) in the two rooms with the working family occupancy profile show that the suburban building is warmer than the central building during the day (Fig. 7.5). This is because the outdoor air temperatures are warmer during daytime (Fig. 7.2) and there is less solar shading from surrounding buildings (Fig. 7.3). The maximum Top in the living room occurs at 17:00 when occupants just return home (except Sunday 23 Feb), with peak values of 33.2 °C (central building) and 34.1 °C (suburban building). The unoccupied upper floor bedroom reaches even hotter temperatures, with peak values of 38.7 °C and 39.3 °C in the central and suburban buildings, respectively.

When occupied, the upstairs bedroom's Top increases by up to 0.4 °C from 21:00 due to heat release from the brick walls and concrete floor, even with windows closed (Fig. 7.5). This thermal mass-related temperature increase is even more significant in the ground floor living room, with values of up to 0.8 °C in the central neighbourhood building and 1.1 °C in the suburban neighbourhood building.

Diurnal changes of T_{op} are similar with an elderly occupancy profile, but there are some differences (Fig. 7.6). The peak living room T_{op} is slightly cooler with windows opened during the daytime occupancy (central = 33.1 °C and suburban = 33.9 °C). However, natural ventilation through the south-facing window of the living room is not effective in cooling the indoor space during high outdoor air temperatures. The elderly occupants are at a higher risk of overheating due to longer occupied periods. Although the peak bedroom T_{op} is reduced to 38.1 °C (central) and 38.7 °C (suburban) with daytime natural ventilation, the maximum T_{op} during bedroom occupancy is still high at 35.1 °C (central) and 35.4 °C (suburban). This suggests that the elderly occupants experience a cooler indoor environment compared to a working family occupancy, but still face the risk of overheating.

During the heatwave period, both occupied rooms exceed the adaptive thermal comfort (T_{max}) overheating thresholds for most of the time. The suburban building has 5.0% more degree-hours exceeding T_{max} during occupied periods compared to the central building, mainly due to larger daytime heat gains under the family occupancy profile. The suburban living room has 62.5% more degree-hours exceeding T_{max}, while the bedroom has 6.3% less. Under the elderly occupancy profile, the central and suburban buildings have 11.9% and 16.2% more total overheating degree-hours, respectively, compared to the family occupancy. This is mainly due to the longer occupied period of the living room and the insufficient cooling provided by natural ventilation during the daytime. These findings suggest that elderly occupants are at higher risk of overheating, particularly during the daytime.

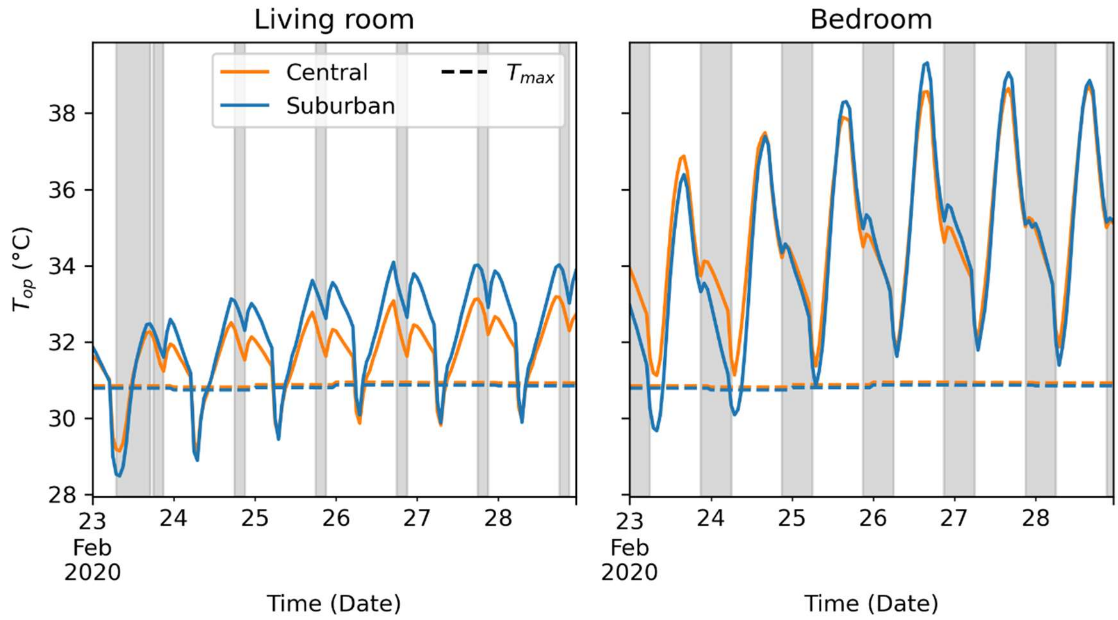

Fig. 7.5. Indoor operative temperature (T_{op}) during a heatwave in two neighbourhoods (Fig. 7.1) when occupied (grey) by the working family schedule in the (a) living room and (b) bedroom (Fig. 7.4).

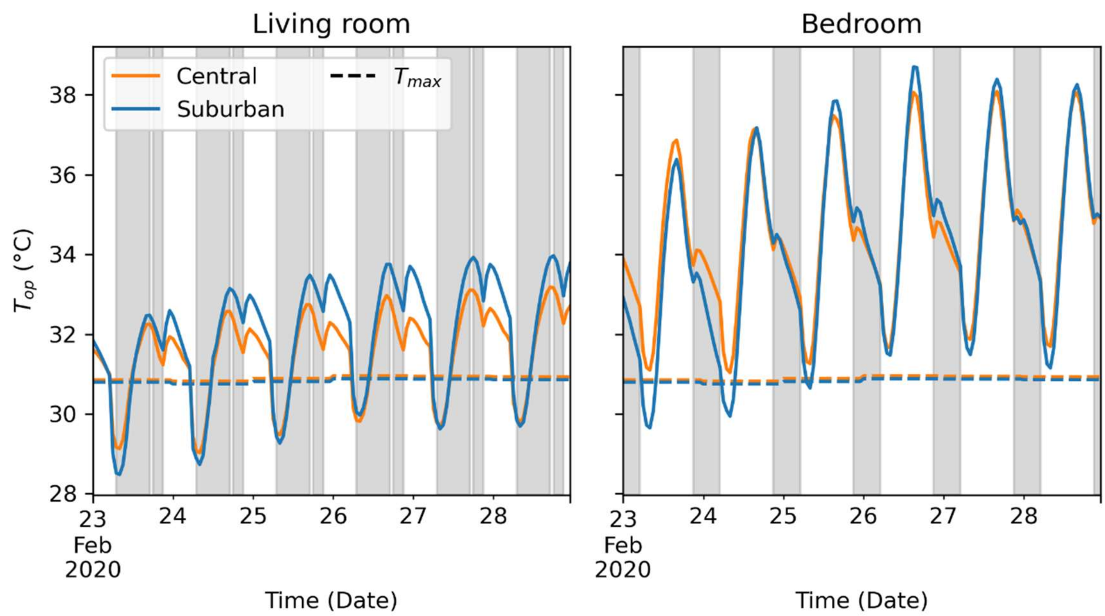

Fig. 7.6. As Fig. 7.5, but elderly occupancy.

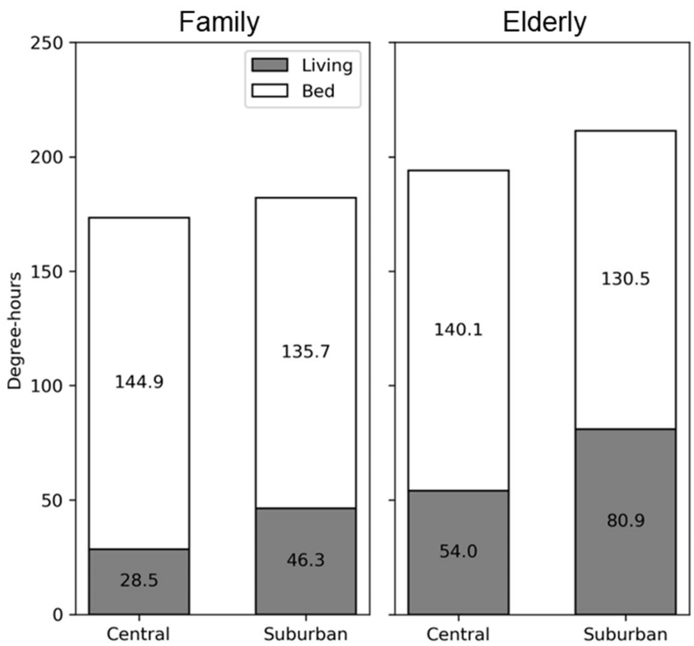

Fig. 7.7. Degree-hours above the adaptive thermal comfort threshold (T_{max}) in different rooms and neighbourhoods for buildings with (a) working family and (b) elderly occupancy profiles.

7.3.2. Effects of interventions: Bedroom

The study models the impacts of interventions (listed in Table 7.2) on overheating degree-hours for both neighbourhoods and two occupancy profiles. The suburban neighbourhood receives more solar radiation, which results in larger passive cooling effects from solar control-related interventions. Among all the interventions, the application of reflective white paint on walls and roofs causes the greatest reduction in both Top and indoor overheating degree-hours in all conditions (as seen in Table 7.3, Fig. 7.9, and 7.10). As heat transfer through the roof is the primary source of overheating in the bedroom, this intervention reduces overheating degree-hours by 89-92% in the suburban neighbourhood and 71-74% in the central neighbourhood, compared to the base case (Table 7.3). The reduction in overheating degree-hours is more significant for the family occupancy, as there is no daytime natural ventilation, and peak Top drops during occupied periods from 21:00 to 5:00, by 2.7 °C (central) and 3.5 °C (suburban). However, modifications related to north-facing bedroom windows are less effective. The replacement of solar control glazing from SGHC 0.73 to 0.1 reduces overheating degree-hours by approximately 10% in the suburban neighbourhood and less than 3% in the central neighbourhood (Table 7.3). The overhang intervention only reduces overheating degree-hours in the bedroom by around 1% as it only blocks diffuse solar radiation, which is not a major heat gain source.

Night ventilation is more effective when outdoor wind speeds are stronger and there is less surrounding building sheltering, as shown in Fig. 7.2. The suburban bedroom experiences a mean nocturnal ventilation rate of 3.8 ACH, while the central bedroom is 2.9 ACH. During the occupied period, both the maximum and average T_{op} are reduced more in the suburban building (0.6 °C, 1.1 °C, respectively) than for the central building (0.5 °C, 1.0 °C, respectively). Night ventilation is the second most effective intervention, reducing bedroom overheating degree-hours for the family profile by up to 39%. However, for the other occupancy profile which already has open windows during other periods, the effect of night ventilation on overheating is slightly smaller.

Roof insulation has limited impact on reducing overheating for the family profile and even has a negative effect for the elderly profile. While roof insulation can reduce the daytime peak T_{op} by up to 3.3 °C by preventing heat conduction into the indoor space, it can trap heat inside the room at night when windows are closed, leading to an increase in T_{op} (Fosas et al., 2018). This is evident in the higher T_{op} observed between 21:00 to 23:00 and the slower decrease after 23:00 until morning, indicating that roof insulation alone is not an effective solution for night-time passive cooling if there is no other means to release heat to the outside except by conduction through the building envelope.

In summary, the most effective intervention to reduce the risk of sleeping overheating is the application of white paint, followed by night ventilation. Interventions related to solar control for windows, such as the use of an overhang and glazing with lower SGHC, are more effective during the daytime but have a reduced effect at night. However, roof insulation should be used with caution as it can trap heat when windows are closed.

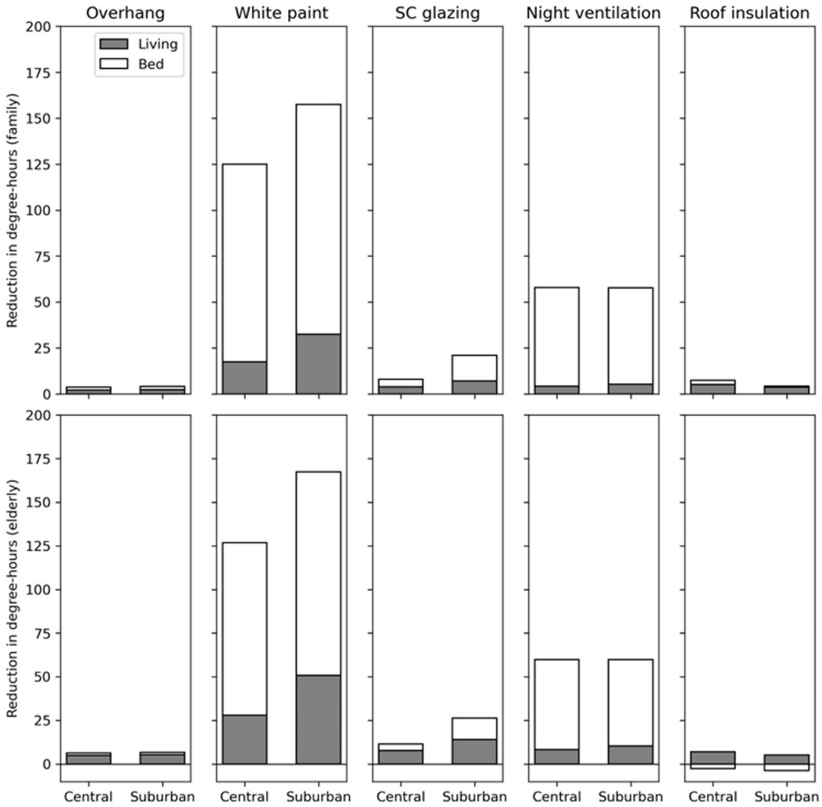

Fig. 7.8. Impact of five interventions in reducing degree-hours above the adaptive thermal comfort threshold (T_{max}) for two rooms in building in two neighbourhoods with (a-e) working family and (f-j) elderly occupancy profiles.

Table 7.3: Degree-hours reduction of interventions (percentage reduction compared to the base case in parentheses) in different conditions.

Intervention	Bedroom				Living room			
	Family		Elderly		Family		Elderly	
	Central	Suburban	Central	Suburban	Central	Suburban	Central	Suburban
Overhang	1.5 (1.0%)	1.8 (1.3%)	1.2 (0.9%)	1.5 (1.1%)	2.2 (7.7%)	2.3 (5.0%)	5.0 (9.3%)	5.3 (6.6%)
White paint	107.5 (74.2%)	125.1 (92.2%)	98.9 (70.5%)	116.6 (89.4%)	17.5 (61.4%)	32.4 (70.0%)	28.0 (51.9%)	50.8 (62.8%)
SC glazing	4.1 (2.8%)	14.0 (10.3%)	3.7 (2.6%)	12.1 (9.3%)	3.9 (13.7%)	7.0 (15.1%)	7.7 (14.3%)	14.1 (17.4%)
Night ventilation	53.8 (37.1%)	52.4 (38.6%)	51.6 (36.8%)	49.7 (38.1%)	4.2 (14.7%)	5.2 (11.2%)	8.3 (15.4%)	10.3 (12.7%)
Roof insulation	2.4 (1.7%)	0.7 (0.5%)	-2.7 (-1.9%)	-3.7 (-2.8%)	5.0 (17.5%)	3.6 (7.8%)	7.1 (13.1%)	5.1 (6.3%)

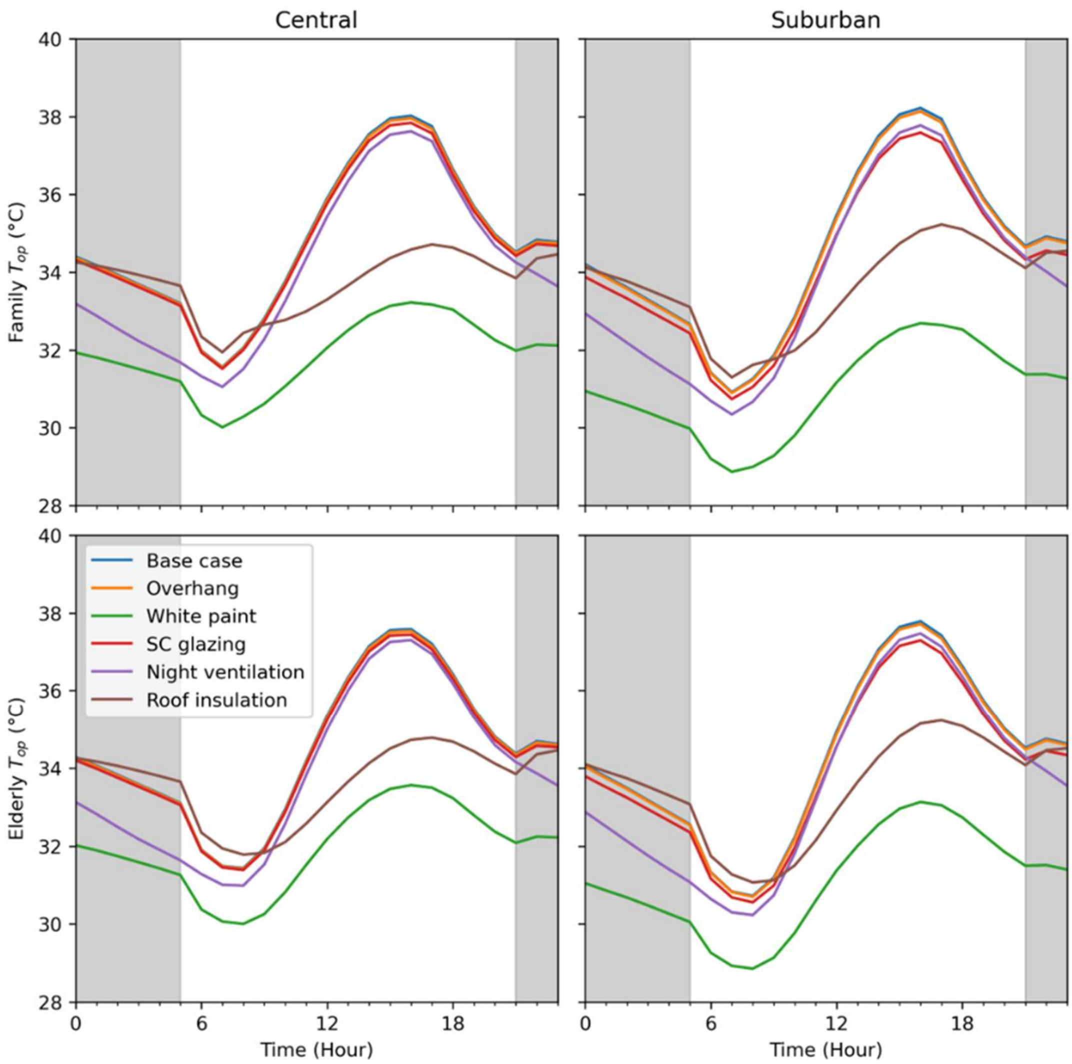

Fig. 7.9. Mean hourly T_{op} during the heatwave period (23 to 28 February 2020) for five interventions (Table 7.2) and the based case for the (a,c) central and (b,d) suburban neighbourhood located buildings with (a,b) family (c,d) elderly occupancy profiles with occupied periods (shading).

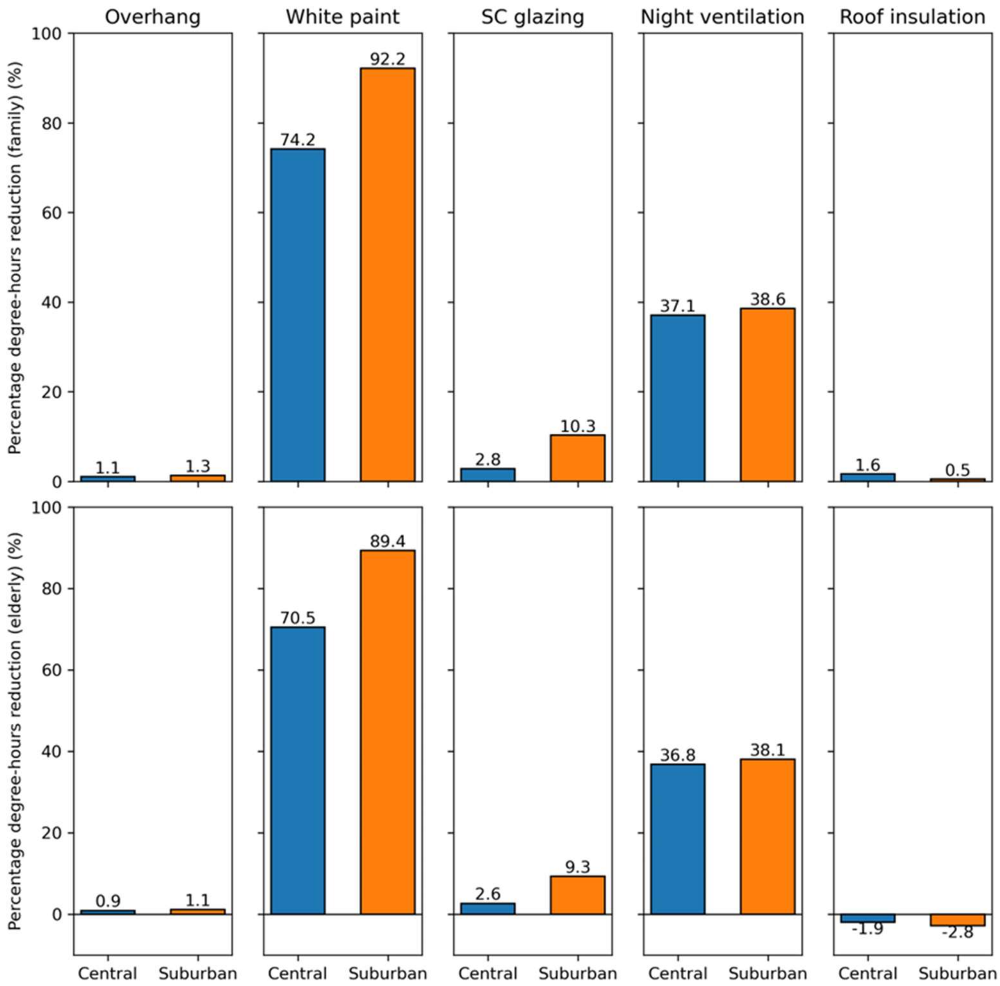

Fig. 7.10. Percentage reduction in overheating degree-hours exceeding the adaptive thermal comfort threshold (T_{max}) during occupied periods with different interventions.

7.3.3. Effects of interventions: Living room

As the occupied periods of living rooms are predominately in the evening (family) or daytime (elderly), the impacts of interventions on overheating are slightly differently from the bedroom (section 7.3.2).

The ground floor living room receives less solar radiation than the first-floor bedroom, resulting in smaller reductions in overheating degree-hours. However, the albedo change (or white paint) remains the most effective intervention, reducing Top during occupied periods by up to 1.3 °C in the suburban neighbourhood. The overhang and solar control glazing have larger effects compared to the bedroom facing north, especially with a south-facing window in the living room. For elderly occupants, the overhang reduces the living room Top by up to 0.2 °C in the afternoon. Although the numbers of overheating degree-hours reduction are higher for the suburban neighbourhood (Table 7.3), the percentage reduction is smaller than that of the central neighbourhood (Fig. 7.12). Solar control glazing reduces Top during occupied periods by up to 0.4 °C for the suburban neighbourhood with elderly occupants. The percentage reduction in overheating degree-hours by solar control glazing at the central neighbourhood is similar to that of night ventilation. In contrast, at the suburban neighbourhood, the cooling effect of solar control glazing is greater than that of night ventilation, making it the second most effective intervention for the living room.

Since the effect of night ventilation on the living room is less direct than on the bedroom, the expected reductions in overheating degree-hours are smaller. Specifically, for the elderly profile, a reduction in T_{op} in the morning of 0.4 to 0.5 °C is expected in the central and suburban neighbourhoods, respectively. However, if windows are open during the day, the temperature differences from the base case are smaller, resulting in maximum T_{op} reductions of around 0.2 °C for both neighbourhoods. For the family profile, the average Top reduction during occupied periods is around 0.1 °C.

Since roof insulation does not directly affect the living room envelopes, it has a smaller effect in reducing peak temperatures compared to the bedroom. The effect of roof insulation is more significant in the central neighbourhood compared to the suburban neighbourhood due to the lower daytime heat gain from solar radiation and hot outdoor air, which is consistent with previous studies (Chvatal and Corvacho, 2009). For the elderly profile, roof insulation reduces T_{op} by 0.3 °C at 15:00 for the central neighbourhood and 0.2 °C for the suburban neighbourhood. The reduction in overheating degree-hours in the central neighbourhood ranges from 13.1% to 17.7%, which is about twice the reduction in the suburban neighbourhood.

In summary, solar control interventions are more effective for the living room, especially for the elderly occupancy and the suburban building. Night ventilation can also reduce T_{op}, especially in the morning. While roof insulation can help reduce the peak daytime T_{op}, it is less effective for the suburban building due to the larger heat gain through windows and walls.

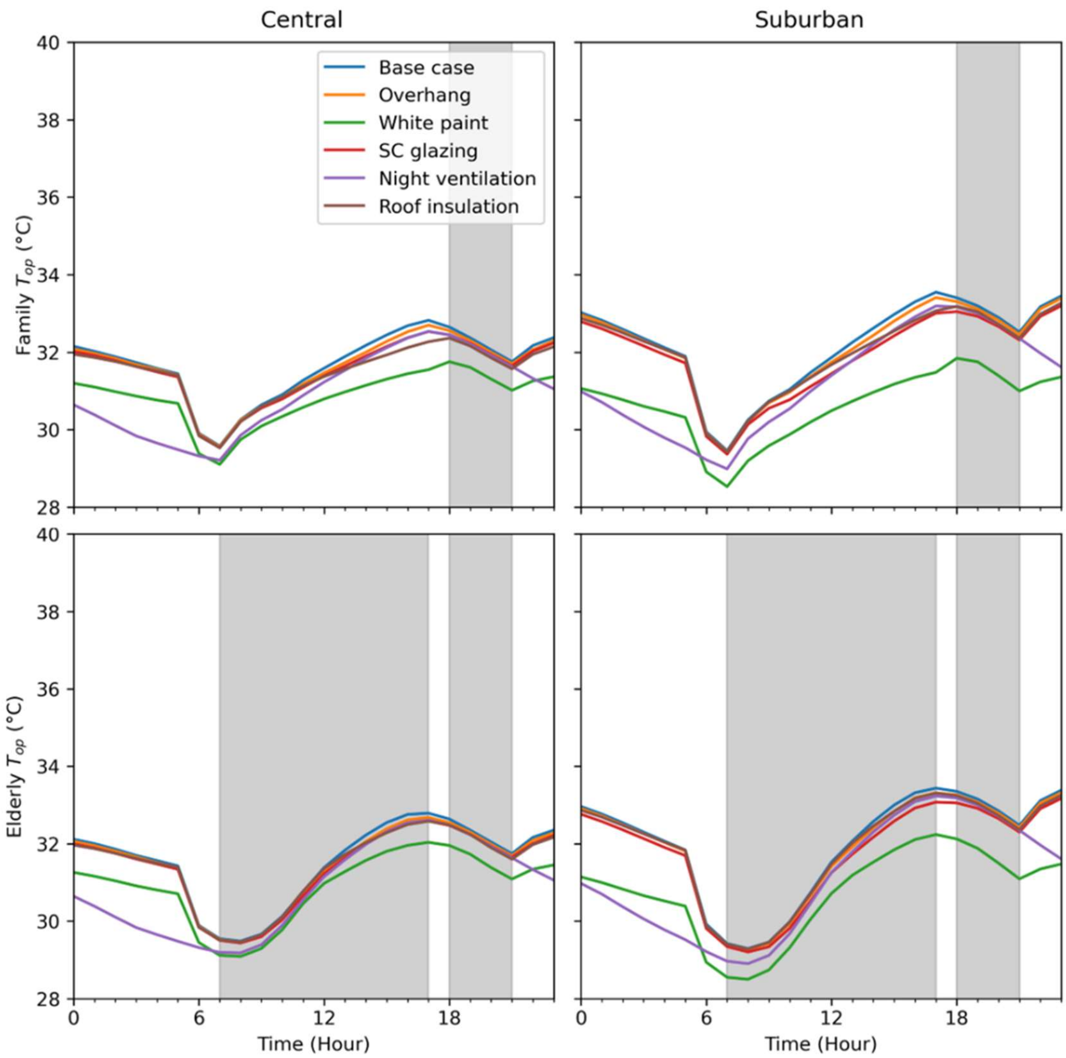

Fig. 7.11. As Fig. 7.9, but for living room.

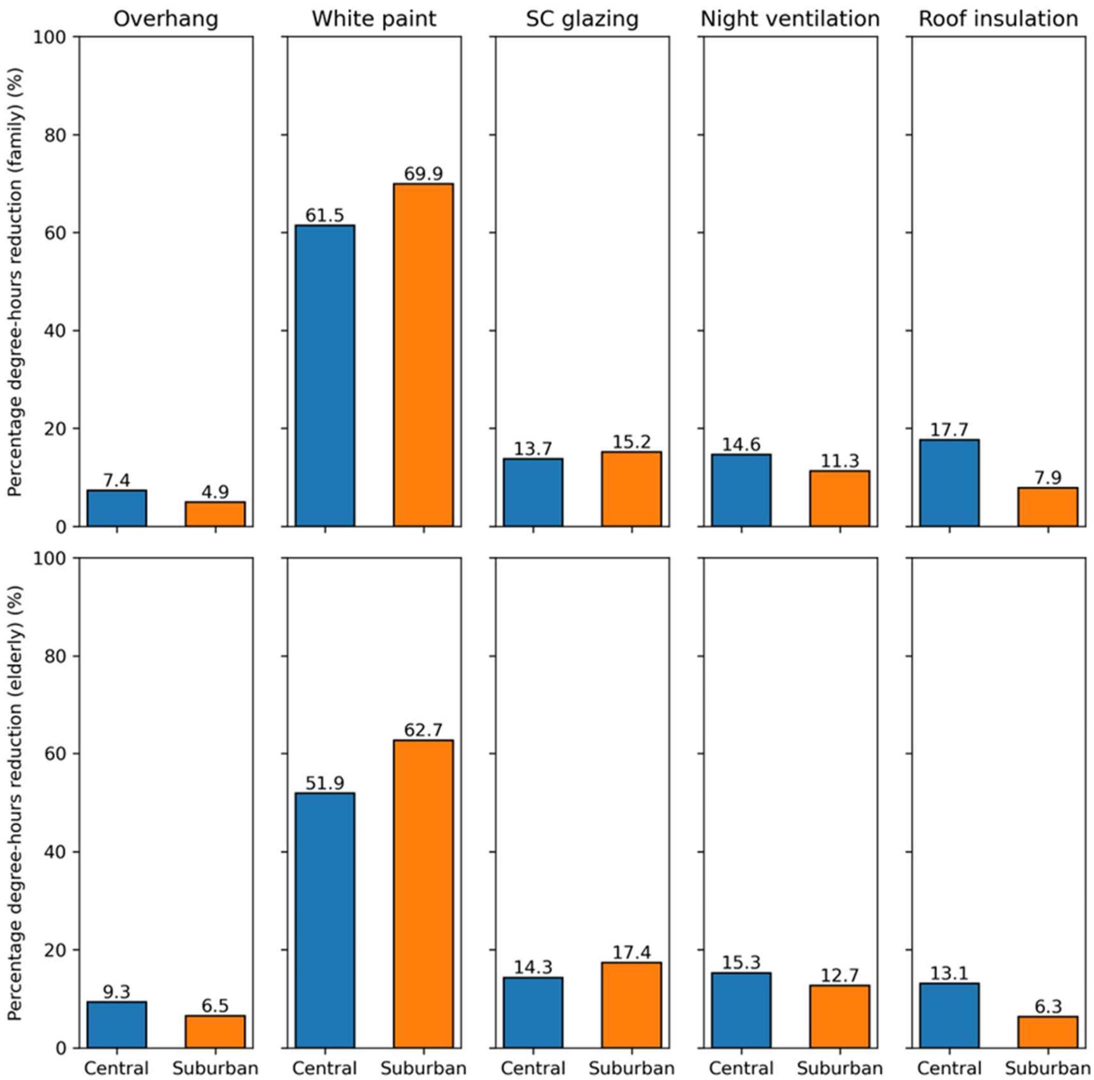

Fig. 7.12. As Fig. 7.10, but for living room.

7.3.4. Combined interventions

To explore the minimization of indoor overheating risk, we consider the optimal combinations of interventions. Combining all interventions results in more effectiveness for the suburban building, as shown in Fig. 7.13. This leads to a reduction of up to 3.8 °C in peak bedroom T_{op} during the occupied period and up to 3.6 °C in mean T_{op} for the working family profile. For the elderly occupancy profile, the peak living Top is reduced by up to 2.0 °C, and for the family profile, the reduction is 2.2 °C. In terms of overheating degree-hours, the bedroom overheating degree-hours are reduced by up to 97.5 % for the suburban building (Fig. 7.15, 7.16). Due to the warmer outdoor air temperature, the reduction in overheating degree-hours is up to 76.8% for the central building. The living room overheating degree-hours in all cases are reduced by at least 93.9%, indicating the high effectiveness of the combined measures.

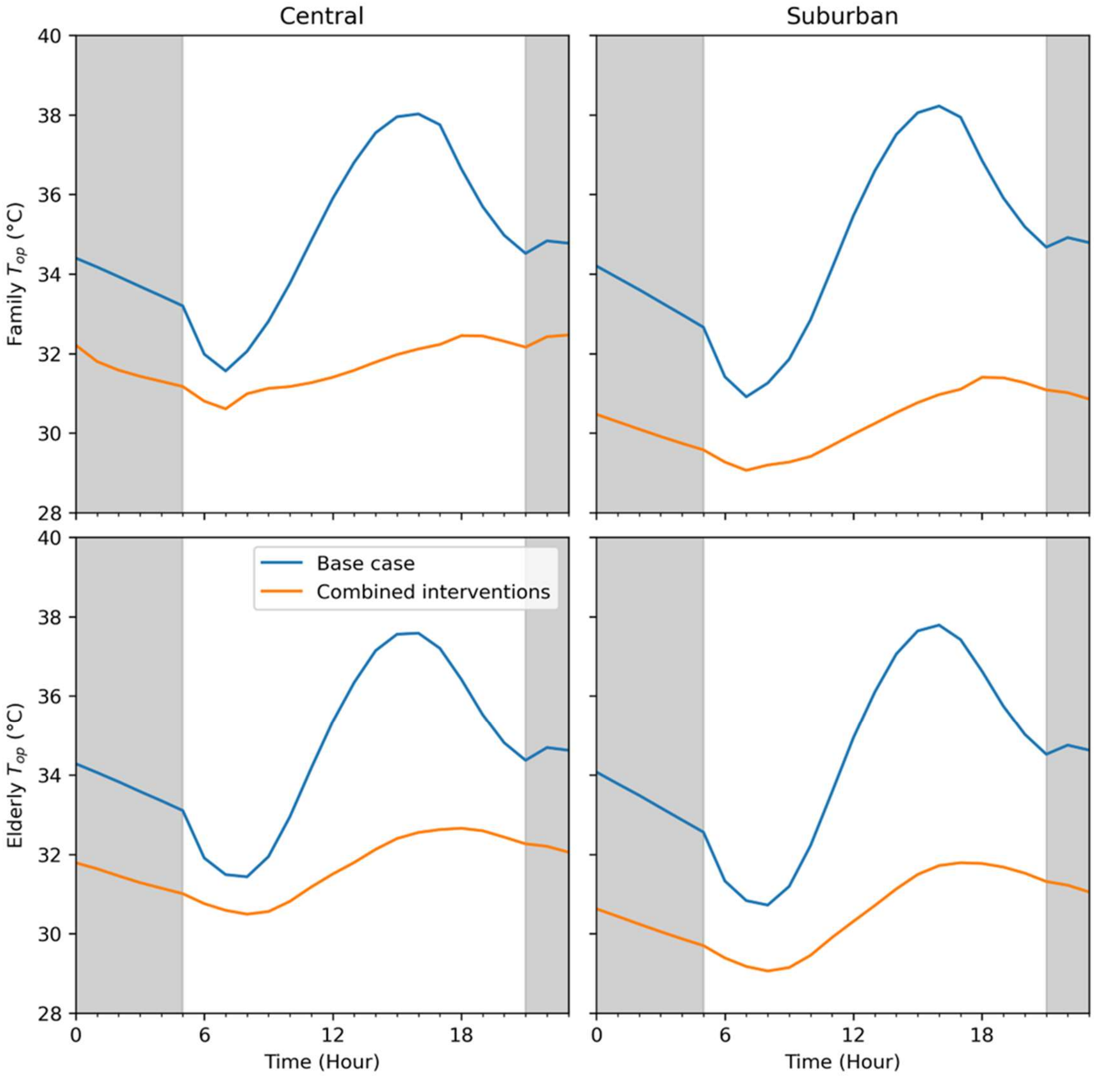

Fig. 7.13. As Fig. 7.9, but for combined interventions.

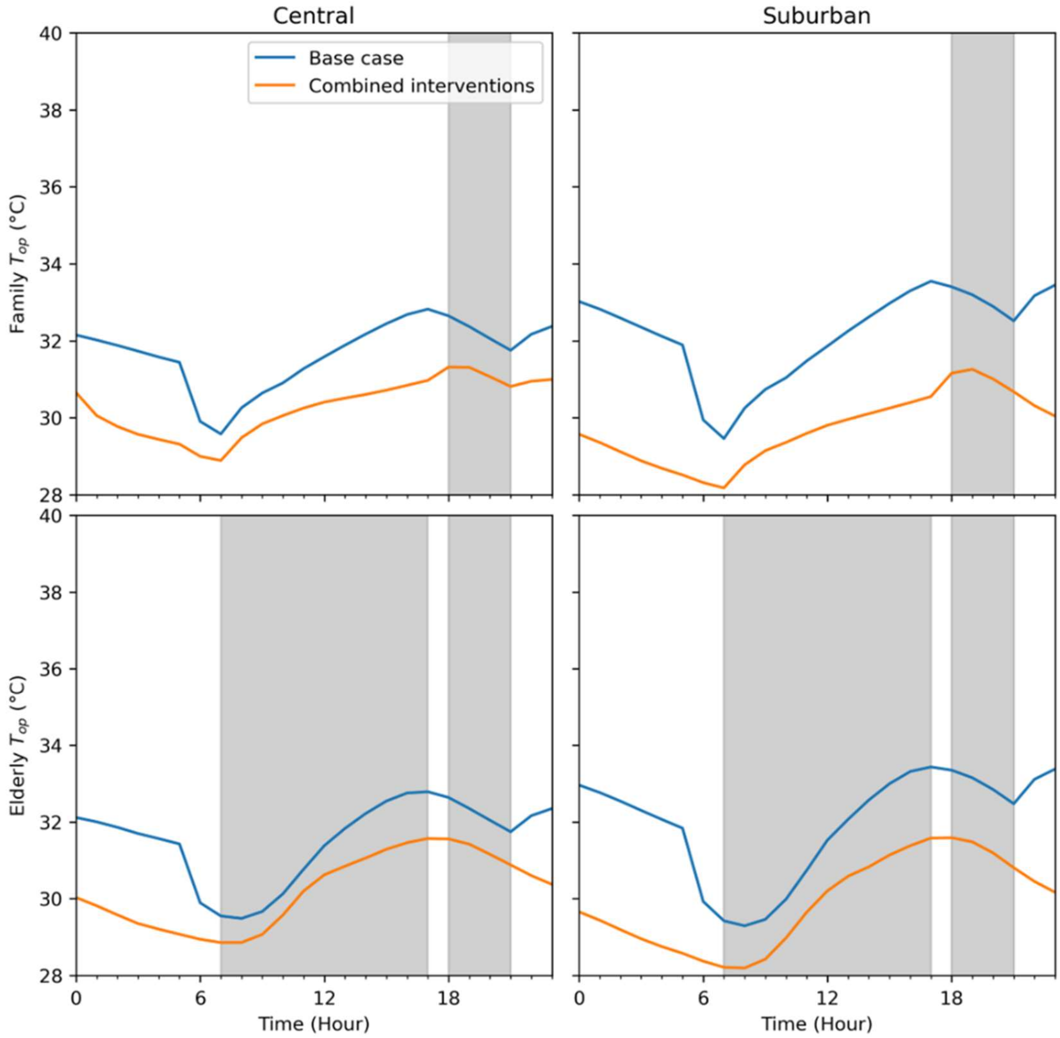

Fig. 7.14. As Fig. 7.11, but for combined interventions.

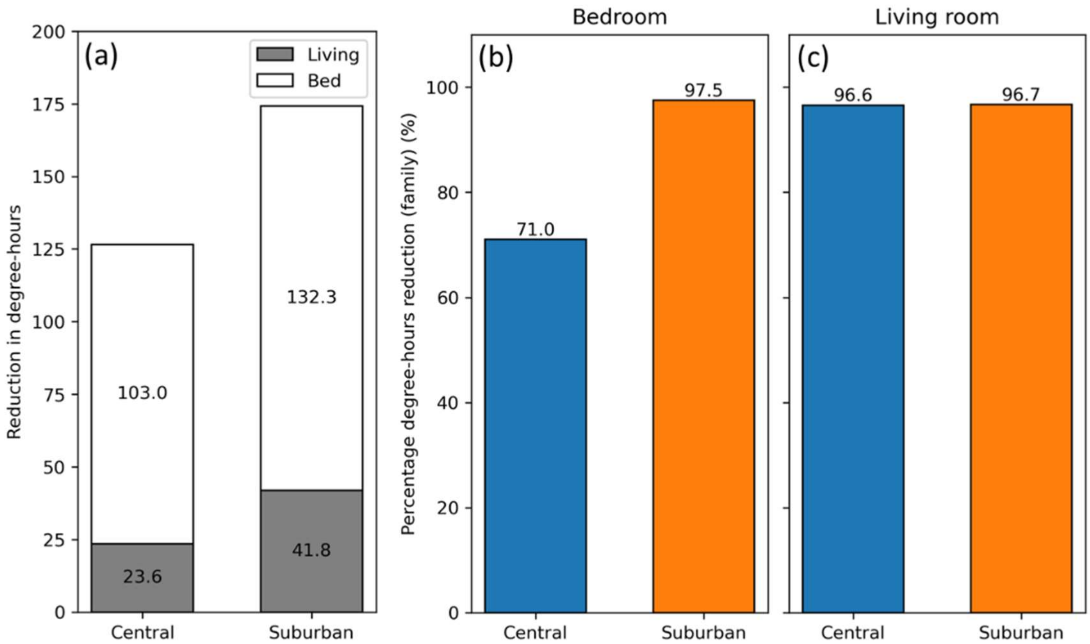

Fig. 7.15. Reduction in (a) overheating degree-hours with combined interventions and (b, c) percentage for the family occupancy profile.

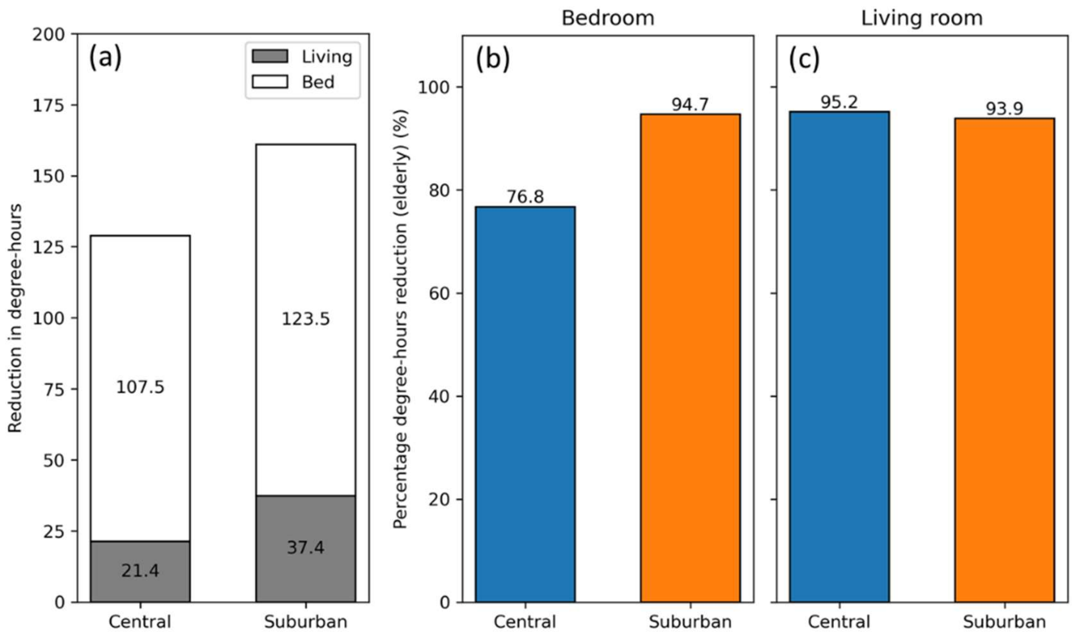

Fig. 7.16. As Fig. 7.15, but for the elderly occupancy profile.

7.4. Discussion

In this study, we used a combination of SUEWS and EnergyPlus to model the indoor overheating risk of a typical Colombo dwelling in two different neighbourhoods. Our results show that the suburban building is more susceptible to indoor overheating due to higher daytime outdoor air temperatures and less solar shading from surrounding buildings. The different neighbourhoods are affected by regional-scale climate patterns, with lower air temperatures in the coastal regions where the city centre is located, and warmer air temperatures in the northeast of the city (Fig. 6.4). Furthermore, local-scale conditions modify the forcing meteorological data, resulting in the suburban neighbourhood being around 1 °C warmer than the central neighbourhood. Despite occasional warmer conditions in the central neighbourhood, the regional forcing data and the suburban neighbourhood tend to be warmer during the daytime. These findings underscore the importance of selecting the appropriate reference rural site when determining urban heat island for a city (Anderson et al., 2018; Hawkins et al., 2004).

This study extends the current understanding of the impact of neighbourhood-scale climates on the effectiveness of passive cooling interventions. Solar radiation related interventions, such as increasing the albedo (e.g. white paint), overhangs, and solar control glazing, are found to be more effective for the suburban building. Additionally, the suburban building benefits more from nocturnal ventilation due to lower outdoor air temperatures and higher wind speeds. Although roof insulation performs well in reducing heat gain from the roof, it can trap heat at night when there are limited ways to release heat, especially for the suburban building with larger daytime solar radiation gains. These findings are consistent with previous studies that suggest the effectiveness of insulation in reducing indoor overheating can depend on other factors related to indoor heat gain and release (Chvatal and Corvacho, 2009; Fosas et al., 2018; Makantasi and Mavrogianni, 2016).

Our assessment of indoor overheating was based on operative temperature, which considers only air temperature and radiation components. However, in hot-humid climates such as Colombo, high humidity can also impact indoor overheating (Budd, 2008). Therefore, incorporating a humidity-related indicator in future studies would provide a more comprehensive assessment of indoor overheating in such climates. Conclusions drawn from interventions depend on the assessment metric used. For example, Kubota et al. (2009) found differences between nocturnal and daytime-only ventilation assessments in terms of daily mean indoor air temperature (1.5 °C higher) and relative humidity (7% lower), which are likely linked to air temperature rather than specific humidity. Furthermore, while we one-way coupled SUEWS-EnergyPlus (i.e., providing outdoor climate data to the building scale), understanding the feedback from buildings to the neighbourhood-scale climate would provide additional insights.

7.5. Conclusion

Sri Lanka residents are likely to have high indoor overheating risk due to the hot-humid climate and low usage of air-conditioning, but understanding of local-scale outdoor climate on indoor overheating risks of Sri Lankan dwellings are limited. Here we use SUEWS combined with EnergyPlus to model the indoor overheating risk of a typical Colombo dwelling in two neighbourhoods with different climates and with two occupancy profiles to assess the effects of common passive cooling measures in different conditions during a heatwave period (23 to 28 February 2020).

The dwelling modelled has high indoor overheating risks throughout the day and night, particularly in the suburban neighbourhood, which experiences higher outdoor air temperatures and less solar shading from surrounding buildings during the daytime. This leads to up to 9% more total overheating degree-hours than in the central neighbourhood. Moreover, occupancy profiles with individuals who stay at home indoors during the daytime (such as the elderly) are at a higher risk of overheating, with up to 16% more overheating degree-hours than in a profile where residents are away during the working week. These findings emphasize the importance of paying attention to vulnerable groups during extreme heat events.

The study finds that among the five interventions considered, reflective white paint is the most effective, reducing indoor overheating degree-hours by up to 92% across all conditions. Interventions on windows, including overhang depth and low SHGC glazing, are also effective during daytime for the living room, with reductions in indoor overheating degree-hours of 9% and 17%, respectively, but are not as effective for the bedroom. Night ventilation is found to be more effective for the bedroom in the suburban neighbourhood, with reductions of up to 39% linked to lower outdoor air temperatures and higher ventilation rates. While roof insulation can reduce the daytime peak temperature of the living room by up to 18%, it can have a negative effect on bedroom overheating due to heat trapping. Combining all interventions can significantly reduce indoor overheating risks by up to 98%.

Our study highlights the importance of considering the neighbourhood-scale climate in indoor overheating analysis. Future research could focus on enhancing the SUEWS-EnergyPlus simulations by exploring the interaction between the building and local climate to achieve two-way coupling.

Chapter 8 Conclusions

Indoor overheating is gaining more attention as climate changes. Exposure to heat can lead to thermal discomfort, heat disorders, reduced productivity and even death in severe cases. Exacerbated by the canopy layer urban heat island, buildings in densely populated urban areas may be in higher risk of overheating. In hot-humid climates such as Sri Lanka, dwellings can have high risks of indoor overheating when there is limited use of air-conditioners.

Although building energy simulation (BES) tools are widely used for predicting and assessing indoor overheating risk, typically an isolated building is modelled without its neighbourhood context. The surrounding buildings can have solar shading effects but will increase the longwave radiation. The reduced wind speed lowers both natural ventilation and heat convection rate. Building materials with large heat storage leads to changes in the diurnal cycle of both indoor and outdoor air temperatures. The impervious surfaces reduce evaporative cooling. Heat emission from human activities will increase the air temperature. Using the BES tool alone cannot take account of all these influences. Previous efforts to combine a BES tool with neighbourhood-scale urban-canopy models do not adequately account for all these neighbourhood factors, notably the modelling of longwave radiation and natural ventilation with urbanised wind speeds are not well addressed. As a result, influences of urban neighbourhood characteristics are also not well understood when using BES tools to assess the risk of indoor overheating.

This thesis uses the urban land surface model, Surface Urban Energy and Water Balance Scheme (SUEWS), and BES tool EnergyPlus to assess the indoor overheating risk of neighbourhood buildings in urban areas. To address the lack of proper longwave radiation simulations in BES, an iterative approach is proposed for EnergyPlus and analysed in different neighbourhood densities and climates. Modifications are done for wind pressure coefficients to improve EnergyPlus's ability in calculating the natural ventilation rate with urbanised wind speeds. The new method is applied in both idealised and real-world case studies. In the idealised case study, the natural ventilation potential of a simplified building is modelled in different neighbourhood densities and climates. In the real-world case study, the spatial and temporal distribution of the population to heat exposure during a heatwave in Colombo, Sri Lanka are accounted for. Analyses are undertaken of the indoor overheating risk for a typical Colombo dwelling in different neighbourhoods.

8.1. Main findings and contributions

Findings of this thesis extend current understanding of influences of urban factors on indoor thermal environment. The methods, datasets, and models created in this thesis can be used in future research. The following sections give detailed findings and contributions in this thesis arising from the four thesis objectives (Section 1.2):

- To improve existing indoor overheating risk assessment by accounting for the urban impacts via combining an urban land surface model [Surface Urban Energy and Water Balance Scheme (SUEWS)] and building energy simulation tool [EnergyPlus]
- To propose a new approach to enhance the inter-building long-wave radiation calculation in EnergyPlus
- To improve the existing approach in EnergyPlus determining wind-driven natural ventilation especially for urban buildings
- To apply the new building-urban climate modelling framework to investigate the impacts of local-scale climate on indoor overheating risks of naturally ventilated dwellings using Colombo, Sri Lanka as a case study

8.1.1. Modelling of inter-building longwave radiation

SUEWS provides data of outdoor air temperatures, relative humidity, wind speeds and their vertical profiles to EnergyPlus. In EnergyPlus, geometry of surrounding buildings can be modelled to consider the solar shading effect on the target building. However, the longwave radiation exchanges between the target building and surrounding buildings are simplified in EnergyPlus by assigning air temperatures to surrounding buildings as surface temperatures, which will cause biases.

This thesis proposes an iterative (or spin-up) approach to calculate the inter-building longwave radiation, which can be used for idealised neighbourhoods that consists of identical buildings. The target building is firstly simulated as isolated, and the building wall surface temperature data are output and assigned to surroundings buildings for the next round of simulation. This process is repeated until convergence is achieved (i.e. differences in wall surface temperatures from the last simulation meets the criteria set).

It is found for simulating buildings in denser neighbourhoods more iterations are needed to achieve convergence. Plan area fraction (λ_P) is used to characterise the neighbourhoods. For a low-density neighbourhood (λ_P =0.1) only one iteration is required, but five iterations are needed at λ_P = 0.6. This approach is evaluated using observations. The results show improvements compared to the default method (assigning air temperatures to surrounding building surfaces).

Simulations are done for three different λ_P and three climates to analyse their impacts on the inter-building longwave radiation. It is found that impacts of inter-building longwave radiation on the indoor overheating risk are larger in the denser neighbourhoods and climates at lower latitudes. At λ_P = 0.6, when comparing the default method to the iterative method, the annual overheating degree hours are underpredicted by up to 25% during the day and 60% at night. The indoor operative temperature is underpredicted by up to 1.4 °C. Clearly these impacts are large and cannot be ignored in the urban settings. The proposed approach is used in Chapters 5 and 7.

8.1.2. Wind pressure coefficients for BES in the urban context

BES tools like EnergyPlus use wind pressure coefficients (C_p) to calculate the wind pressure on building facets and natural ventilation rates. As BES tools are typical developed for isolated buildings, the default C_p data they use are not suitable for buildings in urban neighbourhood settings. Although C_p data of surrounded buildings can be obtained from external databases, there are still problems.

Firstly, from reviewing the literature, it is found most studies use an incorrect combination of wind speeds and C_p data in BES. C_p data are usually derived from wind-tunnel experiments. Given its definition, C_p should have height consistency between the wind-tunnel experiments vertical wind profile and the wind speed height used in the BES calculations. Using C_p data in BES with different heights of wind speed and vertical wind profiles will cause biases. This study proposes methods based on the relationship between wind conditions in the BES and wind-tunnel experiment to modify the C_p data, so as to make them consistent with the wind conditions used in the BES. The incorrectly used C_p data are compared with modified C_p data in different scenarios. Results suggest that in most cases the biases in predicted natural ventilation rates exceed the ±10% limit of ASHRAE-14 (ASHRAE, 2014), highlighting the importance of the modifying approaches proposed in this study.

Secondly, the C_p data given in various databases are all based on the undisturbed wind speed. While in this study, SUEWS provides the urbanised (therefore 'disturbed') wind speed to EnergyPlus. Therefore, this study proposes modifications to the C_p data to make them consistent with the SUEWS urbanised wind conditions. This approach is used in the SUEWS-EnergyPlus simulations in Chapter 5 and 7.

8.1.3. Natural ventilation potential in different neighbourhoods and climates

Natural ventilation is a common passive cooling measure, but it depends largely on the outdoor climate and different driving forces (i.e., wind- and buoyancy-driven). Often the natural ventilation potential (NVP) is assessed with BES tools, but the impacts of urban climate are rarely considered. Some studies combine BES tools with CFD modelling, but their complexity makes them unsuitable for long-term and large-scale simulations. This study combines SUEWS and EnergyPlus, together with methods proposed in Chapter 3 and 4, to assess NVP in different idealised neighbourhoods using different Chinese climate zones as an example. NVP has been extensively assessed in different Chinese climate zones (Table 5.1), but there is a lack of understanding of the impact of urban climate. In this regard, this study can provide useful insights.

This study considers idealised neighbourhoods with λ_P from 0 to 0.6, and the representative city from each climate zone, ranging from the 'very cold' zone to 'warm winter and hot summer' zone. Conventionally, urban buildings have been considered to have a lower NVP than rural buildings due to lower outdoor wind speeds, but this study finds that the climate, λ_P and time of year in combination impacts the NVP. Also, such impacts can vary for different metrics used to assess NVP. This study uses two metrics: the natural ventilation hours (NV-hours) that measures the available duration of natural ventilation providing acceptable indoor air quality and thermal comfort, and the natural ventilation air change rate hours (ACH-hours) that measures the ventilation rate based on NV-hours. When using NV-hours, it is found that increasing λ_P can increase NV-hours in cold climates (e.g. by 6% in Harbin, 'very cold') but decrease NV-hours in warm climates (by around 57% in Guangzhou, 'warm winter hot summer'). This shows the positive role of urban heat islands in cold climates. However, a critical disadvantage of urban areas is the lower wind speeds, which lead to lower ventilation rates (e.g. Harbin: annual median ventilation rate reduced by 50% at λ_P =0.3 and 85% at λ_P =0.6). When the natural ventilation ACH-hour is used as the metric, in all climates the natural ventilation potential decreases in denser neighbourhoods. Therefore, both NV-hours and ACH-hours should be considered in NVP assessments. Besides, it should be noted that air and noise pollution may prevent urban dwellers from opening windows. In this study only the physical atmospheric conditions are considered, and other factors can be further study in future works.

8.1.4. Outdoor and indoor overheating in Colombo, Sri Lanka

The improved urban neighbourhood-building climate modelling framework developed by this study is applied in Colombo to assess the outdoor and indoor overheating risks.

Land cover data for the Colombo region are required at neighbourhood-scale (500 m in this study) for SUEWS modelling. In this thesis multiple sources are used to create the land cover dataset, including building footprints, OpenStreetMap, and supervised classification of remote sensing images. The dataset is available online (Blunn et al., 2022a) and can be used for climate models.

The spatial and temporal population heat exposure map of the city of Colombo and surrounding areas during a heatwave in February 2020 is produced with SUEWS simulation and local population data. Three different heat stress indices considering both temperature and humidity are used to measure the heat exposure risks. Results suggest that during most of the heatwave period (including nights) the study region is above the lowest heat stress warning of all indices, although there are some differences in spatial distribution between indices. Hotspots are evident in areas of large population, notably in the Colombo Municipal Council (Colombo central area) and surrounding coastal urban areas. Some inland areas can be overheated during the day but overall cooler at night.

A development scenario simulated for the Colombo Municipal Council considers expected the changes in land cover and population by 2035. Results suggest with a 35 % increase in population, higher risks at midday will be experienced (cf. current or 2020 conditions). Two mitigation approaches are analysed for the 2035 scenario. It is found that increasing the built-up surface albedo can reduce this 2035 risk by 15%. Increasing tree cover increases humidity and therefore leads to higher heat stress risk so this intervention is inappropriate in a hot-humid climates, although it may have some micro-scale from shading benefits. This needs to be studied in the future.

BES are performed to assess indoor overheating risks in two neighbourhoods (central neighbourhood: $\lambda_P \approx 0.6$; suburban neighbourhood: $\lambda_P \approx 0.1$). Both neighbourhoods are found to have high outdoor heat stress risks due to regional- and local-scale climates from the previous urban-neighbourhood-scale modelling. A Colombo dwelling archetype model is created based on local surveys and previous studies, which can be used in other future Colombo studies.

It is found that the modelled dwelling has high indoor overheating risks during both the day and night, especially in the suburban neighbourhood because of higher outdoor air temperatures and less solar shading from surrounding buildings during the daytime (up to 9% more total overheating degree-hours than the central neighbourhood). Occupancy profiles for those who stay at home indoors during the daytime (e.g. elderly) are at higher risk (up to 16% more overheating degree-hours than a profile where residents are away during the working week), highlighting the need to pay attention to vulnerable groups during extreme heat events. Different commonly used passive cooling interventions are modelled. It is found that effects of interventions can vary with the neighbourhood, highlighting the urban influences on indoor overheating mitigation measures.

This highly resolved multi-scale overheating risk assessment of a South Asian tropical city can provide guidance for urban planners, builders, policy makers as well as individuals to deal with extreme climate conditions. The experience of overheating assessment and mitigation can be used by other cities with similar climates and development status. Approaches of outdoor and indoor overheating modelling, land cover dataset creation and building archetype creation can be widely applied in different cities globally.

8.2. Recommendations for future research

Based on the findings and contributions presented in this thesis, recommendations for future work are summarized by topic.

Simulation of urban buildings

- The iterative approach proposed in this thesis for longwave radiation simulation is for neighbourhoods with identical buildings. Biases are foreseeable when applied in heterogeneous neighbourhoods, but still smaller compared to the EnergyPlus default method of assuming air temperatures can represent the surrounding building surfaces. Future work could evaluate the biases of different methods in real-world neighbourhoods where there is a heterogeneous mix of buildings.
- Here SUEWS and EnergyPlus are one-way coupled (i.e. SUEWS provides outdoor variables to EnergyPlus) but the heat emission from buildings simulated by SUEWS as part of anthropogenic heat are estimated independent of EnergyPlus. Future work could explore feedbacks from EnergyPlus to SUEWS simulations (i.e. two-way coupled).
- Here SUEWS is forced by available climate reanalysis data. Future work could couple SUEWS to a meso-scale weather model (e.g. Weather Research and Forecasting Model (WRF)) to consider city- to regional-scale feedbacks, to improve forecasts. If run in real-time it could be used to provide early warnings of outdoor and indoor overheating risks.

Overheating assessment

- It is critical to select proper indices and metrics when assessing overheating risks, as they have different assumptions and serve different purposes. This study follows the common approaches to use temperature-humidity heat stress indices for outdoor overheating assessment, and the adaptive thermal comfort model for indoor overheating assessment. In the outdoor study, differences are found between the three selected indices, although they use the same variables. Therefore, further works are needed to compare different indices and determine which is suitable in the given conditions. Also, more advanced indices considering the impact of wind and radiation can be used in future studies. For the indoor overheating assessment, the thermal comfort model uses operative temperature as the indicator, which only uses air and radiant temperatures. Considering the hot-humid climate in Colombo, the high humidity can also contribute to indoor heat stress. Thus a heat stress indicator with humidity included could be used in the future.

- When mapping the outdoor heat exposure in Colombo, only the general population distribution is considered. However, specific vulnerable groups have higher risk of overheating (e.g. elderly). Using more detailed population data would improve the understanding of the heat exposure of specific vulnerable groups, allowing hotspots requiring early warning and medical attention to be identified.
- Here indoor overheating risk assessment is performed in two Colombo neighbourhoods. Building simulations could be undertaken for the entire region to map indoor overheating risk, but will require appropriate building models for the different neighbourhoods. Considering proposed future development and expected climate data would allow prediction of indoor overheating risk and assessment of the effects of passive cooling measures.

Appendix 1: Assessment of view factors calculated with Monte Carlo ray-tracing method

The fundamental expression of view factors between two finite surfaces ($F_{1\to 2}$) is (Howell et al., 2010):

$$F_{1\to 2} = \frac{1}{A_1}\int_{A_1}\int_{A_2}\frac{\cos\theta_1\cos\ {}_2}{\pi r_{12}^2}dA_2 dA_1 \qquad \text{(A1.1)}$$

where surfaces 1 and 2 have areas of A_1 and A_2 (m^2) and have their normal at angle θ_1 and θ_2 (rad) to the line of length r_{12} (m) between them.

The view factor between the *boi* north-facing wall and *adj* south-facing wall in the neighbourhood with $\lambda_P = 0.1$ (Fig. A1.1) calculated with the Monte Carlo ray-tracing method (Eq. 3.10) are compared to the result calculated with Eq. A1.1. With 3000 rays the view factor difference between the Monte Carlo ray-tracing result and Eq. A1.1 is < 1 x 10^{-5} (Fig. A1.2).

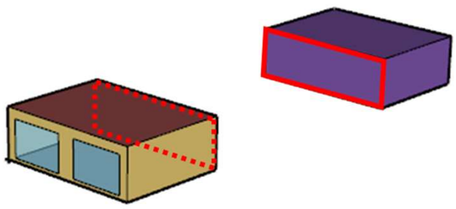

Fig. A1.1. Two surfaces selected for view factor calculation indicated by red boxes.

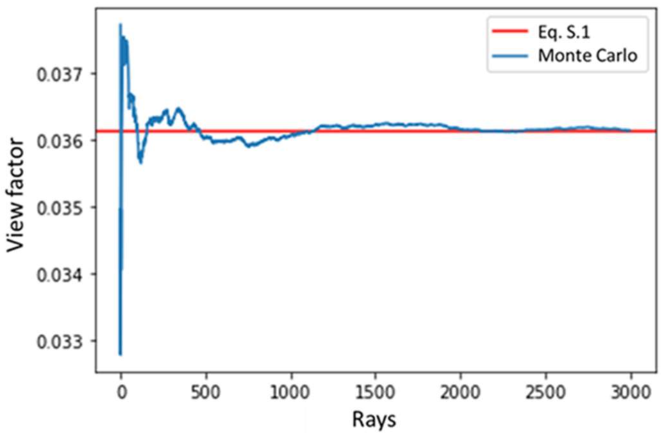

Fig. A1.2. View factors calculated with Monte Carlo method and Eq. A1.1.

Appendix 2: Impact of simplification of adjacent building modelling

Adjacent building facets are assumed to be isotropic during the simulation to save computational cost. The impact of this simplification has been analysed by comparing the simplified detailed facet modelling of the case $boi_{adj\leftarrow a,5}$ with λ_P = 0.6. The north-facing wall (which directly faces windows on adjacent buildings) surface temperature differences are shown in Fig. A2.1. The median difference in north-facing wall surface temperature due to windows simplification is up to 0.2 °C. For other walls, this difference is much smaller (not shown) as they are not facing windows directly.

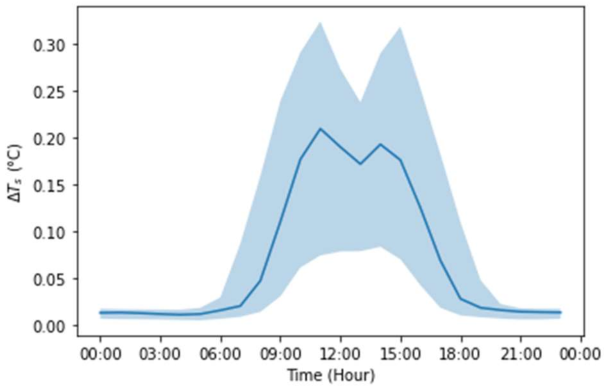

Fig. A2.1. Median diurnal cycle (lines) and inter-quartile ranges (shading) of north-facing wall surface temperature differences (hourly) using $boi_{adj\leftarrow a,5}$ (simplified model – detailed model) during the year in London for plan area fractions λ_P=0.6.

Appendix 3: Differences of external building surface temperatures between iterations – extended

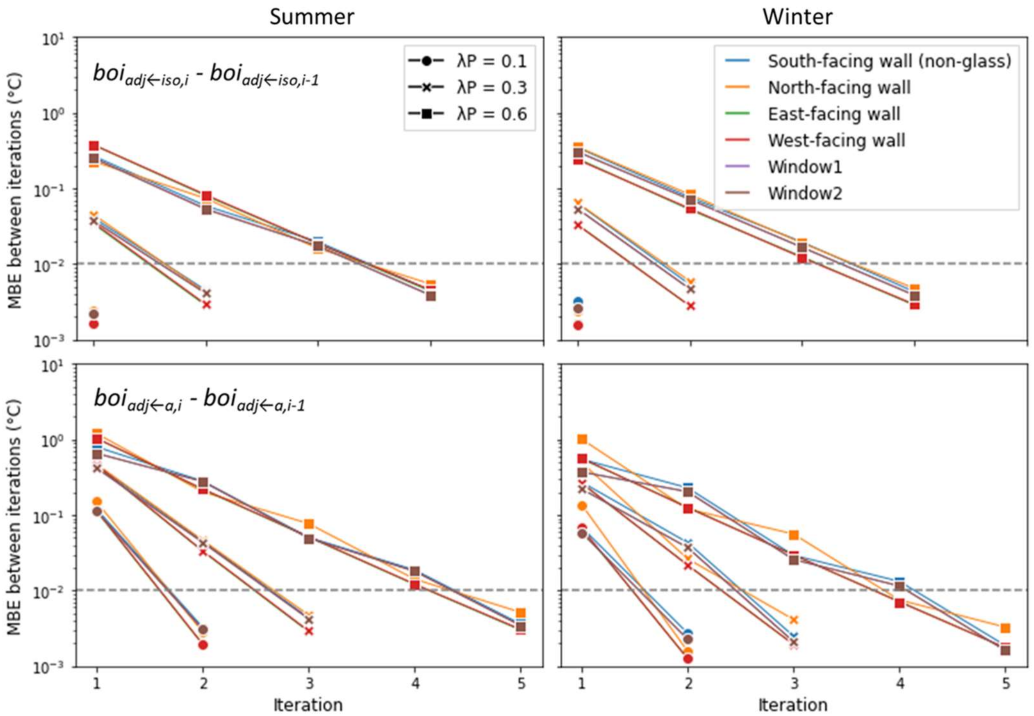

Fig. A3.1. Summer (JJA) and winter (DJF) mean bias error (MBE, section 3.2.4; 10-min timestep, N=52560) in external building surface temperature (cf. previous iteration, Fig. 3.2) for different facets (colour) in London with three plan area fractions (λ_P) (marker) and two initial *adj* surface temperatures (rows) with the convergence criteria (0.01 °C, dashed line). Annual MBE are shown in Fig. 3.4.

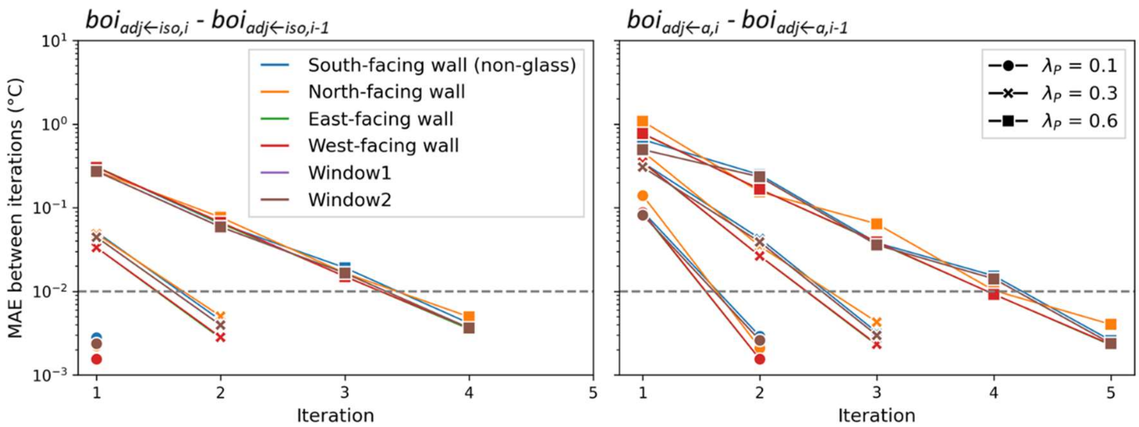

Fig. A3.2. Annual mean absolute error (MAE, section 3.2.4; 10-min timestep, N=52560) in external building surface temperature (cf. previous iteration, Fig. 3.2) for different facets (colour) in London with three plan area fractions (λ_P) (marker) and two initial *adj* surface temperatures (rows) with the convergence criteria (0.01 °C, dashed line). MBE are shown in Fig. 3.4.

Appendix 4: Differences between surface temperatures simulated with different sources of initial surface temperature values at each iteration– extended

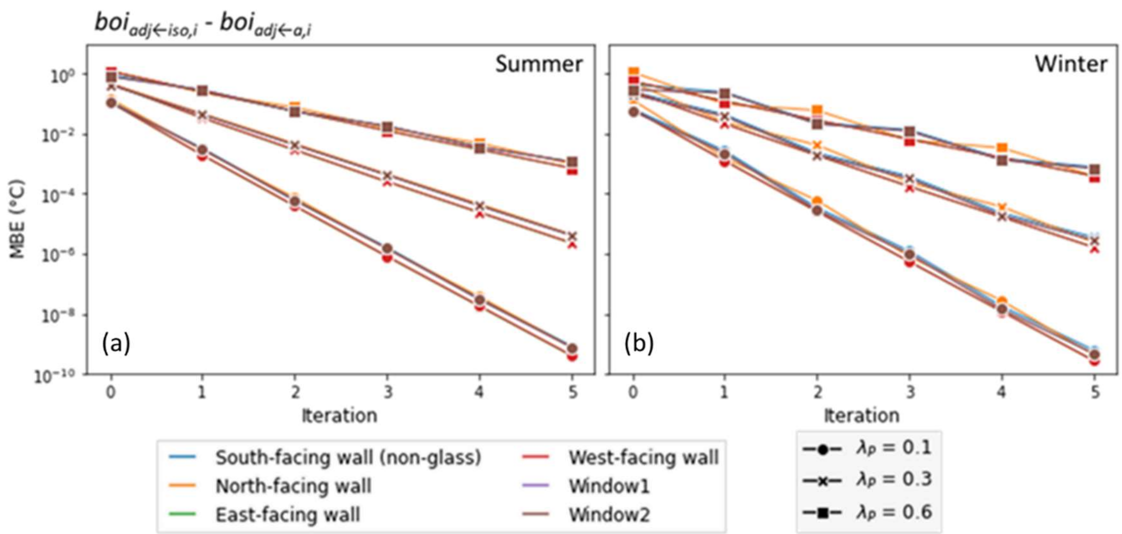

Fig. A4.1. Impact of different initialisations (Fig. 3.2; i.e. iteration 0 refers to $boi_{adj\leftarrow iso}$ - $boi_{adj\leftarrow a}$) on external building surface temperature (metric MBE between results, section 3.2.4; 10-min timestep, N=52560) for different facets (colour) in London with three plan area fractions (λ_P, marker) for (a) summer (JJA) and (b) winter (DJF). Annual MBE are shown in Fig. 3.6.

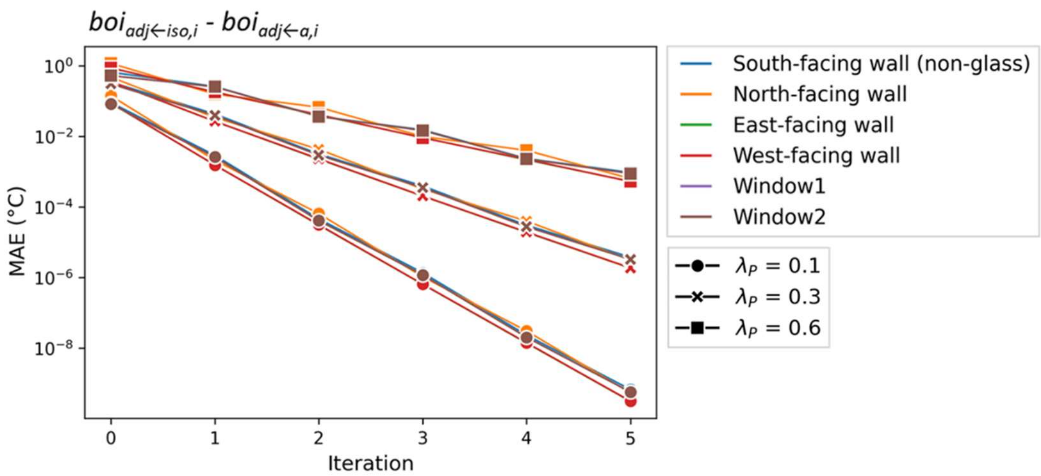

Fig. A4.2. Annual mean absolute error (MAE, section 3.2.4; 10-min timestep, N=52560) in external building surface temperature between iterated results with different initialisations (Fig. 3.2; i.e. iteration 0 refers to $boi_{adj\leftarrow iso}$ - $boi_{adj\leftarrow a}$) for different facets (colour) in London with three plan area fractions (λ_P, marker). Annual MBE are shown in Fig. 3.6.

Appendix 5: $C_{pr,WT}$ vertical profiles from the TPU database

Fig. A5.1 shows the $C_{pr,WT}$ for buildings with various plan area fractions (λ_P). The $C_{pr,WT}$ values are larger for isolated than sheltered buildings. As λ_P increases, the different flow types in in the neighbourhood influence the $C_{pr,WT}$ values. With a λ_P of 0.3 the surrounding buildings modify the wind field, reducing the wind speed close to the target building and therefore lowering the wind pressure. If $\lambda_P = 0.6$, the windward facet has negative $C_{pr,WT}$ values associated with the skimming flow in the high-density neighbourhood.

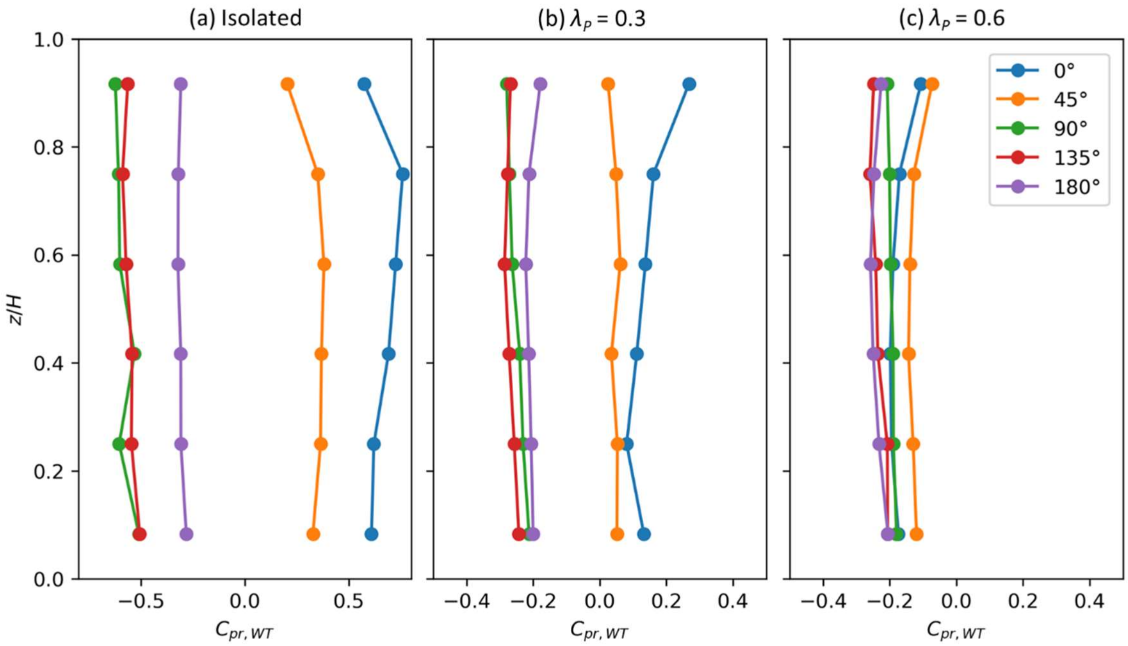

Fig. A5.1. Vertical profiles of $C_{pr,WT}$ on the target building facet with different both incident wind angles and plan area fractions. 0° refers to wind blowing perpendicular to the facet. Data are from the TPU database (TPU, 2007).

Appendix 6: Evaluating independence of $\overline{C_{pl}}$ on the wind profile

To evaluate the assumption that $\overline{C_{pl}}$ is not a function (i.e. independent) of the wind profile, we calculate $\overline{C_{pl}}$ with Eq. 4.12 using the Lim et al. (2016) C_{pr} data at different heights. They used power law wind profiles. Their C_{pr} data are for a vertical central line of the windward facet of an isolated building (Table SM.1). We calculate the $\overline{C_{pr}}$ as the mean of C_{pr} data on the vertical central line and calculate $\overline{C_{pl}}$ with Eq. 4.12. Results show that although not exactly equal, $\overline{C_{pl}}$ values still have much smaller variations at different wind profile exponent α compared to $\overline{C_{pr}}$. Therefore, it is reasonable to assume that $\overline{C_{pl}}$ is not influenced by α.

Table SM.1: Vertical profile of C_{pr} for the central line of the windward facet of a cube with different α. Data are from Fig. 12 of Lim et al. (2016). Here $\overline{C_{pr}}$ and $\overline{C_{pl}}$ are averaged over the vertical central line.

z/H	0	1/7	2/7	3/7	4/7	5/7	6/7	1	$\overline{C_{pr}}$	$\overline{C_{pl}}$	$\overline{C_{pl}}$ differences from α = 0.07
α = 0.07	0.51	0.49	0.62	0.71	0.78	0.81	0.8	0.44	0.65	0.74	0%
α = 0.22	0.4	0.34	0.46	0.56	0.65	0.72	0.74	0.44	0.54	0.78	5.4%
α = 0.39	0.31	0.22	0.32	0.43	0.53	0.62	0.69	0.44	0.45	0.79	6.8%

Appendix 7: Land cover data processing

Table A7.1: Land cover and population datasets used.

Type	Dataset		Reference
Building	Number of storeys (2018)	CMC	Building GIS data (Urban Development Authority, Sri Lanka prepared by Survey Dept. of Sri Lanka) (Blunn et al., 2022a)
Building	CMC building footprint (2014)	CMC	Building GIS data (Urban Development Authority, Sri Lanka prepared by Survey Dept. of Sri Lanka) (Blunn et al., 2022a)
Road	Area		OpenStreetMap contributors (2021)
	Width		Google (2022)
Water	Area		OpenStreetMap contributors (2021)
	Width (narrow waterways)		Google (2022)
Bare soil	Area		Sentinel-2 multiband satellite data (ESA, 2018)

Table A7.2: OpenStreetMap (OSM) vegetation classes are reassigned to fewer classes and converted to land cover fractions. Determination of land cover fractions of each class is based on SCP classification results (LCv1, Fig. 6.6.2) and visual inspection of Google Earth high-resolution satellite (Google, 2022).

OSM vegetated area classes	*Unified class*	*Land cover assumptions*
Golf course, graveyard, zoo, cemetery, recreation ground	Park	50% tree, 50% grass
Forest, scrub, nature reserve, orchard	Forest	80% tree, 20% grass
Farmland, farmyard	Grassland	80% grass, 20% soil
Wetland	Wetland	30% water, 40% tree, 30% grass

Appendix 8: Details of bootstrapping – building fractions outside of the CMC

Linear regression models are developed to minimise bias in the SCP building fraction prediction outside of the CMC. Cross-validation methods are used to develop the models, evaluate their predictive performance, and provide aggregated model outputs (building fraction predictions). The CMC area is divided into 195 grids for cross validation. Each grid has a building fraction based on the CMC building footprint (true value) and a SCP building fraction (predicted value). For each resampling, the original dataset containing 195 pairs of true and predicted building fractions are divided into a training sample and a test sample for model evaluation. The resampling is iterated multiple times to obtain more representative results

The model performance of three cross-validation methods is compared – the 10-fold cross validation (Efron and Tibshirani, 1986; Molinaro et al., 2005), bootstrapping (Efron and Tibshirani, 1986), and Monte Carlo cross validation (Xu and Liang, 2001). Results (Table A8.1) show that with 10000 iterations models developed with bootstrapping have better performance in terms of both bias and standard deviation. This agrees with Kim (2009), who suggests that bootstrapping is recommended for small original dataset sizes (< 200 samples). Bootstrapping is therefore used as the cross-validation method.

As an alternative to using SCP building fraction outside of the CMC, the Global Human Settlement (GHS) built-up dataset (Florczyk et al., 2019) is considered. However, a larger MAE (7.55%) is found compared to the corrected SCP (Table A8.1).

To evaluate the bootstrap corrected SCP prediction outside of the CMC, three grids representing high-, mid- and low-density areas outside the CMC are selected. To get the 'true' land cover fractions, 500 dots are placed randomly in each grid, and the underlying land cover type is recorded for each dot, based on visual inspection of Google Earth high-resolution satellite imagery (Google, 2022). The corrected SCP results are compared with visual estimation results and show reasonable accuracy (Fig. A8.1).

Table A8.1: Comparison of building fraction mean absolute error (MAE) and standard deviation (SD) with different cross validation (CV) approaches

	100 iterations		10000 iterations	
	MAE (%)	SD (%)	MAE (%)	SD (%)
10-Fold CV	5.32	0.93	5.32	1.01
Bootstrapping	5.72	0.19	4.00	0.27
Monte Carlo CV	5.41	0.77	5.32	0.75

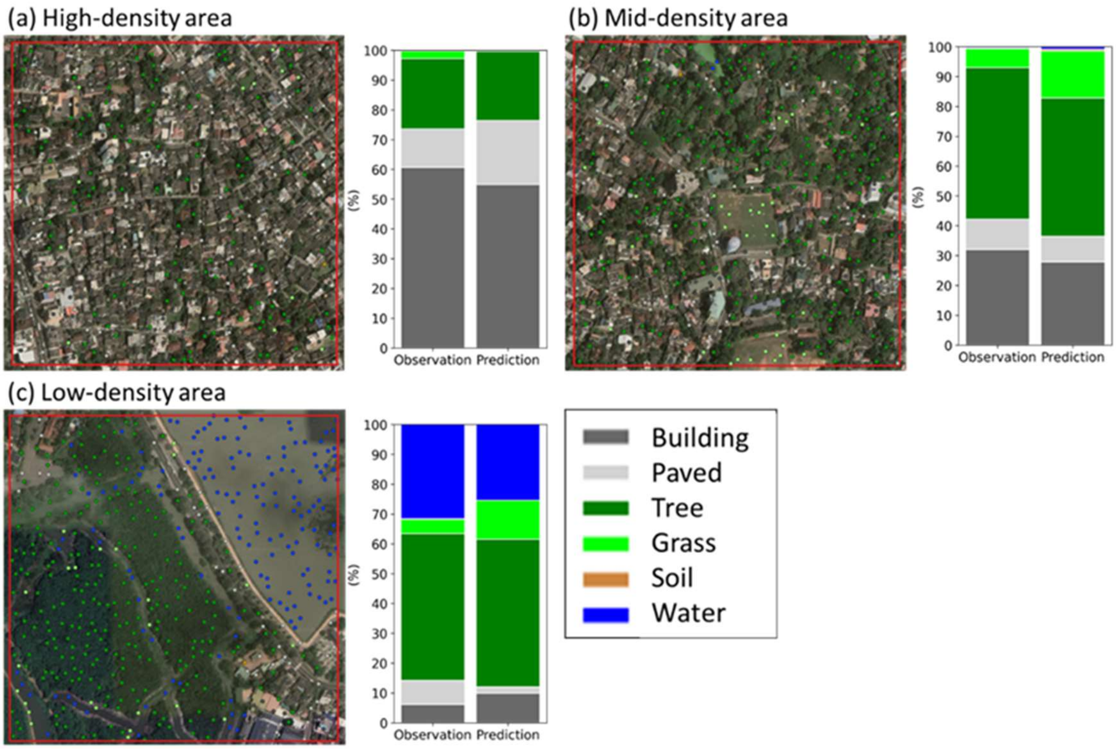

Figure A8.1: Comparison of observed (visual inspection of dots) and predicted (corrected SCP results) land cover fractions in three 500 m grids. The colour of each dot corresponds to the underlying land cover identified via visual inspection. Image source: Google Earth (Google, 2022).

Appendix 9: Coefficients used in the Heat Index (units °C)

Table A9.1: Coefficients of the Heat Index (I_H) in °C for Eq. 6.2.

c_1	-8.784695	c_4	-0.14611605	c_7	2.211732×10^{-3}
c_2	1.61139411	c_5	$-1.2308094 \times 10^{-2}$	c_8	7.2546×10^{-4}
c_3	2.338549	c_6	$-1.6424828 \times 10^{-2}$	c_9	-3.582×10^{-6}

Appendix 10: Occupancy schedule and internal heat gains for the Colombo dwelling archetype

Table A10.1: The two occupancy schedules (Mavrogianni et al., 2014; Porritt et al., 2012) simulated (a) family four and (b) two stay-at-home adults. The different behaviours on weekends and elderly behaviours are given in parentheses.

	Adult occupants (family weekend and elderly in parentheses)			Children occupants		
Time	Room	Activity	Heat gain (W)	Room	Activity	Heat gain (W)
00:00	Bedroom	Sleeping	72	Bedroom	Sleeping	54
01:00	Bedroom	Sleeping	72	Bedroom	Sleeping	54
02:00	Bedroom	Sleeping	72	Bedroom	Sleeping	54
03:00	Bedroom	Sleeping	72	Bedroom	Sleeping	54
04:00	Bedroom	Sleeping	72	Bedroom	Sleeping	54
05:00	Bathroom 1	Shower	108	Bathroom	Shower	81
06:00	Kitchen /dining room	Cooking/eating	108	Dining room	Eating	81
07:00 - 16:00	Away (living room)	Away (relaxing)	0 (108)	Away (living room)	Away (relaxing)	0 (81)
17:00	Dining room	Eating	108	Dining room	Eating	81
18:00	Living room	Relaxing	108	Study room	Studying	81
19:00	Living room	Relaxing	108	Study room	Studying	81
20:00	Living room	Relaxing	108	Study room	Studying	81
21:00	Bedroom	Sleeping	72	Bedroom	Sleeping	54
22:00	Bedroom	Sleeping	72	Bedroom	Sleeping	54
23:00	Bedroom	Sleeping	72	Bedroom	Sleeping	54

Appendix 11: Wind pressure coefficients for Colombo dwelling natural ventilation calculation

Table A10.2: Wind pressure coefficients for the Colombo dwelling archetype (Fig. 7.4) in different neighbourhoods (Fig. 7.1). Calculated with methods in Section 4.3.3.

Neighbourhood	Facet orientation	0°	45°	90°	135°	180°
Central	S/N facet	-2.43	-2.59	-3.4	-3.89	-3.4
	E/W facet	-2.92	-3.08	-3.24	-3.73	-3.24
Suburban	S/N facet	1.18	1.11	-1.04	-1.34	-0.84
	E/W facet	1.11	-0.84	-1.34	-2.08	-0.57

References

Ahmed, M., Suphachalasai, S., 2014. Assessing the Costs of Climate Change and Adaptation in South Asia. Asian Development Bank.

Akins, R.E., Cermak, J.E., 1976. Wind pressure on buildings. Colorado State University.

Akins, R.E., Peterka, J.A., Cermak, J.E., 1979. Averaged pressure coefficients for rectangular buildings. In: Zement-Kalk-Gips. pp. 369–380.

Albuquerque, D.P., Mateus, N., Avantaggiato, M., Carrilho da Graça, G., 2020. Full-scale measurement and validated simulation of cooling load reduction due to nighttime natural ventilation of a large atrium. Energy Build. 224, 110233.

Allegrini, J., Dorer, V., Carmeliet, J., 2012. Influence of the urban microclimate in street canyons on the energy demand for space cooling and heating of buildings. Energy Build. 55, 823–832.

Allegrini, J., Dorer, V., Carmeliet, J., 2016. Impact of radiation exchange between buildings in urban street canyons on space cooling demands of buildings. Energy Build. 127, 1074–1084.

Allen, L., Lindberg, F., Grimmond, C.S.B., 2011. Global to city scale urban anthropogenic heat flux: model and variability. Int. J. Climatol. 31, 1990–2005.

Anđelković, A.S., Mujan, I., Dakić, S., 2016. Experimental validation of a EnergyPlus model: Application of a multi-storey naturally ventilated double skin façade. Energy Build. 118, 27–36.

Anderson, C.I., Gough, W.A., Mohsin, T., 2018. Characterization of the urban heat island at Toronto: Revisiting the choice of rural sites using a measure of day-to-day variation. Urban Clim. 25, 187–195.

Anderson, M., Carmichael, C., Murray, V., Dengel, A., Swainson, M., 2013. Defining indoor heat thresholds for health in the UK. Perspect. Public Health 133, 158–164.

ANSI/ASHRAE, 2011. Standard Method of Test for the Evaluation of Building Energy Analysis Computer Programs. Atlanta.

ANSI/ASHRAE, 2013a. ANSI/ASHRAE Standard 55 - thermal environmental conditions for human occupancy. Atlanta, USA.

ANSI/ASHRAE, 2013b. Ventilation for Acceptable Indoor Air Quality.

ANSI/ASHRAE, 2019. ANSI/ASHRAE/IES Standard 90.1-2019 -- Energy standard for buildings except low-rise residential buildings. Atlanta.

Ao, X., Grimmond, C.S.B., Ward, H.C., Gabey, A.M., Tan, J., Yang, X.Q., Liu, D., Zhi, X., Liu, H., Zhang, N., 2018. Evaluation of the Surface Urban Energy and Water Balance Scheme (SUEWS) at a dense urban site in Shanghai: Sensitivity to anthropogenic heat and irrigation. J. Hydrometeorol. 19, 1983–2005.

Arasteh, D., Kohler, C., Griffith, B., 2009. Modeling Windows in Energy Plus with Simple Performance Indices. Berkeley.

ASHRAE, 2001. International Weather for Energy Calculations (IWEC Weather Files) Users Manual and CD-ROM. ASHRAE, Atlanta.

ASHRAE, 2005. ASHRAE Handbook : Fundamentals. American Society of Heating, Refrigerating and Air-Conditioning Engineers, Atlanta.

ASHRAE, 2014. ASHRAE Guideline 14: Measurement of Energy, Demand, and Water Savings. Atlanta.

Auliciems, A., Szokolay, S. V, 2007. Thermal comfort, 2nd ed. PLEA, Brisbane, Australia.

Awbi, H.B., 2003. Ventilation of Buildings, Second. ed. Taylor & Francis Group, New York.

Axley, J., 2007. Multizone Airflow Modeling in Buildings: History and Theory. HVAC&R Res. 13, 907–928.

Aynsley, R., 1999. Estimating summer wind driven natural ventilation potential for indoor thermal comfort. J. Wind Eng. Ind. Aerodyn. 83, 515–525.

Bandara, R.M.P.S., Kumanayake, R.P., Kanthi, J.K., 2011. Energy Performance Analysis of the Cafeteria Building of a Sri Lankan University through Energy Modelling. In: Annual Transactions of IESL. The Institution of Engineers, Sri Lanka, Colombo, pp. 272–280.

Baniassadi, A., Heusinger, J., Sailor, D.J., 2018. Energy efficiency vs resiliency to extreme heat and power outages: The role of evolving building energy codes. Build. Environ. 139, 86–94.

Baniassadi, A., Sailor, D.J., Krayenhoff, E.S., Broadbent, A.M., Georgescu, M., 2019. Passive survivability of buildings under changing urban climates across eight US cities. Environ. Res. Lett. 14, 074028.

Barnett, A.G., Tong, S., Clements, A.C.A., 2010. What measure of temperature is the best predictor of mortality? Environ. Res. 110, 604–611.

Bayraktar, N.T., Ok, V., 2019. Numerical evaluation of the effects of different types of shading devices on interior occupant thermal comfort using wind tunnel experimental data. Build. Simul. 12, 683–696.

Beck, H.E., Zimmermann, N.E., McVicar, T.R., Vergopolan, N., Berg, A., Wood, E.F., 2018. Present and future Köppen-Geiger climate classification maps at 1-km resolution. Sci. Data 2018 51 5, 1–12.

Beckmann, S.K., Hiete, M., Beck, C., 2021. Threshold temperatures for subjective heat stress in urban apartments—Analysing nocturnal bedroom temperatures during a heat wave in Germany. Clim. Risk Manag. 32, 100286.

Belleri, A., Lollini, R., Dutton, S.M., 2014. Natural ventilation design: An analysis of predicted and measured performance. Build. Environ. 81, 123–138.

Belmans, B., Aerts, D., Verbeke, S., Audenaert, A., Descamps, F., 2019. Set-up and evaluation of a virtual test bed for simulating and comparing single- and mixed-mode ventilation strategies. Build. Environ. 151, 97–111.

Beshir, M., Ramsey, J.D., 1988. Heat stress indices: A review paper. Int. J. Ind. Ergon. 3, 89–102.

Best, M.J., Grimmond, C.S.B., 2014. Importance of initial state and atmospheric conditions for urban land surface models' performance. Urban Clim. 10, 387–406.

Best, M.J., Grimmond, C.S.B., 2015. Key Conclusions of the First International Urban Land Surface Model Comparison Project. Bull. Am. Meteorol. Soc. 96, 805–819.

Bhamare, D.K., Rathod, M.K., Banerjee, J., 2019. Passive cooling techniques for building and their applicability in different climatic zones—The state of art. Energy Build. 198, 467–490.

Blazejczyk, K., Epstein, Y., Jendritzky, G., Staiger, H., Tinz, B., 2012. Comparison of UTCI to selected thermal indices. Int. J. Biometeorol. 56, 515–535.

Blunn, L., Xie, X., Grimmond, S., Luo, Z., Sun, T., Perera, N., Ratnayake, R., Emmanuel, R., 2022a. Spatial and temporal variation of anthropogenic heat emissions in Colombo, Sri Lanka - Data files [WWW Document]. Zenodo. URL https://doi.org/10.5281/zenodo.7245097

Blunn, L., Xie, X., Grimmond, S., Luo, Z., Sun, T., Perera, N., Ratnayake, R., Emmanuel, R., 2022b. Spatial and temporal variation of anthropogenic heat emissions in Colombo, Sri Lanka.

Boccalatte, A., Fossa, M., Gaillard, L., Menezo, C., 2020. Microclimate and urban morphology effects on building energy demand in different European cities. Energy Build. 224, 110129.

Botti, A., Leach, M., Lawson, M., Hadjidimitriou, N.S., 2022. Developing a meta-model for early-stage overheating risk assessment for new apartments in London. Energy Build. 254, 111586.

Bouyer, J., Inard, C., Musy, M., 2011. Microclimatic coupling as a solution to improve building energy simulation in an urban context. Energy Build. 43, 1549–1559.

Brake, R., Bates, G., 2002. A Valid Method for Comparing Rational and Empirical Heat Stress Indices. Ann. Occup. Hyg. 46, 165–174.

BRE/DECC, 2012. The Government's Standard Assessment Procedure for Energy Rating of Dwellings: SAP 2012.

Bre, F., Gimenez, J.M., 2022. A cloud-based platform to predict wind pressure coefficients on buildings. Build. Simul. 15, 1507–1525.

Bre, F., Silva, A.S., Ghisi, E., Fachinotti, V.D., 2016. Residential building design optimisation using sensitivity analysis and genetic algorithm. Energy Build. 133, 853–866.

Brooke Anderson, G., Bell, M.L., Peng, R.D., 2013. Methods to calculate the heat index as an exposure metric in environmental health research. Environ. Health Perspect. 121, 1111–1119.

Bruse, M., 2004. ENVI-met 3.0: Updated Model Overview.

Brutsaert, W., 2005. Hydrology. Cambridge University Press.

BSI, 2007. BS EN 15251: 2007: Indoor environmental parameters for design and assessment of energy performance of buildings- addressing indoor air quality, thermal environment, lighting and acoustics. British Standards Institution, London.

Budd, G.M., 2008. Wet-bulb globe temperature (WBGT)-its history and its limitations. J. Sci. Med. Sport 11, 20–32.

Bueno, B., Norford, L., Pigeon, G., Britter, R., 2011. Combining a Detailed Building Energy Model with a Physically-Based Urban Canopy Model. Boundary-Layer Meteorol. 140, 471–489.

Buzan, J.R., Oleson, K., Huber, M., 2015. Implementation and comparison of a suite of heat stress metrics within the Community Land Model version 4.5. Geosci. Model Dev 8, 151–170.

CABEE, 2021. China Building Energy Consumption and Carbon Emission Research Report.

Carrilho Da Graça, G., Martins, N.R., Horta, C.S., 2012. Thermal and airflow simulation of a naturally ventilated shopping mall. Energy Build. 50, 177–188.

Causone, F., 2016. Climatic potential for natural ventilation. Archit. Sci. Rev. 59, 212–228.

CEN, 2007. EN 15251:2007 - Indoor environmental input parameters for design and assessment of energy performance of buildings addressing indoor air quality, thermal environment, lighting and acoustics. Brussels, Belgium.

Chan, A.L.S., 2011. Developing a modified typical meteorological year weather file for Hong Kong taking into account the urban heat island effect. Build. Environ. 46, 2434–2441.

Chen, Y., Tong, Z., Malkawi, A., 2017. Investigating natural ventilation potentials across the globe: Regional and climatic variations. Build. Environ. 122, 386–396.

Chen, Y., Tong, Z., Wu, W., Samuelson, H., Malkawi, A., Norford, L., 2019. Achieving natural ventilation potential in practice: Control schemes and levels of automation. Appl. Energy 235, 1141–1152.

Cheng, J., Qi, D., Katal, A., Wang, L., Stathopoulos, T., 2018. Evaluating wind-driven natural ventilation potential for early building design.

Cheng, Y.T., Lung, S.C.C., Hwang, J.S., 2019. New approach to identifying proper thresholds for a heat warning system using health risk increments. Environ. Res. 170, 282.

Cheng, Z., Li, L., Bahnfleth, W.P., 2016. Natural ventilation potential for gymnasia – Case study of ventilation and comfort in a multisport facility in northeastern United States. Build. Environ. 108, 85–98.

Cheung, S.S., McLellan, T.M., Tenaglia, S., 2000. The thermophysiology of uncompensable heat stress: Physiological manipulations and individual characteristics. Sport. Med. 29, 329–359.

Chew, L.W., Liu, X., Li, X.-X., Norford, L.K., 2021. Interaction between heat wave and urban heat island: A case study in a tropical coastal city, Singapore. Atmos. Res. 247, 105134.

Chvatal, K.M.S., Corvacho, H., 2009. The impact of increasing the building envelope insulation upon the risk of overheating in summer and an increased energy consumption. J. Build. Perform. Simul. 2, 267–282.

Ciancio, V., Falasca, S., Golasi, I., Curci, G., Coppi, M., Salata, F., 2018. Influence of Input Climatic Data on Simulations of Annual Energy Needs of a Building: EnergyPlus and WRF Modeling for a Case Study in Rome (Italy). Energies 11, 2835.

CIBSE, 2006. CIBSE Guide A: Environmental design, 7th ed. Chartered Institution of Building Services Engineers, London.

CIBSE, 2013. TM52: The Limits of Thermal Comfort: Avoiding Overheating in European Buildings. Chartered Institution of Building Services Engineers, London.

CIBSE, 2015. CIBSE Guide A: Environmental design, 8th ed. London.

Clarke, J., 2001. Energy simulation in building design, 2nd ed. Routledge, Abingdon.

Congedo, L., 2021. Semi-Automatic Classification Plugin: A Python tool for the download and processing of remote sensing images in QGIS. J. Open Source Softw. 6, 3172.

Costanzo, V., Yao, R., Xu, T., Xiong, J., Zhang, Q., Li, B., 2019. Natural ventilation potential for residential buildings in a densely built-up and highly polluted environment. A case study. Renew. Energy 138, 340–353.

Cóstola, D., Blocken, B., Hensen, J.L.M.L.M., 2009. Overview of pressure coefficient data in building energy simulation and airflow network programs. Build. Environ. 44, 2027–2036.

Cóstola, D., Blocken, B., Ohba, M., Hensen, J.L.M., 2010. Uncertainty in airflow rate calculations due to the use of surface-averaged pressure coefficients. Energy Build. 42, 881–888.

d'Ambrosio Alfano, F.R., Palella, B.I., Riccio, G., 2011. Thermal environment assessment reliability using temperature -Humidity indices. Ind. Health 49, 95–106.

de Dear, R., Xiong, J., Kim, J., Cao, B., 2020. A review of adaptive thermal comfort research since 1998. Energy Build. 214, 109893.

de Dear, R.J., Brager, G.S., 1998. Developing an adaptive model of thermal comfort and preference. In: ASHRAE Transactions. pp. 145–167.

de Dear, R.J., Brager, G.S., 2002. Thermal comfort in naturally ventilated buildings: revisions to ASHRAE Standard 55. Energy Build. 34, 549–561.

Demanuele, C., Mavrogianni, A., Davies, M., Kolokotroni, M., Rajapaksha, I., 2012. Using localised weather files to assess overheating in naturally ventilated offices within London's urban heat island. Build. Serv. Eng. Res. Technol. 33, 351–369.

Dengel, A., Swainson, M., Ormandy, D., Ezratty, V., 2016. Overheating in dwellings, Bre.

Department of Census & Statistics, 2012. Census of Population and Housing 2012. Colombo.

DesignBuilder, 2022. DesignBuilder v7 help [WWW Document]. URL https://designbuilder.co.uk/helpv7.0/index.htm (accessed 11.21.22).

Di Napoli, C., Pappenberger, F., Cloke, H.L., 2019. Verification of Heat Stress Thresholds for a Health-Based Heat-Wave Definition. J. Appl. Meteorol. Climatol.

58, 1177–1194.

Di Perna, C., Stazi, F., Casalena, A.U., D'Orazio, M., 2011. Influence of the internal inertia of the building envelope on summertime comfort in buildings with high internal heat loads. Energy Build. 43, 200–206.

Disaster Management Centre, 2022. Weather Reports [WWW Document]. URL http://www.dmc.gov.lk/index.php?option=com_dmcreports&view=reports&Itemid=274&limit=0&search=&report_type_id=2&fromdate=&todate=&lang=en (accessed 4.8.22).

Doctor-Pingel, M., Vardhan, V., Manu, S., Brager, G., Rawal, R., 2019. A study of indoor thermal parameters for naturally ventilated occupied buildings in the warm-humid climate of southern India. Build. Environ. 151, 1–14.

Dogan, T., Kastner, P., 2021. Streamlined CFD simulation framework to generate wind-pressure coefficients on building facades for airflow network simulations. Build. Simul. 14, 1189–1200.

Dong, J., Peng, J., He, X., Corcoran, J., Qiu, S., Wang, X., 2020. Heatwave-induced human health risk assessment in megacities based on heat stress-social vulnerability-human exposure framework. Landsc. Urban Plan. 203, 103907.

Efron, B., Tibshirani, R., 1986. Bootstrap Methods for Standard Errors, Confidence Intervals, and Other Measures of Statistical Accuracy. Stat. Sci. 1, 54–75.

Emmanuel, R., 2004. Estimating the environmental suitability of wall materials: preliminary results from Sri Lanka. Build. Environ. 39, 1253–1261.

Emmanuel, R., Johansson, E., 2006. Influence of urban morphology and sea breeze on hot humid microclimate: the case of Colombo, Sri Lanka. Clim. Res. 30, 189–200.

Emmerich, S.J., Dols, W.S., Axley, J.W., 2001. Natural ventilation review and plan for design and analysis tools. National Institute of Standards and Technology, Gaithersburg.

Energy Research Institute, Lawrence Berkeley National Laborator, Rocky Mountain Institute, 2016. Reinventing fire: China – A roadmap for China's revolution in energy consumption and production to 2050, executive summary.

EnergyPlus, 2022. GitHub - NREL/EnergyPlus [WWW Document]. URL https://github.com/NREL/EnergyPlus (accessed 7.18.22).

Environment and Climate Change Canada, 2019. Warm season weather hazards - Canada.ca [WWW Document]. URL https://www.canada.ca/en/environment-climate-change/services/seasonal-weather-hazards/warm-season-weather-hazards.html (accessed 9.29.22).

Epstein, Y., Moran, D.S., 2006. Thermal Comfort and the Heat Stress Indices. Ind. Health 44, 388–398.

ESA, 2018. Sentinel-2 products specification document.

ESCAP, 2015. Disasters in Asia and the Pacific: 2015 Year in Review.

Esri, 2022. World Imagery [WWW Document]. URL https://www.arcgis.com/home/item.html?id=10df2279f9684e4a9f6a7f08febac2a9 (accessed 4.1.22).

Evins, R., Dorer, V., Carmeliet, J., 2014. Simulating external longwave radiation exchange for buildings. Energy Build. 75, 472–482.

Faggianelli, G.A., Brun, A., Wurtz, E., Muselli, M., 2014. Natural cross ventilation in buildings on Mediterranean coastal zones. Energy Build. 77, 206–218.

Fang, C., Sill, B.L., 1995. Pressure distribution on a low-rise building model subjected to a family of boundary layers. J. Wind Eng. Ind. Aerodyn. 56, 87–105.

Fanger, P.O., 1970. Thermal comfort. Analysis and applications in environmental engineering. In: Thermal Comfort. Analysis and Applications in Environmental Engineering. Danish Technical Press., Copenhagen.

Fanger, P.O., Toftum, J., 2002. Extension of the PMV model to non-air-conditioned buildings in warm climates. Energy Build. 34, 533–536.

Feist, W., Pfluger, R., Kaufmann, B., Kah, O., Schneiders, J., 2007. Passive House Planning Package 2007 1, 7.

Figueiredo, A., Kämpf, J., Vicente, R., 2016. Passive house optimization for Portugal: Overheating evaluation and energy performance. Energy Build. 118, 181–196.

Fletcher, M.J., Johnston, D.K., Glew, D.W., Parker, J.M., 2017. An empirical evaluation of temporal overheating in an assisted living Passivhaus dwelling in the UK. Build. Environ. 121, 106–118.

Florczyk, A.J., Corbane, C., Ehrlich, D., Freire, S., Kemper, T., Maffenini, L., Melchiorri, M., Pesaresi, M., Politis, P., Schiavina, M., Sabo, F., Zanchetta, L., 2019. GHSL data package 2019. Luxembourg.

Fosas, D., Coley, D.A., Natarajan, S., Herrera, M., Fosas de Pando, M., Ramallo-Gonzalez, A., 2018. Mitigation versus adaptation: Does insulating dwellings increase overheating risk? Build. Environ. 143, 740–759.

Frayssinet, L., Merlier, L., Kuznik, F., Hubert, J.-L., Milliez, M., Roux, J.-J., 2018. Modeling the heating and cooling energy demand of urban buildings at city scale. Renew. Sustain. Energy Rev. 81, 2318–2327.

Gagge, A.P., Stolwijk, J.A.J., Hardy, J.D., 1967. Comfort and thermal sensations and associated physiological responses at various ambient temperatures. Environ. Res. 1, 1–20.

Gamero-Salinas, J., Monge-Barrio, A., Kishnani, N., López-Fidalgo, J., Sánchez-Ostiz, A., 2021. Passive cooling design strategies as adaptation measures for lowering the indoor overheating risk in tropical climates. Energy Build. 252, 111417.

Geletič, J., Lehnert, M., Jurek, M., 2020. Spatiotemporal variability of air temperature during a heat wave in real and modified landcover conditions: Prague and Brno (Czech Republic). Urban Clim. 31, 100588.

Germano, M., 2007. Assessing the natural ventilation potential of the Basel region. Energy Build. 39, 1159–1166.

Ghiaus, C., Allard, F., Santamouris, M., Georgakis, C., Nicol, F., 2006. Urban environment influence on natural ventilation potential. Build. Environ. 41, 395–406.

Gidhagen, L., Olsson, J., Amorim, J.H., Asker, C., Belusic, D., Carvalho, A.C., Engardt, M., Hundecha, Y., Körnich, H., Lind, P., Lindstedt, D., Olsson, E., Rosberg, J., Segersson, D., Strömbäck, L., 2020. Towards climate services for European cities: Lessons learnt from the Copernicus project Urban SIS. Urban Clim. 31, 100549.

Gimenez, J.M., Bre, F., Nigro, N.M., Fachinotti, V., 2018. Computational modeling of natural ventilation in low-rise non-rectangular floor-plan buildings. Build. Simul. 11, 1255–1271.

Google, 2022. Google Earth imagery [WWW Document]. URL http://www.google.com/earth/index.html (accessed 1.23.22).

Gough, H.L., Barlow, J.F., Luo, Z., King, M.F., Halios, C.H., Grimmond, C.S.B., 2020. Evaluating single-sided natural ventilation models against full-scale idealised measurements: Impact of wind direction and turbulence. Build. Environ. 170, 106556.

Gracik, S., Heidarinejad, M., Liu, J., Srebric, J., 2015. Effect of urban neighborhoods on the performance of building cooling systems. Build. Environ. 90, 15–29.

Green, H., Bailey, J., Schwarz, L., Vanos, J., Ebi, K., Benmarhnia, T., 2019. Impact of heat on mortality and morbidity in low and middle income countries: A review of the epidemiological evidence and considerations for future research. Environ. Res. 171, 80–91.

Grimmond, C.S.B., Blackett, M., Best, M.J., Baik, J.-J., Belcher, S.E., Beringer, J., Bohnenstengel, S.I., Calmet, I., Chen, F., Coutts, A., Dandou, A., Fortuniak, K., Gouvea, M.L., Hamdi, R., Hendry, M., Kanda, M., Kawai, T., Kawamoto, Y., Kondo, H., Krayenhoff, E.S., Lee, S.-H., Loridan, T., Martilli, A., Masson, V., Miao, S., Oleson, K., Ooka, R., Pigeon, G., Porson, A., Ryu, Y.-H., Salamanca, F., Steeneveld, G.J., Tombrou, M., Voogt, J.A., Young, D.T., Zhang, N., 2011. Initial results from Phase 2 of the international urban energy balance model comparison. Int. J. Climatol. 31, 244–272.

Grimmond, C.S.B., Blackett, M., Best, M.J., Barlow, J., Baik, J.J., Belcher, S.E., Bohnenstengel, S.I., Calmet, I., Chen, F., Dandou, A., Fortuniak, K., Gouvea, M.L., Hamdi, R., Hendry, M., Kawai, T., Kawamoto, Y., Kondo, H., Krayenhoff, E.S., Lee, S.H., Loridan, T., Martilli, A., Masson, V., Miao, S., Oleson, K., Pigeon, G., Porson, A., Ryu, Y.H., Salamanca, F., Shashua-Bar, L., Steeneveld, G.J., Tombrou, M., Voogt, J., Young, D., Zhang, N., 2010. The International Urban Energy Balance Models Comparison Project: First Results from Phase 1. J. Appl. Meteorol. Climatol. 49, 1268–1292.

Grimmond, C.S.B., Cleugh, H.A., Oke, T.R., 1991. An objective urban heat storage model and its comparison with other schemes. Atmos. Environ. Part B. Urban Atmos. 25, 311–326.

Grimmond, C.S.B., Oke, T.R., 1991. An evapotranspiration-interception model for urban areas. Water Resour. Res. 27, 1739–1755.

Grimmond, C.S.B., Oke, T.R., 1999a. Aerodynamic Properties of Urban Areas Derived from Analysis of Surface Form. J. Appl. Meteorol. 38, 1262–1292.

Grimmond, C.S.B., Oke, T.R., 1999b. Heat Storage in Urban Areas: Local-Scale Observations and Evaluation of a Simple Model. J. Appl. Meteorol. 38, 922–940.

Grimmond, C.S.B., Oke, T.R., 2002. Turbulent Heat Fluxes in Urban Areas: Observations and a Local-Scale Urban Meteorological Parameterization Scheme

(LUMPS). J. Appl. Meteorol. 41, 792–810.

Grimmond, C.S.B., Oke, T.R., Steyn, D.G., 1986. Urban Water Balance: 1. A Model for Daily Totals. Water Resour. Res. 22, 1397–1403.

Grimmond, S., 2007. Urbanization and global environmental change: local effects of urban warming. Geogr. J. 173, 83–88.

Grosso, M., 1992. Wind pressure distribution around buildings: a parametrical model. Energy Build. 18, 101–131.

Guo, W., Liang, S., Li, W., Xiong, B., Wen, H., 2022. Combining EnergyPlus and CFD to predict and optimize the passive ventilation mode of medium-sized gymnasium in subtropical regions. Build. Environ. 207, 108420.

Gupta, R., Gregg, M., 2013. Preventing the overheating of English suburban homes in a warming climate. Build. Res. Inf. 41, 281–300.

Halwatura, R.U., Jayasinghe, M.T.R., 2007. Strategies for improved micro-climates in high-density residential developments in tropical climates. Energy Sustain. Dev. 11, 54–65.

Halwatura, R.U., Jayasinghe, M.T.R., 2008. Thermal performance of insulated roof slabs in tropical climates. Energy Build. 40, 1153–1160.

Hamdy, M., Carlucci, S., Hoes, P.-J., Hensen, J.L.M., 2017. The impact of climate change on the overheating risk in dwellings—A Dutch case study. Build. Environ. 122, 307–323.

Han, Y., Taylor, J.E., Pisello, A.L., 2017. Exploring mutual shading and mutual reflection inter-building effects on building energy performance. Appl. Energy 185, 1556–1564.

Harman, I.N., Finnigan, J.J., 2007. A simple unified theory for flow in the canopy and roughness sublayer. Boundary-Layer Meteorol. 123, 339–363.

Harman, I.N., Finnigan, J.J., 2008. Scalar Concentration Profiles in the Canopy and Roughness Sublayer. Boundary-Layer Meteorol. 129, 323–351.

Hawkins, T.W., Brazel, A.J., Stefanov, W.L., Bigler, W., Saffell, E.M., 2004. The Role of Rural Variability in Urban Heat Island Determination for Phoenix, Arizona. J. Appl. Meteorol. 43, 476–486.

Heaviside, C., Macintyre, H., Vardoulakis, S., 2017. The Urban Heat Island: Implications for Health in a Changing Environment. Curr. Environ. Heal. reports 4, 296–305.

Heaviside, C., Vardoulakis, S., Cai, X.M., 2016. Attribution of mortality to the urban heat island during heatwaves in the West Midlands, UK. Environ. Heal. A Glob. Access Sci. Source 15, 49–59.

Heracleous, C., Michael, A., 2018. Assessment of overheating risk and the impact of natural ventilation in educational buildings of Southern Europe under current and future climatic conditions. Energy 165, 1228–1239.

Hersbach, H., Bell, B., Berrisford, P., Hirahara, S., Horányi, A., Muñoz-Sabater, J., Nicolas, J., Peubey, C., Radu, R., Schepers, D., Simmons, A., Soci, C., Abdalla, S., Abellan, X., Balsamo, G., Bechtold, P., Biavati, G., Bidlot, J., Bonavita, M., De Chiara, G., Dahlgren, P., Dee, D., Diamantakis, M., Dragani, R., Flemming, J., Forbes, R., Fuentes, M., Geer, A., Haimberger, L., Healy, S., Hogan, R.J., Hólm, E., Janisková, M., Keeley, S., Laloyaux, P., Lopez, P., Lupu, C., Radnoti, G., de Rosnay, P., Rozum, I., Vamborg, F., Villaume, S., Thépaut, J.N., Muñoz-Sabater, J., Nicolas, J., Peubey, C., Radu, R., Schepers, D., Simmons, A., Soci, C., Abdalla, S., Abellan, X., Balsamo, G., Bechtold, P., Biavati, G., Bidlot, J., Bonavita, M., Chiara, G., Dahlgren, P., Dee, D., Diamantakis, M., Dragani, R., Flemming, J., Forbes, R., Fuentes, M., Geer, A., Haimberger, L., Healy, S., Hogan, R.J., Hólm, E., Janisková, M., Keeley, S., Laloyaux, P., Lopez, P., Lupu, C., Radnoti, G., Rosnay, P., Rozum, I., Vamborg, F., Villaume, S., Thépaut, J.N., 2020. The ERA5 global reanalysis. Q. J. R. Meteorol. Soc. 146, 1999–2049.

Hiyama, K., Glicksman, L., 2015. Preliminary design method for naturally ventilated buildings using target air change rate and natural ventilation potential maps in the United States.

Holmes, S.H., Phillips, T., Wilson, A., 2016. Overheating and passive habitability: Indoor health and heat indices. Build. Res. Inf. 44, 1–19.

Howell, J.R., Siegel, R., Menguc, M.P., 2010. Thermal radiation heat transfer, 5th ed. CRC Press LLC, Bosa Roca.

Hsieh, C.-M., Li, J.-J., Zhang, L., Schwegler, B., 2018. Effects of tree shading and transpiration on building cooling energy use. Energy Build. 159, 382–397.

Huang, H., Deng, X., Yang, H., Zhou, X., Jia, Q., 2020. Spatio-Temporal Mechanism Underlying the Effect of Urban Heat Island on Cardiovascular Diseases. Iran. J. Public Health 49, 1455.

Humphreys, M.A., Nicol, J.F., 2002. The validity of ISO-PMV for predicting comfort votes in every-day thermal environments. Energy Build. 34, 667–684.

Hwang, R.-L., Lin, C.-Y., Huang, K.-T., 2017. Spatial and temporal analysis of urban heat island and global warming on residential thermal comfort and cooling energy in Taiwan. Energy Build. 152, 804–812.

Hwang, R.L., Lin, T.P., Lin, F.Y., 2020. Evaluation and mapping of building overheating risk and air conditioning use due to the urban heat island effect. J. Build. Eng. 32, 101726.

Im, E.S., Pal, J.S., Eltahir, E.A.B., 2017. Deadly heat waves projected in the densely populated agricultural regions of South Asia. Sci. Adv. 3.

Indraganti, M., 2010. Adaptive use of natural ventilation for thermal comfort in Indian apartments. Build. Environ. 45, 1490–1507.

Indraganti, M., Ooka, R., Rijal, H.B., 2013. Field investigation of comfort temperature in Indian office buildings: A case of Chennai and Hyderabad. Build. Environ. 65, 195–214.

Integrated Environmental Solutions, 2018. MacroFlo calculation methods [WWW Document]. URL https://help.iesve.com/ve2018/ (accessed 6.30.22).

IPCC, 2014. Climate Change 2014: Synthesis Report. Geneva, Switzerland.

ISO, 1984. ISO 7730:1984 - Moderate thermal environments — Determination of the PMV and PPD indices and specification of the conditions for thermal comfort.

ISO, 2004. ISO 7933:2004 - Ergonomics of the thermal environment — Analytical determination and interpretation of heat stress using calculation of the predicted heat strain.

ISO, 2017. ISO 7243:2017 - Ergonomics of the thermal environment — Assessment of heat stress using the WBGT (wet bulb globe temperature) index.

Israel Meteorological Service, 2022. Questions and Answers | Israel Meteorological Service [WWW Document]. URL https://ims.gov.il/en/node/318 (accessed 9.30.22).

Jamaludin, A.A., Hussein, H., Mohd Ariffin, A.R., Keumala, N., 2014. A study on different natural ventilation approaches at a residential college building with the internal courtyard arrangement. Energy Build. 72, 340–352.

Jandaghian, Z., Berardi, U., 2020. Analysis of the cooling effects of higher albedo surfaces during heat waves coupling the Weather Research and Forecasting model with building energy models. Energy Build. 207.

Järvi, L., Grimmond, C.S.B., Christen, A., 2011. The Surface Urban Energy and Water Balance Scheme (SUEWS): Evaluation in Los Angeles and Vancouver. J. Hydrol. 411, 219–237.

Järvi, L., Grimmond, C.S.B., Taka, M., Nordbo, A., Setälä, H., Strachan, I.B., 2014. Development of the Surface Urban Energy and Water Balance Scheme (SUEWS) for cold climate cities. Geosci. Model Dev. 7, 1691–1711.

JICA, 2014. Urban transportation system development project for Colombo metropolitan region and suburbs (CoMTrans), final report.

Joe, J., Choi, W., Kwon, H., Huh, J.H., 2013. Load characteristics and operation strategies of building integrated with multi-story double skin facade. Energy Build. 60, 185–198.

Johansson, E., Emmanuel, R., 2006. The influence of urban design on outdoor thermal comfort in the hot, humid city of Colombo, Sri Lanka. Int. J. Biometeorol. 51, 119–133.

Johari, F., Peronato, G., Sadeghian, P., Zhao, X., Widén, J., 2020. Urban building energy modeling: State of the art and future prospects. Renew. Sustain. Energy Rev. 128, 109902.

Johnson, M.H., Zhai, Z.J., Krarti, M., 2012. Performance evaluation of network airflow models for natural ventilation, HVAC and R Research.

Kalkstein, L.S., Eisenman, D.P., de Guzman, E.B., Sailor, D.J., 2022. Increasing trees and high-albedo surfaces decreases heat impacts and mortality in Los Angeles, CA. Int. J. Biometeorol. 66, 911–925.

Kanda, M., Kanega, M., Kawai, T., Moriwaki, R., Sugawara, H., 2007. Roughness Lengths for Momentum and Heat Derived from Outdoor Urban Scale Models. J. Appl. Meteorol. Climatol. 46, 1067–1079.

Katavoutas, G., Founda, D., 2019. Intensification of thermal risk in Mediterranean climates: evidence from the comparison of rational and simple indices. Int. J. Biometeorol. 63, 1251–1264.

Kent, C.W., Lee, K., Ward, H.C., Hong, J.-W., Hong, J., Gatey, D., Grimmond, S., 2018.

Aerodynamic roughness variation with vegetation: analysis in a suburban neighbourhood and a city park. Urban Ecosyst. 21, 227–243.

Kesten, D., Tereci, A., Strzalka, A.M., Eicker, U., 2012. A method to quantify the energy performance in urban quarters. In: HVAC and R Research. pp. 100–111.

Kilbourne, E.M., 1996. Heat Waves and Hot Environments. Public Heal. Consequences Disasters 245–269.

Kim, D., Cox, S.J., Cho, H., Yoon, J., 2018. Comparative investigation on building energy performance of double skin façade (DSF) with interior or exterior slat blinds. J. Build. Eng. 20, 411–423.

Kim, J.H., 2009. Estimating classification error rate: Repeated cross-validation, repeated hold-out and bootstrap. Comput. Stat. Data Anal. 53, 3735–3745.

Knoll, B., Phaff, J., de Gids, W., 1996. Pressure coefficient simulation program. Air Infiltration Rev. 17, 1–5.

Kokkonen, T. V., Grimmond, C.S.B., Räty, O., Ward, H.C., Christen, A., Oke, T.R., Kotthaus, S., Järvi, L., 2018. Sensitivity of Surface Urban Energy and Water Balance Scheme (SUEWS) to downscaling of reanalysis forcing data. Urban Clim. 23, 36–52.

Kong, J., Zhao, Y., Carmeliet, J., Lei, C., 2021. Urban Heat Island and Its Interaction with Heatwaves: A Review of Studies on Mesoscale. Sustainability 13, 10923.

Kovats, R.S., Hajat, S., 2007. Heat Stress and Public Health: A Critical Review. Annu. Rev. Public Health 29, 41–55.

Kovats, R.S., Hajat, S., 2008. Heat Stress and Public Health: A Critical Review. Annu. Rev. Public Health 29, 41–55.

Kubota, T., Chyee, D.T.H., Ahmad, S., 2009. The effects of night ventilation technique on indoor thermal environment for residential buildings in hot-humid climate of Malaysia. Energy Build. 41, 829–839.

Lan, L., Wargocki, P., Lian, Z., 2011. Quantitative measurement of productivity loss due to thermal discomfort. Energy Build. 43, 1057–1062.

Lawrence, M.G., 2005. The Relationship between Relative Humidity and the Dewpoint Temperature in Moist Air: A Simple Conversion and Applications. Bull. Am. Meteorol. Soc. 86, 225–234.

Li, D., Bou-Zeid, E., 2013. Synergistic Interactions between Urban Heat Islands and Heat Waves: The Impact in Cities Is Larger than the Sum of Its Parts. J. Appl. Meteorol. Climatol. 52, 2051–2064.

Li, D.H.W., Wong, S.L., 2007. Daylighting and energy implications due to shading effects from nearby buildings. Appl. Energy 84, 1199–1209.

Li, Y., Li, X., 2015. Natural ventilation potential of high-rise residential buildings in northern China using coupling thermal and airflow simulations. Build. Simul. 8, 51–64.

Liddament, M., 1986. Air infiltration calculation techniques: an applications guide. Coventry.

Lim, C.L., 2020. Fundamental Concepts of Human Thermoregulation and Adaptation to Heat: A Review in the Context of Global Warming. Int. J. Environ. Res. Public Health 17, 7795.

Lim, J., Akashi, Y., Ooka, R., Kikumoto, H., Choi, Y., 2017. A probabilistic approach to the energy-saving potential of natural ventilation: Effect of approximation method for approaching wind velocity. Build. Environ. 122, 94–104.

Lim, J., Ooka, R., Kikumoto, H., 2016. Effect of diurnal variation in wind velocity profiles on ventilation performance estimates. Energy Build. 130, 397–407.

Lima, I., Scalco, V., Lamberts, R., 2019. Estimating the impact of urban densification on high-rise office building cooling loads in a hot and humid climate. Energy Build. 182, 30–44.

Lindberg, F., Grimmond, C.S.B., Gabey, A., Huang, B., Kent, C.W., Sun, T., Theeuwes, N.E., Järvi, L., Ward, H.C., Capel-Timms, I., Chang, Y., Jonsson, P., Krave, N., Liu, D., Meyer, D., Olofson, K.F.G., Tan, J., Wästberg, D., Xue, L., Zhang, Z., 2018a. Urban Multi-scale Environmental Predictor (UMEP): An integrated tool for city-based climate services. Environ. Model. Softw. 99, 70–87.

Lindberg, F., Grimmond, C.S.B.S.B., Gabey, A., Huang, B., Kent, C.W., Sun, T., Theeuwes, N.E., Järvi, L., Ward, H.C., Capel-Timms, I., Chang, Y., Jonsson, P., Krave, N., Liu, D., Meyer, D., Olofson, K.F.G., Tan, J., Wästberg, D., Xue, L., Zhang, Z., 2018b. Urban Multi-scale Environmental Predictor (UMEP): An integrated tool for city-based climate services. Environ. Model. Softw. 99, 70–87.

Liu, C., Kershaw, T., Fosas, D., Ramallo Gonzalez, A.P., Natarajan, S., Coley, D.A., 2017. High resolution mapping of overheating and mortality risk. Build. Environ. 122, 1–14.

Liu, J., Heidarinejad, M., Gracik, S., Srebric, J., 2015. The impact of exterior surface convective heat transfer coefficients on the building energy consumption in urban neighborhoods with different plan area densities. Energy Build. 86, 449–463.

Lobelia, 2022. Past Climate Explorer [WWW Document]. URL https://era5.lobelia.earth/en/?lon=79.98222086167539&lat=7.029321369050912&zoom=18 (accessed 10.3.22).

Loridan, T., Grimmond, C.S.B., Offerle, B.D., Young, D.T., Smith, T.E.L., Järvi, L., Lindberg, F., 2011. Local-Scale Urban Meteorological Parameterization Scheme (LUMPS): Longwave Radiation Parameterization and Seasonality-Related Developments. J. Appl. Meteorol. Climatol. 50, 185–202.

Luo, X., Hong, T., Tang, Y.-H., 2020. Modeling Thermal Interactions between Buildings in an Urban Context. Energies 13, 2382.

Luo, Z., Zhao, J., Gao, J., He, L., 2007. Estimating natural-ventilation potential considering both thermal comfort and IAQ issues. Build. Environ. 42, 2289–2298.

Macpherson, R.K., 1962. The Assessment of the Thermal Environment. A Review. Occup. Environ. Med. 19, 151–164.

Makantasi, A.-M., Mavrogianni, A., 2016. Adaptation of London's social housing to climate change through retrofit: a holistic evaluation approach. Adv. Build. Energy Res. 10, 99–124.

Martinopoulos, G., Serasidou, A., Antoniadou, P., Papadopoulos, A.M., 2018. Building Integrated Shading and Building Applied Photovoltaic System Assessment in the Energy Performance and Thermal Comfort of Office Buildings. Sustainability 10, 4670.

Martins, N.R., Carrilho Da Graça, G., 2017. Simulation of the effect of fine particle pollution on the potential for natural ventilation of non-domestic buildings in European cities.

Masson, V., 2000. A physically-based scheme for the urban energy budget in atmospheric models. Boundary-Layer Meteorol. 94, 357–397.

Masterson, J.M., Richardson, F.A., 1979. Humidex, a method of quantifying human discomfort due to excessive heat and humidity, Environment Canada. Atmos. Environ. Serv. Downsview, Ontario 151, 1–79.

Mavrogianni, A., Davies, M., Taylor, J., Chalabi, Z., Biddulph, P., Oikonomou, E., Das, P., Jones, B., 2014. The impact of occupancy patterns, occupant-controlled ventilation and shading on indoor overheating risk in domestic environments. Build. Environ. 78, 183–198.

Mavrogianni, A., Wilkinson, P., Davies, M., Biddulph, P., Oikonomou, E., 2012. Building characteristics as determinants of propensity to high indoor summer temperatures in London dwellings. Build. Environ. 55, 117–130.

McGill, G., Sharpe, T., Robertson, L., Gupta, R., Mawditt, I., 2017. Meta-analysis of indoor temperatures in new-build housing. Build. Res. Inf. 45, 19–39.

McLeod, R.S., Hopfe, C.J., Kwan, A., 2013. An investigation into future performance and overheating risks in Passivhaus dwellings. Build. Environ. 70, 189–209.

McLeod, R.S., Swainson, M., 2017. Chronic overheating in low carbon urban developments in a temperate climate. Renew. Sustain. Energy Rev.

McPherson, E.G., Nowak, D., Heisler, G., Grimmond, S., Souch, C., Grant, R., Rowntree, R., 1997. Quantifying urban forest structure, function, and value: the Chicago Urban Forest Climate Project. Urban Ecosyst. 1997 11 1, 49–61.

Md Din, M.F., Lee, Y.Y., Ponraj, M., Ossen, D.R., Iwao, K., Chelliapan, S., 2014. Thermal comfort of various building layouts with a proposed discomfort index range for tropical climate. J. Therm. Biol. 41, 6–15.

Mei, S.J., Hu, J.T., Liu, D., Zhao, F.Y., Li, Y., Wang, Y., Wang, H.Q., 2017. Wind driven natural ventilation in the idealized building block arrays with multiple urban morphologies and unique package building density. Energy Build. 155, 324–338.

Menne, M.J., Durre, I., Vose, R.S., Gleason, B.E., Houston, T.G., 2012. An overview of the global historical climatology network-daily database. J. Atmos. Ocean. Technol. 29, 897–910.

Miller, C., Thomas, D., Kämpf, J., Schlueter, A., 2018. Urban and building multiscale co-simulation: case study implementations on two university campuses. J. Build. Perform. Simul. 11, 309–321.

Mills, G., 2006. Progress toward sustainable settlements: a role for urban climatology. Theor. Appl. Climatol. 84, 69–76.

Mogul, R., Mitra, E., Suri, M., Saifi, S., 2022. India and Pakistan heatwave is "testing the limits of human survivability," expert says. CNN.

Mohamed, S., Srinavin, K., 2005. Forecasting labor productivity changes in construction using the PMV index. Int. J. Ind. Ergon. 35, 345–351.

MoHURD, 2012. Evaluation standard for indoor thermal environment in civil buildings (GB/T50785-2012). Ministry of Housing and Urban-rural Development, P.R. China, Beijing.

MoHURD, 2015. Design standard for energy efficiency of public buildings (GB50189-2015). Ministry of Housing and Urban-rural Development, P.R. China, Beijing.

MoHURD, 2016. Code for thermal design of civil building (GB50176-2016). Ministry of Housing and Urban-rural Development, P.R. China, Beijing.

Molinaro, A.M., Simon, R., Pfeiffer, R.M., 2005. Prediction error estimation: a comparison of resampling methods. Bioinformatics 21, 3301–3307.

Moradi, M., Krayenhoff, E.S., Aliabadi, A.A., 2022. A comprehensive indoor–outdoor urban climate model with hydrology: The Vertical City Weather Generator (VCWG v2.0.0). Build. Environ. 207, 108406.

Morgan, C., Foster, J.A., Poston, A., Sharpe, T.R., 2017. Overheating in Scotland: contributing factors in occupied homes. Build. Res. Inf. 45, 143–156.

Morrison, W., Kotthaus, S., Grimmond, C.S.B., Inagaki, A., Yin, T., Gastellu-Etchegorry, J.P., Kanda, M., Merchant, C.J., 2018. A novel method to obtain three-dimensional urban surface temperature from ground-based thermography. Remote Sens. Environ. 215, 268–283.

Morrison, W., Kotthaus, S., Grimmond, S., 2021. Urban surface temperature observations from ground-based thermography: intra- and inter-facet variability. Urban Clim. 35, 100748.

Morrison, W., Yin, T., Lauret, N., Guilleux, J., Kotthaus, S., Gastellu-Etchegorry, J.-P.P., Norford, L., Grimmond, S., 2020. Atmospheric and emissivity corrections for ground-based thermography using 3D radiative transfer modelling. Remote Sens. Environ. 237, 111524.

Mulville, M., Stravoravdis, S., 2016. The impact of regulations on overheating risk in dwellings. Build. Res. Inf. 44, 520–534.

National Weather Service, 2022. Heat Forecast Tools [WWW Document]. URL https://www.weather.gov/safety/heat-index (accessed 4.12.22).

Nicol, F., 2004. Adaptive thermal comfort standards in the hot–humid tropics. Energy Build. 36, 628–637.

Nicol, F., Humphreys, M., 2010. Derivation of the adaptive equations for thermal comfort in free-running buildings in European standard EN15251. Build. Environ. 45, 11–17.

Nicol, F., Humphreys, M., Roaf, S., 2012. Adaptive Thermal Comfort: Principles and Practice, 1st ed. Routledge, London, UK.

Nicol, J.F., Hacker, J., Spires, B., Davies, H., 2009. Suggestion for new approach to overheating diagnostics. https://doi.org/10.1080/09613210902904981 37, 348–357.

Nicol, J.F., Humphreys, M.A., 2002. Adaptive thermal comfort and sustainable thermal standards for buildings. Energy Build. 34, 563–572.

O'lenick, C.R., Baniassadi, A., Michael, R., Monaghan, A., Boehnert, J., Yu, X., Hayden, M.H., Wiedinmyer, C., Zhang, K., Crank, P.J., Heusinger, J., Hoel, P., Sailor, D.J., Wilhelmi, O. V., 2020. A Case-Crossover Analysis of Indoor Heat Exposure on Mortality and Hospitalizations among the Elderly in Houston, Texas. Environ. Health Perspect. 128, 1–17.

Offerle, B., Grimmond, C.S.B., Oke, T.R., 2003. Parameterization of Net All-Wave Radiation for Urban Areas. J. Appl. Meteorol. 42, 1157–1173.

Oikonomou, E., Davies, M., Mavrogianni, A., Biddulph, P., Wilkinson, P., Kolokotroni, M., 2012. Modelling the relative importance of the urban heat island and the thermal quality of dwellings for overheating in London. Build. Environ. 57, 223–238.

Oke, T.R., 1982. The energetic basis of the urban heat island. Q. J. R. Meteorol. Soc. 108, 1–24.

Oke, T.R., 1987. Boundary layer climates, 2nd ed. Routledge, Taylor and Francis Group, London, UK.

Oke, T.R., Mills, G., Christen, A., Voogt, J.A., 2017. Urban climates. Cambridge University Press, Cambridge.

Oleson, K.W., Bonan, G.B., Feddema, J., Jackson, T., 2011. An examination of urban heat island characteristics in a global climate model. Int. J. Climatol. 31, 1848–1865.

Oleson, K.W., Monaghan, A., Wilhelmi, O., Barlage, M., Brunsell, N., Feddema, J., Hu, L., Steinhoff, D.F., 2015. Interactions between urbanization, heat stress, and climate change. Clim. Change 129, 525–541.

Olsen, E.L., Chen, Q., 2003. Energy consumption and comfort analysis for different low-energy cooling systems in a mild climate. Energy Build. 35, 560–571.

Omidvar, H., Sun, T., Grimmond, S., Bilesbach, D., Black, A., Chen, J., Duan, Z., Gao, Z., Iwata, H., McFadden, J.P., 2022. Surface Urban Energy and Water Balance Scheme (v2020a) in vegetated areas: parameter derivation and performance evaluation using FLUXNET2015 dataset. Geosci. Model Dev. 15, 3041–3078.

OpenStreetMap contributors, 2021. Planet dump retrieved from https://planet.osm.org [WWW Document]. URL https://www.openstreetmap.org (accessed 8.31.21).

Oropeza-Perez, I., Østergaard, P.A., 2013. Potential of natural ventilation in temperate countries-A case study of Denmark.

Oudin Åström, D., Bertil, F., Joacim, R., 2011. Heat wave impact on morbidity and mortality in the elderly population: A review of recent studies. Maturitas 69, 99–105.

Park, B., Lee, S., 2020. Investigation of the Energy Saving Efficiency of a Natural Ventilation Strategy in a Multistory School Building. Energies 2020, Vol. 13, Page 1746 13, 1746.

Patankar, A., 2017. Colombo: Exposure, Vulnerability, and Ability to Respond to Floods .

Pathan, A., Mavrogianni, A., Summerfield, A., Oreszczyn, T., Davies, M., 2017. Monitoring summer indoor overheating in the London housing stock. Energy Build. 141, 361–378.

Pathirana, S., Rodrigo, A., Halwatura, R., 2019. Effect of building shape, orientation, window to wall ratios and zones on energy efficiency and thermal comfort of naturally ventilated houses in tropical climate. Int. J. Energy Environ. Eng. 10, 107–120.

Pathirana, S.M., Halwatura, R.U., 2020. Effect of occupant behaviour on household energy efficiency in Sri Lanka. In: Proceedings of the National Engineering Research Symposium (NERS 2020). National Engineering Research and Development Centre of Sri Lanka, pp. 170–176.

Patil, K.N., Kaushik, S.C., 2015. Study of climatic potential for natural ventilation in buildings for typical Indian cities. Int. J. Vent. 13, 369–380.

Perera, N.G.R., Emmanuel, R., 2018. A “Local Climate Zone” based approach to urban planning in Colombo, Sri Lanka. Urban Clim. 23, 188–203.

Pesic, N., Roset Calzada, J., Muros Alcojor, A., 2018. Natural ventilation potential of the Mediterranean coastal region of Catalonia. Energy Build. 169, 236–244.

Phadke, A., Medrano, F.A., Chu, T., Sailor, D.J., Baniassadi, A., O’lenick, C.R., Wilhelmi, O. V, 2019. The growing threat of heat disasters. Environ. Res. Lett. 14, 054006.

Pisello, A.L., Castaldo, V.L., Poli, T., Cotana, F., 2014. Simulating the Thermal-Energy Performance of Buildings at the Urban Scale: Evaluation of Inter-Building Effects in Different Urban Configurations. J. Urban Technol. 21, 3–20.

Porritt, S., Shao, L., Cropper, P., Goodier, C., 2011. Adapting dwellings for heat waves. Sustain. Cities Soc. De Montfort University.

Porritt, S.M., Cropper, P.C., Shao, L., Goodier, C.I., 2012. Ranking of interventions to reduce dwelling overheating during heat waves. Energy Build. 55, 16–27.

Porritt, S.M.M., Cropper, P.C.C., Shao, L., Goodier, C.I.I., 2012. Ranking of interventions to reduce dwelling overheating during heat waves. Energy Build. 55, 16–27.

Psomas, T., Heiselberg, P., Duer, K., Bjørn, E., 2016. Overheating risk barriers to energy renovations of single family houses: Multicriteria analysis and assessment. Energy Build. 117, 138–148.

Public Health England, 2015. Heatwave plan for England Protecting health and reducing harm from severe heat and heatwaves. London.

QGIS Development Team, 2022. QGIS geographic information system [WWW Document]. URL https://www.qgis.org (accessed 9.11.22).

Quah, A.K.L., Roth, M., 2012. Diurnal and weekly variation of anthropogenic heat emissions in a tropical city, Singapore. Atmos. Environ. 46, 92–103.

Raftery, P., Lee, E., Webster, T., Hoyt, T., Bauman, F., 2014. Effects of furniture and contents on peak cooling load. Energy Build. 85, 445–457.

Rahif, R., Amaripadath, D., Attia, S., 2021. Review on Time-Integrated Overheating

Evaluation Methods for Residential Buildings in Temperate Climates of Europe. Energy Build. 252, 111463.

Rajapaksha, I., Nagai, H., Okumiya, M., 2003. A ventilated courtyard as a passive cooling strategy in the warm humid tropics. Renew. Energy 28, 1755–1778.

Rajapaksha, U., 2020. Environmental Heat Stress on Indoor Environments in Shallow, Deep and Covered Atrium Plan Form Office Buildings in Tropics. Climate 8, 36.

Raji, B., Tenpierik, M.J., Bokel, R., van den Dobbelsteen, A., 2020. Natural summer ventilation strategies for energy-saving in high-rise buildings: a case study in the Netherlands. Int. J. Vent. 19, 25–48.

Ramamurthy, P., Bou-Zeid, E., 2017. Heatwaves and urban heat islands: A comparative analysis of multiple cities. J. Geophys. Res. Atmos. 122, 168–178.

Ramponi, R., Angelotti, A., Blocken, B., 2014a. Energy saving potential of night ventilation: Sensitivity to pressure coefficients for different European climates. Appl. Energy 123, 185–195.

Ramponi, R., Gaetani, I., Angelotti, A., 2014b. Influence of the urban environment on the effectiveness of natural night-ventilation of an office building. Energy Build. 78, 25–34.

Ran, J., Tang, M., 2018. Passive cooling of the green roofs combined with night-time ventilation and walls insulation in hot and humid regions. Sustain. Cities Soc. 38, 466–475.

Rathnayake, N.U., Perera, N.G.R., Emmanuel, M.P.R., 2020. Anthropogenic heat implications of Colombo core area development plan. IOP Conf. Ser. Earth Environ. Sci. 471, 012002.

Ratnaweera, C., Hestnes, A.G., 1996. Enhanced cooling in typical Sri Lankan dwellings. Energy Build. 23, 183–190.

Rawat, M., Singh, R.N., 2022. A study on the comparative review of cool roof thermal performance in various regions. Energy Built Environ. 3, 327–347.

Ridley, I., Bere, J., Clarke, A., Schwartz, Y., Farr, A., 2014. The side by side in use monitored performance of two passive and low carbon Welsh houses. Energy Build. 82, 13–26.

Robinson, D., Haldi, F., Kämpf, J., Leroux, P., Perez, D., Rasheed, A., Wilke, U., 2009. Citysim: Comprehensive micro-simulation of resource flows for sustainable urban planning. IBPSA 2009 - Int. Build. Perform. Simul. Assoc. 2009 1083–1090.

Rocklöv, J., Forsberg, B., Ebi, K., Bellander, T., 2014. Susceptibility to mortality related to temperature and heat and cold wave duration in the population of Stockholm County, Sweden. Glob. Health Action 7.

Roghanchi, P., Kocsis, K.C., 2018. Challenges in Selecting an Appropriate Heat Stress Index to Protect Workers in Hot and Humid Underground Mines. Saf. Health Work 9, 10.

Roth, M., Oke, T.R., 1995. Relative Efficiencies of Turbulent Transfer of Heat, Mass, and Momentum over a Patchy Urban Surface. J. Atmos. Sci. 52, 1863–1874.

Rothfusz, L.P., 1990. The heat index equation (or, more than you ever wanted to know about heat index). Fort Worth, US.

Royapoor, M., Roskilly, T., 2015. Building model calibration using energy and environmental data. Energy Build. 94, 109–120.

Ruiz, G.R., Bandera, C.F., 2017. Validation of calibrated energy models: Common errors. Energies 10, 1587.

Sadeghi, M., Wood, G., Samali, B., de Dear, R., 2020. Effects of urban context on the indoor thermal comfort performance of windcatchers in a residential setting. Energy Build. 219, 110010.

Saif, J., Wright, A., Khattak, S., Elfadli, K., 2021. Keeping cool in the desert: using wind catchers for improved thermal comfort and indoor air quality at half the energy. Buildings 11, 100.

Sailor, D.J., 2011. A review of methods for estimating anthropogenic heat and moisture emissions in the urban environment. Int. J. Climatol. 31, 189–199.

Sakiyama, N.R.M., Mazzaferro, L., Carlo, J.C., Bejat, T., Garrecht, H., 2021. Natural ventilation potential from weather analyses and building simulation. Energy Build. 231, 110596.

Salvati, A., Coch Roura, H., Cecere, C., 2017. Assessing the urban heat island and its energy impact on residential buildings in Mediterranean climate: Barcelona case study. Energy Build. 146, 38–54.

Santamouris, M., Kolokotsa, D., 2013. Passive cooling dissipation techniques for buildings and other structures: The state of the art. Energy Build. 57, 74–94.

Santamouris, M., Papanikolaou, N., Livada, I., Koronakis, I., Georgakis, C., Argiriou, A., Assimakopoulos, D.., 2001. On the impact of urban climate on the energy consumption of buildings. Sol. Energy 70, 201–216.

Santamouris, M., Pavlou, K., Synnefa, A., Niachou, K., Kolokotsa, D., 2007. Recent progress on passive cooling techniques: Advanced technological developments to improve survivability levels in low-income households. Energy Build. 39, 859–866.

Santiago, J.L., Martilli, A., 2010. A dynamic urban canopy parameterization for mesoscale models based on computational fluid dynamics Reynolds-averaged Navier–Stokes microscale simulations. Boundary-Layer Meteorol. 137, 417–439.

Schellen, L., Van Marken Lichtenbelt, W.D., Loomans, M.G.L.C., Toftum, J., De Wit, M.H., 2010. Differences between young adults and elderly in thermal comfort, productivity, and thermal physiology in response to a moderate temperature drift and a steady-state condition. Indoor Air 20, 273–283.

Schoetter, R., Cattiaux, J., Douville, H., 2015. Changes of western European heat wave characteristics projected by the CMIP5 ensemble. Clim. Dyn. 45, 1601–1616.

Schulze, T., Eicker, U., 2013. Controlled natural ventilation for energy efficient buildings. Energy Build. 56, 221–232.

Schünemann, C., Schiela, D., Ortlepp, R., 2021. How window ventilation behaviour affects the heat resilience in multi-residential buildings. Build. Environ. 202, 107987.

Schwingshackl, C., Sillmann, J., Vicedo-Cabrera, A.M., Sandstad, M., Aunan, K., 2021.

Heat Stress Indicators in CMIP6: Estimating Future Trends and Exceedances of Impact-Relevant Thresholds. Earth's Futur. 9, 1–17.

Shapiro, Y., Seidman, D.S., 1990. Field and clinical observations of exertional heat stroke patients. Med. Sci. Sports Exerc. 22, 6–14.

Sharma, A., Andhikaputra, G., Wang, Y.-C., 2022. Heatwaves in South Asia: Characterization, Consequences on Human Health, and Adaptation Strategies. Atmosphere (Basel). 13, 734.

Shepard, D., 1964. A two-dimensional interpolation for irregularly-spaced data function. Proc. Ass. Comput. Mach. 517–524.

Short, C.A., Song, J., Mottet, L., Chen, S., Wu, J., Ge, J., 2018. Challenges in the low-carbon adaptation of China's apartment towers. Build. Res. Inf. 46, 899–930.

Simath, S., Emmanuel, R., 2022. Urban thermal comfort trends in Sri Lanka: the increasing overheating problem and its potential mitigation. Int. J. Biometeorol. 66, 1865–1876.

Singh, M.C., Garg, S.N., Jha, R., 2008. Different glazing systems and their impact on human thermal comfort—Indian scenario. Build. Environ. 43, 1596–1602.

Smith, A., Lott, N., Vose, R., 2011. The Integrated Surface Database: Recent Developments and Partnerships. Bull. Am. Meteorol. Soc. 92, 704–708.

Song, J., Huang, X., Shi, D., Lin, W.E., Fan, S., Linden, P.F., 2021. Natural ventilation in London: Towards energy-efficient and healthy buildings. Build. Environ. 195, 107722.

Sorgato, M.J., Melo, A.P., Lamberts, R., 2016. The effect of window opening ventilation control on residential building energy consumption. Energy Build. 133, 1–13.

Southall, R.G., 2018. An assessment of the potential of supply-side ventilation demand control to regulate natural ventilation flow patterns and reduce domestic space heating consumption. Energy Build. 168, 201–214.

Sri Lanka Ministry of Environment, 2019. The Kigali cooling plan strategy for Sri Lanka.

Sri Lanka Sustainable Energy Authority, 2021. Energy Efficiency Building Code of Sri Lanka. Colombo.

Stazi, F., Bonfigli, C., Tomassoni, E., Di Perna, C., Munafò, P., 2015. The effect of high thermal insulation on high thermal mass: Is the dynamic behaviour of traditional envelopes in Mediterranean climates still possible? Energy Build. 88, 367–383.

Stazi, F., Tomassoni, E., Di Perna, C., 2017. Super-insulated wooden envelopes in Mediterranean climate: Summer overheating, thermal comfort optimization, environmental impact on an Italian case study. Energy Build. 138, 716–732.

Steadman, R.G., 1979a. The Assessment of Sultriness. Part I: A Temperature-Humidity Index Based on Human Physiology and Clothing Science. J. Appl. Meteorol. 18, 861–873.

Steadman, R.G., 1979b. The assessment of sultriness. Part II: effects of wind, extra radiation and barometric pressure on apparent temperature. J. Appl. Meteorol. 18, 874–885.

Steadman, R.G., 1984. A Universal Scale of Apparent Temperature. J. Clim. Appl. Meteorol. 23, 1674–1687.

Stewart, I.D., Oke, T.R., 2012. Local Climate Zones for Urban Temperature Studies. Bull. Am. Meteorol. Soc. 93, 1879–1900.

Stretton, M.A., Morrison, W., Hogan, R.J., Grimmond, S., 2022. Evaluation of the SPARTACUS-Urban Radiation Model for Vertically Resolved Shortwave Radiation in Urban Areas. Boundary-Layer Meteorol. 184, 301–331.

Stull, R., 2011. Wet-Bulb Temperature from Relative Humidity and Air Temperature. J. Appl. Meteorol. Climatol. 50, 2267–2269.

Sun, T., Grimmond, S., 2019. A Python-enhanced urban land surface model SuPy (SUEWS in Python, v2019.2): Development, deployment and demonstration. Geosci. Model Dev. 12, 2781–2795.

Sun, T., Järvi, L., Omidvar, H., Theeuwes, N., Lindberg, F., Li, Z., Grimmond, S., 2020. Urban-Meteorology-Reading/SUEWS: 2020a Release.

Sundell, J., Levin, H., Nazaroff, W.W., Cain, W.S., Fisk, W.J., Grimsrud, D.T., Gyntelberg, F., Li, Y., Persily, A.K., Pickering, A.C., Samet, J.M., Spengler, J.D., Taylor, S.T., Weschler, C.J., 2011. Ventilation rates and health: multidisciplinary review of the scientific literature. Indoor Air 21, 191–204.

Sung, U.J., Cho, S., Seo, D.H., Song, K.D., 2013. Analysis of reduced cooling load for a multistorey-building incorporating a ventilated double skin façade with a solar chimney channel. Int. J. Vent. 11, 381–391.

Swami, M. V, Chandra, S., 1987. Procedures for calculating natural ventilation airflow rates in buildings. Cape Canaveral.

Tabatabaei Sameni, S.M., Gaterell, M., Montazami, A., Ahmed, A., 2015. Overheating investigation in UK social housing flats built to the Passivhaus standard. Build. Environ. 92, 222–235.

Tan, J., Zheng, Y., Tang, X., Guo, C., Li, L., Song, G., Zhen, X., Yuan, D., Kalkstein, A.J., Li, F., Chen, H., 2010. The urban heat island and its impact on heat waves and human health in Shanghai. Int. J. Biometeorol. 54, 75–84.

Tan, Z., Deng, X., 2017. Assessment of natural ventilation potential for residential buildings across different climate zones in Australia. Atmosphere (Basel). 8, 177.

Tan, Z., Lau, K.K.L., Ng, E., 2016. Urban tree design approaches for mitigating daytime urban heat island effects in a high-density urban environment. Energy Build. 114, 265–274.

Tang, Y., Sun, T., Luo, Z., Omidvar, H., Theeuwes, N., Xie, X., Xiong, J., Yao, R., Grimmond, S., 2021. Urban meteorological forcing data for building energy simulations. Build. Environ. 204, 108088.

Taylor, J., Davies, M., Mavrogianni, A., Chalabi, Z., Biddulph, P., Oikonomou, E., Das, P., Jones, B., 2014. The relative importance of input weather data for indoor overheating risk assessment in dwellings. Build. Environ. 76, 81–91.

Taylor, J., Wilkinson, P., Davies, M., Armstrong, B., Chalabi, Z., Mavrogianni, A., Symonds, P., Oikonomou, E., Bohnenstengel, S.I., 2015. Mapping the effects of urban heat island, housing, and age on excess heat-related mortality in London. Urban Clim. 14, 517–528.

Taylor, N.A.S., 2000. Principles and Practices of Heat Adaptation. J. Human-Environment Syst. 4, 11–22.

Tennenbaum, J., Sohar, E., Adar, R., Gilat, T., 1961. The Physiological Significance of the Cumulative Discomfort Index (Cum. D.I.). Harefuah 60, 315–19.

Terjung, W.H., O'Rourke, P.A., 1981. Energy input and resultant surface temperatures for individual urban interfaces, selected latitudes and seasons. Arch. Meteorol. Geophys. Bioclimatol. Ser. B 29, 1–22.

Theeuwes, N.E., Ronda, R.J., Harman, I.N., Christen, A., Grimmond, C.S.B., 2019. Parametrizing horizontally-averaged wind and temperature profiles in the urban roughness sublayer. Boundary-Layer Meteorol. 173, 321–348.

Thom, E.C., 1959. The Discomfort Index. Weatherwise 12, 57–61.

Thorsson, S., Lindberg, F., Eliasson, I., Holmer, B., 2007. Different methods for estimating the mean radiant temperature in an outdoor urban setting. Int. J. Climatol. 27, 1983–1993.

Tillson, A.-A., Oreszczyn, T., Palmer, J., 2013. Assessing impacts of summertime overheating: some adaptation strategies. Build. Res. Inf. 41, 652–661.

Toesca, A., David, D., Kuster, A., Lussault, M., Johannes, K., 2022. An urban thermal tool chain to simulate summer thermal comfort in passive urban buildings. Build. Environ. 215, 108987.

Tong, S., Wong, N.H., Tan, E., Jusuf, S.K., 2019. Experimental study on the impact of facade design on indoor thermal environment in tropical residential buildings. Build. Environ. 166, 106418.

Tong, Z., Chen, Y., Malkawi, A., 2017. Estimating natural ventilation potential for high-rise buildings considering boundary layer meteorology. Appl. Energy 193, 276–286.

Tong, Z., Chen, Y., Malkawi, A., Liu, Z., Freeman, R.B., 2016. Energy saving potential of natural ventilation in China: The impact of ambient air pollution. Appl. Energy 179, 660–668.

Toparlar, Y., Blocken, B., Maiheu, B., van Heijst, G.J.F., 2017. A review on the CFD analysis of urban microclimate. Renew. Sustain. Energy Rev. 80, 1613–1640.

Tout, D.G., 1980. The discomfort index, mortality and the London summers of 1976 and 1978. Int. J. Biometeorol. 1980 244 24, 323–328.

TPU, 2007. Aerodynamic database for low-rise buildings. Tokyo, Japan.

TRNSYS, 2009. TRNSYS 17: Mathematical reference.

U.S. Department of Energy, 2020a. Chapter 1: Overview. In: EnergyPlus Version 9.4.0 Documentation: Engineering Reference. pp. 20–24.

U.S. Department of Energy, 2020b. Engineering Reference [WWW Document]. URL https://energyplus.net/documentation

U.S. Department of Energy, 2020c. Chapter 8: Air Heat Balance Manager / Processes. In: EnergyPlus Version 9.4.0 Documentation: Engineering Reference. pp. 58–168.

U.S. Department of Energy, 2020d. Chapter 5: Climate, Sky and Solar/Shading Calculations. In: EnergyPlus Version 9.4.0 Documentation: Engineering Reference. pp. 187–224.

U.S. Department of Energy, 2020e. Chapter 17: Simulation Models – Encyclopedic Reference. In: EnergyPlus Version 9.4.0 Documentation: Engineering Reference. pp. 1277–1325.

U.S. Department of Energy, 2020f. Chapter 13: Alternative modeling processes. In: EnergyPlus Version 9.4.0 Documentation: Engineering Reference. pp. 601–705.

U.S. Department of Energy, 2020g. EnergyPlus version 9.4.0 documentation: Input output reference.

UDA, 2018. Re-amendment to the City of Colombo development plan (amendment) – 2008.

UN, 2015. Paris Agreement.

UNEP, 2020. 2020 Global Status Report for Buildings and Construction: Towards a Zero-emission, Efficient and Resilient Buildings and Construction Sector. Nairobi.

United Nations, 2018. World Urbanization Prospects 2018 [WWW Document]. URL https://population.un.org/wup/ (accessed 6.6.22).

United Nations, 2019. World Population Prospects 2019: Highlights. New York.

Urban Development Authority of Sri Lanka, 2020. Urban Development Authority Planning & Development Regulations 2020. Colombo.

UrbaWind, 2022. URBAWIND | The urban wind modeling software - METEODYN [WWW Document]. URL https://meteodyn.com/business-sectors/microclimate-and-urban-planning/13-urba-wind.html (accessed 7.18.22).

Vallati, A., Mauri, L., Colucci, C., 2018. Impact of shortwave multiple reflections in an urban street canyon on building thermal energy demands. Energy Build. 174, 77–84.

van Hooff, T., Blocken, B., 2010. On the effect of wind direction and urban surroundings on natural ventilation of a large semi-enclosed stadium. Comput. Fluids 39, 1146–1155.

van Hooff, T., Blocken, B., Hensen, J.L.M., Timmermans, H.J.P., 2014. On the predicted effectiveness of climate adaptation measures for residential buildings. Build. Environ. 82, 300–316.

Van Nguyen, T., De Troyer, F., 2018. New surrogate model for wind pressure coefficients in a schematic urban environment with a regular pattern. Atmosphere (Basel). 9, 113.

Vartholomaios, A., 2017. A parametric sensitivity analysis of the influence of urban form on domestic energy consumption for heating and cooling in a Mediterranean city. Sustain. Cities Soc. 28, 135–145.

Vellei, M., Herrera, M., Fosas, D., Natarajan, S., 2017. The influence of relative humidity on adaptive thermal comfort. Build. Environ. 124, 171–185.

Virk, G., Mylona, A., Mavrogianni, A., Davies, M., 2015. Using the new CIBSE design summer years to assess overheating in London: Effect of the urban heat island on design. Build. Serv. Eng. Res. Technol. 36, 115–128.

Wang, B., Malkawi, A., 2019. Design-based natural ventilation evaluation in early stage for high performance buildings. Sustain. Cities Soc. 45, 25–37.

Ward, H.C., Kotthaus, S., Järvi, L., Grimmond, C.S.B., 2016. Surface Urban Energy and Water Balance Scheme (SUEWS): Development and evaluation at two UK sites. Urban Clim. 18, 1–32.

Warren, P.R., 1977. Ventilation through openings on one wall only. In: International Conference on Heat and Mass Transfer in Buildings. Dubrovnik.

Warren, P.R., Parkins, L.M., 1984. Single-sided ventilation through open windows. In: Document - Swedish Council for Building Research. p. 487.

WHO, 2016. Climate and health country profile – 2015: Sri Lanka. Geneva, Switzerland.

Winkelmann, F.C., 2001. Modeling Windows in EnergyPlus. Proc. Build. Simul. 2001 1–11.

WMO, 2017. Guide to meteorological instruments and methods of observation. WMO, Geneva.

WMO, 2018. Guide to meteorological instruments and methods of observation, 2018th ed. WMO, Geneva.

Wood, C.R., Lacser, A., Barlow, J.F., Padhra, A., Belcher, S.E., Nemitz, E., Helfter, C., Famulari, D., Grimmond, C.S.B., 2010. Turbulent Flow at 190 m Height Above London During 2006–2008: A Climatology and the Applicability of Similarity Theory. Boundary-Layer Meteorol. 2010 1371 137, 77–96.

Xiong, J., Yao, R., Grimmond, S., Zhang, Q., Li, B., 2019. A hierarchical climatic zoning method for energy efficient building design applied in the region with diverse climate characteristics. Energy Build. 186, 355–367.

Xu, K., Lu, R., Mao, J., Chen, R., Ke, X.U., Riyu, L.U., Jiangyu, M., Ruidan, C., 2019. Circulation anomalies in the mid–high latitudes responsible for the extremely hot summer of 2018 over northeast Asia. New pub KeAi 12, 231–237.

Xu, Q.S., Liang, Y.Z., 2001. Monte Carlo cross validation. Chemom. Intell. Lab. Syst. 56, 1–11.

Yamanaka, T., Kotani, H., Iwamoto, K., Kato, M., 2006. Natural, wind-forced ventilation caused by turbulence in a room with a single opening. Int. J. Vent.

Yan, D., Xia, J., Tang, W., Song, F., Zhang, X., Jiang, Y., 2008. DeST — An integrated building simulation toolkit Part I: Fundamentals. Build. Simul. 2008 12 1, 95–110.

Yang, L., Zhang, G., Li, Y., Chen, Y., 2005. Investigating potential of natural driving forces for ventilation in four major cities in China. Build. Environ. 40, 738–746.

Yang, W., Quan, Y., Jin, X., Tamura, Y., Gu, M., 2008. Influences of equilibrium atmosphere boundary layer and turbulence parameter on wind loads of low-rise buildings. J. Wind Eng. Ind. Aerodyn. 96, 2080–2092.

Yang, X., Yao, L., Peng, L.L.H., Jiang, Z., Jin, T., Zhao, L., 2019. Evaluation of a diagnostic equation for the daily maximum urban heat island intensity and its application to building energy simulations. Energy Build. 193, 160–173.

Yang, X., Zhao, L., Bruse, M., Meng, Q., 2012. An integrated simulation method for building energy performance assessment in urban environments. Energy Build. 54, 243–251.

Yao, R., Li, B., Steemers, K., Short, A., 2009. Assessing the natural ventilation cooling potential of office buildings in different climate zones in China. Renew. Energy 34, 2697–2705.

Yin, W., Zhang, G., Yang, W., Wang, X., 2010. Natural ventilation potential model considering solution multiplicity, window opening percentage, air velocity and humidity in China. Build. Environ. 45, 338–344.

Yoon, N., Norford, L., Malkawi, A., Samuelson, H., Piette, M.A., 2020. Dynamic metrics of natural ventilation cooling effectiveness for interactive modeling. Build. Environ. 180, 106994.

You, W., Qin, M., Ding, W., 2013. Improving building facade design using integrated simulation of daylighting, thermal performance and natural ventilation. Build. Simul. 6, 269–282.

Zhang, A., Gao, C., Zhang, L., 2005. Numerical simulation of the wind field around different building arrangements. J. Wind Eng. Ind. Aerodyn. 93, 891–904.

Zhang, R., Lam, K.P., Yao, S., Zhang, Y., 2013. Coupled EnergyPlus and computational fluid dynamics simulation for natural ventilation. Build. Environ. 68, 100–113.

Zhang, Y., Lin, K., Zhang, Q., Di, H., 2006. Ideal thermophysical properties for free-cooling (or heating) buildings with constant thermal physical property material. Energy Build. 38, 1164–1170.

Zhong, H.Y., Sun, Y., Shang, J., Qian, F.P., Zhao, F.Y., Kikumoto, H., Jimenez-Bescos, C., Liu, X., 2022. Single-sided natural ventilation in buildings: a critical literature review. Build. Environ. 212.

Zingre, K.T., Wan, M.P., Tong, S., Li, H., Chang, V.W.C., Wong, S.K., Thian Toh, W.B., Leng Lee, I.Y., 2015. Modeling of cool roof heat transfer in tropical climate. Renew. Energy 75, 210–223.

Zune, M., Tubelo, R., Rodrigues, L., Gillott, M., 2021. Improving building thermal performance through an integration of Passivhaus envelope and shading in a tropical climate. Energy Build. 253.